Superior Pinning Properties in Nano-Engineered $YBa_2Cu_3O_{7-\delta}$

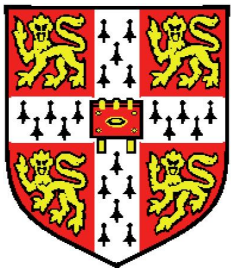

Giorgio Ercolano

Department of Materials Science & Metallurgy

Corpus Christi College

This dissertation is submitted for the degree of

Doctor of Philosophy

2011

Si qui forte mearum ineptiarum
lectores eritis manusque uestras
non horrebitis admouere nobis...

Declaration

I declare that, except where otherwise stated, this dissertation is the result of my own work and includes nothing which is the outcome of work done in collaboration.

No part of this dissertation had been submitted at Cambridge or any other University for a degree, diploma or other qualification.

The length including tables, footnotes, bibliography and appendices do not exceedes the limit of 60000 words.

Giorgio Ercolano
Cambridge
April 2011

Acknowledgements

This dissertation describes the research work on controlled nano-engineering of high temperature superconducting materials carried out at Cambridge University Materials Science and Metallurgy Department in the Device Materials Group between November 2007 and February 2011.

I would like to express my gratitude to my supervisor, Prof. Judith MacManus-Driscoll, for the help and valuable advice provided during this project.

I would also like to acknowledge...

Dr Stuart Wimbush *for the helpfull discussions on nanoinclusions flux pinning and on the vortex path model*

Dr John Durrell and Dr Marcus Weigand *for the trainings and help on microfabrication and critical current measures*

Dr Sophie Harrington *for the helpfull discussions on pulsed laser deposition of doped* $YBa_2Cu_3O_{7-\delta}$ *thin films and target preparation*

Dr Marco Bianchetti *for the practical help with the photolithography and critical currents characterisation of the thin films and for the usefull discussions*

Prof. Haiyan Wang, Joon Lee Hwan and Dr Lata Sahonta *for the amazing TEM work*

Dr Xavier Moia and Dr Thomas Fix *for the valuable discussions on structural data interpretation*

Dr Nadia Stelmashenko *for the help with the atomic force microscope*

Mary Vickers *for the help with the x-ray diffraction analysis*

and Dr Lara San-Emeterio-Alvarez, Dr David Muoz-Rojas, Diana Iza, Oon Jew Lee and Dr Sohini Kar *for the support*

The work described in this dissertetion was supported by NESPA, Nano-Engineered Superconductors for Power Application, a framework of the Marie Curie Research Training Network, funded within the EUs 6° framework program.

Superior Pinning Properties in Nano-Engineered $YBa_2Cu_3O_{7-\delta}$

Giorgio Ercolano

Large electrical current transport in the absence of energy losses is the key factor in commercial applications of high temperature superconductors. This thesis demonstrates an easy and inexpensive bottom-up technique to produce self assembled nanorods, segmented nanorods as well as nanoparticles in $YBa_2Cu_3O_{7-\delta}$ thin films grown by pulsed laser deposition. The structural and morphological characteristic of the pinning landscapes produced are investigated and correlated to their effects on the superconducting properties of the thin films.

In particular two pinning landscapes are investigated: Ba_2YNbO_6 nanorods are grown in $YBa_2Cu_3O_{7-\delta}$ thin films using a Ba_2YNbO_6 doped $YBa_2Cu_3O_{7-\delta}$ pulsed laser deposition targets and $Ba_2(Y/Gd)(Nb/Ta)O_6$ segmented nanorods together with $(Y/Gd)_2O_3$ nanoparticles are grown in $(Y/Gd)Ba_2Cu_3O_{7-\delta}$ thin films using a Ba_2YNbO_6 + Gd_3TaO_7 doped $YBa_2Cu_3O_{7-\delta}$ pulsed laser deposition targets.

The Ba_2YNbO_6 + $YBa_2Cu_3O_{7-\delta}$ is deeply characterised and the effects of the deposition parameters are analysed. Ba_2YNbO_6 is demonstrated to be an interesting novel pinning addition capable to increase the critical current and to reduce the $YBa_2Cu_3O_{7-\delta}$ critical currents angular dependencies anisotropy.

The Ba_2YNbO_6 + Gd_3TaO_7 + $YBa_2Cu_3O_{7-\delta}$ is found to produce a new complex pinning landscape extremely effective. At high fields the synergetic combination of the different defects typology is shown

to generate an interesting new feature in the critical current angular dependencies.

Chapter 1 is an introduction to superconductivity, the fundamentals of the field are briefly presented. In chapter 2 the discussion in focused on pinning in high temperature superconductors. Cuprates and in particular $YBa_2Cu_3O_{7-\delta}$ are presented. The pinning phenomenon and the practical pinning engineering in thin films is also discussed in this chapter. Chapter 3 describes the thin films preparation methods and the characterisation techniques used in the research work. Chapter 4 and 5 are focused on the Ba_2YNbO_6 doped $YBa_2Cu_3O_{7-\delta}$ thin films. Chapter 4 is an introduction to Ba_2YNbO_6 doped $YBa_2Cu_3O_{7-\delta}$, the preliminary results obtained on Ba_2YNbO_6 doped $YBa_2Cu_3O_{7-\delta}$ thin films are shown in this chapter. The crystalline structure, the morphology and the superconducting properties of thin films deposited adopting different deposition parameters are analysed and discussed in chapter 5. In chapter 6 the new complex pinning landscape of $Ba_2(Y/Gd)(Nb/Ta)O_6$ and $(Y/Gd)_2O_3$ in $(Y/Gd)Ba_2Cu_3O_{7-\delta}$ is presented. Concluding remarks on the research described in the work ends the thesis in a brief final chapter 7.

Contents

List of Figures

Chapter 1

Introduction

Superconductivity, a state of matter with a century of history. In the introduction of this dissertation is presented a road map of the main scientific milestones in superconductivity, from its discovery in 1911 to the latest high temperature superconductor discovered.

1.1 The discovery of superconductivity

First discovered by the Nobel prize winner H. Kamerling Onnes [7], the superconductive state is characterized by one of the most intriguing properties of matter, the capacity to transport an electric current without the appearance of any resistive process. In other words the possibility to transfer and transform energy with reduced losses.

H. K. Onnes was awarded the Nobel Prize in Physics in 1913 *"for his investigations on the properties of matter at low temperatures which led, inter alia, to the production of liquid helium"*. In 1908 he was the first scientist able to liquefy helium [8]; in 1911, during his following investigation on the properties of matter at low temperature, he wrote about *The Disappearance of the resistance of mercury*. He discovered that the resistance of mercury becomes practically zero when this is cooled below 4.2 K [9]. Onnes realized that zero resistance was a new property that would have characterized a different state of matter, as a matter of the fact in his Nobel lecture he said *"the mercury at 4.2 K has entered a new*

state, which owing to its particular electrical properties, can be called the state of superconductivity."

1.2 The Meissner effect and the London penetration depth

Another milestone in the superconductivity history was the discovery of the Meissner effect, in 1933 Walther Meissner and Robert Ochsenfeld, during their researches on the magnetoelectric properties of matter *in very low temperatures*, observed a sudden change in current distribution and in magnetic induction at the beginning of superconductance. They discovered that tin and lead samples expel the magnetic field when cooled below the transition temperature, in other words when the transition from normal to superconductive state occurs [10].

One of the main implications of the Meissner effect is that superconductivity is something different from perfect conductivity. If two different samples, a superconductor and an ideal perfect conductor, are cooled in their zero resistance state and after that an external magnetic field is applied, both the sample would react to the external magnetic field in the same way. The rise of Faraday shielding superficial currents would prevent the penetration of the external magnetic field in the samples. On the other hand if the same two samples are cooled in their zero resistance state while the field is applied, the magnetic field distribution would not change in the perfect conductor, because there would be no induced electromotive force, instead the superconductor will expel the flux also in this second scenario (figure 1.1).

A superconducting phase does not allow magnetic flux density to exist whether it is field cooled or not, even a magnetic flux preexisting the transition will be expelled.

A few years later, in 1935, a theoretical description of the Meissner effect was found by Fritz and Heinz London [11]. They were able to relate the current distribution to the electromagnetic field. A key factor in the London brothers research was the definition of the magnetic flux penetration depth. Flux expulsion is related to the presence of screening currents. Since only a finite current density

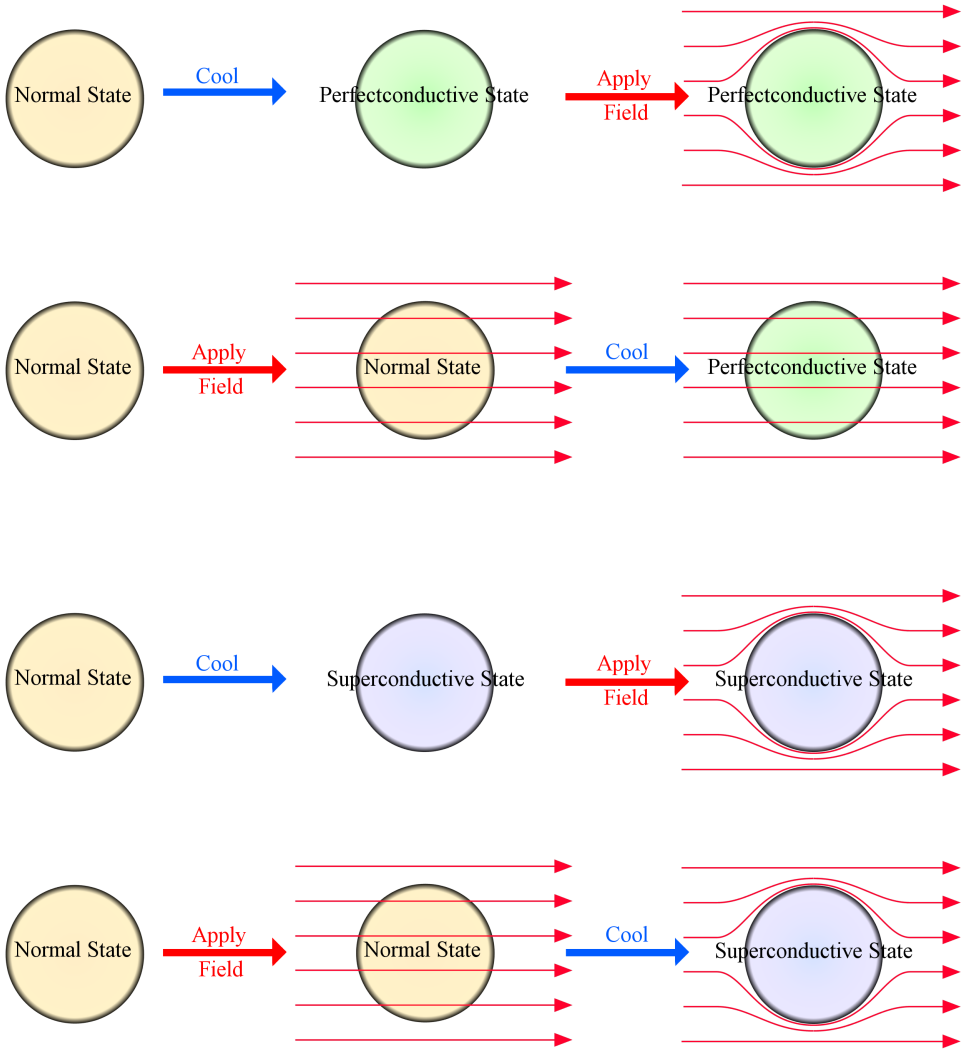

Figure 1.1: Differences in magnetisation behaviours of a perfect conductor and a superconductor, the Meissner effect. a) Perfect conductor cooled in zero field; b) Perfect conductor cooled in applied magnetic field; c) Superconductor cooled in zero field; d) Superconductor cooled in applied magnetic field.

can be carried in a superconductor, a surface layer in which the screening currents flow has to have a finite thickness. For this reason the magnetic flux density does not decay abruptly at the superconductor surface, but decays gradually penetrating the material. The flux penetration depth, λ, is commonly called the London penetration depth. In simple geometries λ is the characteristic length over which the field density decays exponentially.

1.3 Critical magnetic field, critical current density. Two types of superconductors

From an experimental point of view it was clear that the superconductive state disappears when a sufficiently large magnetic field is applied. The field at which the superconductivity is destroyed is called the critical magnetic field, and it is usually denoted as H_c. This field value is strictly related to another fundamental value, the critical current density. If an increasing magnetic field is applied to a superconductor the shielding currents will also increase to produce a zero magnetic flux density, H_c is the value at which the shielding current density reaches the critical value (J_c). When the applied external field strength is equal to H_c the superconductor is incapable of carrying any transport current, this is due to the fact that the total current is the sum of both shielding and transport currents thus if the shielding current has reached the J_c no others current can be added without exceed the critical current density and therefore destroy the superconductivity.

In 1950 Vitaly Lazarevich Ginzburg and Lev Davidovič Landau developed a mathematical phenomenological theory to model superconductivity [12]. The theory, describes the macroscopic phenomena in superconductivity relying on general thermodynamics arguments. Despite the lack of explanation of the microscopic mechanisms of superconductivity this theory was fundamental to understand the differences between two main classes of superconductors. Based on the general theory of the second order phase transitions proposed by Landau in 1937, the main variable of the model is the "order parameter" ψ which has a finite value below the transition and zero above it. One of the key results of the model is the definition of two characteristic length: the coherence length and penetration

depth. The coherence length ξ, expresses the distance over which the order parameters can differ by a significant amount, in other words represents the distance over which a superconductive phase can become normal. The penetration depth is the characteristic length over which the field density decays, the same characteristic length derived in the London theory. The Ginzburg-Landau equations allow the calculation of the energy associated to the formation of a boundary between a normal region and a superconducting region, thus it is possible to predict at which ξ/λ ratio such a boundary is thermodynamically favored. The equations of the theory depend only on the dimensionless material constant, κ, defined as the ratio between λ and ξ.

The energy associated to the formation of a boundary between a normal region and a superconductive region is at the base of Alexei A. Abrikosov prediction of a mixed state in which superconductivity and magnetic flux coexist. It was known that for κ values above $1/\sqrt{2}$ the surface energy between the superconducting and normal layers would have been negative. Abrikosov decided to solve the Ginzburg-Landau equations for κ values above $1/\sqrt{2}$. He found that the magnetic flux and superconductivity could indeed coexist as an array of cylinders of normal conducting material parallel to the field direction surrounded by shielding current vortices in a matrix of superconducting material, the geometric features of this array strongly depend on temperature and field strength [13]. He stated that *"in the case $\kappa >> 1$ ($\lambda >> \xi$) every vortex has a "core" of size ξ, where the order parameter varies rapidly, and the outer region of the size λ where the magnetic field decays to zero"* [14] (figure 1.2). Between current vortices a repulsive force arises and the normal core are usually ordered in triangular or square lattice [15, 16].

The last outstanding result of Abrikosov's calculations was that the magnetic flux passing through an area bounded by a superconducting electrical current is quantized and that the quantum of magnetic flux is a constant ϕ_0, it is independent from the material as long as it is superconductive. This quantized flux is normally referred as a fluxon ($\Phi_0 \approx 2.067 \times 10^{-15}$ Wb).

The presence of the mixed state is confirmed by the magnetization behaviour of type II superconductors that is different from that of type I. A type II superconductor has two different critical field strength values: the lower critical field,

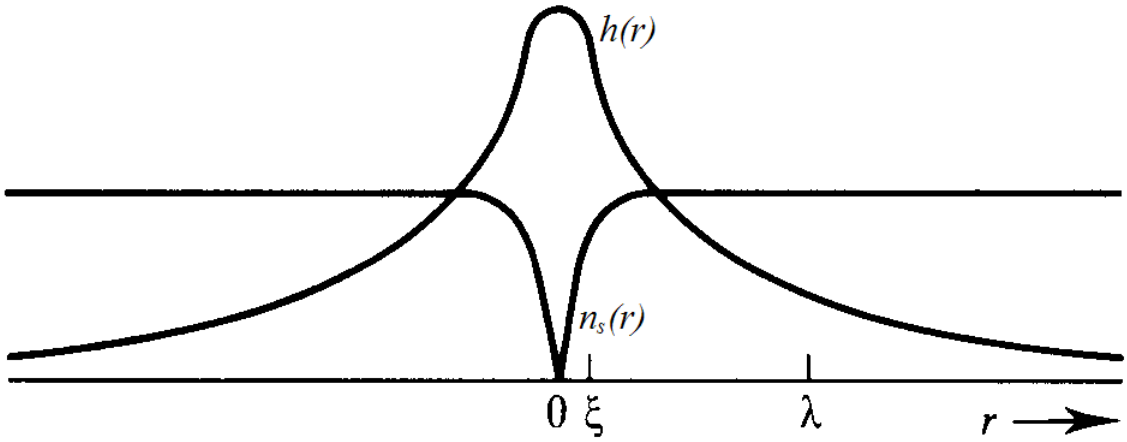

Figure 1.2: Structure of an isolated Abrikosov vortex [1]

H_{c1}, that is the value below which the Meissner effect is present and the entire magnetic flux is expelled, and the upper critical field, H_{c2}, that is the value above which superconductivity is destroyed. For fields value between H_{c1} and H_{c2} a type II superconductor is in the mixed state predicted by Abrikosov (figure 1.3).

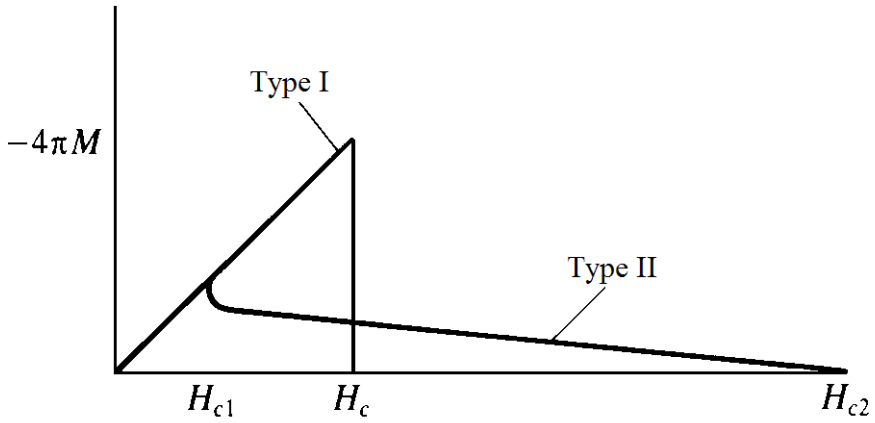

Figure 1.3: Magnetisation curves for a type I and a type II superconductor [1]

1.4 Finally a microscopic theory of superconductivity

Since the discovery of superconductivity most of the brilliant minds of the twentieth century theoretical physics tried to find a microscopic theory to explain the phenomenon and failed. Almost fifty years passed from the the discovery of the phenomenon to the publication of a microscopic theory of superconductivity. In 1957 Bardeen, Cooper and Schrieffer published their theory on a paper entitled *"Theory of Superconductivity"* [17], the theory, known as the BCS theory after the scientist initials, explain *"a second-order phase transition at the critical temperature, T_c an electronic specific heat varying as $exp(-T_0/T)$ near $T = 0K$ and other evidence for an energy gap for individual particle-like excitations, the Meissner-Ochsenfeld effect ($B = 0$), effects associated with infinite conductivity ($E = 0$), and the dependence of T_c on isotopic mass, $T_c\sqrt{M} = const.$"*

The theory is based on the coupling of electrons in *Cooper pairs* [18] due to phonon-electron interactions. The interactions between the vibrations of the lattice and the electrons generate an attractive force, when this interaction overcome the Coulomb repulsive interaction the coupling is probable. In the BCS this coupling of the electron leads to the formation of a gap in the electrons energy band, thus any further interactions with an associated energy lower than the gap can not occurs. In a superconductor below T_c the scattering of coupled electron by the lattice (dissipative process) has an associated energy that is lower than the gap, thus it does not happen.

The BCS theory is a rigorous quantum mechanical description of the superconductive phenomenon, a more detailed description of the theory would require a discussion which goes beyond the intent of this chapter.

1.5 The high temperature superconductors revolution

Since Onnes discovery only metallic materials (mainly type I superconductors) and metal alloys (mainly type II superconductors) were thought to be supercon-

ductive. From 1986 onward an acceleration in the scientific achievements leaded to discovery of different families of superconductors.

In 1986 Johannes Georg Bednorz and Karl Alexander Müller discovered high T_c superconductivity in the Ba-La-Cu-O system [19], a year later they were awarded with the Noble prize in Physics *"for their important breakthrough in the discovery of superconductivity in ceramic materials"*. The discovery of the first cuprate based ceramic superconductor with a T_c of 30 K obtained a considerable interest and started an incredible and productive research race. The result of this intellectual spring was the achievement of T_c above 100 K that were considered impossible only a few years before. In 1987 the Y-Ba-Cu-O system was discovered, $T_c = 93$ K [20], was the first material to be in a superconductive state above the liquid nitrogen boiling temperature. A year later two other cuprates were discovered to be superconductive at even higher temperatures, the Bi-Sr-Ca-Cu-O with a T_c of 108 K [21] and the Tl-Ca/Ba-Cu-O with a T_c of 120 K [22]. These materials are hard to process, but the high-T_c together with the high H_c and J_c made of these materials the ideal candidates for most practical applications. However, despite the large amount of research and published work, a complete theoretical knowledge of this class of superconductors is still missing, in particular the superelectron condensation mechanism is still unknown.

In the last few years other two non-cuprate materials were discovered to be superconductive and deserve a mention for the interest that the scientific community has shown to these newcomers. Magnesium Diboride, T_c of 39 K, discovered in 2001 [23] is interesting for the low-cost of the raw material and for the cable manufacturing process easy and inexpensive when compared to that of cuprates based cables [24–27]. And last, a new family of iron-based superconductors was discovered in 2006 [28], as with the Bednorz-Müller discovery of cuprates this discovery started a productive race in the search of similar compounds with better properties [29–32]. However in this case after four years the compound with the highest T_c of the family is still below the liquid nitrogen boiling point: the samarium-doped Sr-Fe-As-F has a T_c of 56 K [33].

Chapter 2

Pinning in $YBa_2Cu_3O_{7-\delta}$ thin films

$YBa_2Cu_3O_{7-\delta}$ is undoubtedly one the most promising materials to use in high temperature superconducting cables. Companies and research centers are currently working and studying to achieve better performances, lower production costs and a wider understanding of the physical processes that limit loss less current transport capability.

2.1 Cuprates

The two most studied superconductors based on cuprate perovskites are the YBCO ($YBa_2Cu_3O_{7-\delta}$) and the BSCCO system, the most common superconductors used from the BSCCO system are the Bi-2212 ($Bi_2Sr_2CaCu_2O_8$) and the Bi-2223 ($Bi_2Sr_2Ca_2Cu_3O_{10}$). Cuprates are considered as extreme type II superconductors and show an intrinsic anisotropy, a layered structure and an extremely small coherence length ξ of the order of a few nm. The small ξ implies a large upper critical field, considering that at H_{c2} the normal cores are as densely packed as the coherence length limit allows and that each core carries a quantized flux ϕ it is possible to estimate the upper critical field value as:

$$H_{c2} = \frac{\phi}{\pi\xi^2} \tag{2.1}$$

On the other hand disorder on the atomic scale can influence the superconductive properties.

2.1.1 Weaklinks and the texturing of cuprates

Despite the large critical current densities measured for $YBa_2Cu_3O_{7-\delta}$ single crystals, or for epitaxial $YBa_2Cu_3O_{7-\delta}$ films on single crystals ($J_c > 10^6 MAcm^{-2}$ at 4.2 K) [34, 35] one of the main problems that kept $YBa_2Cu_3O_{7-\delta}$, away from the production of superconducting cables were the low J_c values measured and in general the poor connectivity in polycrystalline samples [36]. Soon it became clear that the critical current densities across grain boundaries are a function of the misorientation angle of the grains' crystalline lattices. The ratio of the grain boundary critical current density to the critical current density in the grains varies by two orders of magnitude, changing from almost 1 when the grain are well aligned to a drastically reduced value of about $\frac{1}{50}$ when the grains tilt angle is above 20 [37].

The BSCCO cuprates show similar behaviours [38], however a self texturing process, that aligns the grains when the BSCCO wires are produced by a simple *"powder in tube"* method, minimize the problematic related to the weaklinks of the cuprates. The self grain alignment is the reason why large critical current densities were "easily" obtained in the BSCCO conductors [39] while, when similar method were applied to the $YBa_2Cu_3O_{7-\delta}$, only rather low critical current densities were achieved [40, 41]. Due to this fact, despite the higher J_c, the lower anisotropy and the better in-field performance of the epitaxial $YBa_2Cu_3O_{7-\delta}$ films [35], the first cuprate based superconductors to enter the market were the BSCCO tapes.

Today a second generation of coated conductors is entering the scene. These new high temperatures superconducting cables are based on $YBa_2Cu_3O_{7-\delta}$. The texturing issues were solved adopting two new production techniques: epitaxial $YBa_2Cu_3O_{7-\delta}$ on highly textured buffer layers deposited by using ion beam assisted deposition (IBAD) [42] and epitaxial $YBa_2Cu_3O_{7-\delta}$ on rolling-assisted biaxially-textured substrates (RABiTS) [43]. In both the process the $YBa_2Cu_3O_{7-\delta}$ is deposited epitaxially on a textured buffer layer. In the IBAD

technique the texturing is obtained during the buffer layer deposition while in the RABiTS the substrate (usually a nickel alloy) is textured by a thermo-mechanical treatment before the buffer layer deposition [44].

Once the production of long length textured $YBa_2Cu_3O_{7-\delta}$ conductors was achieved the $YBa_2Cu_3O_{7-\delta}$ has become the cuprate in use in new coated superconductors, thus an optimisation of the material properties has become one of the most important topics.

2.2 $YBa_2Cu_3O_{7-\delta}$

An interesting and complex crystal structure underlie the excellent $YBa_2Cu_3O_{7-\delta}$ properties. For this reason any optimal description of the material has to start with a description of the crystalline structure.

2.2.1 Crystal structure

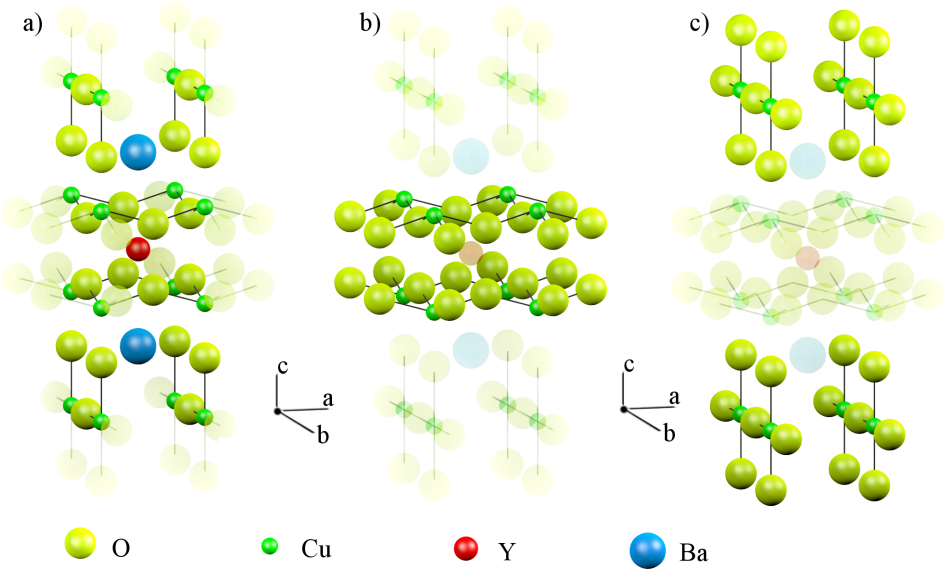

Figure 2.1: a) Crystal Structure of $YBa_2Cu_3O_{7-\delta}$; b) CuO_2 planes; c) CuO chains.

The $YBa_2Cu_3O_{7-\delta}$ crystal structure is described in figure 2.1a, it is an orthorhombic, distorted, oxygen deficient perovskite [45].

The lattice parameters of this orthorhombic structure are $a = 0.3822$ nm, $b = 0.3891$ nm and $c = 1.1677$ nm [46, 47]. The lattice difference between a and b is small enough to allow epitaxial growth of $YBa_2Cu_3O_{7-\delta}$ on cubic substrates. As a result a large number of twin boundaries are usually formed [48, 49], therefore the results of most of the macroscopic measurements are an average of the properties measured over the a and b directions. However since the anisotropy within the ab-plane is small usually an uniaxial anisotropy ab-plane c-axis is assumed.

Another usual description of the crystal structure is focused on the Cu-O system. In this description $YBa_2Cu_3O_{7-\delta}$ is pictured as a layered structure made of two distorted planes of Cu-O_2 separated by Y^{+3} ions, and Cu-O copper chains coordinated with Ba^{+2} ions at the edge of the unit cell. The Cu-O_2 copper planes are evidenced in figure 2.1b and the Cu-O copper chains in figure 2.1c.

2.2.2 Oxygen deficiency

Oxygen content is a key factor in $YBa_2Cu_3O_{7-\delta}$ as it determines to the structure and properties of the materials [2, 50, 51]. A detailed study of the effects of the oxygen content on the superconductive properties as well as the crystal structure was published in 1990 by Cava R J *et al.* [2].

The key results of their work was the discovery that on changing the oxygen content form 7 to 6 (δ changes from 0 to 1) the $YBa_2Cu_3O_{7-\delta}$ shows changes in T_c from 92 K to 60 K followed by the disappearance of superconductivity (figure 2.2a) as well as a structural transition from orthorhombic to tetragonal (figure 2.2b). Furthermore Cava R J *et al.* found that the oxygen content variation involves only the oxygen sites along the Cu-O chains.

A direct consequence of this knowledge is that good oxygenation is crucial to achieve high T_c and that any effort to improve the $YBa_2Cu_3O_{7-\delta}$ performance has to take into account the importance of oxygen content. As a matter of fact most of the $YBa_2Cu_3O_{7-\delta}$ production processes include an annealing step in a concentrated oxygen environment.

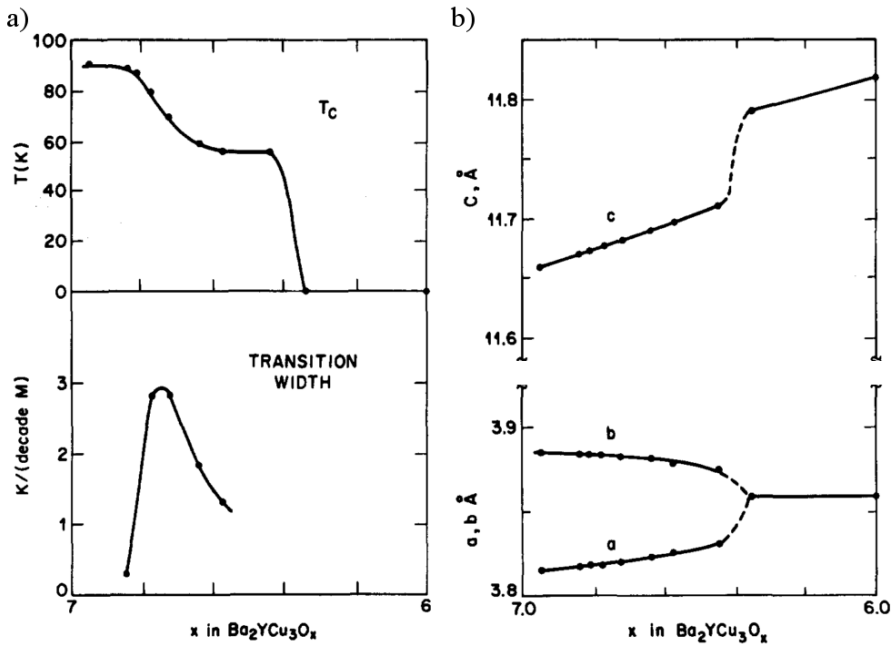

Figure 2.2: a) Superconductive transition temperature T_c for ten samples of Ba_2YCuO_x with varying x values; b) Refined crystallographic cell parameters for Ba_2YCuO_x with varying x values; from [2].

2.3 Pinning

In $YBa_2Cu_3O_{7-\delta}$ the loss-less current transport capabilities are usually also limited by the mobility of the Abrikosov vortices. More deeply the critical current density is determined by complex interactions between the transport currents and the induced magnetic flux lines and the interactions between the flux lines and the nanostructure of the materials.

Vortex phenomena is a complex field of solid state matter which is still evolving. The aim of this section is to give a brief introduction to the phenomenon in order to understand the possible interactions, and the improvements that an engineered nanostructure can induce on the critical currents. The following brief introduction is based on an exhaustive description of the phenomenon that was published in 1994 by Blatter G. *et al.* [52].

2.3.1 The dissipative phenomenon

When a transport current is applied, the flux lines start to move. The movement is due to the action of the Lorentz force (note that c is a constant and η is the friction coefficient):

$$F_L = j \wedge B/c \tag{2.2}$$

$$f_L = (\Phi_0/c) j \wedge n \tag{2.3}$$

In the absence of external flux pinning mechanisms the only counter force is the friction force:

$$F_\eta = -\eta v \tag{2.4}$$

At the equilibrium v is the steady-state velocity and $F_L = F_\eta$ thus v can be derived as:

$$v = j \wedge B/c\eta \tag{2.5}$$

The flux motion generate a finite electric field E:

$$E = B \wedge v/c \tag{2.6}$$

A finite electric field coexisting with a current density generate a dissipation, E and j are parallel thus the power dissipated is:

$$P = (j \wedge B)^2/c^2\eta \tag{2.7}$$

In a scenario where the friction force is the only force opposing the Lorentz force it would be impossible to realize a dissipation-free current flow.

2.3.2 Dissipation-free current flow, the pinning force

To achieve a dissipation-free current flow, the flux lines have to be pinned in place. In other words v has to be equal 0 also when $F_L \neq 0$. An additional static force, a pinning force F_{pin}, has to counter the Lorentz force and be active when the flux lines are not moving ($v = 0$).

The flux lines interact with any defects in the lattice. Since the formation of a normal region leads to the loss of the condensate state increasing the energy associated to the system, any region of the material in which the superconducting order parameter is already depressed constitute a region in which the presence of a flux line is energetically favourable. Therefore any region in which the superconducting order parameter is depressed will contribute to a finite pinning force density F_{pin}.

The critical current density is the current at which the Lorentz force is equal to the pinning force since any further increment of the current flow would lead to an imbalanced increment of the Lorentz force ($F_L > F_{pin}$) and subsequently a flux motion ($v \neq 0$) and power dissipation. Therefore assuming $F_L = F_{pin}$ and $j \perp B$, J_c can be derived as:

$$j_c = cF_{pin}/B \tag{2.8}$$

In order to increase J_c it is necessary to increase the pinning force F_{pin}.

2.3.3 Defects as pinning centers

A single flux line can interact with different class of defects [53, 54]. Each class is characterised by a characteristic dimension. Defects smaller than ξ in each dimension are called point defects and the saved condensation energy is proportional to the defect volume. In anisotropic materials, since ξ is a function of direction, the pinning force provided by this class of defects is also a function of the force direction. Defects with one dimension larger than the others are named linear defects while defects with two dimensions larger than the other are planar defects. In high temperature superconductors naturally occurring defects like dislocation are linear defects and act like pinning lines while twin planes, stacking faults are planar defects and act as pinning planes. In $YBa_2Cu_3O_{7-\delta}$ and cuprates in general the layered crystal structure and the consequent ordered stacking of layers with different superconducting order parameter are an additional array of pinning planes parallels to the *ab*-planes of the crystal figure 2.1.

Linear and planar defects, as well as defects with specific spatial arrangements can lead to directional pinning, increasing the pinning potential with respect to a specific direction of the applied magnetic field. As an example the pinning force provided by a dislocation to a flux line will be higher if the flux line and the dislocation are parallel. In the same way, an ordered array of nanoparticles can act as a linear defect providing the higher pinning potential to flux lines that are able to penetrate the sample in the same direction of the array.

In conventional $YBa_2Cu_3O_{7-\delta}$ thin films the J_c is the highest when measured with the applied magnetic field parallel to the *ab*-planes of the crystal. This is a direct consequence of the directional planar pinning provided by the specific cuprates layers.

A last thing to note is that, even if the single interactions between flux lines and defects are at the base of the material response, in most field values and temperature conditions (especially high temperatures) the materials properties are given by the simultaneous interactions of many flux lines with many different defects [55,56]. For this reason a theoretical approach to describe the overall material behaviour is usually too complex, thus an experimental approach is usually more productive when dealing with pinning engineering. Nevertheless the theo-

retical achievements greatly enhance the understanding of the physics processes underling the complex behaviours of pinning engineered enhanced superconductors.

2.4 Practical Pinning Engineering

Defects engineering of $YBa_2Cu_3O_{7-\delta}$ to increase the J_c values has been and is today one of the hot topics of superconductive materials science. Large electrical current transport in absence of energy losses is the key factor in commercial application of high temperature superconductors. Since energy losses arise from vortices movements a solution has been researched in nanostructured defects landscape capable to pin the vortices in place. The higher is the efficiency of the pinning landscape the higher is the current value threshold at which the losses appears.

Different pinning landscapes and different techniques have been adopted during the years by researchers, in the following sections an overview of the most interesting works is given.

2.4.1 Non superconducting secondary phase addition

The secondary phase addition is an attractive way to introduce defects. It can be adopted both in films grown by physical processes and in films grown by chemical processes.

The first example of pinning engineering in $YBa_2Cu_3O_{7-\delta}$ thin films by the introduction of a non superconducting epitaxial second phase is the addition of $BaZrO_3$ [57]. MacManus-Driscoll *et al.* in 2004 were able to produce high quality $YBa_2Cu_3O_{7-\delta}$ thin films with improved J_c (up to a factor of 5) in the magnetic field by introducing $BaZrO_3$ powder in a Pulsed Laser Deposition (PLD) target of $YBa_2Cu_3O_{7-\delta}$. They achieved an epitaxial growth of a cubic non-superconducting phase in an epitaxial grown high quality $YBa_2Cu_3O_{7-\delta}$ thin film. An improvement of both the random and directional pinning was obtained. In particular a large increment of J_c was measured with the magnetic field applied parallel to the c-axis of the film. Furthermore, by using TEM (Transmission Electron Microscopy)

analysis, *c*-axis oriented columnar defects were found evidencing the correlation between the defects landscape and the pinning potential. This pioneering work is the first of a long series of research articles aiming to produce the ideal pinning landscape adopting a standard industrial ready deposition technique and avoiding technological complications [58–63].

$BaZrO_3$ is not the only secondary phase to produce columnar defects, during the years also $BaSnO_3$ [64–66], RE_3TaO_7 [67], Ba_2YTaO_7 [68] where found to produce similar columnar defects. All these phases produce *c*-axis oriented columns, but the mean width, the spacing and the linearity of the columnar defects produced varies. The variation is dependent on both the phase and the process parameters adopted. A common feature of all this heteroepitaxial columnar defects is the perovskite crystal structure with the only exception of a pyrochlore phase (RE_3TaO_7 [67]).

In this work the same technique is used to produce nanostructured $YBa_2Cu_3O_{7-\delta}$ thin film with superior pinning properties adopting a Nb based perovskite as secondary phase as well as in a Nb and Ta simultaneous addition that will result in the complex ideal pinning landscape that will be described later in the thesis.

When giving also a small overview of the milestones in the $YBa_2Cu_3O_{7-\delta}$ pinning engineering fields the achievements obtained in chemical solution nanostructured $YBa_2Cu_3O_{7-\delta}$ films have to be reported. Gutierrez *et al.*, in 2007, were able to obtain a dense nanodispersion of defects in $YBa_2Cu_3O_{7-\delta}$ thin films by introducing $BaZrO_3$ [69]. In their work an entirely chemical process was adopted and randomly oriented $BaZrO_3$ nanoparticles were reported as the basis of a strong isotropic pinning.

Another widely used technique used to produce pinning enhanced $YBa_2Cu_3O_{7-\delta}$ is the multiple target ablation in pulsed laser deposition [70–73]. A secondary phase can be introduced by ablating multiple targets in a so called pseudo-multilayer deposition [70,71]. Haugan *et al.* were able to improve the pinning properties of $YBa_2Cu_3O_{7-\delta}$ by introducing particles of nanometric size of YBa_2CuO_5 (referred as 211) by growth of alternating layers of ultra thin 221 and $YBa_2Cu_3O_{7-\delta}$ [70]. This multiple bilayer structures were obtained by ablating in sequence a target made of pure $YBa_2Cu_3O_{7-\delta}$ and a target of pure YBa_2CuO_5 us-

ing a computer driven target's carousel. Adopting the same technique Campbell *et al.* deposited Y_2O_3 - $YBa_2Cu_3O_{7-\delta}$ pseudo-multilayer films achieving similar results to Haugan [71].

Recently a Nb doped $YBa_2Cu_3O_{7-\delta}$ was also produced adopting the multiple target deposition [74].

Multiple target ablation, when compared to single composite target ablation, has the advantage of having a certain degree of control over some dispersion parameters allowing a change in the number of laser pulses for each layer (the amount of material deposited from each target), and, in theory some control can also be achieved on the deposition parameters adopted for each target. In practice the change of certain deposition parameters like oxygen pressure or substrate temperature during the film deposition would over complicate the deposition process, therefore in almost all the works adopting this technique the only parameters that are tuned during the secondary phase target ablation are pulse frequency and laser energy.

2.4.2 Alternative routes

Other possible routes to increase defects concentration in $YBa_2Cu_3O_{7-\delta}$ thin films have been experimented in recent years and deserve citation. The first is substrate decoration which can be achieved adopting different techniques. The idea is to deposit nanoparticles or nanoislands on the substrate before the $YBa_2Cu_3O_{7-\delta}$ film []. The nanoparticles can be deposited by pulsed laser deposition [75–80], sputtering [81–84] or even with gas-phase prepared nanoparticles [85] and TFA-MOD [86]. These particles will then induce stresses and therefore defects in the film by introducing distortions at the substrate-film interface.

The last two techniques differ from the others as they are not based on the addition of a secondary phase. Improved pinning can be achieved by exchanging a certain amount of Y with different rare-earth elements [87]. Enhanced low-field pinning is shown by mixed rare-earth barium cuprate films, while Y based film with large radius rare-earth elements substitution have improved pinning up to at least 7 T. Irradiation with high energy heavy ions has also been adopted in $YBa_2Cu_3O_{7-\delta}$ single crystal pinning research [88–93] and in thin film studies

[94–99] for its capability to introduce linear defects along the ballistic directions. Despite the interesting and unique features of this technique its high complexity make the irradiation process unpractical.

Chapter 3

Experimental Techniques

This chapter describes the experimental techniques adopted in the sample preparation and characterisation. The first section will focus on the sample deposition followed by a description of the micro bridge patterning together with the electrode deposition. The structural and morphological characterisation techniques are described in the second section. These measurements are mainly performed on unpatterned samples (as deposited samples), and with the only exception of the TEM are non destructive measures. The last section of the chapter describes the transport measures, these are the main characterisation of the superconducting properties.

3.1 Sample Preparation

As anticipated in the previous chapter, the nanostructuring technique adopted in this thesis is the introduction of one or more secondary phases in the $YBa_2Cu_3O_{7-\delta}$. These additional phases are included in the films by introducing the materials directly to the targets used in the pulsed laser deposition.

The collection of experimental techniques used to prepare the samples analysed in this work are presented in this section. Below is given a description of the pulsed laser deposition system utilized and a discussion of the technical solutions adopted to obtain the best possible control of the process parameters. A tight control of process parameters is crucial in obtaining a good repeatability. The

sintering procedure applied to the pulsed laser deposition target preparation is described after the deposition technique while the photolithographic process performed to obtain the micro bridge patterning and the electrodes deposition are explained at the end of the section.

3.1.1 Pulsed Laser Deposition

Pulsed laser deposition (PLD) is a valuable choice for depositing extremely pure films because it reproduces exactly the target composition, multilayer materials can be done rather easily, it is the fastest route to prototyping any thin film coating and, most importantly, very high quality $YBa_2Cu_3O_{7-\delta}$ thin films can be easily produced. As a matter of the fact of its extreme versatility, a considerable amount of research work in $YBa_2Cu_3O_{7-\delta}$ pinning engineering has been carried out adopting pulsed laser deposition as deposition technique [100–104].

Pulsed laser deposition is one of the physical vapor deposition (PVD) adopted to grow high quality thin films. A target of the desired composition is ablated by a high power pulsed laser, the material ablated from the target forms a plasma plume of energized ions that after traveling though a controlled atmosphere are deposited on an heated substrate forming a thin coating film. Once these ions reach the film surface thay are usually referred to as adatoms. In particular adatom is the term used to describe a single atom adsorbed on a surface. To obtain high quality thin films it is necessary to control several parameters during the deposition. These parameters are the substrate temperature, the oxygen pressure in the chamber, the laser energy and the frequency of the laser pulses [105, 106].

All the samples in this work were deposited in a $YBa_2Cu_3O_{7-\delta}$ dedicated deposition system to minimize contamination issues. This system is equipped with a Lambda Physik KrF excimer laser ($\lambda = 248$ nm, fluence = 2 mJcm^{-2}) and the laser beam is admitted to a ultra high vacuum (UHV) chamber through a quartz window. Periodic cleaning of the window as well as a constant monitoring of the energy admitted in chamber ensure homogeneity of the ablating energies over the time. Others quartz windows are mounted on the sides of the UHV chamber and are generally used for growth and plume monitoring, secondary substrate surface

temperature monitoring and for laser-target-substrate alignment.

A focal lens is positioned outside the chamber and it is used to focus the laser on the targer in order to form a 2 mm x 3 mm rectangular spot on the target surface. The laser spot geometry influence the plume geometry: a large spot generates a small plume thus a small region in which the deposition is uniform; a small spot generates a large plume and a large region in which the deposition is uniform but as a consequence the deposition rate is reduced. The laser spot geometry adopted in this work allows a uniform deposition in a region $\approx$ 1.4 cm x 1.4 cm at $\approx$ 5 cm away from the target surface and uniform films are easily obtained on 1 cm x 0.5 cm substrates.

The substrate surface temperature is monitored using an external pyrometer while a secondary visible light laser, aligned to the primary excimer laser, is used during the aligning task. Figure 3.1 shows a schematic of a typical pulsed laser deposition system.

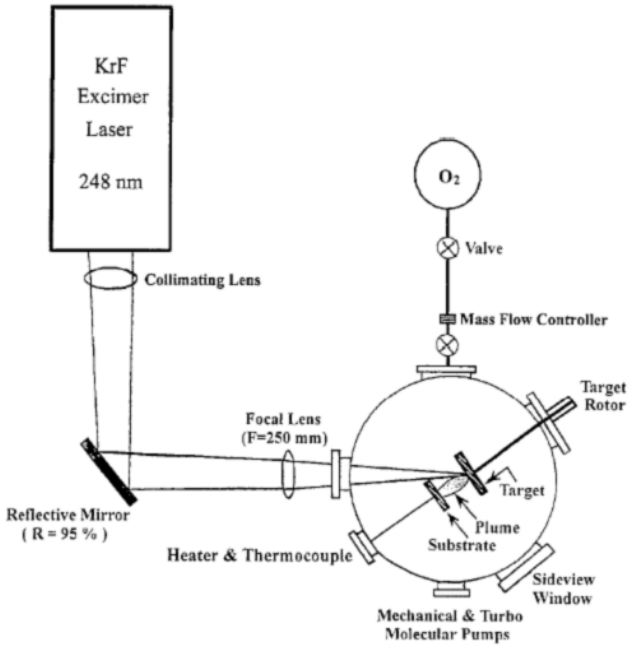

Figure 3.1: Schematic of a typical pulsed laser deposition system [3]

The substrates used are *(001)* aligned single crystals of $SrTiO_3$ (STO), these

are glued to an heater/holder with an high thermal conducting silver paste. The temperature of the heater is controlled using a PID controller that controls the power supply of the heating elements measuring the internal temperature of the heater block with a thermocouple. Since the thermocouple is inserted in the heater the use of the external pyrometer to monitor the substrate surface temperature is adopted to avoid substrate temperature variations between different depositions. This variations could rise from unavoidable differences in the thermal conductivity between the heater and the substrate. A variable ΔT between the thermocouple the pyrometer measure is usually present. This ΔT is mainly due to the position of the thermocouple. The thermocouple is placed inside the heater and at high temperatures a large energy dissipation due to radiating processes generates large thermal gradients between the center of the heater, where the thermocouple is positioned, and its surface, where the substrate is glued. Furthermore the impossibility to reproduce the same thermal contact in every deposition adds a variability to the discussed ΔT. This variable ΔT and the fact that the substrate surface temperature is the one that determines the atoms mobility, make the substrate surface temperature directly measured by the external pyrometer the only possible choice as reference temperature.

The target is mounted on a rotating carousel equipped with a plume shutter. The target is rotated to provide a uniform ablation. while the shutter is used to protect the substrate from the plume during a pre-deposition ablation process. This pre-ablation process is adopted to remove the target surface layer and to ensure that the entire deposition is realized under similar target conditions. The laser ablation induces modification to the surface morphology of the target inducing a continuous fusion-recrystallization cycle. It is important to induce these morphologic modifications before starting the thin film deposition without allowing the plume to reach the substrate.

The vacuum system is a common two stage system equipped with a rotary pump and turbomolecular pump, an additional multi channel mass flow controller is also present. The rotary pump is used to pump down the chamber pressure from ambient pressure to mid vacuum ($\sim 10^3$ mbar to $\sim 10^{-3}$ mbar) and to provide a backing pressure $\leq 10^{-3}$ mbar to the turbomolecular pump. The turbomolecular pump is used from mid vacuum to high vacuum ($\sim 10^{-3}$ mbar to

$\leq 10^{-6}$ mbar). Depositions are performed in a pure oxygen atmosphere with an oxygen pressure of 0.3 mbar. These pure oxygen deposition atmospheres are realized by first reaching high vacuum ($\leq 10^{-6}$ mbar) using the turbomolecular pump and then venting oxygen while controlling the chamber pressure by simultaneously controlling the oxygen incoming flow with the mass controller and the extraction pump power.

In a typical deposition the laser is operated in constant energy mode and the fluence is monitored and kept at $\approx$ 2 mJcm^{-2}, the pulse frequencies adopted are between 1 and 10 Hz. Usually each deposition is performed using $\sim$ 4500 pulses to obtain a film thickness of $\sim$ 500 nm. The distance between the target and the substrate is $\sim$ 5 cm. An optimal oxygenation of the samples is obtained with an in situ low temperature annealing of 1 hr. This step is realized cooling the sample to $\approx$ 520 °C and raising the oxygen pressure to 500 mbar.

All thin films produced in this research work were deposited on $SrTiO_3$ *(001)* single crystal substrates. This substrate is commonly used in $YBa_2Cu_3O_{7-\delta}$ epitaxial growth by pulsed laser deposition. It allows high quality films to be deposited and it was chosen for ease of comparison with previous work. In particular the use of $SrTiO_3$ *(001)* allows the comparison of the properties of the sample produced with a large amount of existing data without introducing unnecessary variables.

Oxygen content, grain orientation and film morphology are determinant parameters of the films superconducting properties. All these features are strongly influenced by the deposition parameters adopted. Almost twenty years of research in the field has provided a good knowledge of the processability windows of pure $YBa_2Cu_3O_{7-\delta}$. High quality $YBa_2Cu_3O_{7-\delta}$ thin films deposition is technological knowledge already acquired and thus will not be discussed. An exhaustive review on pulsed laser deposition of pure $YBa_2Cu_3O_{7-\delta}$ thin films was published by Singh *et al.* [3].

3.1.2 Target Preparation

All the pulsed laser deposition targets used to produce the samples used in this work were prepared from sintered powders. Although commercial pure

$YBa_2Cu_3O_{7-\delta}$ targets are available it was chosen to produce pure $YBa_2Cu_3O_{7-\delta}$ targets in laboratory in order to avoid differences in the superconducting properties which may arise from different target quality rather than different targets composition.

The process adopted to produce the targets is the same for both the pure and the composite ones. Powder are pressed in the form of a cylindrical target and the sintered at 950 °C in oxygen flow for 12hr in a dedicated tubular furnace. A detailed scheme of the thermal process is reported in figure 3.2.

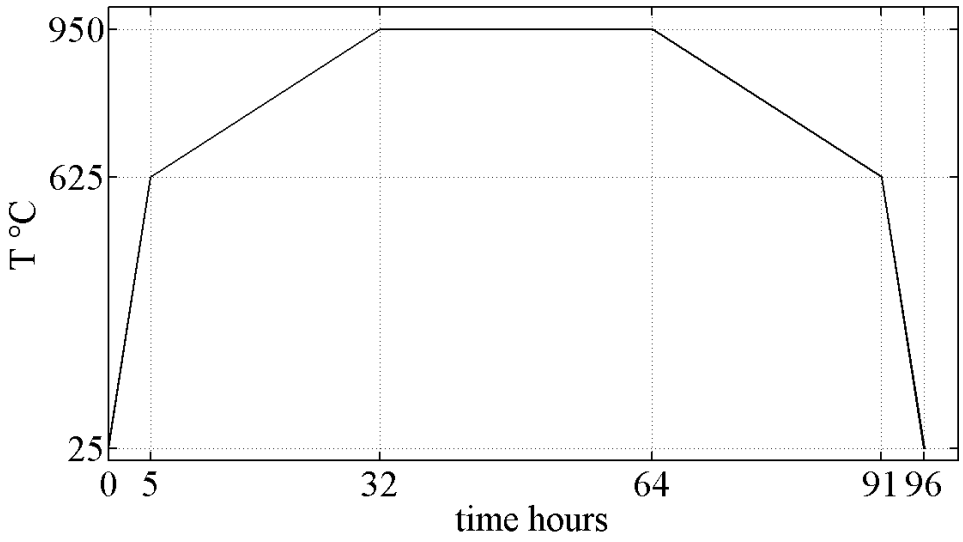

Figure 3.2: The target sintering thermal process

Pure $YBa_2Cu_3O_{7-\delta}$ powder (SCI Engineered Materials 99.999%) is used in both pure and composite targets. The secondary phases used in this work are Ba_2YNbO_6 and Gd_3TaO_7. Targets produced by mixing pure $YBa_2Cu_3O_{7-\delta}$ with 5 mol% of Ba_2YNbO_6 powder were adopted in the deposition of the samples discussed in the next chapter. Targets produced by mixing pure $YBa_2Cu_3O_{7-\delta}$ with 2.5 mol% of Ba_2YNbO_6 powder and 2.5 mol% of Gd_3TaO_7 precursor were used in the deposition of the samples discussed in the last chapter.

The Gd_3TaO_7 precursor mixed with the pure $YBa_2Cu_3O_{7-\delta}$ and the Ba_2YNbO_6 in the target were 99.99% Gd_2O_3 and Ta_2O_5.

3.1.3 Sample Patterning

While measuring the critical current density J_c a limited critical current I_c is desired. A low I_c reduce a series of problematic side effects and technological complication during the measure. A large I_c would require large current transfer, this implies powerful currents sources, large conducting cables connecting the sample and large electrodes trough which transfer the currents to the sample. Further more since it is impossible to eliminate the contact resistances a large transfer current passing trough any residual contact resistance will cause the dissipation of large energies. To avoid an increment of the sample temperature, caused by the heat generated in the dissipations at the contact, a powerful cooling system should also be provided.

Considering equation 3.1 the easiest way to reduce I_c is the reduction of the superconductor's cross section.

$$I_c = j_c S_{Supercond.} \tag{3.1}$$

A reduction of the cross section $S_{supercond.}$ simplifies the measure of the large J_c typical of the $YBa_2Cu_3O_{7-\delta}$ thin films (usually $J_c > 10^6$ MAcm^{-2}) and is obtained by introducing current tracks of micrometric width with a lithographic process. A reduction of the contact resistances can be obtained with the deposition of an electrode array through which the currents are transferred to the sample. Also the electrodes are deposited with a lithographic process.

The electrode deposition is realized with the lift-off process described below.

First a layer of a commercial positive photoresist (AZ 4533) is spin coated on the sample (spin at 6000 rpm for 45 s), then the resist layer is baked at 110 °C for 1 minute to allow the resist network reticulation (figure 3.3b).

An intense blue light is projected on the coated sample surface using a projection mask aligner for 24 s, the mask projected at this stage is composed of two rows of six square holes, the intense blue light is projected on the sample only through these twelve squares.

The exposed regions of the positive photoresist become soluble to a developing solution while the unexposed regions remain insoluble, thus after a developing stage the two rows of six square holes printed on the mask are transferred to

the photoresist coating layer. The developing stage is realized by the submersion of the samples in a 3_{vol} : 1_{vol} H_2O:AZ351B developing solution (AZ351B is a commercial developer). The duration of the developing stage is a key factor not always predictable: it has to be long enough to ensure that the resist layer is completely removed in the areas that were exposed to the light but at the same time an over lasting developing stage is to be avoided since it can cause resist removal from the unexposed zones. In order to optimally time the duration, the developing step is divided in several steps of reduced duration followed by the observation of the sample surface with an optical microscope until the resist layer is completely removed from the exposed areas (figure 3.3c).

Once the developing stage is successfully completed a silver layer and a gold layer are deposited on the sample surface in an ion milling magnetron sputtering hybrid system. The Ag / Au bilayer deposition is preceded by an ion milling step to remove the passivated layer on the superconducting film ensuring the optimal connectivity between the Ag layer and the $YBa_2Cu_3O_{7-\delta}$ surface (figure 3.3d).

The last step of the lift-off process, which gives the name to the technique, is realized by submerging the samples in acetone in an ultrasonic bath. The acetone dissolves the photoresist layer and the resist removal causes the lift-off (delamination) of the Ag / Au bilayer deposited on it while the metals deposited directly on the $YBa_2Cu_3O_{7-\delta}$ surface in the areas that were not covered by the resist forms the electrodes. In this way two rows of six Ag / Au electrodes are deposited on the films (figure 3.3e).

The track pattern transfer (the micro bridge formation) is obtained with a process similar to the electrode deposition until the developing stage. In this process the mask used project the light in the areas of the samples from which is necessary to remove the superconducting material. Thus after the developing stage, the resist layer is the exact copy of the desired tracks pattern (figure 3.3g), the effective film etching can then by realized either by a physical or chemical process (dry etching or wet etching). Very small features (≤ 10 μm) are usually realized with a dry etching because the chemical etching could blur the features. Since the smallest feature in this work, the tracks width, is $\approx$ 50 μm both processes are equally effective. The dry etching is performed in an argon ion milling system where energized ions removes material from the sample surfaces.

The wet etching is realized by submerging the sample in a HCl diluted solution (0.01M) with the acid dissolving the unprotected $YBa_2Cu_3O_{7-\delta}$ from the sample (figure 3.3h).

A schematic of the sample at the different stages of the process is reported in figure 3.3 while a micrography showing a single track and fractions of two electrodes in shown in figure 3.4

Five tracks ($\approx$ 50 μm in width), each one connected to four Ag / Au electrodes, are patterned on the samples using the described techniques.

3.2 Structural Morphological characterisation

In this section are listed the scientific investigation techniques adopted to characterise the crystal structures and the morphology at the nanoscale of the samples. Since these techniques are commonly adopted by materials scientists working in thin films, as well as different fields, they will not be discussed in detail. In this section only a presentation of the answers that can be achieved with the analysis performed is given.

3.2.1 Structural Analysis

Phase and orientation analysis are performed using x-ray diffraction. Performing this non destructive technique it is possible to gather information on the crystal phases present in the thin films and their orientation. The distribution of grain orientations is described by the crystalline texture. Random texture describes films with randomly oriented grains, fibre texture is a term used to describe films in which grains have one crystallographic axis parallel to the substrate normal but are randomly oriented in plane, and epitaxial growth (or epitaxial alignment) describes films made of grains that have a fixed orientation in plane. A scan in Bragg-Brentano geometry will give information on the spacing of the crystalline planes that are oriented perpendicularly to the substrate surface. The analysis are usually performed in the geometrical configuration reported in figure 3.5, and in this configuration only the diffraction peaks associated to the planes with the normal oriented perpendicular to the substrate surface will be registered.

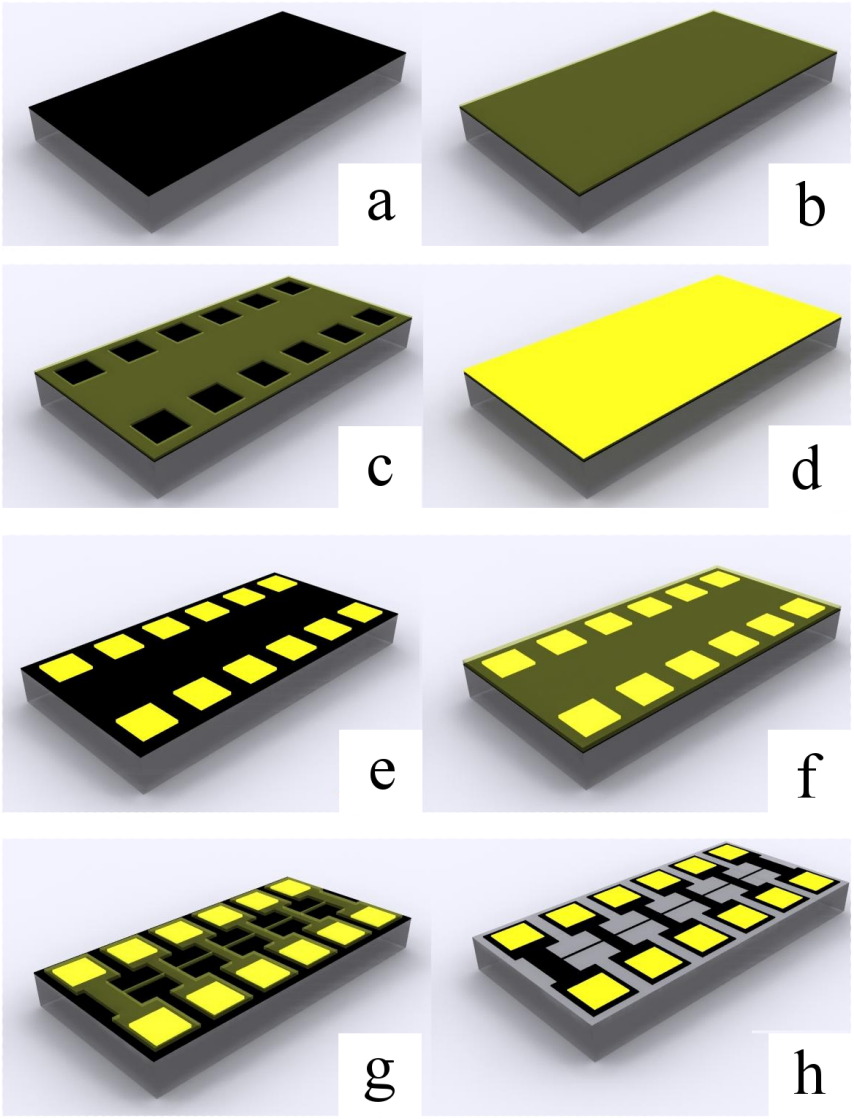

Figure 3.3: Sketches of a sample at the different stages of a photolithographic process. a) As deposited sample; b) Sample after the first spin coating of the photoresist; c) Sample after the developing of the electrode mask; d) Sample after the silver layer and gold layer deposition. e) Sample after the lift-off process; f) Sample after the second spin caoting of the photoresist; g) Sample after the developing of the trak mask; h) Sample after the milling/cleaning process.

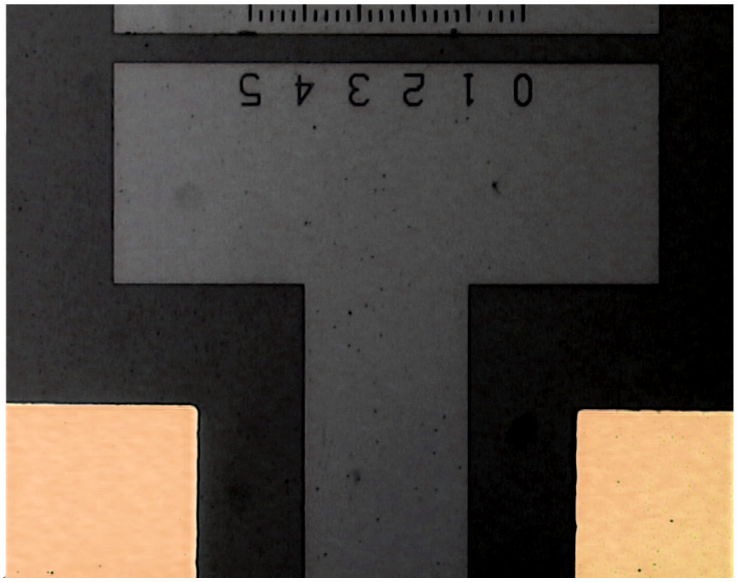

Figure 3.4: Micrography of the surface of a patterned sample

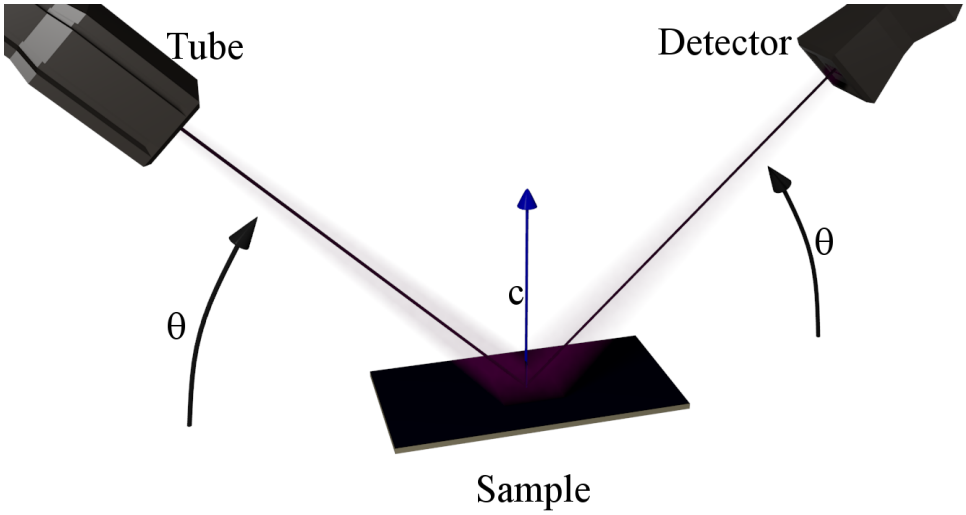

Figure 3.5: Schematic of a diffractometer operated in the Bragg-Brentano Geometry

The possible presence of an epitaxial growth is easily evidenced by the presence of only the peaks indexed *(00l)* since this will be the experimental proof that the crystalline *c*-axis is the only crystal axis oriented perpendicular to the substrate surface. The analysis of the diffraction peaks gathered in this geometry allows the determination of the crystalline composition of the samples and a first information on the orientation of the phases. A limitation of this typology of x-ray diffraction analysis is to only gather information of the so called out of planes diffraction. The determination of the out of plane orientations allows to distinguish a random texture from a fibre texture or an epitaxial growth.

In order to determine whether a film can be described by a fiber texture or an epitaxial growth it is necessary to analyse the in plane orientation of the crystalline phases. The in plane orientation analysis is performed with the so called ϕ scan. In figure 3.6 a sketch of the geometrical configuration in which the ϕ scans are done is reported.

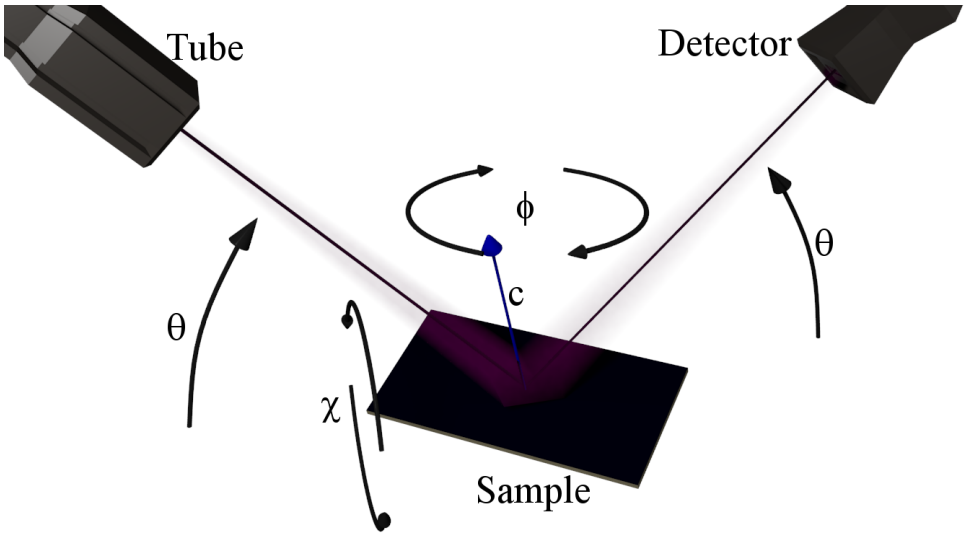

Figure 3.6: Schematic of a diffractometer geometry operating a ϕ scan

In a ϕ scan the sample orientation χ, the tube and detectors position θ are predetermined to focus the machinery on a specific in plane diffraction peak. The scan is then performed varying the sample ϕ angle and measuring the intensity

of the diffracted x-rays at the different ϕ values. In this way it is possible to asses the in plane orientation of a given crystalline phase and determine whether that specific crystalline phase is growing following the orientation of the substrate crystalline axis or is growing with a determined offset or is not following any specific orientation. This technique is valid if the phases were rightly determined and if the peaks on which the analysis system is focused are unique.

These first two x-ray diffraction techniques described are an optimal solution in the determination of the crystalline phases and their orientation but are limited when determining the epitaxy quality. They give little to no information on the on the spread of the orientation angles that is usually below the resolution of systems adopted when operated in the geometrical configuration described. Further more the presence of small fraction of randomly oriented crystalline phases could easily remain undetermined by these analysis. A randomly oriented fraction of a given oriented phase could be interpreted as noise when performing a ϕ scan.

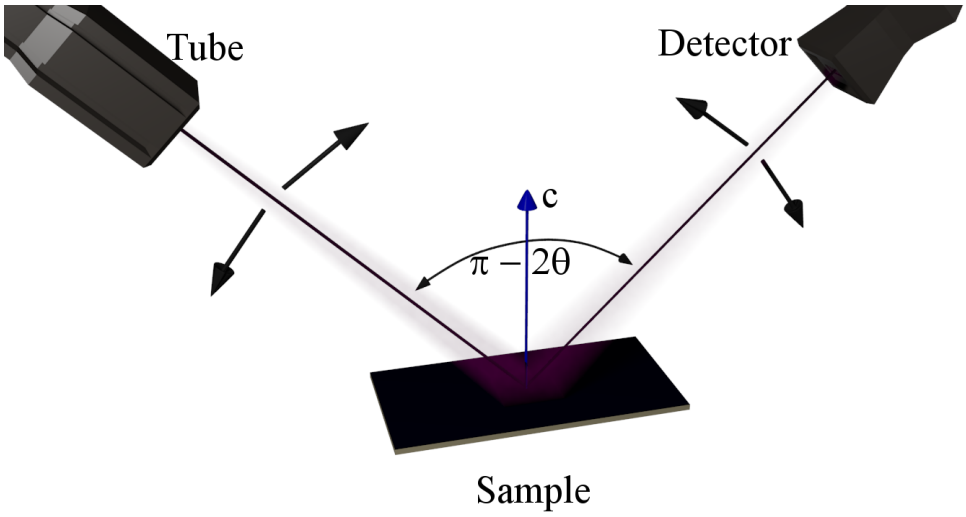

Figure 3.7: Schematic of a diffractometer geometry operating a rocking curve scan

In order to address the epitaxy quality and the strain levels rocking curves and reciprocal space maps are gathered.

A rocking curve (ω scan) is an analysis of the angular spread of a determined

planar direction. It is realised by scanning with a fixed 2θ (a fixed $\pi - 2\theta$) a small windows of positive and negative offsets ω (figure 5.2). The full width half maximum of the peaks measured gives an indication of the angular spread of the planar direction analysed.

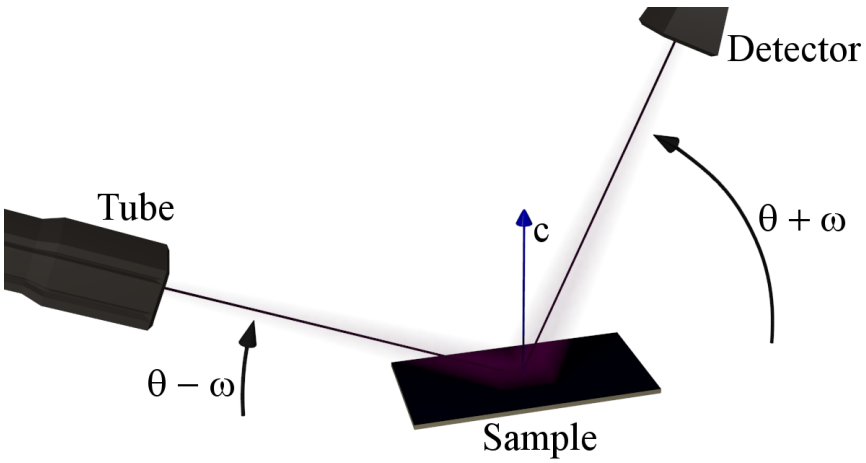

Figure 3.8: Schematic of a diffractometer geometry scanning a reciprocal space map

A reciprocal space map is the detailed study of the x-ray diffraction in a small window of 2θ and ω angles. A reciprocal space map can be obtained by measuring a set of $\omega/2\theta$ scans with different ω-offset angles around a specific reciprocal space reflection, determined by ω and 2θ (figure 3.8). The intensity of the diffracted signal is then plotted on a map with coordinates q_z and q_x that are the reciprocal of the spacing d_z and d_x thus it is possible to directly calculate the lattice parameters. The position of the diffraction peaks and their shape gives information on the mean lattice spacing and on the strain of the phase analysed.

It is also possible to establish if a phase is relaxed or strained with respect to the substrate. As a downside the reciprocal space maps are time consuming measures and therefore the windows around a specific diffraction angles are usually the smallest possible. Even if in theory it would be possible to gather a complete maps this are always avoided for the impracticality of the time required.

3.2.2 Microscopy

The knowledge of the crystalline phases, their orientation and strains level represents only a partial knowledge of a film quality. Furthermore since the pinning potential is related to the nanostructuration of the phases, a study of the morphology on the nanometric scale is fundamental. Only by knowing the grain morphology and the shape, spacing and orientation of a secondary phase it is then possible to relate the defect landscape to the pinning properties. Furthermore it is possible to evaluate the strength and weaknesses of a defects distribution in order to improve the properties increasing the points of strength and decreasing the weaknesses of a pinning landscape generating ideals defects distribution.

There are two main scientific investigation tools capable to fulfill the task: the atomic force microscopy (AFM) and the transmission electron microscopy (TEM).

AFM [107] is used to investigate the surface topography of the samples, from the topography is possible to evaluate the homogeneity of a film and the roughness of the surface. In addition to shapes and dimensions of the grain in samples characterised by a smooth surface is also possible to investigate the presence and distribution of secondary phases. The technique is non destructive and it is also fast and reliable, unfortunately the only information gathered concern the samples surface, thus only a partial information of the defects distribution can be obtained. As an example it would be impossible from an AFM only investigation to establish whether a secondary phase particle is a *c*-axis oriented defects or a plate like *ab*-planes oriented particles. For these reasons it is necessary to complete the information with TEM.

TEM gives information on the distribution and orientation of the phases in the sample. It is a powerful tool but is a time consuming and destructive technique. Nevertheless it is fundamental when picturing the pinning landscapes produced in the films. Essentially with this technique are taken images of the samples cross-section at the nanometric scale. A direct observation of the nanoparticles introduced in the samples is obtained. Furthermore analysing the electron diffraction pattern taken with the same technique it is possible to confirm and complete the phase and orientation analysis produced the the x-ray diffraction. A TEM

allows to take different electron diffraction patterns from different locations of the sample thus allows to gather separated electron diffraction pattern from the different phases present in the sample. TEM is also adopted to perform local strain analysis to complete the information on the average strain obtained with the reciprocal space maps.

Cross-section TEM images were taken by JEOL 2010 analytical microscope with a point-to-point resolution of 0.20 nm. High resolution TEM and scanning transmission electron microscopy analysis was conducted using FEI Tecnai F20 with a point-to-point resolution of 0.18 nm. Cross-sectional samples for TEM analysis were prepared by a standard manual grinding and thinning procedure followed by a final ion polishing step (Gatan PIPS 691 precision ion polishing system).

3.3 Superconductivity Properties characterisation

The final part of this chapter is dedicated to on overview of the techniques adopted to characterize the superconducting transport properties of the sample produced. The three main properties analysed are the transition temperature T_c, the critical current density as a function of the applied magnetic field value $J_c(B)$ and the critical current density as a function of the direction of the applied magnetic field $J_c(B, \theta)$. It is evident that the target is to achieve the highest possible J_c and T_c and to minimize the detrimental effect of an increasing value of the applied magnetic field on J_c. This set of measurements gives complete information on the quality and effectiveness of the defects landscape in the creation of an ideal pinning enhanced thin film $YBa_2Cu_3O_{7-\delta}$ based superconductors.

The first measure always performed is the determination of the transition temperature T_c. This measure is performed by a straight forward technique. A 4 point resistance measure is realized applying the smallest transport current possible that minimize the noise while not affecting the transition temperature (usually I $\leq 10^{-6}$ A). The resistance is measured while reducing the temperature from T_{Amb} to 77 K. The transition temperature is then associated with the

temperature at which the resistance disappears. The attribution of T_c is not unique, in some work it is attributed to the temperature with the maximum of the $\frac{\partial \rho}{\partial T}$ or with the mean point of the transition, in this work the most restrictive condition is chosen. The reason to chose the most restrictive condition for the determination of T_c is that this condition takes into account the homogeneity of a sample and that a sample will not be considered superconductive until a complete superconductive link is generated between the probing electrodes.

The critical current density as a function of the applied magnetic field value $J_c(B)$ and the critical current density as a function of the direction of the applied magnetic field $J_c(B, \theta)$ are measured with the same technique. The only difference is the parameter that is changing during the measurement. In the $J_c(B)$ measure the direction of the applied magnetic field is constant (usually B$\|$ c-axis and B $\|$ ab-planes) and the applied magnetic field value is increased. In the $J_c(B, \theta)$ measurement the applied magnetic field value is constant and the direction is changed.

The core of the measurement is the individuation of the critical transport current I_c. To fulfill this task the current is increased in small step and a voltage value is measured for each current value until the voltage reaches a maximum value ($V = 10^{-5}V$), from the $I-V$ curve obtained the current value at which the voltage is equal to a defined criterion ($V_c = 10^{-6}Vcm^{-1}$) is derived and that value is defined as the I_c value. Knowing the I_c and the geometry of the micro bridge the J_c is easily calculated using equation 3.1. The derivation of the I_c value can be achieved by adopting different technique: a linear interpolation around the criterion voltage, a polynomial interpolation over a n-point windows around the criterion or fitting the $I - V$ data with the following equation:

$$I = I_c(\frac{V}{V_c})^n \tag{3.2}$$

The different I_c derivation techniques lead to little or no variation of the value derived. Never the less the technique adopted in the work is the fitting with the equation 3.2 since it is more reliable in the case of noisy measures.

The $J_c(B)$ and the $J_c(B, \theta)$ measurements are basically realised with a set of $I - V$ measures in different magnetic fields intensity and geometry. Both $J_c(B)$

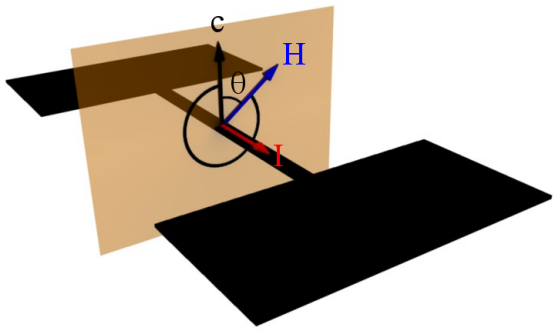

Figure 3.9: Schematic of the geometry for the determination of $J_c(B, \theta)$

and $J_c(B, \theta)$ measurements are performed in maximum Lorentz force configuration ($I \perp B$) figure 3.9.

Chapter 4

Ba_2YNbO_6 doped $YBa_2Cu_3O_{7-\delta}$: preliminary results

In this chapter are reported the results of the study of the Nb doping of $YBa_2Cu_3O_{7-\delta}$ thin films. The effects on the nanostructure of the films as well as the superconducting properties are discussed. The study in this chapter includes the preliminary results obtained on Ba_2YNbO_6 doped $YBa_2Cu_3O_{7-\delta}$ thin films deposited by pulsed laser deposition.

4.1 The Nb introduction in the $YBa_2Cu_3O_{7-\delta}$

The introduction of a secondary phase in the $YBa_2Cu_3O_{7-\delta}$ that has been described in the previous chapter is now a widely used tool to increase the pinning properties of commercial conductor as well as research labs advanced materials.

When introducing new pinning additions to $YBa_2Cu_3O_{7-\delta}$ adopting the pulsed laser deposition technique, it is important to consider that the phase which forms may not be the one which is added to the $YBa_2Cu_3O_{7-\delta}$ in the target. The phase that forms is the most thermodynamically and epitaxially stable. As a matter of the fact if Zr^{4+} is added to the $YBa_2Cu_3O_{7-\delta}$ the phase that forms is $Ba(Zr,Y)O_3$ [57] while when Sn^{4+} is added $BaSnO_3$ forms [64–66]. The addition of Ta^{5+} was reported to form both RE_3TaO_7 [67] and Ba_2YTaO_7 [68]. Considering the optimal results obtained with the Ta^{5+} in this chapter the effects of

another large, highly charged ion, Nb^{5+}, are presented.

4.1.1 Nb doped ceramic samples

The first introduction of Nb in $YBa_2Cu_3O_{7-\delta}$ was reported soon after the discovery of the $YBa_2Cu_3O_{7-\delta}$. In 1988 Kuwabara M *et al.* reported an increased J_c value in Nb_2O_5 doped $YBa_2Cu_3O_{7-\delta}$ ceramic samples [108]. The effects of Nb was unclear but the authors reported that almost all the Nb added was not incorporated in the $YBa_2Cu_3O_{7-\delta}$ and was instead segregated to form a secondary phase. An elemental distribution map showing that the Cu element did not coexist with the Nb while both Y and Ba did and the discovery that Nb was no longer in the from of oxide made the authors claim the formation of a secondary compound with Y and Ba.

In 1989 Greaves C. and Slater P.R. published a study on the Nb and Ta substitution in the $REBa_2Cu_3O_7$ (RE = Y, Eu, La) [109]. They suggest the presence of two possible products, the $REBa_2Cu_2MO_8$ and the Ba_2REMO_6 + CuO (M = Nb, Ta). They observed that the energy difference between the two possible products is small and that, since in the double perovskite structure the rare earth cation is in the small octahedral site, the stability of the perovskite structure is reduced when large RE^{3+} ions are used. The authors observed that for RE = Y, Eu the phases formed where $REBa_2Cu_3O_7$, Ba_2REMO_6 and CuO while a substitution and the consequent formation of the $REBa_2Cu_2MO_8$ phase was only observed for RE = La. From their studies it is evident that doping $YBa_2Cu_3O_{7-\delta}$ (RE = Y) with Nb or Ta leads to the formation of the Ba_2YNbO_6 and Ba_2YTaO_6.

A few years later, in 1993, the diffraction pattern of a sample with composition $YBa_2Cu_2.95Nb_0.005O_{7-\delta}$ was reported in a paper from Strukova G. K. *et al.* [110,111]. They also found the presence of an $YBa_2Cu_3O_{7-\delta}$ orthorhombic phase (a = 0.3827 nm, b = 0.3894 nm, c = 1.1718 nm), a Ba_2YNbO_6 cubic perovskite phase (a = 0.4218 nm) and a small amount of CuO. They also reported that the intensity of the lines corresponding to the Ba_2YNbO_6 increased with increasing the Nb content. They attributed a greater stability of the Ba_2YNbO_6 secondary phase when compared to $YBa2Cu_{3-x}Nb_xO_{7-\delta}$ to the low solubility of the Nb in

the $YBa_2Cu_3O_{7-\delta}$.

Recently, in 2003, Babu N. H. *et al.* reported the presence of $Y_2Ba_4Cu_xNb_{1-x}O_y$, a phase similar to Ba_2YNbO_6 with Cu partially substituting Nb, in $YBa_2Cu_3O_{7-\delta}$ bulk doped with Nb [112]. Improved J_c was observed in the doped samples [113]. In 2009 Yeoh W. K. *et al.* reported enhanced flux pinning at high field in $YBa_2Cu_3O_{7-\delta}$ single grain bulk samples doped with NbO_2 and related the improved pinning to the formation of a Nb rich phase within the $YBa_2Cu_3O_{7-\delta}$ [114].

4.1.2 Ba_2YNbO_6 use in $YBa_2Cu_3O_{7-\delta}$ thin film

The stability and compatibility of the Nb-based double perovskite Ba_2YNbO_6 with the $YBa_2Cu_3O_{7-\delta}$ was studied by Paulose K V *et al.* in 1992 [4]. They found that annealing a 1:1 mole mixture of $YBa_2Cu_3O_{7-\delta}$ and Ba_2YNbO_6 for 16 hr at 950 °C there was absolutely no reaction (figure 4.1).

The stability and compatibility of the Ba_2YNbO_6 with the $YBa_2Cu_3O_{7-\delta}$ made it a candidate for a novel substrate in the $YBa_2Cu_3O_{7-\delta}$ thin film deposition. The difficulties encountered in the production of large Ba_2YNbO_6 single crystal have prevented the use this material as a substrate, nevertheless high quality high temperature superconductor thin films and electronic devices were fabricated adopting Ba_2YNbO_6 as a new buffer layer [115, 116].

The only early report on the use of Ba_2YNbO_6 to enhance flux pinning in $YBa_2Cu_3O_{7-\delta}$ thin film is a work published in 1995 from Jia J. H. *et al.* [117]. The authors report on thin Nb added $YBa_2Cu_3O_{7-\delta}$ deposited on ZrO_2 substrates by a dc magnetron sputtering method. The secondary phase formed in the film is reported to be the Ba_2YNbO_6 perovskite but the effects on the critical current registered were negative. The conclusions of this early research were that the Ba_2YNbO_6 secondary phase does not play a role in the flux pinning process.

More then 10 years later, in 2007, Nb doped $ErBa_2Cu_3O_{7-\delta}$ was successfully produced by pulsed laser deposition [118–122], in this work the authors report that *c*-axis oriented nanorods of Ba_2ErNbO_6 were formed in the $ErBa_2Cu_3O_{7-\delta}$. However the effects of the nanorods on the critical current values were not clearly explained. The presence on these *c*-axis oriented nanorods seemed to have effects

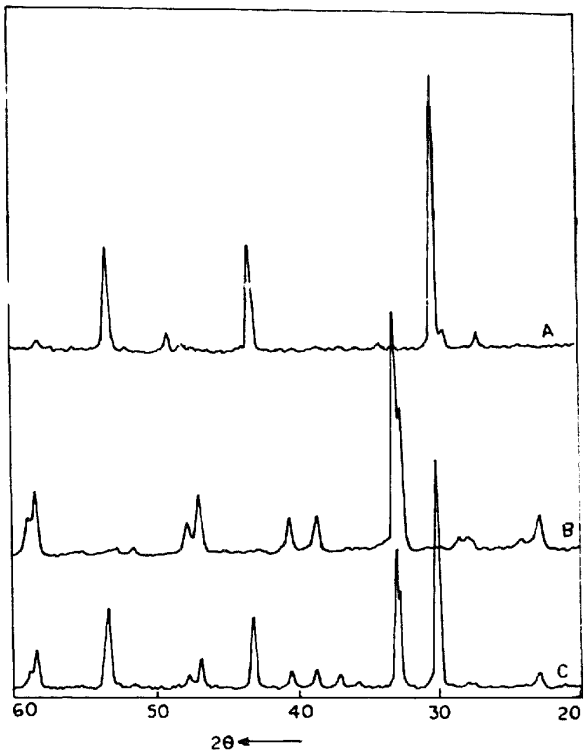

Figure 4.1: Powder diffraction patter for a) pure Ba_2YNbO_6, b) pure $YBa_2Cu_3O_{7-\delta}$, c) 1:1 mole mixture of $YBa_2Cu_3O_{7-\delta}$:Ba_2YNbO_6 heated at 950 °C for 15 hr. [4]

on the pinning performances of the films only when the latter were grown under certain condition and a window of processability was undefined.

Recently, successful formation of Ba_2YNbO_6 nanorods in $YBa_2Cu_3O_{7-\delta}$ thin films grown by pulsed laser deposition has been reported by several authors [5, 74,123,124]. The article [5] is part of this thesis, it is the first attempt to produce Ba_2YNbO_6 - $YBa_2Cu_3O_{7-\delta}$ thin films by pulsed laser ablation of a mixed target, and contains the first results obtained. These results will be described in the following section of this chapter. In conclusion Ba_2YNbO_6 is a good pinning phase candidate for the following reasons:

- The large Nb^{+5} does not substitute the Cu in $YBa_2Cu_3O_{7-\delta}$
- Ba_2YNbO_6 is the most stable Nb compound in a $YBa_2Cu_3O_{7-\delta}$ matrix
- Ba_2YNbO_6 forms in a wide processing window
- Ba_2YNbO_6 nanoparticles forms self-assemble in nanorods in a similar manner to $BaZrO_3$
- The large lattice mismatch between Ba_2YNbO_6 and $YBa_2Cu_3O_{7-\delta}$ should provide additional pinning inducing lattice distortion in $YBa_2Cu_3O_{7-\delta}$

4.2 Ba_2YNbO_6 perovskite additions to $YBa_2Cu_3O_{7-\delta}$: the preliminary results

In this section is reported the first results obtained by the addition of the Ba_2YNbO_6 perovskite pinning phase to the $YBa_2Cu_3O_{7-\delta}$. The results were discussed in a feasibility study published in early 2010 in Superconductor Science and Technology [5].

4.2.1 The Ba_2YNbO_6 synthesis, the pulsed laser deposition target preparation and thin films deposition

The technique adopted to produce the single phase Ba_2YNbO_6 powder is the same described and successfully used by Paulose K V *et al.* [4]. Ba_2YNbO_6

powder were produced mixing and grinding stoichiometric quantity of 99.99% Y_2O_3, $Ba(NO_3)_2$, Nb_2O_5 and a minimal amount of CuO_2 followed by a solid state reaction at 1450 °C for 24 h in flowing O_2. In order to achieve a complete reaction and thus produce a single phase Ba_2YNbO_6 two successive grinding and reaction were needed. The minimal amount of CuO_2 ($\approx 0.5\%_{wt.}$) was added to the oxides mixture because it is described to greatly enhance the powder reactivity. The reaction enhancing effect of the CuO_2 is explained by the fact that CuO_2 presence introduce in the system a low energy reaction intermediate lowering the energy barrier of the overall reaction [4].

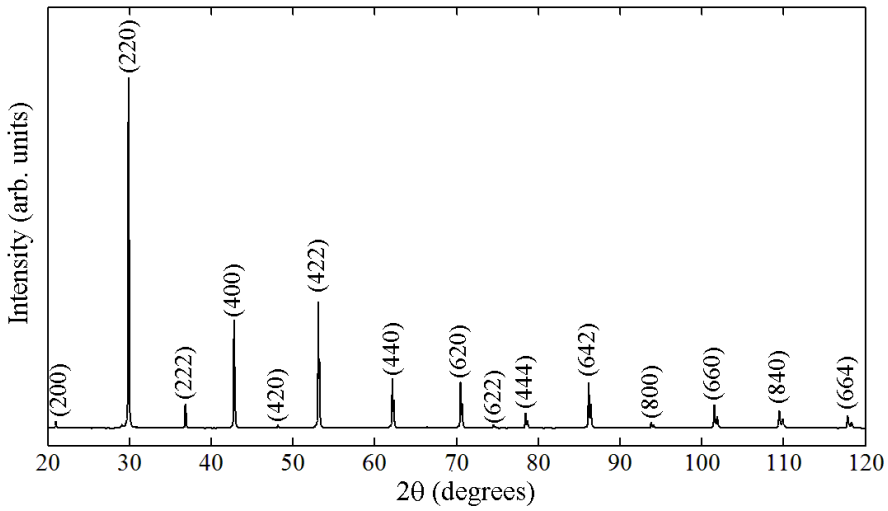

Figure 4.2: Powder diffraction patter for Ba_2YNbO_6powder produced. Adapted from [5].

In the figure 4.2 are shown the results of an x-ray analysis in the Bragg-Brentano geometry ($\theta - 2\theta$ scan) of the Ba_2YNbO_6 powder produced by the described solid state reaction. No impurities or secondary phase peaks are found, given the minimal amount of CuO_2 that was added is not expected to be easily evidenced. The quantity involved is too small to be separated from the noise levels that are usually present in this typologies of measures. The lattice parameters calculated form the x-ray data is a = 0.844 nm ± 0.001 nm. The lattice parameter derived is in agreement with the data recorded in the Joint Committee on Powder

Diffraction Standards database (JCPDS) as well as the data presented in more recent studies [125].

The Ba_2YNbO_6 production process described constitutes a reliable source of pure single phase Ba_2YNbO_6 to use, together the $YBa_2Cu_3O_{7-\delta}$ commercial powder, in the pulsed laser deposition target preparation.

The target sintering procedure adopted for the samples discussed in this section is exactly the general procedure described in the previous chapter, the Ba_2YNbO_6 doping amount in the target adopted in this study is $5\%mol$. The control pure $YBa_2Cu_3O_{7-\delta}$ target is sintered adopting the same technique. More sophisticated procedures were also adopted to produce advanced targets, the modification to the processes will be described in the appropriate spaces.

The pulsed laser deposition parameters adopted for both pure $YBa_2Cu_3O_{7-\delta}$ control thin films and the Ba_2YNbO_6 added samples are summarized in table 4.1.

Parameter	Value
Substrate Temperature	770 °C
Chamber Pressure	0.3 mbar flowing O_2
Laser Fluence	2 Jcm^{-2}
Repetition Rate	5 Hz
Number of Pulses	4500
Annealing Time	1 hr
Annealing Temperature	520 °C
Annealing Pressure	500 mbar O_2

Table 4.1: Pulsed laser deposition parameters

All the thin films deposited were measured to be of $\approx$ 0.5 μm thickness.

4.2.2 Crystalline structure analysis: x-ray diffraction data

The first analysis realized on deposited films when using a new target composition are usually x-ray diffraction structural analysis to investigate the crystalline phases produced in the samples, their orientation and possibly the strains and lattice distortions arising form the large interfaces of nanostructured composite materials.

4.2.2.1 Crystalline phases identification

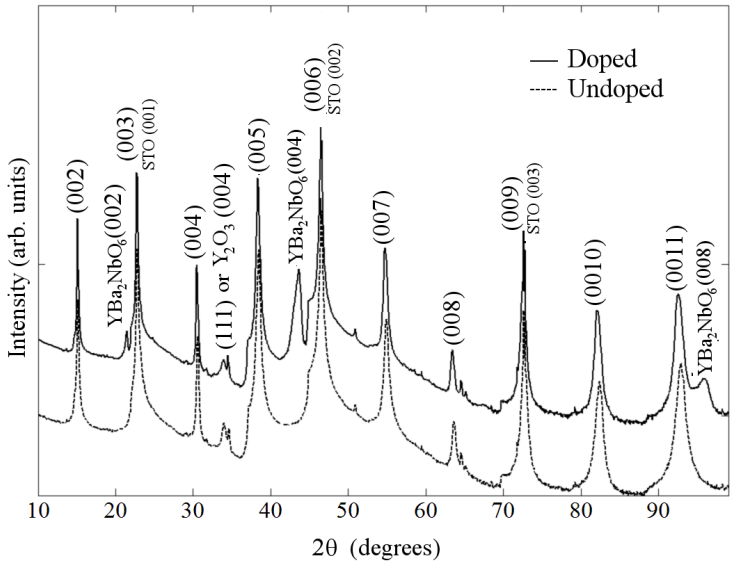

Figure 4.3: X-ray diffraction data for undoped $YBa_2Cu_3O_{7-\delta}$ and 5%*mol* Ba_2YNbO_6 doped film deposited on $SrTiO_3$. Adapted from [5].

The first relevant results reported in figure 4.3 is that the x-ray diffraction data collected in the Bragg-Brentano geometry from the deposited thin films (both doped and pure) shows only the diffraction peaks related to the $(00l)$ planes from the $YBa_2Cu_3O_{7-\delta}$, the Ba_2YNbO_6 and the $SrTiO_3$. This is evidence that also the doped thin films have the usual c-axis orientation of pure $YBa_2Cu_3O_{7-\delta}$ thin films deposited on *(001)* $SrTiO_3$ single crystal.

The only difference evidenced by the comparison of the diffraction data gathered from the pure $YBa_2Cu_3O_{7-\delta}$ control thin films and the Ba_2YNbO_6 doped ones is the presence of the peaks related to the *(00l)* planes of the Ba_2YNbO_6. It is possible to conclude that the stability of the Ba_2YNbO_6 - $YBa_2Cu_3O_{7-\delta}$ system during the pulsed laser deposition does not differ from the proved stability at high temperatures [4], thus the only secondary crystalline phase introduced in the thin films deposited is the Ba_2YNbO_6. Furthermore a first hint of the Ba_2YNbO_6 orientation is revealed by the presence of only the *(00l)* planes diffraction peaks, the non superconducting phase is aligned *out-of-plane* with the $YBa_2Cu_3O_{7-\delta}$

matrix.

To conclude the crystalline phases identification a small discussion has to be given about a small peak at $2\theta \approx 34°$. This peak is present in both the pure $YBa_2Cu_3O_{7-\delta}$ and the Ba_2YNbO_6 doped thin films thus its presence can not be associated with the Ba_2YNbO_6 doping. The intensity is lower than that from the *(004)* and *(008)* Ba_2YNbO_6 peaks, and the Ba_2YNbO_6 doping level is only $5\%mol$. A peak at $2\theta \approx 34°$ in the $YBa_2Cu_3O_{7-\delta}$ system could be associated with the *(111)* $YBa_2Cu_3O_{7-\delta}$ peaks or with the *(004)* Y_2O_3. The first could be due to a minimal fraction of misaligned grains, a small fraction *a* grown grains can explain the peaks presence and it is commonly found at lower deposition temperature that the one adopted in these films. The second could be formed starting from a minimal Y imbalance in the target and considering that the peaks is also present in the pure $YBa_2Cu_3O_{7-\delta}$ control sample, this minimal imbalance should be in the commercial pure $YBa_2Cu_3O_{7-\delta}$ powder adopted in the target sintering process. Nevertheless, since the intensity is very small and the peak is not related to the Ba_2YNbO_6 doping, its presence does not influence the results.

4.2.2.2 Crystalline phases orientation

The assessment of the *in-plane* texture is realized by ϕ scans. The technique is described in the previous chapter and the results obtained analysing a $5\%mol$ Ba_2YNbO_6 doped film are summarized in figure 4.4.

The *(202)* Ba_2YNbO_6 peak ($\chi = 45°$, $2\theta = 30.03°$) reveal an *in-plane* alignment since it matches both the *(101)* $SrTiO_3$ ($\chi = 45°$, $2\theta = 32.46°$) and the *(202)* $YBa_2Cu_3O_{7-\delta}$ ($\chi = 57.06°$, $2\theta = 27.62°$) peaks. This direct observation of a *cube on cube* growth of the Ba_2YNbO_6 with the $YBa_2Cu_3O_{7-\delta}$ combined with the *out-of-plane* *c*-axis homogeneous orientation demonstrated in figure 4.3 suggest full heteroepitaxy between the $YBa_2Cu_3O_{7-\delta}$, the Ba_2YNbO_6 and the $SrTiO_3$.

A last point should be made on the diffraction peaks choice for the ϕ scans. Some authors perform the analysis on the *(103)* $YBa_2Cu_3O_{7-\delta}$ ($\chi = 45°$, $2\theta = 32.8°$) peak and not the *(102)* $YBa_2Cu_3O_{7-\delta}$ used in this work. Unfortunately the first is extremely close to *(101)* $SrTiO_3$ and in most analysers the two peaks

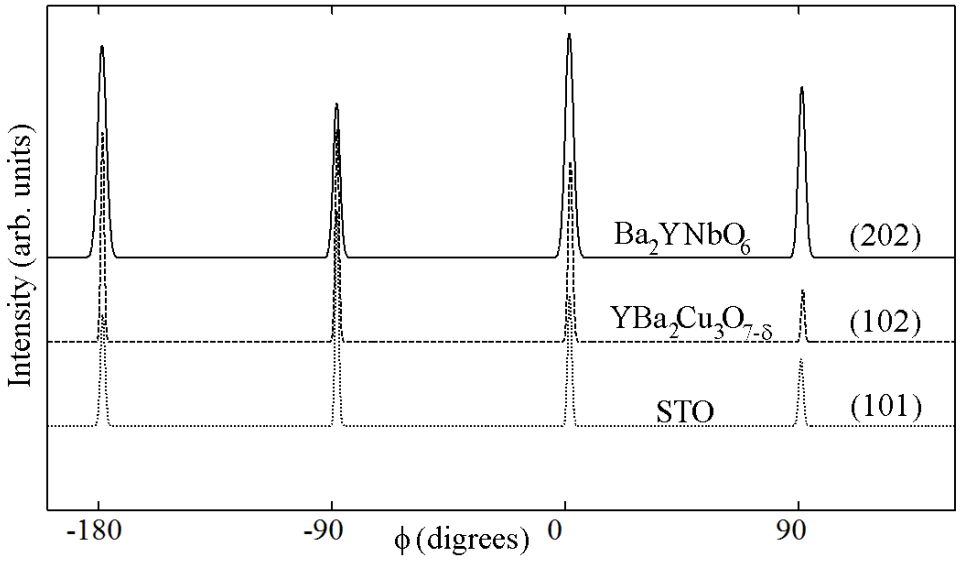

Figure 4.4: X-ray diffraction data from ϕ scans of *(101)* $SrTiO_3$, *(102)* $YBa_2Cu_3O_{7-\delta}$, *(202)* $Ba_2YNbO_6$from a 5%*mol* Ba_2YNbO_6 doped film. Adapted from [5].

overlap. Since the intensity of the *(101)* $SrTiO_3$ peak in much higher that the intensity of the *(103)* $YBa_2Cu_3O_{7-\delta}$ peak choosing the latter as reference peak for the $YBa_2Cu_3O_{7-\delta}$ *in-plane* orientation assessment could lead to misinterpretation.

4.2.2.3 Crystallographic matching and strain

Once the phase orientations are known it is possible to propose a crystallographic matching model and to evaluate the lattice mismatch of Ba_2YNbO_6 with $YBa_2Cu_3O_{7-\delta}$.

In figure 4.5a is presented the matching of $YBa_2Cu_3O_{7-\delta}$ with Ba_2YNbO_6 viewed along the *b*-axis ($[010]_{YBCO}$ direction). In this view 3 unit cells of the cubic Ba_2YNbO_6 match 2 unit cells of $YBa_2Cu_3O_{7-\delta}$. The *c*-axis mismatch (related to $YBa_2Cu_3O_{7-\delta}$) can be calculated with the following equation:

$$\frac{3a_{BYNO} - 2c_{YBCO}}{2c_{YBCO}} = +8.34\% \tag{4.1}$$

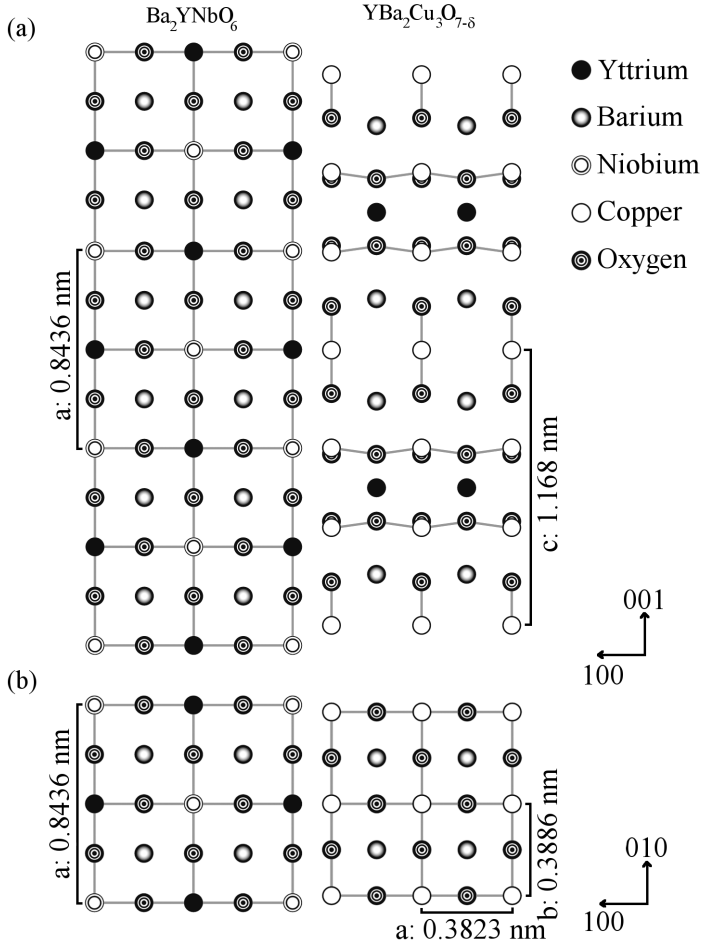

Figure 4.5: Crystallographic matching of $YBa_2Cu_3O_{7-\delta}$ with Ba_2YNbO_6. a) *b*-axis view and b) *c*-axis view [5].

In order to have a perfect lattice match along the c-axis the Ba_2YNbO_6 lattice should be compressed along the c-axis. In the doped film the $(00l)$ peaks from the Ba_2YNbO_6 are indeed shifted to higher angles compared to the bulk values (figure 4.3). The resulting lattice parameter is of 0.830 nm ± 0.001 nm instead of the 0.844 nm ± 0.001 nm resulting from the powder scan (figure 4.2). This confirms the presence of a compressive strain of ≈ 1.7%, this strain is much lower than the theoretically derived mismatch. In addition the *(00l)* $YBa_2Cu_3O_{7-\delta}$ diffraction peaks are slightly shifted towards lower 2θ values (in the opposite direction of the Ba_2YNbO_6 diffraction peaks) thus the $YBa_2Cu_3O_{7-\delta}$ c-axis lattice parameter seems to be extended to higher values. A tensile strain of ≈ 0.4% can be derived from the lattice value of 1.173 nm calculated from the diffraction data presented in figure 4.3. Nevertheless the overall strain given by the Ba_2YNbO_6 contraction and the $YBa_2Cu_3O_{7-\delta}$ extension is lower than the theoretical value thus an additional strain relief mechanism is most likely to be playing a matching role. The formation of misfit dislocations is one the possible strain relief mechanism and such defects formation has been previously reported in $BaZrO_3$ doped $YBa_2Cu_3O_{7-\delta}$ [126]. A semicoherent interface could also be responsible of the reduced strain levels in the crystalline structures.

In figure 4.5b the matching of $YBa_2Cu_3O_{7-\delta}$ with Ba_2YNbO_6 looking along the c-axis ($[001]_{YBCO}$ direction) is presented. The matching between the $YBa_2Cu_3O_{7-\delta}$ and the Ba_2YNbO_6 crystalline lattices is realised with 1 unit cell of Ba_2YNbO_6 and 2 unit cell of $YBa_2Cu_3O_{7-\delta}$. The averaged *in-plane* lattice mismatch (averaged along the a-axis and b-axis) is given by the following equation:

$$\frac{a_{BYNO} - 2a_{YBCO}}{4a_{YBCO}} + \frac{a_{BYNO} - 2b_{YBCO}}{4b_{YBCO}} = +9.42\% \tag{4.2}$$

This large lattice mismatch, larger than the others studied non superconducting phase additions, should be beneficial for low field pinning thanks to possible localized strain fields at the Ba_2YNbO_6-$YBa_2Cu_3O_{7-\delta}$ interface [127], but it likely to produce self-assembled columnar arrays of defects that are shorter and wider than those produced with pinning addition with lower lattice mismatch [64], and similar to those produced with $BaZrO_3$ addition [57].

4.2.3 Nanostructure analysis: Atomic Force Microscopy and Transmission Electron Microscopy

X-ray diffraction analysis is a powerful tool to investigate the crystalline structures and their orientation but they reveals little information on the nanostructuring of these phases. To investigate the nanostructure nanoscale microscopy has to be performed. In this section the surface topography is discussed by analysing atomic force microscopy images while the morphological distribution of the secondary pinning phase and the distortion in the $YBa_2Cu_3O_{7-\delta}$ lattice are studied with cross-section transmission electron microscopy.

4.2.3.1 Surface topography (Atomic Force Microscopy)

In figure 4.6 are reported atomic force micrographs of a pure $YBa_2Cu_3O_{7-\delta}$ and a 5%*mol* Ba_2YNbO_6 doped film surface.

An analysis of the root mean square roughness performed on the surface topography of the 5 μm $\times$ 5 μm scans gives information on the quality of the two films in examination. The root main square roughness of the pure $YBa_2Cu_3O_{7-\delta}$ thin film is $\approx$ 9.1 nm (figure 4.6a), a slightly lower value of $\approx$ 7.8 nm was calculated for the 5%*mol* Ba_2YNbO_6 doped thin film (figure 4.6c).

Carefully analysing both the 5 μm $\times$ 5 μm images it is evident that a small amount of particulate is present on the surfaces of both thin films, these superficial particles of diameter $\geq$ 250 nm were deposited on the growing film during the deposition and are a well known and studied in consequence of a pulsed laser deposition process in which the substrate is perpendicular to the plume and the target density is not optimal [105, 128]. Improved techniques could be adopted to reduce and eliminate this phenomenon [128–132]; in applications that require a perfectly clean surface adopting these methods is recommended. In this case the presence of the particulate is not a major issue and as shown later is not evidently reducing the overall superconducting properties. Furthermore since the particulate is present on the surfaces of both doped and undoped thin films it should not be related to the Ba_2YNbO_6 doping. Nevertheless in the next section higher quality films obtained from higher density target are discussed.

The grain growth morphology is affected by the Ba_2YNbO_6 presence in the

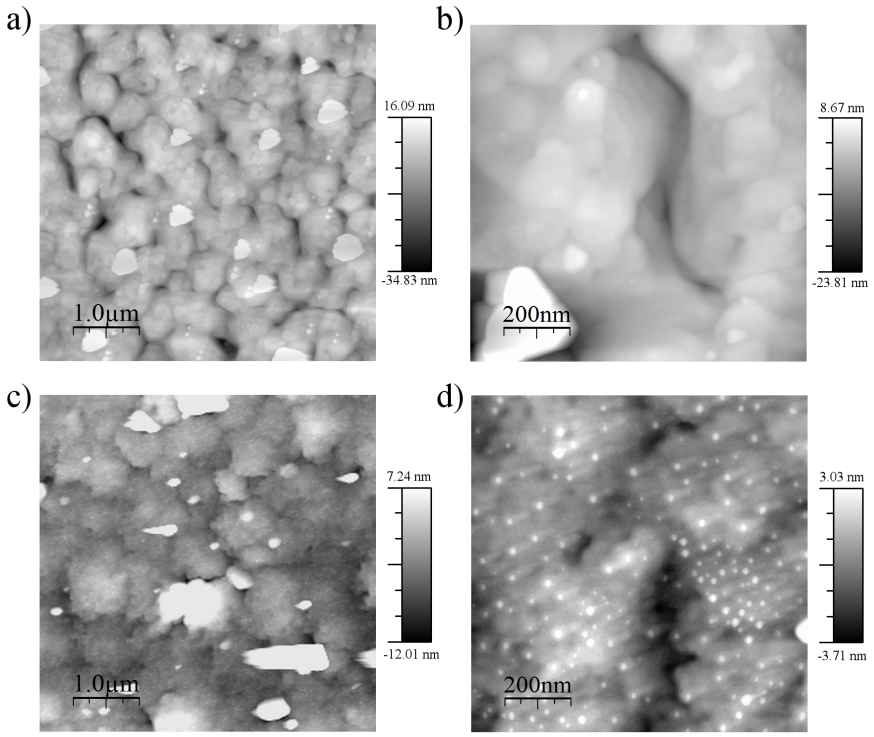

Figure 4.6: Atomic Force Microscopy surface image of a pure $YBa_2Cu_3O_{7-\delta}$ and a 5%*mol* Ba_2YNbO_6 doped $YBa_2Cu_3O_{7-\delta}$ thin films. a) 5 μm $\times$ 5 μm surface area of pure $YBa_2Cu_3O_{7-\delta}$; b) 1 μm $\times$ 1 μm surface area of pure $YBa_2Cu_3O_{7-\delta}$; c) 5 μm $\times$ 5 μm surface area of 5%*mol* Ba_2YNbO_6 doped $YBa_2Cu_3O_{7-\delta}$; d) 1 μm $\times$ 1 μm surface area of 5%*mol* Ba_2YNbO_6 doped $YBa_2Cu_3O_{7-\delta}$

doped $YBa_2Cu_3O_{7-\delta}$ thin film. The first difference is the fact that in the Ba_2YNbO_6 sample the diameter of the growth grains appear to be slightly larger, the mean diameter measured in the undoped $YBa_2Cu_3O_{7-\delta}$ film in $\approx$ 500 nm while the one measured in the Ba_2YNbO_6 doped $YBa_2Cu_3O_{7-\delta}$ is $\approx$ 1 μm. This can be explained by a lower nucleation rate in the Ba_2YNbO_6 doped film. The second difference is the grain boundary shape, rough in Ba_2YNbO_6 doped $YBa_2Cu_3O_{7-\delta}$ films and smooth in undoped $YBa_2Cu_3O_{7-\delta}$ films.

The main difference between the surface morphology of the doped film and that of the pure $YBa_2Cu_3O_{7-\delta}$ is evidenced by the comparison of the 1μm $\times$1μm scans, figure 4.6b and 4.6d. The latter shows superficial particles of $\approx$ 15-20 nm in diameter that are absent in the image of taken from the pure $YBa_2Cu_3O_{7-\delta}$ thin film. These superficial particles, that are to be attributed to the Ba_2YNbO_6 presence, are uniformly distributed over the sample surface and are not segregated at the grain boundary. This is a first experimental evidence that a uniformly distributed array of defects based on Ba_2YNbO_6 is possibile given that the Ba_2YNbO_6 is able to grow inside a $YBa_2Cu_3O_{7-\delta}$ crystal in the form of nanometric inclusion and is not expelled from the growing $YBa_2Cu_3O_{7-\delta}$ grains during the deposition (figure 4.6d).

4.2.3.2 Cross-section transmission electron microscopy

The morphology of the Ba_2YNbO_6 inclusions was studied with the use of cross sectional imaging of the sample by transmission electron microscopy. In figure 4.7 is shown cross-section transmission micrography of a 5%*mol* Ba_2YNbO_6 doped thin film. Nanorods aligned with the *c*-axis of the films are evidently shown.

The nanorods imaged are $\approx$ 10 nm in diameter and the spacing between two adjoining rods is $\approx$ 40 nm. A similar spacing is observed in the superficial particles shown by the atomic force microscopy scan reported in figure 4.6d. These similar spacing values is a validation of the assumption that the particles observed on the surface by using the atomic force microscopy are related to the nanorods terminating at the film surface. The diameter of the particles observed on the surface with the atomic force microscopy appears to be larger then the diameter of the nanorods observed with the transmission electron microscopy. There are

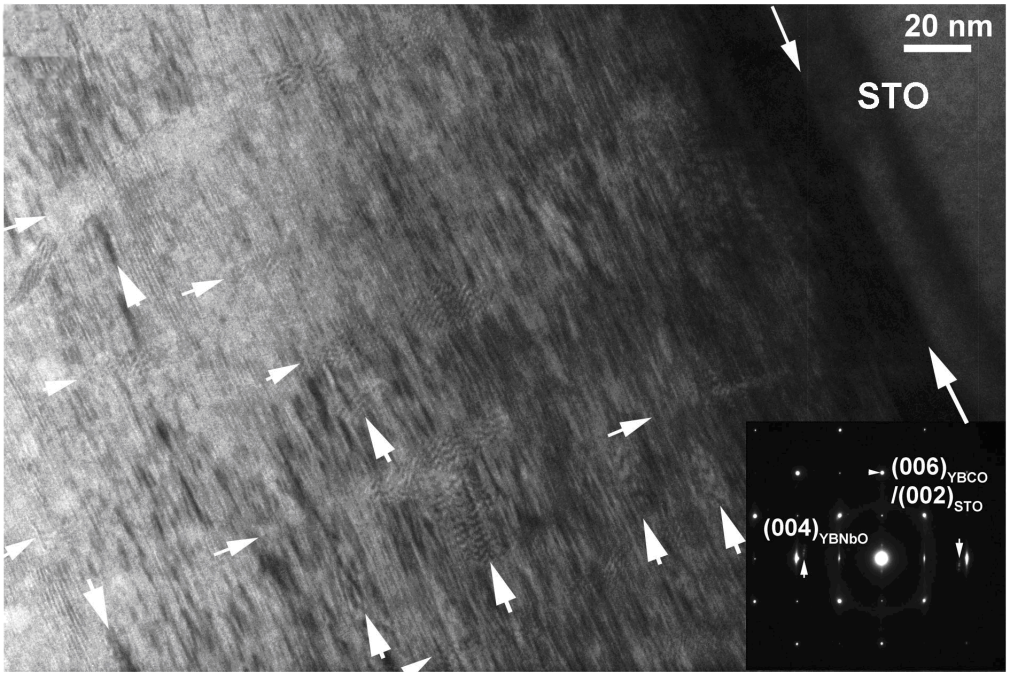

Figure 4.7: Transmission electron microscope cross-sectional image of a 5%*mol* Ba_2YNbO_6 doped $YBa_2Cu_3O_{7-\delta}$ thin film. White arrows in the direction of the *c*-axis mark the position of self assembled Ba_2YNbO_6 nanorods parallel to the *c*-axis. Larger white arrows parallel to the $YBa_2Cu_3O_{7-\delta}$ *ab*-planes mark the position of nanoparticles and of the interface between the substrate and the thin film. Inset shows selected area electron diffraction pattern taken from a region in proximity of a Ba_2YNbO_6 inclusion showing diffraction spot of Ba_2YNbO_6 $YBa_2Cu_3O_{7-\delta}$ and $SrTiO_3$. *(TEM images from Prof. H Wang research group at Texas A&M University).*

two plausible explanations that are not mutually exclusive but may be jointly responsible for the observed difference. The first explanation is found in the fact that the superficial particles might actually have a larger diameter because at the surface the ions mobility is higher and there may also be further agglomeration immediately after the deposition is terminated. The second possible explanation is related to differences in the resolution of the two methods of analysis used. In particular, the resolution of the atomic force microscopy depends on the diameter of the tip adopted. Tips with a larger diameter can make features appear larger than they are in reality. This aberration is absent in the transmission electron microscopy where the captured images are not subjected to the described deformation.

Additional information that can be derived from the nanorods spacing is the matching field. The matching field is the field value at which the spatial density of defects is equal to that of the flux lines passing through the superconductor. At this field value the pinning potential is the highest since in theory each and every flux line should be pinned by a single nanorod. Unfortunately, unlike a perfect Abrikosov lattice, it is not possible to identify a triangular or square arrangement of flux lines in superconductors with defects. In fact, the flux lines tend to change their spatial arrangement to overlap the defects distribution. Nevertheless it is at least possible to have an estimation of the matching field by using the mean spacing of the nanorods noticing that for a random distribution this tends to be higher than that derived for a square distribution and lower that that of a triangular distribution. The equations reported below refer to the matching field calculation derived for a square and a triangular distribution (note that Φ_0 is the quantized flux $\approx 2.067 \times 10^{-15}$ Wb and d is the defects average spacing)

$$H^* = \frac{\Phi_0}{d^2} \tag{4.3}$$

$$H^* = \frac{2\sqrt{3}\Phi_0}{3d^2} \tag{4.4}$$

Calculating the matching field for a defects average spacing of $\approx$ 40 nm applying the formula derived for a square distribution 4.3 gives a matching field $H^* \approx 1.29$ T. Applying the formula derived for triangular distribution 4.4 the

calculated matching field H^* is $\approx$ 1.49 T. The applied magnetic field value in which the pinning potential of the analysed thin films should be higher is between 1.29 T and 1.49 T.

In order to validate and complete the x-ray diffraction data reported in the previous section an electron diffraction pattern of the cross section is shown in the inset to figure 4.7. It is possible to observe a set of streaky diffraction dots for the *(004)* Ba_2YNbO_6. The presence of streaky dots is related to large Ba_2YNbO_6 *c*-axis distortions. These distortions were expected due to the fact that the x-ray analysis reported a compressive strain along the *c*-axis of the Ba_2YNbO_6 in the order of $\approx$ 1.7%. The lattice spacing *d (004)* calculated from the electron diffraction pattern is $\approx$ 0.214 nm, indicating a lattice parameter a $\approx$ 0.856 nm. This lattice parameter value, while being broadly consistent with the x-ray measurements and confirming the secondary phase as the Ba_2YNbO_6 double perovskite, does not confirm the compressive nature of the strain.

In the cross sectional images the nanorod inclusions are not the only nanoinclusions evidenced. A small fraction of nanoparticles are evidenced by the white arrows parallel to the *ab*-planes. The presence of both self assembled nanorods and nanoparticles is a feature which was already observed in $BaZrO_3$ added $YBa_2Cu_3O_{7-\delta}$ as well as $RETa_3O_7$ added $YBa_2Cu_3O_{7-\delta}$, the amount of nanoparticles is related to the deposition condition [133,134]. In the work of Boris Maiorov *et al.*, published in 2009, an interesting discussion of the beneficial effects resulting from simultaneous presence of both nanorods and nanoparticles is reported. In their work it is shows how the synergetic combination of such 1D defects (nanorods) and point defects (nanoparticles) can strongly enhance the flux pinning by preventing some low energy depinning mechanism to take place. In particular it is discussed how the flux jump from two adjacent nanorods with a double kink propagation mechanism is associated with a higher energetic barrier when a nanoparticle is introduced between the two adjacent nanorods or when the nanorods are not highly linear, continuous and are not all perfectly parallel to the *c*-axis.

Analysing the higher magnification images (figure 4.8a and 4.8b) it is clear how the nanorods formed by the Ba_2YNbO_6 are wider ($\approx$ 10 nm) than the $RETa_3O_7$ ($\approx$ 5 nm) and $BaZrO_3$ ($\approx$ 7-8 nm), with a larger angle spread around the *c*-

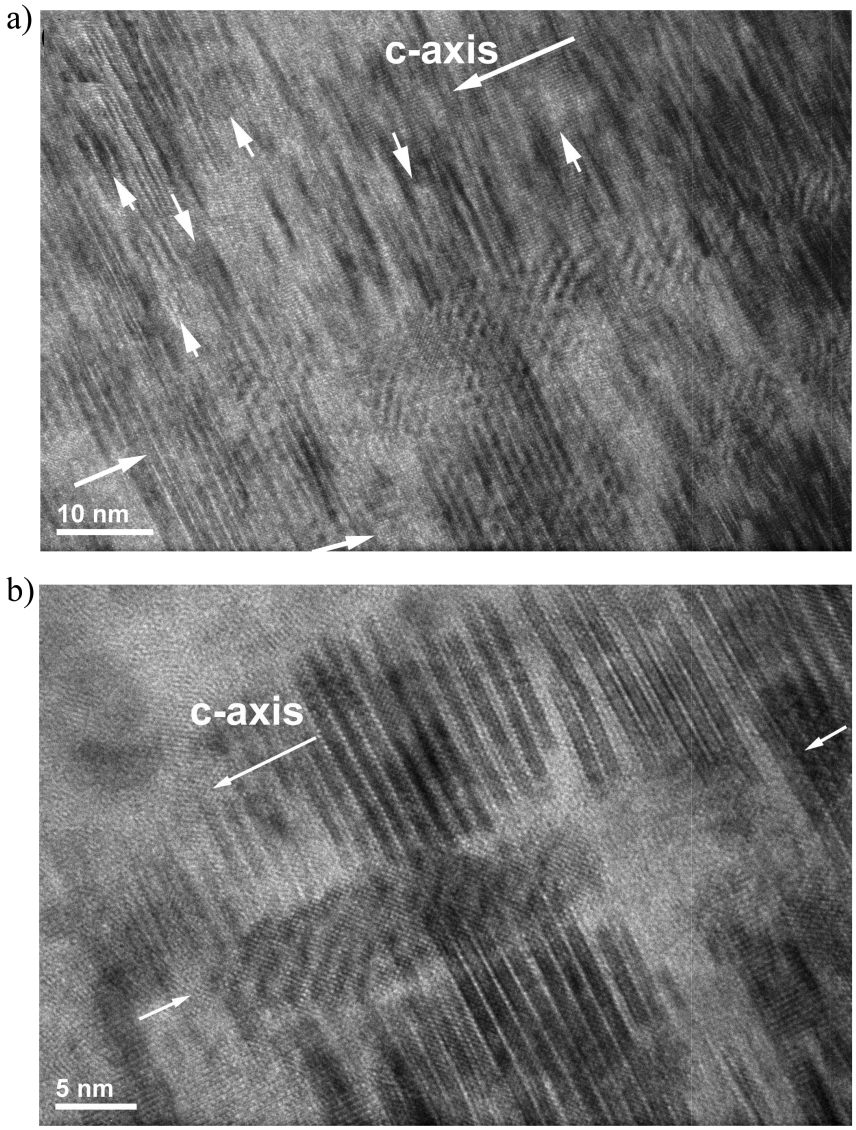

Figure 4.8: Transmission electron microscope cross-sectional image of a 5%*mol* Ba_2YNbO_6 doped $YBa_2Cu_3O_{7-\delta}$ thin film. White arrows in the direction of the $YBa_2Cu_3O_{7-\delta}$ *c*-axis mark the position of self assembled Ba_2YNbO_6 nanorods parallel to the *c*-axis. Arrows parallel to the $YBa_2Cu_3O_{7-\delta}$ *ab*-planes mark the position of nanoparticles. The Ba_2YNbO_6 nanorods presence is indicated by the Moire fringes arising from lattice mismatch between Ba_2YNbO_6 and $YBa_2Cu_3O_{7-\delta}$. *(TEM images from Prof. H Wang research group at Texas A&M University).*

axis and shorter $\approx$ 100 nm as opposed to whole film thickness. Furthermore adding the simultaneous presence of nanoparticles and nanorods the resulting pinning landscape should be optimal in minimizing the low energy depinning mechanism efficiency. On the downside the fact that the nanorods tend to be wider indicates a lower rate of nucleation than $RETa_3O_7$, $BaZrO_3$ and $BaSnO_3$. The main consequence is a lower defects density at equal volumetric doping that should result in a lower pinning efficiency at high field values.

One last thing to notice in this transmission electron microscopy study of the Ba_2YNbO_6 doped $YBa_2Cu_3O_{7-\delta}$ sample is the evidence of how the $YBa_2Cu_3O_{7-\delta}$ lattice is deformed by the nanorod inclusions. As perfectly pictured in figure 4.8b the $YBa_2Cu_3O_{7-\delta}$ *ab*-planes are curved around the nanorods. The lattice mismatch between the $YBa_2Cu_3O_{7-\delta}$ and the Ba_2YNbO_6 induce buckling of the $YBa_2Cu_3O_{7-\delta}$ crystalline planes around the nanorods. Superconductivity is then expected to be depressed in the region surrounding the Ba_2YNbO_6 nanorods. The high possibility of additional pinning from strain fields in the vicinity of Ba_2YNbO_6-$YBa_2Cu_3O_{7-\delta}$ interfacial regions is once more evidenced.

4.2.4 The superconducting properties: T_c, $J_c(B)$ and $J_c(B,\theta)$

A preliminary study of the effects of Ba_2YNbO_6 inclusions in $YBa_2Cu_3O_{7-\delta}$ can not be considered complete without the analysis of the main superconducting properties. Once the crystalline structure and the nanostructure of the sample have been discussed it is necessary, in order to have an overall picture of Ba_2YNbO_6 performance, to evaluate the effective superconducting properties. Considering a power application such as superconducting cable or a more sophisticated application such as superconducting coils for magnets, the most important properties to evaluate are the transition temperature T_c, the variation of the critical current density as a function of the applied magnetic field value $J_c(B)$ and the variation of the critical current density as a function of the direction at which the magnetic field is applied $J_c(B,\theta)$.

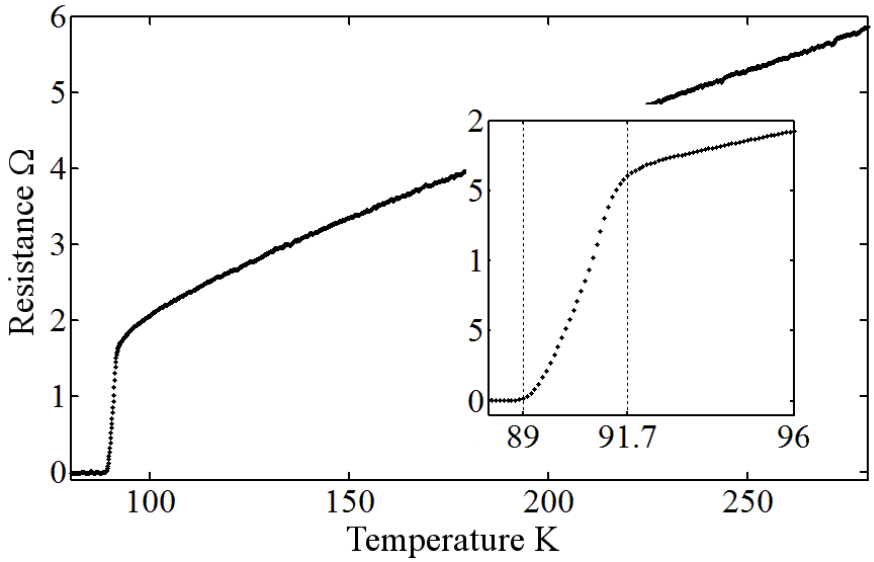

Figure 4.9: Resistance variation with the temperature measured on a 5%*mol* Ba_2YNbO_6 doped $YBa_2Cu_3O_{7-\delta}$ thin film. The inset shows the region of the superconducting transition magnified.

4.2.4.1 Transition temperature, T_c

In figure 4.9 is reported the resistance measured on a 50 μm width current track patterned on 5%*mol* Ba_2YNbO_6 doped $YBa_2Cu_3O_{7-\delta}$ thin film. The transition temperature T_c measured as the temperature at which the resistance disappears is $T_c = 89$ K. The reduction in the T_c is lower than expected. Reduced T_cs have been reported for most of the doped $YBa_2Cu_3O_{7-\delta}$ films produced [57,68,118,119]. The T_c reduction is usually a function of the volumetric amount of the doping and the lattice distortion induced. It is important to notice that similar T_c reductions were observed in 5%*mol* $BaZrO_3$ doped $YBa_2Cu_3O_{7-\delta}$ thin films [67], but the volumetric amount of Ba_2YNbO_6 in 5%*mol* Ba_2YNbO_6 doped $YBa_2Cu_3O_{7-\delta}$ thin films is higher than that of $BaZrO_3$ in a 5%*mol* $BaZrO_3$ doped $YBa_2Cu_3O_{7-\delta}$ thin film. In particular a 5%*mol* Ba_2YNbO_6 doped $YBa_2Cu_3O_{7-\delta}$ thin film contains a 4.2%*vol* of Ba_2YNbO_6 while a $BaZrO_3$ in a 5%*mol* $BaZrO_3$ doped $YBa_2Cu_3O_{7-\delta}$ thin film contains a 1.8%*vol* of $BaZrO_3$ thus the T_c reduction registered in the Ba_2YNbO_6 doped scenario is lower than explected.

Two main informations can be derived from the observation of this small T_c reduction. First, the $YBa_2Cu_3O_{7-\delta}$ planes buckling around the nanorods (pictured in the transmission electron microscopy figure 4.8b) is an effective strain sink capable of limiting the strain field propagation in a region close to the nanorods, for this reason the detrimental effects of the strain on the transition temperature are minimal. Second, as it was expected from earlier report on Nb doped $YBa_2Cu_3O_{7-\delta}$ ceramics, the Nb do not substitute in the $YBa_2Cu_3O_{7-\delta}$ and the Ba_2YNbO_6 do not react with the superconducting lattice. In other words the Nb remains enclosed in the stable Ba_2YNbO_6 and the only effects on the $YBa_2Cu_3O_{7-\delta}$ crystalline structure are related to the lattice accommodation of the mismatch.

4.2.4.2 The critical current density

Despite the slightly reduced T_c the critical current density J_c is improved over the whole field values window analysed.

In figure 4.10 is reported $J_c(B)$ measurements up to 1 T with the field applied parallel to the c-axis ($B \| c$) at 77 K for a pure $YBa_2Cu_3O_{7-\delta}$ thin film and a $5\% mol$ Ba_2YNbO_6 doped $YBa_2Cu_3O_{7-\delta}$ thin film. It is evident that the J_c is higher for the doped thin film and that at 1 T the J_c is a higher by a factor of ≈ 2.

In the $J_c(B)$ measurements there is a region for low values of the applied magnetic field in which the critical current J_c can be approximated with the following equation:

$$J_c(B) \approx J_c(0)^{-\alpha * B} \tag{4.5}$$

The lower the α value the lower is the J_c reduction with increasing the applied magnetic field value. In the log-log plot shown in the inset are reported the calcutad α values for both the films. The lower α value calculated for the Ba_2YNbO_6 doped $YBa_2Cu_3O_{7-\delta}$ thin film is an indication of a higher pinning potential. The calculated α value for the Ba_2YNbO_6 doped $YBa_2Cu_3O_{7-\delta}$ sample is $\alpha = 0.37$ that is lower than the $\alpha = 0.51$ calculated for $YBa_2Cu_3O_{7-\delta}$ films of this study.

The measurements shown in figure 4.10 are exhaustive in describing the Ba_2YNbO_6

effects when the field is applied parallel to the c-axis, but in order to have a more complete picture of the Ba_2YNbO_6 efficiency as a pinning additive it is necessary to investigate the angular dependence of J_c. The angular dependence of the critical current density at 77 K for an applied field value of 0.5 T is reported in figure 4.11.

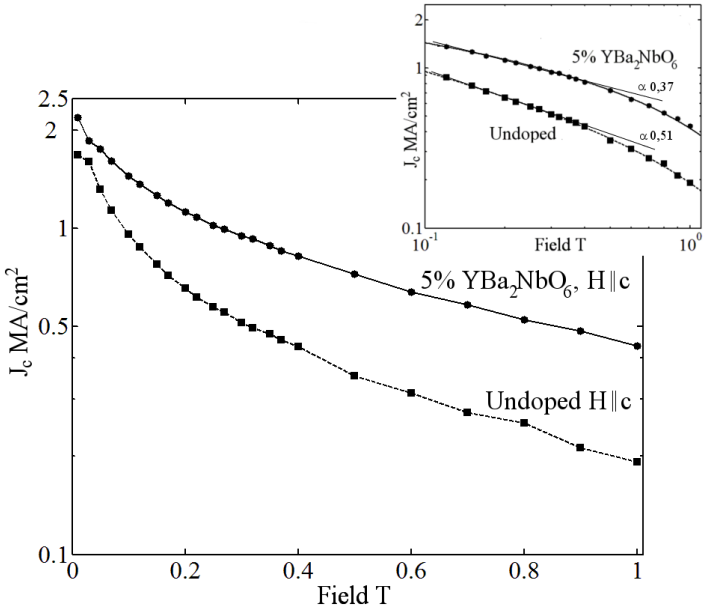

Figure 4.10: Critical current density variation with the applied magnetic field value measured on a pure $YBa_2Cu_3O_{7-\delta}$ and a 5%*mol* Ba_2YNbO_6 doped $YBa_2Cu_3O_{7-\delta}$ thin films at 77 K and field applied parallel to the c-axis of the $YBa_2Cu_3O_{7-\delta}$. The inset shows data on a logaritmic axis and the calculated α values.

The main characteristic of the $J_c(B,\theta)$ measured for the 5%*mol* Ba_2YNbO_6 doped $YBa_2Cu_3O_{7-\delta}$ thin film is a strongly reduced anisotropy compared to the $J_c(B,\theta)$ measured for the undoped $YBa_2Cu_3O_{7-\delta}$ thin film. The reduced anisotropy is related to an increase of the pinning potential when field is applied parallel to the Ba_2YNbO_6 nanorods. Since the nanorods are growing parallel to the c-axis of the $YBa_2Cu_3O_{7-\delta}$ (figure 4.7) the pinning potential, and thus the J_c, is increased when the field is applied parallel to the c-axis of the thin film,

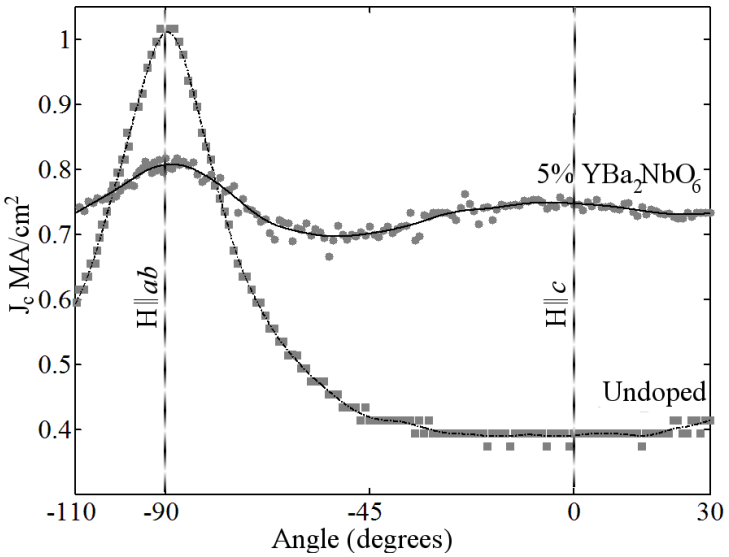

Figure 4.11: Critical current density variation with the direction of the applied magnetic field measured on a pure $YBa_2Cu_3O_{7-\delta}$ and a 5%*mol* Ba_2YNbO_6 doped $YBa_2Cu_3O_{7-\delta}$ thin films at 77 K and magnetic flux density = 0.5 T

which is orthogonal to the sample surface. Furthermore the anisotropy is reduced also by a reduction of the J_c when the field is applied parallel to the *ab*-plane of the $YBa_2Cu_3O_{7-\delta}$.

The two changes in the pinning potential described can be related to the presence of Ba_2YNbO_6. The increment of the critical current density, J_c, when the field is applied parallel to the Ba_2YNbO_6 nanorods was expected and has been described for all the secondary phases forming *c*-axis aligned nanorods. In general when the field is applied parallel to the direction of any form of one dimensional defects, such as Ba_2YNbO_6 nanorods, the interaction between the flux lines and the defects is maximized and for this reason the pinning effectiveness of the defects is optimal. At the same time the interruption of the intrinsic pinning layer of the $YBa_2Cu_3O_{7-\delta}$ (*ab*-planes) generated by the introduction of the Ba_2YNbO_6 nanorods together with the induced buckling of the $YBa_2Cu_3O_{7-\delta}$ crystalline planes around the nanorods could be responsible for the observed reduction of the critical current density when the field is applied parallel to the *ab*-planes of the $YBa_2Cu_3O_{7-\delta}$.

An interesting feature that can be observed when comparing the effects of the Ba_2YNbO_6 introduction in the $YBa_2Cu_3O_{7-\delta}$ to the angular dependence of the critical current density with the effects of the other pinning secondary phases (Ba(Zr,Y)O_3, $RETa_3O_7$, $BaSnO_3$ and Ba_2YTaO_7) is that the Ba_2YNbO_6 nanorods appears to be effective over a larger angular range producing a broader c-axis peak. The formation of shorted nanorods not perfectly oriented parallel to the c-axis of the $YBa_2Cu_3O_{7-\delta}$ (discussed in the transmission electron microscopy analysis) could be the reason behind this increased effectiveness over the angles the magnetic field application.

To conclude the $J_c(B,\theta)$ analysis a small discussion on the effects of the Ba_2YNbO_6 nanoparticles observed in transmission electron microscopy of the thin film cross-section (figure 4.8a) has to be done. Nanoparticles are usually related to an increase of the isotropic pinning [69]. A strong additional isotropic pinning increases the critical current density, J_c, independently of the angle at which the magnetic field is applied. Thus the presence of nanoparticles would have no effect on the shape of the $J_c(B,\theta)$. On the other hand the reduced pinning potential observed when the magnetic field is applied parallel to the ab-planes of $YBa_2Cu_3O_{7-\delta}$ would suggest that an addition of isotropic pinning is absent. In reality the conclusion that can be made is that if nanoparticles are effectively adding an isotropic pinning to the Ba_2YNbO_6 doped $YBa_2Cu_3O_{7-\delta}$ thin film this is lower than the reduction of the ab-pinning potential generated by the Ba_2YNbO_6 introduction. Furthermore it is important to remember that the synergetic combination of Ba_2YNbO_6 nanorods and nanoparticles can strongly enhance the pinning provided by the Ba_2YNbO_6 nanorods to the fields applied parallel to the c-axis of the $YBa_2Cu_3O_{7-\delta}$ [134].

4.2.5 Concluding remarks to the preliminary results

In this section were reported the first results obtained by the addition of the Ba_2YNbO_6 perovskite pinning phase to $YBa_2Cu_3O_{7-\delta}$. The double perovskite Ba_2YNbO_6 results as a stable secondary phase that can be used with positive results as a pinning additive. Ba_2YNbO_6 is capable of forming c-axis oriented nanorods which result in shorter, wider nanorods than those generated by the

other known pinning additives; furthermore the Ba_2YNbO_6 nanorods are oriented parallel to the c-axis of the $YBa_2Cu_3O_{7-\delta}$ but with a larger splay angles range. For these reason the Ba_2YNbO_6 nanorods appear to be effective over a relatively large angular range of magnetic field application and not only when the field is applied parallel to c-axis of the $YBa_2Cu_3O_{7-\delta}$.

Chapter 5

Ba_2YNbO_6 doped $YBa_2Cu_3O_{7-\delta}$: the deposition parameters

The study in this chapter is an evaluation of how the production process parameters affect the formation of the secondary phase and the overall epitaxial quality of the thin films. Furthermore it is discussed how the epitaxial quality of the film and the morphology of the secondary phase influence the superconductive properties.

5.1 Ba_2YNbO_6 perovskite additions to $YBa_2Cu_3O_{7-\delta}$: the effects of the deposition rate on the nanostructure and the superconducting properties

The results obtained from the preliminary study on Ba_2YNbO_6 doped $YBa_2Cu_3O_{7-\delta}$ thin films showed that the secondary phase Ba_2YNbO_6 can be added into a mixed $YBa_2Cu_3O_{7-\delta}$-Ba_2YNbO_6 pulsed laser deposition target to obtain pinning enhanced superconducting thin films. In order to investigate the real potential of the double perovskite Ba_2YNbO_6 a study of the influence of the two principal deposition parameters on the nanostructure and the superconducting properties of Ba_2YNbO_6 doped $YBa_2Cu_3O_{7-\delta}$ thin films was performed.

A set of 5%*mol* Ba_2YNbO_6 doped $YBa_2Cu_3O_{7-\delta}$ thin films was deposited by varying the deposition rate. The crystalline structure, nanostructure and superconducting properties of the thin films produced were analyzed. In this section are reported the analysis results that allows a better understanding of the Ba_2YNbO_6-$YBa_2Cu_3O_{7-\delta}$ system overall and they demonstrate the possibility to tune the nano structure and the pinning properties of the Ba_2YNbO_6 doped $YBa_2Cu_3O_{7-\delta}$ thin films by adjusting the deposition parameters.

5.1.1 Ba_2YNbO_6 doped $YBa_2Cu_3O_{7-\delta}$ target preparation and thin film deposition

The target used in the pulsed laser deposition of Ba_2YNbO_6 doped thin films analysed in this section is similar to the one that was described in the previous section. Since the preliminary study reported in the previous section evidenced a small fraction of particulates on the thin film surfaces (see 4.2.3.1), a variation to the production process of the target adopted for the analysis described in this section was implemented. Densification of the pulsed laser deposition target is a first countermeasure to the formation of particulate on the deposited thin film surface. In order to achieve a more dense target, once sintered a first time it was subjected to a subsequent regrinding. The powders obtained by the second grinding were again pressed in the form of a cylindrical target and the sintered at 950 °C in oxygen flow for additional 12hr.

The laser pulses repetition rate was systematically modified to study its effects on the nanostructure and pinning properties of the deposited thin films. The laser pulse repetition rate variation changes the maximum time allowed to the ions migration on the surface of a growing film before new higher energy ions are deposited from a subsequent laser pulse. A higher rate increases the deposition rate but lowers the *"free migration"* time. This parameter has a direct effect on the migration time and thus a direct effect on the crystalline and nanostructure of the growing films. In particular repetition rates of 1, and 10 Hz and substrate temperatures of 780 °C were investigated. In the table below 5.1 are summarized the pulsed laser deposition parameters adopted for the deposition of the Ba_2YNbO_6 doped $YBa_2Cu_3O_{7-\delta}$ thin films analysed in this section.

Parameter	Value
Substrate Temperature	780 °C
Chamber Pressure	0.3 mbar flowing O_2
Laser Fluence	2 Jcm^{-2}
Repetition Rate	1, 10 Hz
Number of Pulses	4500
Annealing Time	1 hr
Annealing Temperature	520 °C
Annealing Pressure	500 mbar O_2

Table 5.1: Pulsed laser deposition parameters

All the Ba_2YNbO_6 doped $YBa_2Cu_3O_{7-\delta}$ thin films deposited were measured to be of $\approx$ 0.4 μm thickness. Some additional thicker samples of $\approx$ 0.7 μm thickness where also deposited using 8000 laser pulses.

5.1.2 Crystalline structure analysis: x-ray diffraction data

Similarly to the crystalline phases characterization realised for the first Ba_2YNbO_6 doped $YBa_2Cu_3O_{7-\delta}$ system, reported in the previous section, the crystalline structures of all the samples produced for the study of the effects of the deposition parameters were analysed with an extensive use of the x-ray diffraction technique.

5.1.2.1 Crystalline phases identification, phases orientation

The x-ray diffraction data collected in the Bragg-Brentano geometry to identify the crystalline phases as well as the *in*-plane texture analysis by examination of ϕ scans don't add additional information to the ones gathered in the previous section. The results obtained at the different growth condition closely matches each other. For this reason it is hard to understand if there are differences in the crystalline structures of the Ba_2YNbO_6 doped $YBa_2Cu_3O_{7-\delta}$ thin films that were deposited in the different conditions described.

At a first x-ray diffraction analysis all the samples appears to have similar crystalline features. The only diffraction peaks evidenced by x-ray diffraction analysis in the Bragg-Brentano geometry ($\theta - 2\theta$ scan) are those related to the

$(00l)$ planes from the $YBa_2Cu_3O_{7-\delta}$, the Ba_2YNbO_6 and the $SrTiO_3$. Furthermore also the ϕ scans closely matches for the different thin films and confirms the *in*-plane orientation discussed in the previous section.

In conclusion the $\theta - 2\theta$ and the ϕ scans are not capable at identifying differences in the crystalline structures and varying laser pulses repetition rate do not change the fact that the Ba_2YNbO_6 doped $YBa_2Cu_3O_{7-\delta}$ thin films deposited con be mainly described as epitaxial $YBa_2Cu_3O_{7-\delta}$ films with the presence of a *cube on cube* oriented Ba_2YNbO_6 perovskite within the $YBa_2Cu_3O_{7-\delta}$.

5.1.2.2 Epitaxy quality: rocking curve

Even if the standard x-ray diffraction analysis does not detect differences in the crystalline structure, a first classification can be made on the basis of the epitaxial quality. The quality of the $YBa_2Cu_3O_{7-\delta}$ epitaxy with the $SrTiO_3$ can be analysed by the rocking curve detection. The half maximum width of the diffraction peaks resulting from a rocking curve scan is an indication of the angular spread of the *c*-axis orientation. The lower the spread, the higher is the *c*-axis alignment.

Thin Film	$SrTiO_3$ (002)	$YBa_2Cu_3O_{7-\delta}$ (005)	Ba_2YNbO_6 (004)
$YBa_2Cu_3O_{7-\delta}$ (1 Hz)	0.10	0.18	
$YBa_2Cu_3O_{7-\delta}$ (10 Hz)	0.12	0.18	
doped $YBa_2Cu_3O_{7-\delta}$ (1 Hz)	0.11	0.15	1.0
doped $YBa_2Cu_3O_{7-\delta}$ (10 Hz)	0.10	0.20	2.1

Table 5.2: Full Width Half Maximum values of the $SrTiO_3$ *(002)*, $YBa_2Cu_3O_{7-\delta}$ *(005)* and Ba_2YNbO_6 *(004)* rocking curves measured on pure $YBa_2Cu_3O_{7-\delta}$ and $5\%_{mol}$ Ba_2YNbO_6 doped $YBa_2Cu_3O_{7-\delta}$ thin films deposited at a substrate temperature of 780 °C and repetition rate of 1 and 10 Hz.

In the table 5.2 is reported the full width half maximum (FWHM) values of the rocking curves around the *(002)* $SrTiO_3$, *(005)* $YBa_2Cu_3O_{7-\delta}$ and *(004)* Ba_2YNbO_6 planes of the different samples. The FWHM values of the $YBa_2Cu_3O_{7-\delta}$ do not reveal an evident pattern and the most relevant information is that the $YBa_2Cu_3O_{7-\delta}$ *c*-axis orientation do not appear to be influenced by the deposition rate in absence of the Ba_2YNbO_6 phase. The Ba_2YNbO_6 FWHM values instead shows that the sample deposited at higher deposition rate (higher

laser repetition rate) shows a larger FWHM value than the one obtained for the sample deposited at lower deposition rate. Larger *"free migration"* time allow the formation of a Ba_2YNbO_6 crystalline lattice with a higher *c*-axis alignment.

One thing to notice is that since the Ba_2YNbO_6 is growing inside a $YBa_2Cu_3O_{7-\delta}$ lattice its orientation quality is strictly related to $YBa_2Cu_3O_{7-\delta}$. More precisely the Ba_2YNbO_6 lattice does not present a better *c*-axis orientation alignment than the $YBa_2Cu_3O_{7-\delta}$ lattice in which it is formed, on the other hand it is also true that a poorly oriented Ba_2YNbO_6 can be formed in a perfectly oriented $YBa_2Cu_3O_{7-\delta}$ matrix.

While it is possible to use a technique developed to investigate the *c*-axis alignment quality of thin films to also analyse that of the Ba_2YNbO_6 nanoparticles and nanorods it is not possible to directly compare the FWHM obtained for the Ba_2YNbO_6 nanoinclusions with those obtained with the $YBa_2Cu_3O_{7-\delta}$ thin films. In general, since the Ba_2YNbO_6 is a dopant and its quantity is only a fraction of the $YBa_2Cu_3O_{7-\delta}$, the intensity x-ray diffraction peaks related to the Ba_2YNbO_6 are $\approx$ 2 orders of magnitude lowers than those related to the $YBa_2Cu_3O_{7-\delta}$. Furthermore the morphological nature of the Ba_2YNbO_6, nanorods and nanoparticles, is responsible for an additional broadening of the Ba_2YNbO_6 peaks in the diffraction pattern that is related to the size of the phase and not the strain or orientation. For these reason the FWHM values obtained from the Ba_2YNbO_6 should be taken as a comparison between the different *c*-axis degrees of the Ba_2YNbO_6 phase only.

5.1.2.3 Epitaxy quality: reciprocal space maps

The rocking curve were used to investigate the quality of the *c*-axis alignment for both the Ba_2YNbO_6 and $YBa_2Cu_3O_{7-\delta}$ separately but while a first information on the Ba_2YNbO_6 phase was revealed it was impossible to obtain additional information on the $YBa_2Cu_3O_{7-\delta}$. In order to further investigate the effects of the deposition parameters on the overall epitaxial quality of the $YBa_2Cu_3O_{7-\delta}$ and Ba_2YNbO_6 nanoparticles reciprocal space maps were gathered for a pure $YBa_2Cu_3O_{7-\delta}$ thin film, and two Ba_2YNbO_6 doped $YBa_2Cu_3O_{7-\delta}$ thin films. In particular the Ba_2YNbO_6 doped films were deposited adopting different repetition

rate of the ablating pulsed laser, 1 and 10 Hz, but maintaining the same substrate temperature of 780 °C; the pure $YBa_2Cu_3O_{7-\delta}$ was deposited at 1 Hz and the same substrate temperature.

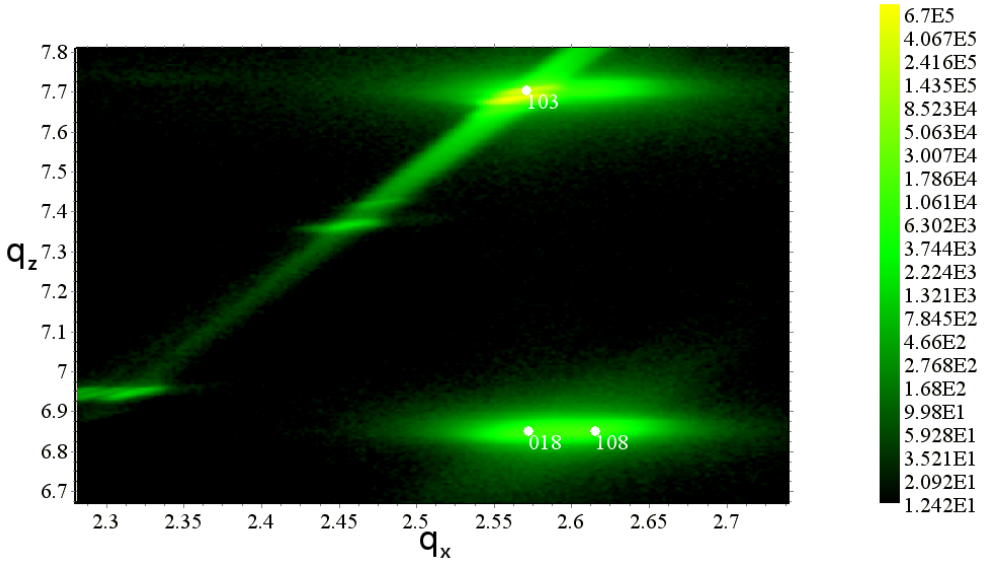

Figure 5.1: X-ray diffraction reciprocal space map measured on a pure $YBa_2Cu_3O_{7-\delta}$ thin film.

In figure 5.1 is reported the reciprocal space map gathered from a pure $YBa_2Cu_3O_{7-\delta}$ sample. There are three main diffraction peaks, the *(103)* of the $SrTiO_3$ and the *(109)* - *(019)* of the $YBa_2Cu_3O_{7-\delta}$ are overlapping each other while is clearly visible the *(108)* - *(018)* of the $YBa_2Cu_3O_{7-\delta}$. The $YBa_2Cu_3O_{7-\delta}$ peaks are actually formed by two different peaks related to the inevitable twins formation. It is impossible to distinguish between the *(108)* and the *(018)* $YBa_2Cu_3O_{7-\delta}$ peaks because the two peaks are too close in the reciprocal space that they appear as a single large peak, the theoretical peaks position indicated in the reciprocal space maps are well between the peaks boundary and the center of the peak is between this two theoretical position as expected in twin formations.

It is possible from the reciprocal space maps to calculate the lattice parameters directly from the coordinate of a peak in the reciprocal space if the *(h,k,l)* index is known. Remembering that the reciprocal space coordinates (q_x and q_z) are the reciprocal of the lattice spacing (d_x and d_z) the lattice parameters a,b and c for

a *(h,0,l)* and a *(0,k,l)* can be calculated applying the following formulas:

for a *(h,0,l)* peak

$$a = \frac{h}{q_x} \tag{5.1}$$

$$c = \frac{l}{q_z} \tag{5.2}$$

for a *(0,k,l)* peak

$$b = \frac{k}{q_x} \tag{5.3}$$

$$c = \frac{l}{q_z} \tag{5.4}$$

In figure 5.1 it is easier to calculate the $YBa_2Cu_3O_{7-\delta}$ lattice parameters from the *(108)-(018)* peaks since these are not overlapping with the any other phases peak. Its important to notice that similarly to the lattice mismatch calculated in the last section since it not possible to separate the *(108)* peak from the *(018)* the lattice parameter calculated from the q_x coordinate of the reciprocal space map refers to an average value between the a and b lattice parameters. The average ab calculated from the a and b bulk values ($a = 0.382$ nm and $b = 0.388$ nm), is $ab_{bulk} = 0.385$ nm and it is perfectly in line with the average value calculated from the *(108)-(018)* $YBa_2Cu_3O_{7-\delta}$ taken from the reciprocal space map in figure 5.1 where a $q_x = 2.60$ nm^{-1} also gives a $ab = 0.385$ nm. Similarly the $YBa_2Cu_3O_{7-\delta}$ c lattice parameter bulk value is $c = 1.168$ nm and from a $q_z = 6.85$ nm^{-1} a $c = 1.168$ nm is calculated. The $YBa_2Cu_3O_{7-\delta}$ thin film while being epitaxial with the SrTiO_3 substrate it is relaxed and the lattice parameters have the same value reported in literature for bulk $YBa_2Cu_3O_{7-\delta}$.

Focusing on the *(103)* $SrTiO_3$ diffraction peak at $q_x = 2.56$ nm^{-1} and $q_z = 7.68$ nm^{-1}, it is evident that additional diffraction peaks of *(103)* are present. The presence of these additional peaks is related to the use of a x-ray incident beam that is not monochrome and, even if the main quantity of x-rays are the Cu K_α with $\lambda = 0.15405$ nm, there are also secondary x-rays generated at different λ that are the cause of the additional diffraction peaks presence. The intensity of the secondary peaks is lower and these are only visible for the high intensity $SrTiO_3$

diffraction peaks. Another feature related to the *(103)* $SrTiO_3$ is a diagonal line also only visible for the high intensity diffraction generated by the substrate, also this line is an artifact generated by the absence of a monochromator in particular the line is generated by non copper x-rays emissions.

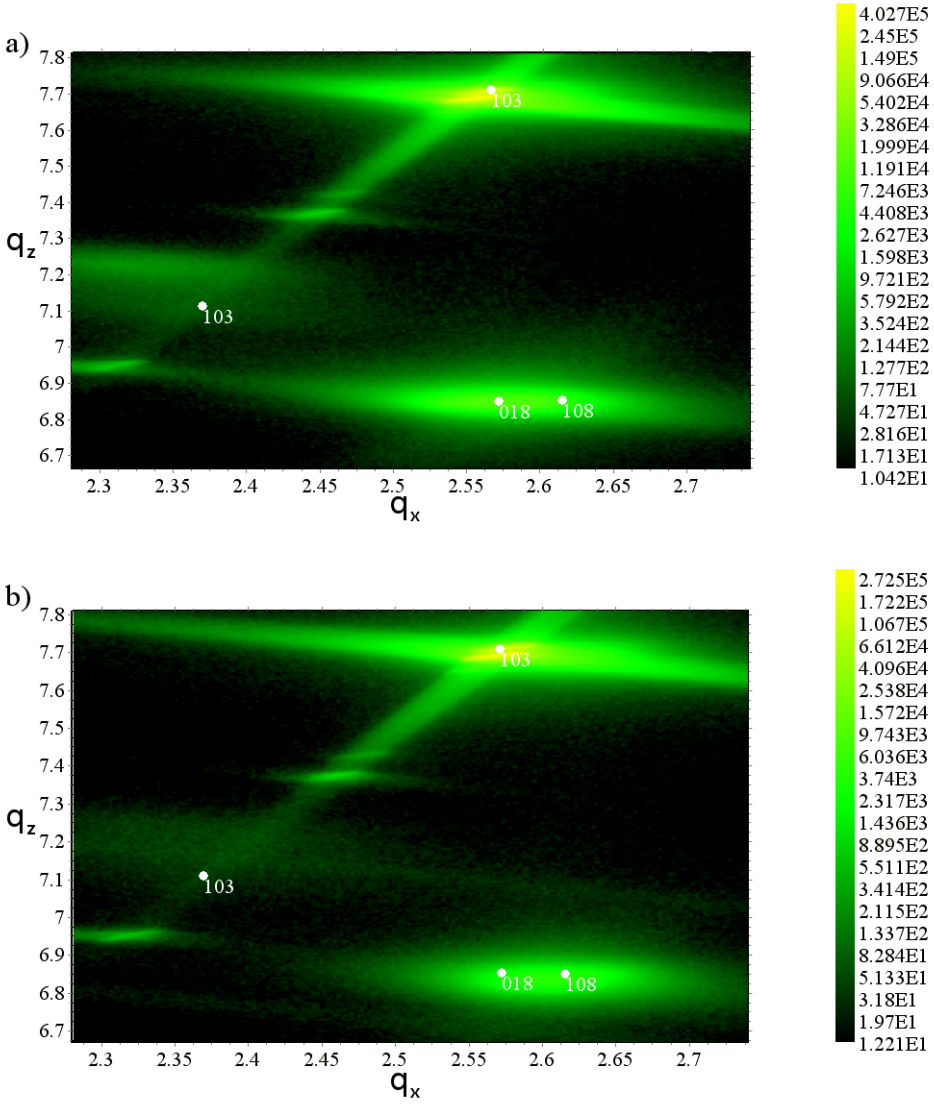

Figure 5.2: X-ray diffraction reciprocal space map measured on $5\%_{mol}$ Ba_2YNbO_6 doped $YBa_2Cu_3O_{7-\delta}$ thin films. a) Film deposition rate of 1 Hz; b) Film deposition rate of 10 Hz.

In figure 5.2 are reported the reciprocal space map gathered from a Ba_2YNbO_6 doped $YBa_2Cu_3O_{7-\delta}$ sample deposited at 1 Hz repetition rate (figure 5.2a) and a Ba_2YNbO_6 doped $YBa_2Cu_3O_{7-\delta}$ thin film deposited at 10 Hz repetition rate (figure 5.2b). In addition to the three main diffraction peaks also present in figure 5.1, that are related to the $YBa_2Cu_3O_{7-\delta}$ and the substrate, the (103) Ba_2YNbO_6 peak is also present. Comparing the image in figure 5.1 with the images in figure 5.2 the *(103)* Ba_2YNbO_6 peak is not the only evident difference, a broadening of the $YBa_2Cu_3O_{7-\delta}$ related peaks is a second clear effect of the Ba_2YNbO_6 doping. The broadening of the $YBa_2Cu_3O_{7-\delta}$ peaks in the Ba_2YNbO_6 doped samples could be related to the buckling of the crystalline $YBa_2Cu_3O_{7-\delta}$ planes around Ba_2YNbO_6 nanoinclusion discussed in the last section. The fact that overall the lattice parameter of the $YBa_2Cu_3O_{7-\delta}$ does not seem to change confirms that the broadening is related to a local distortion, like planes buckling.

Finally a direct indication of the effects of the deposition parameters on the crystalline structure can be obtained by the comparison of the reciprocal space maps of the two different Ba_2YNbO_6 doped $YBa_2Cu_3O_{7-\delta}$ thin films (figure 5.2a and 5.2b). First the *(103)* Ba_2YNbO_6 peak shape and intensity appear to be different in the two samples. In particular the Ba_2YNbO_6 peak of the 10 Hz sample (figure 5.2b) has a lower intensity and a long tail is present. These two features could be evidence of the existence of a fraction of randomly oriented Ba_2YNbO_6 that is absent in the 1 Hz sample (figure 5.2a). From the *(103)* Ba_2YNbO_6 peak of the 1 Hz sample it is possible to calculate the lattice parameters a of the Ba_2YNbO_6 phase in the planar direction and in the $YBa_2Cu_3O_{7-\delta}$ c-axis direction from the q_x and q_z values respectively. Applying the equations 5.1 and 5.2 on the $q_x = 2.32$ nm^{-1} and $q_z = 7.22$ nm^{-1} taken from figure 5.2a the lattice parameters $a = 0.430$ nm along the planar direction and $c = 0.415$ nm are calculated. The Ba_2YNbO_6 phase lattice parameter bulk value is $a = 0.422$ nm, and comparing this value with those calculated from the reciprocal space map it is clear that the Ba_2YNbO_6 is subjected to a compressive strain along the $YBa_2Cu_3O_{7-\delta}$ c-axis direction and an elongation strain along the $YBa_2Cu_3O_{7-\delta}$ ab-planes direction. The deformation calculated for the two different direction are + 1.9 % along the ab-planes direction and - 1.66 % along the c-axis direction. Considering the morphological nature of the Ba_2YNbO_6 inclusions it is possible

to explain why the compressive strain is only acting in the *c*-axis direction even if the lattice mismatch calculated from the bulk values (*in-plane* lattice mismatch = + 9.42 % and *c*-axis lattice mismatch = + 8.34 %) indicate a compressive strain in all directions. The Ba_2YNbO_6 is mainly forming nanorods aligned parallel to the *c*-axis of the $YBa_2Cu_3O_{7-\delta}$ thus the interface between the Ba_2YNbO_6 and the $YBa_2Cu_3O_{7-\delta}$ is developing prevalentely along the *c*-axis direction; for this reason the minimization of the mismatch along the *c*-axis direction is energetically more relevant. The difficulty to identify unique q_x and q_z values in the low intensity peak of the Ba_2YNbO_6 measured from the the 10 Hz deposited thin film makes not possible the repetition of the calculations performed on the 1 Hz deposited sample.

Analysing the *(108)-(018)* $YBa_2Cu_3O_{7-\delta}$ peaks in figure 5.2 additional information on the effects of the deposition rate on the $YBa_2Cu_3O_{7-\delta}$ lattice is obtained. The broadening of the peak related to the Ba_2YNbO_6 doping is slightly more relevant in the Ba_2YNbO_6 doped $YBa_2Cu_3O_{7-\delta}$ thin film deposited with a laser repetition rate of 10 Hz. This indicates that the $YBa_2Cu_3O_{7-\delta}$ region affected by lattice distortions (buckling of the crystalline planes) is larger when the deposition rate is higher. There are two possible explanation of this evidence, in particular either a larger region of $YBa_2Cu_3O_{7-\delta}$ may be affected by lattice distortions around each nanoinclusion or the Ba_2YNbO_6 nanoinclusions density may be higher. The phase that is more directly affected by diffusion processes, and thus by the deposition rate, is the Ba_2YNbO_6. The Nb ions must in fact diffuse on larger region of the surface in order to form the Ba_2YNbO_6 nanoinclusions. For this reason the higher density of Ba_2YNbO_6 inclusions is more likely the cause of the increased lattice distortion.

In figure **??** is shown a direct comparison of the *(108)-(018)* $YBa_2Cu_3O_{7-\delta}$ peaks in the different films, the indication of the peaks' position as well as the half maximum intensity isolines allow direct visualization of the effects of the presence of Ba_2YNbO_6 on the $YBa_2Cu_3O_{7-\delta}$ crystalline structure.

The broadening of the $YBa_2Cu_3O_{7-\delta}$ peaks is not the only difference, the lattice parameters measured from the reciprocal space map of the Ba_2YNbO_6 doped $YBa_2Cu_3O_{7-\delta}$ thin film deposited at 10 Hz is different from the one measured from the film deposited at 1 Hz. In particular, from the *(108)-(018)* $YBa_2Cu_3O_{7-\delta}$ peak

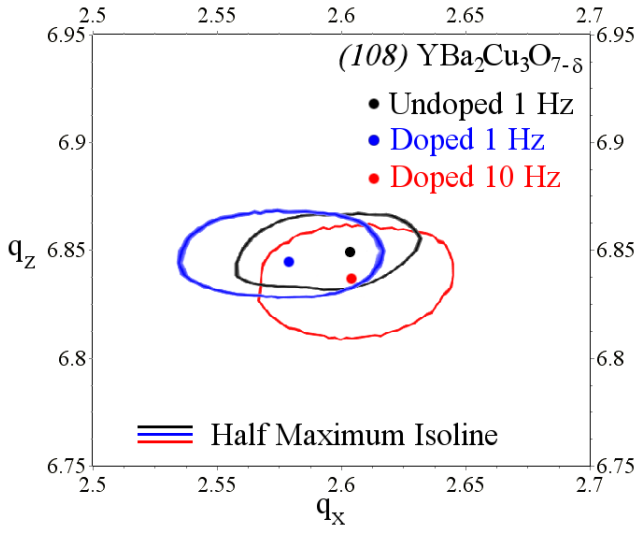

Figure 5.3: Half maximum intesity insoline and peak position comparison for the *(108)(018)* $YBa_2Cu_3O_{7-\delta}$ peaks from figure 5.1 and 5.2.

of the reciprocal space map measured on the film deposited at 1 Hz ($q_x = 2.58$ nm^{-1} and $q_z = 6.85$ nm^{-1}) the lattice parameters $ab = 0.388$ nm and $c = 1.168$ nm are calculated, while from the *(108)-(018)* $YBa_2Cu_3O_{7-\delta}$ peak of the reciprocal space map measured on the film deposited at 10 Hz ($q_x = 2.60$ nm^{-1} and $q_z = 6.83$ nm^{-1}) are calculated the lattice parameters $ab = 0.385$ nm and $c = 1.171$ nm. In conclusion the $YBa_2Cu_3O_{7-\delta}$ in the film deposited at 1 Hz appears to better match the $SrTiO_3$ substrate while not being affected on the overall c-axis spacing by the Ba_2YNbO_6 presence at all. On the other hand the $YBa_2Cu_3O_{7-\delta}$ in the film deposited at 10 Hz maintains the ab bulk value (complete relaxation) but the c lattice parameter is slightly larger. This is an indication that the lattice distortion generated by the Ba_2YNbO_6 doping is influencing a region of the $YBa_2Cu_3O_{7-\delta}$ lattice that is large enough to be noticed when measuring the overall c lattice parameter value.

The information obtained from the analysis of the *(108)-(018)* $YBa_2Cu_3O_{7-\delta}$ peak measured in the reciprocal space is summarised in table 5.3.

Sample	Peak coordinates q_x / q_z 2θ / ω	Lattice parameters ab c
Undoped $YBa_2Cu_3O_{7-\delta}$	2.60 nm^{-1} / 6.85 nm^{-1} 68.69 ° / 13.58 °	0.385 nm 1.168 nm
Doped $YBa_2Cu_3O_{7-\delta}$ (1 HZ)	2.58 nm^{-1} / 6.85 nm^{-1} 68.60 ° / 13.66 °	0.388 nm 1.168 nm
Doped $YBa_2Cu_3O_{7-\delta}$ (10 Hz)	2.60 nm^{-1} / 6.83 nm^{-1} 68.59 ° / 13.42 °	0.385 nm 1.171 nm

Table 5.3: *(108)-(018) $YBa_2Cu_3O_{7-\delta}$ peak analysis.*

5.1.3 Nanostructure analysis: Atomic Force Microscopy and Transmission Electron Microscopy

The analysis of the nanostructure reveals interesting differences between the Ba_2YNbO_6 doped $YBa_2Cu_3O_{7-\delta}$ thin film deposited at 10 Hz and those deposited at 1 Hz. Similarly to what was done in the previous section the surface topography is discussed by analysing atomic force microscopy images while the morphological distribution of the secondary pinning phase and the distortion in the $YBa_2Cu_3O_{7-\delta}$ lattice are studied with cross-section transmission electron micrography.

5.1.3.1 Surface topography (Atomic Force Microscopy)

A comparison between the surface topography of samples deposited at different rates is reported in figure 5.4, in particular the surfaces of samples of different thickness ($\approx$ 700 nm and 400 nm) deposited at 1 and 10 Hz are investigated.

The first evident effect of increasing the laser repetition rate is a the presence of smaller growth grains. Comparing the surfaces of sample with similar thickness (figure 5.4a and 5.4b or 5.4c and 5.4d) it is clearly shown that the crystalline grains are smaller in the samples grown at 10 Hz repetition rate. As expected, a reduced *"free migration"* time can then be associated with a reduced accretion of the grains. The first result is that the thin film deposited with a repetition rate of 10 Hz is formed of a higher number of smaller grains when compared to a thin film deposited with a repetition rate of 1 Hz. The direct consequence of

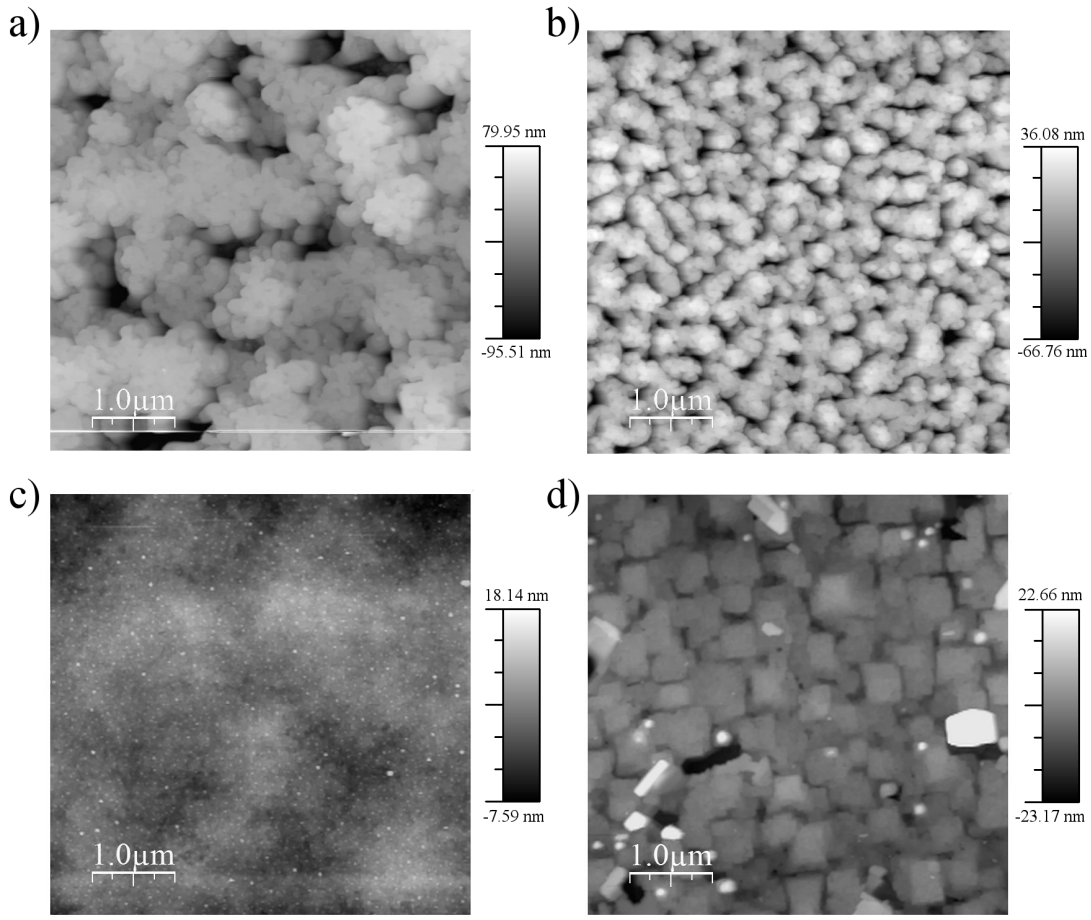

Figure 5.4: Atomic Force Microscopy surface image (5 μm $\times$ 5 μm) of 5%$_{mol}$ Ba_2YNbO_6 doped $YBa_2Cu_3O_{7-\delta}$ thin films deposited at a substrate temperature of 780 °C, repetition rate of 1 Hz and 10 Hz with a thickness of 700 nm and 400 nm. a) 1 Hz and 700 nm; b) 10 Hz and 700 nm; c) 1 Hz and 400 nm; d) 10 Hz and 400 nm.

the morphology described is clearly shown by the comparison of the thicker films surfaces, figure 5.4a and 5.4b. It is in fact clear that the connectivity shown by the grains in figure 5.4b is reduced. Furthermore by the same comparison it appears that the surfacial morphology of the thin film deposited at the higher repetition rate is a scaled down version of the one shown by the film deposited at 1 Hz. A similar analysis could be made comparing the surface morphologies of the thinner films (figure 5.4c and 5.4d) but it is difficult to visualise the grains boundaries in the smooth surface of the thinner film deposited at 1 Hz.

With a more accurate analysis of the images another feature can be deduced. In particular, as expected, the grain dimension is not affected by the film thickness. Focusing on the thin films deposited with a repetition rate of 10 Hz (figure 5.4b and 5.4d) the grains dimension appears to be similar. However the shape of the boundaries turn from the well defined straight lines of the thinner film (figure 5.4d) to the more chaotic boundaries of the thicker sample (figure 5.4b). This is a evidence that the grains connectivity is also reduced when the thickness is increased.

A fine dispersion of superficial nanoparticles is shown in figure 5.4c. Similar nanoparticles where also evidenced in the previous section (figure 4.6d) and where attributed to the Ba_2YNbO_6 presence. It is impossible to picture the same small nanoparticles in atomic force micrography taken on samples with a higher roughness (figure 5.4a and 5.4b) because the increased scale flatten the small topographic features. It is unclear why the superficial nanoparticles are absent (or invisible) in the thinner film deposited with a repetition rate of 10 Hz (figure 5.4d). Since its surface is shown in a similar scale to the 1 Hz film the absence of the nanoparticles is an additional indication of a morphological difference induced by the different deposition rate.

The root mean square roughness values calculated from the surface topographies shown in figure 5.4 are reported in table 5.4. The calculated roughness values are higher in the 700 nm thick films then in the 400 nm thick films. However, there is no evidence of a direct influence of the repetition rate on these values.

A last note on this surface topography study has to be made on the target improved quality. As stated earlier a densified target was prepared to avoid the

Repetition Rate, Thickness	Root mean square roughness
1 Hz, 400 nm	2.12 nm
10 Hz, 400 nm	7.12 nm
1 Hz, 700 nm	34.14 nm
10 Hz, 700 nm	21.41 nm

Table 5.4: Root mean square roughness calculated from the surface topography of $5\%_{mol}$ Ba_2YNbO_6 doped $YBa_2Cu_3O_{7-\delta}$ thin films deposited at a substrate temperature of 780 °C, repetition rate of 1 Hz and 10 Hz with a thickness of 700 nm and 400 nm.

presence of particulates on the film surface. Comparing the surface topographies shows in this section with the earlier study reported (section 4.2.3.1) it is evident that the changes in the production process of the pulsed laser deposition targets solved the particulate issue.

5.1.3.2 Cross-section transmission electron microscopy

The cross-section images taken using the transmission electron microscopy clearly show the strong influence of the laser pulse repetition rate on the nanostructure of the Ba_2YNbO_6 doped $YBa_2Cu_3O_{7-\delta}$ thin films.

In figure 5.5 are reported the transmission electron micrographs taken on the films grown at 1 Hz and 10 Hz at different magnification. Columnar defects are shown with a good contrast only in the film deposited at 1 Hz (figure 5.5a and 5.5b) and are indicated by arrows parallel to the c-axis of the $YBa_2Cu_3O_{7-\delta}$. In the film deposited at 10 Hz some shadows parallel to the c-axis of the $YBa_2Cu_3O_{7-\delta}$ are present and could be related to the presence of Ba_2YNbO_6 nanorods. Nevertheless the contrast in figure 5.5c and 5.5d is lower and these columnar defects are not clearly identified. The reduced contrast can be related to a lower orientation degree as well as to larger distortion. Once more the Ba_2YNbO_6 inclusions nanostructure is shown to be the phase influenced more by the deposition rate.

Focusing on the images related to the Ba_2YNbO_6 doped $YBa_2Cu_3O_{7-\delta}$ thin film deposited at laser pulse rate of 1 Hz, it is possible to analyse the morphology of the nanorods parallel to the c-axis of the $YBa_2Cu_3O_{7-\delta}$. The nanorods diameter is $\approx$ 10 nm and their spacing is $\approx$ 40 nm. Similarly to the case reported in

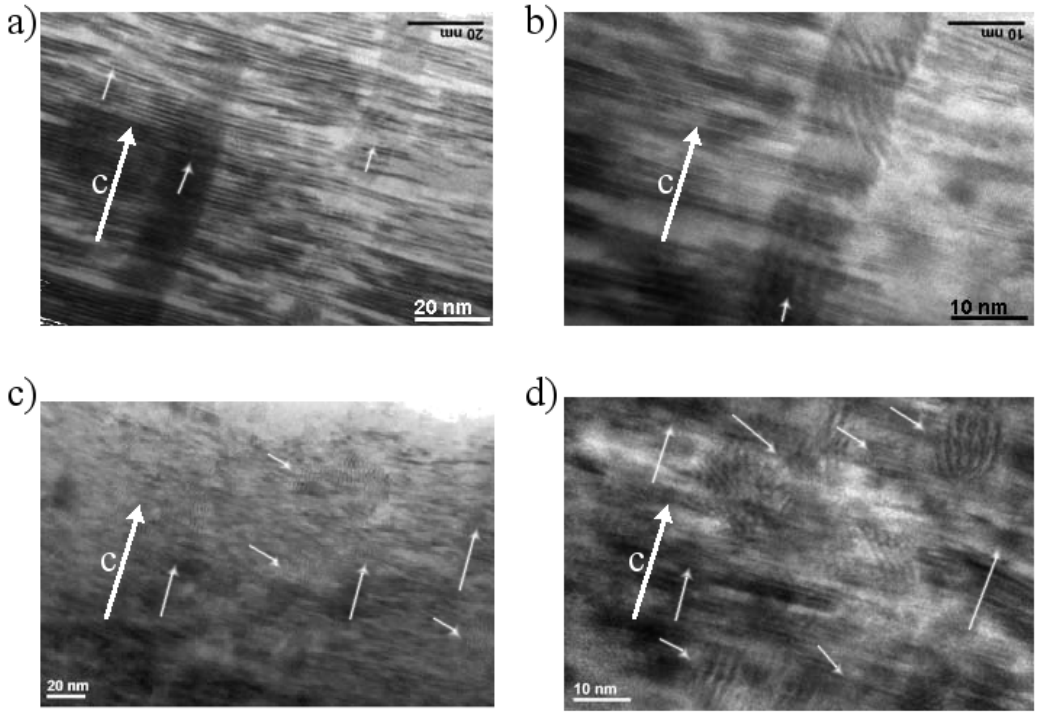

Figure 5.5: Transmission electron microscope cross-sectional image of a 5%*mol* Ba_2YNbO_6 doped $YBa_2Cu_3O_{7-\delta}$ thin film deposited with a laser pulse rates of 1 Hz (a, b) and 10 Hz (c, d). White arrows in the direction of the $YBa_2Cu_3O_{7-\delta}$ *c*-axis mark the position of self assembled Ba_2YNbO_6 nanorods parallel to the *c*-axis. Arrows parallel to the $YBa_2Cu_3O_{7-\delta}$ *ab*-planes mark the position of nanoparticles. *(TEM images from Prof. H Wang research group at Texas A&M University).*

the last section where a Ba_2YNbO_6 doped $YBa_2Cu_3O_{7-\delta}$ deposited with a laser pulse rate of 5 Hz showed same structures with similar spacing. Repeating once more the matching field calculation also the films deposited at 1 Hz should have a matching field value between 1.29 T and 1.49 T. Comparing figure 5.5a with figure 4.8a two differences are evident: the nanorods in the film deposited at a laser pulse rate of 1 Hz appears to be continuous and longer than the $\approx$ 100 nm length of the nanorods showed in the film deposited at 5 Hz; in the film deposited at 1 Hz there is no sign of the nanoparticles that where shown in the 5 Hz case.

The film deposited at a laser pulses rate of 10 Hz (figure 5.5c and 5.5d) is the one that differs the most. The nanorods are not clearly visible but a large number of nanoparticles is present. In general from the transmission electron microscopy analysis this film appears to have the less ordered $YBa_2Cu_3O_{7-\delta}$ lattice and an almost completely disordered Ba_2YNbO_6 nanostructure.

It is interesting to see that the nanoparticles and nanorods presence is largely influenced by the laser pulses rate. The nanoparticles are absent in the 1 Hz films, their presence increase increasing the laser pulse rate up to the 10 Hz film where they appear to be the dominant nanoinclusion. On the other hand the nanorods are long, linear and almost perfectly parallel to the $YBa_2Cu_3O_{7-\delta}$ c-axis in the film deposited at a laser pulse of 1 Hz; are shorter ($\approx$ 100 nm) with a large angle spread to the $YBa_2Cu_3O_{7-\delta}$ c-axis in the film deposited at a laser pulse of 5 Hz (see section 4.2.3.2); are distorted and not clearly imaged in the film deposited at a laser pulse of 10 Hz.

The Ba_2YNbO_6 inclusions generate distortion in the $YBa_2Cu_3O_{7-\delta}$ lattice. The influence of the laser pulse rate on the nanostructure of the Ba_2YNbO_6 inclusions is then transferred to the $YBa_2Cu_3O_{7-\delta}$ lattice distorted by those inclusions. In transmission electron microscope images of the Ba_2YNbO_6 doped $YBa_2Cu_3O_{7-\delta}$ films deposited at pulse rates of 1 Hz and 5 Hz the $YBa_2Cu_3O_{7-\delta}$ crystalline planes parallel to the ab direction appear to be distorted only in the regions close the nanorods and the planes buckling in this small region appear as an effective strain sink. On the other hand a similar buckling of the planes does not appear to be effective in respect of the high density of the nanoparticles growing in the Ba_2YNbO_6 doped $YBa_2Cu_3O_{7-\delta}$ deposited at 10 Hz. The $YBa_2Cu_3O_{7-\delta}$ lattice appears to be distorted with continuity and the entire lattice seems to be

affected by the Ba_2YNbO_6 presence. The high density of nanoparticles appears to be the most likely cause. In particular, the reduced distance between the Ba_2YNbO_6 inclusions do not allow full relaxation of the $YBa_2Cu_3O_{7-\delta}$ lattice.

5.1.4 The superconducting properties: T_c, $J_c(B)$ and $J_c(B,\theta)$

The crystalline structure and the nanostructure of Ba_2YNbO_6 doped $YBa_2Cu_3O_{7-\delta}$ thin films deposited at different rates have been analysed. In particular the nanostructure was found to be heavily influenced by the laser pulse rate. In this section the superconducting transport properties (T_c, $J_c(B)$ and the $J_c(B,\theta)$) are analysed and related to the nanostructural feature evidenced. In addition to the Ba_2YNbO_6 doped $YBa_2Cu_3O_{7-\delta}$ thin films deposited at 1 Hz and 10 Hz also films deposited at 5 Hz where characterized. The crystalline structure and nanostructure morphology of Ba_2YNbO_6 doped $YBa_2Cu_3O_{7-\delta}$ thin films deposited at 5 Hz was analysed in the preliminary study. Nevertheless, since the transport properties characterisation performed in the preliminary study presented was limited to low field values ($J_c(B)$ up to 1 T and $J_c(B,\theta)$ measured at 0.5 T), the transport properties of new films deposited at laser pulses repetition rate of 5 Hz adopting the densified pulsed laser deposition target are characterised in order to obtain a more complete picture of the effects of the deposition rate.

5.1.4.1 Transition temperature, T_c

The transition temperature does not appear to be effected by the laser pulses repetition rate adopted. The T_c measured from all the Ba_2YNbO_6 doped $YBa_2Cu_3O_{7-\delta}$ thin films produced is reduced by a small amount ($\approx$ 3 K) when compared to the T_c measured from a pure $YBa_2Cu_3O_{7-\delta}$ thin film.

In figure 5.6 are reported the resistance measured on a 50 μm width current track patterned on pure $YBa_2Cu_3O_{7-\delta}$ thin film and 5%*mol* Ba_2YNbO_6 doped $YBa_2Cu_3O_{7-\delta}$ thin films deposited at a laser pulses repetition rate of 1, 5 and 10 Hz. The transition temperature T_c, measured as the temperature at which the resistance disappears, is reported in table 5.5.

The T_c reduction is in line with the one measured in the preliminary study (section 4.2.4.1), thus the same considerations can be done and the Ba_2YNbO_6

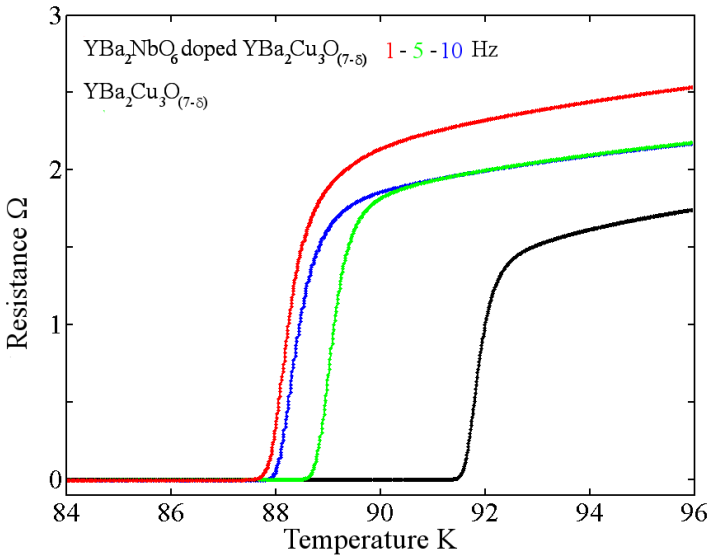

Figure 5.6: Resistance variation with the temperature measured on a pure $YBa_2Cu_3O_{7-\delta}$ thin film deposited at a substrate temperature of 780 °C and laser pulses repetition rates of 1 Hz and on 5%*mol* Ba_2YNbO_6 doped $YBa_2Cu_3O_{7-\delta}$ thin films deposited at a substrate temperature of 780 °C and laser pulses repetition rates of 1, 5 and 10 Hz.

stability within the $YBa_2Cu_3O_{7-\delta}$ matrix is confirmed. Furthermore it is important to notice that despite the higher disorder pictured by the transmission electron microscopy the transition temperature measured on the Ba_2YNbO_6 doped $YBa_2Cu_3O_{7-\delta}$ thin film deposited at 10 Hz is almost equal to the one measured on the thin film deposited at a laser pulses repetition rate of 1 Hz. In conclusion the fact that the higher defects density is not related to a further reduction of the transition temperature could be the evidence that connected regions of the $YBa_2Cu_3O_{7-\delta}$ lattice only marginally distorted by the Ba_2YNbO_6 inclusion may be present also in the thin films deposited at laser pulses repetition rate of 10 Hz.

Thin Film	Transition Temperature T_c
pure $YBa_2Cu_3O_{7-\delta}$ (1 Hz)	91.5 K
Ba_2YNbO_6 doped $YBa_2Cu_3O_{7-\delta}$ (1 Hz)	87.8 K
Ba_2YNbO_6 doped $YBa_2Cu_3O_{7-\delta}$ (5 Hz)	88.8 K
Ba_2YNbO_6 doped $YBa_2Cu_3O_{7-\delta}$ (10 Hz)	88.0 K

Table 5.5: Transition Temperature T_c collected from the resistance variation with temperature measurements shown in figure 5.6.

5.1.4.2 The critical current density

Once again despite the slightly reduced transition temperatures T_c the first evident effect of the Ba_2YNbO_6 doping is improved critical current densities J_c values over the whole field range analysed.

In figure 5.7 are reported $J_c(B)$ measurements up to 6 T with the field applied parallel to the c-axis ($B \| c$) at 77 K for a pure $YBa_2Cu_3O_{7-\delta}$ thin film and 5%mol Ba_2YNbO_6 doped $YBa_2Cu_3O_{7-\delta}$ thin films deposited at a laser pulses repetition rate of 1, 5 and 10 Hz. The $J_c(B)$ values measured on the Ba_2YNbO_6 doped $YBa_2Cu_3O_{7-\delta}$ thin films deposited at laser pulses repetition rate of 1 and 5 Hz are similar. This is an evidence that the pinning potential is similar when the field is applied parallel to the $YBa_2Cu_3O_{7-\delta}$ c-axis.

The J_c values measured on the film deposited at 10 Hz are lower then those measured on the other Ba_2YNbO_6 doped $YBa_2Cu_3O_{7-\delta}$ films in the low field region (B $\leq$ 2 T) but are the highest when the applied field is above 2 T. A possible explanation can be found in the higher density of Ba_2YNbO_6 nanoinclu-

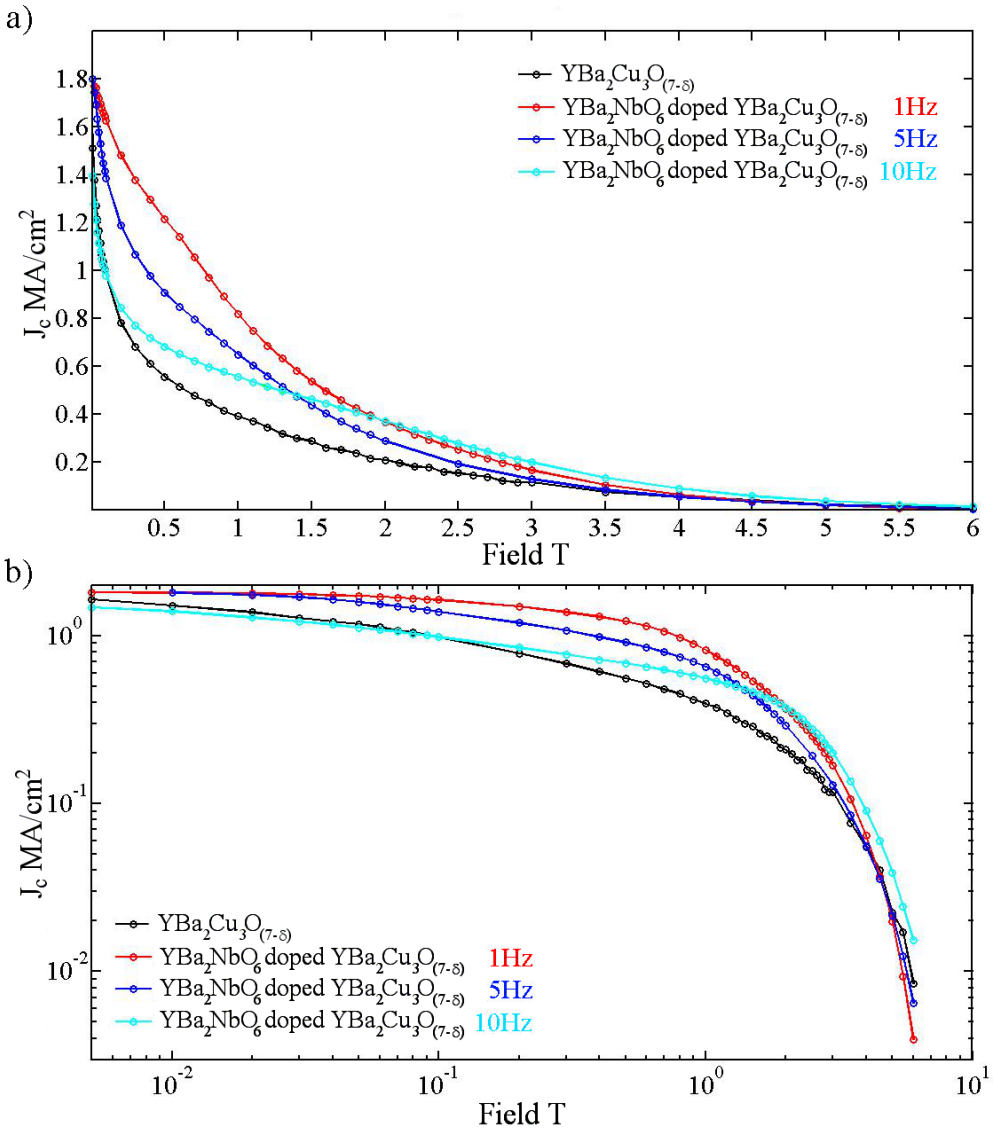

Figure 5.7: Critical current density variation with the applied magnetic field value measured on a pure $YBa_2Cu_3O_{7-\delta}$ thin film deposited at a substrate temperature of 780 °C and laser pulses repetition rates of 1 Hz and on 5%*mol* Ba_2YNbO_6 doped $YBa_2Cu_3O_{7-\delta}$ thin films deposited at a substrate temperature of 780 °C and laser pulses repetition rates of 1, 5 and 10 Hz. The field is applied parallel to the *c*-axis of the $YBa_2Cu_3O_{7-\delta}$, T = 77 K. The data are on a log-linear plot (a) and a log-log plot (b).

sions. The matching field values (1.29 T $\leq H^* \leq$ 1.59 T) calculated from the Ba_2YNbO_6 nanorods were similar in the 1 Hz and 5 Hz films. Unfortunately, due to the high distortions resulting in low transmission electron image contrast it was not possible to calculate a matching field for the 10 Hz film. However, since the lower spacing of the inclusion was evidenced, a higher matching field value was expected.

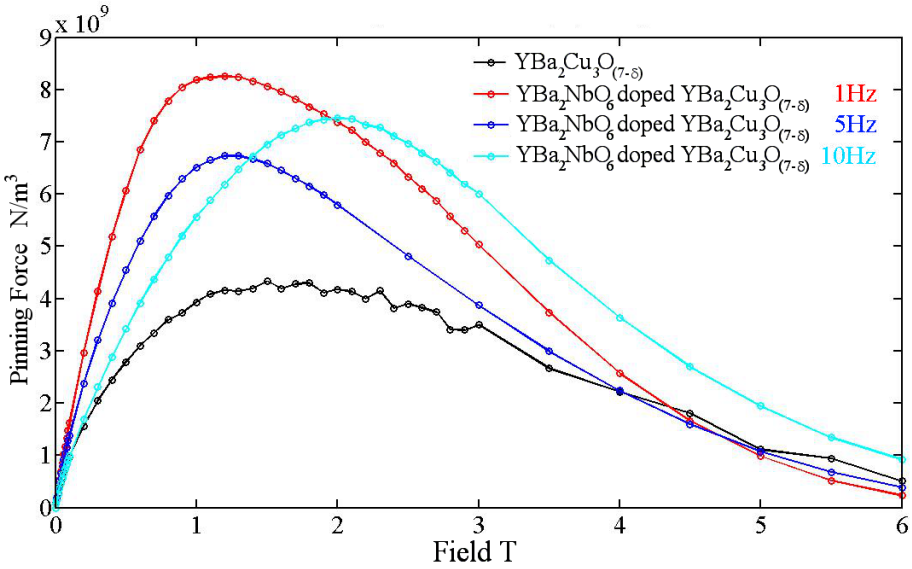

Figure 5.8: Pinning force calculated from data reported in figure 5.7

To better visualize the effect of different matching field values in figure 5.8 is reported the pinning force calculated as $J_c(B) \times B$ from the data reported in figure 5.7. The pinning force maximum for the Ba_2YNbO_6 doped $YBa_2Cu_3O_{7-\delta}$ thin films deposited at 1 and 5 Hz are located at a field valued of $\approx$ 1.4 T. It is worth noticing that this value is perfectly in line with the matching field values predicted from the nanorods spacing measured on the images acquired with the electron transmission microscopy. The fact that the pinning force maximum for the Ba_2YNbO_6 doped $YBa_2Cu_3O_{7-\delta}$ thin film deposited at 10 Hz is shifted towards higher field values confirm the higher matching field value that was expected from the higher Ba_2YNbO_6 inclusion density.

Table 5.6 reporting the α values calculated from data in figure 5.7 complete

Thin Film	α
pure $YBa_2Cu_3O_{7-\delta}$ (1 Hz)	0.47
Ba_2YNbO_6 doped $YBa_2Cu_3O_{7-\delta}$ (1 Hz)	0.32
Ba_2YNbO_6 doped $YBa_2Cu_3O_{7-\delta}$ (5 Hz)	0.37
Ba_2YNbO_6 doped $YBa_2Cu_3O_{7-\delta}$ (10 Hz)	0.39

Table 5.6: α calculated from the data reported in figure 5.7.

the $J_c(B)$ analysis. The α values are reduced when the Ba_2YNbO_6 is added to $YBa_2Cu_3O_{7-\delta}$ and the higher value is the one calculated for the Ba_2YNbO_6 doped $YBa_2Cu_3O_{7-\delta}$ deposited at a laser pulse repetition rate of 10 Hz is $\alpha = 0.39$ which is lower than $\alpha = 0.47$ calculated for the pure $YBa_2Cu_3O_{7-\delta}$ sample. The reason why the highest α value is the one calculated the 10 Hz Ba_2YNbO_6 doped $YBa_2Cu_3O_{7-\delta}$ film is that the pinning landscape generated in this film is effective at high field more then it is at low field and that α is calculated in the very low field regime (B $\leq$ 1 T). At low field values the pinning potential is not fully developed since the high density of nanoinclusions may reduce the energy associated with flux jumps between adjoining defects reducing the pinning potential.

To complete the analysis of the effects that different laser pulses repetition rates have on the nanostructure and properties of Ba_2YNbO_6 doped $YBa_2Cu_3O_{7-\delta}$ thin films the critical current density variation as a function of the external magnetic field direction is measured. In figure 5.9 are reported $J_c(B, \theta)$ measurements at 77 K and 0.5, 1 T for a pure $YBa_2Cu_3O_{7-\delta}$ thin film and 5%*mol* Ba_2YNbO_6 doped $YBa_2Cu_3O_{7-\delta}$ thin films deposited at a laser pulses repetition rate of 1, 5 and 10 Hz.

The first important result is that even if all the Ba_2YNbO_6 doped $YBa_2Cu_3O_{7-\delta}$ thin films shows an higher J_c value when the field is applied parallel to the $YBa_2Cu_3O_{7-\delta}$ *c*-axis the only thin film that shows higher J_c values than pure $YBa_2Cu_3O_{7-\delta}$ when the field is applied parallel to the *ab*-planes is the thin film deposited at a laser pulses repetition rate of 1 Hz. It is evident that the pinning potential along the *ab*-planes of the Ba_2YNbO_6 doped $YBa_2Cu_3O_{7-\delta}$ thin film deposited at 5 and 10 Hz is reduced. The cause of this reduction can not be indicated in the nanorods inclusion because these are the dominant inclusion type in the Ba_2YNbO_6 doped $YBa_2Cu_3O_{7-\delta}$ deposited at 1 Hz and its *ab*-direction pinning

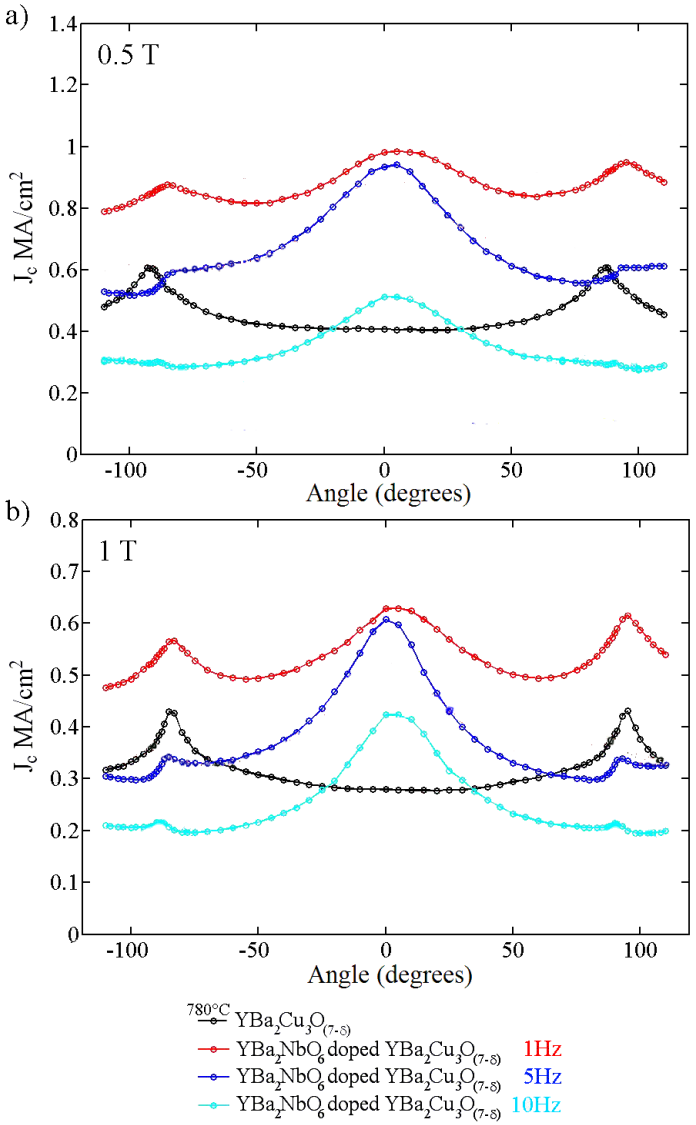

Figure 5.9: Critical current density variation with the direction of the applied magnetic field measured on a pure $YBa_2Cu_3O_{7-\delta}$ thin film deposited at a substrate temperature of 780 °C and laser pulses repetition rates of 1 Hz and on 5%*mol* Ba_2YNbO_6 doped $YBa_2Cu_3O_{7-\delta}$ thin films deposited at a substrate temperature of 780 °C and laser pulses repetition rates of 1, 5 and 10 Hz. a) Applied magnetic flux density = 0.5 T, T = 77 K; b) Applied magnetic flux density = 1 T, T = 77 K.

potential is similar if not better then the one shown by the pure $YBa_2Cu_3O_{7-\delta}$ film. The *ab*-direction reduction of the J_c could be associated with the lower connectivity evidenced in the Ba_2YNbO_6 doped $YBa_2Cu_3O_{7-\delta}$ thin films deposited at 5 Hz and 10 Hz. It is certain that the loss of pinning capability when the field is applied parallel to the $YBa_2Cu_3O_{7-\delta}$ *ab*-planar direction is related to the interruption of the crystalline *ab*-planes continuity. There are two main sources of planar continuity interruption: the nanorods and the grain boundaries. The nanorods generate a local hole through the planes and a possible loss of continuity in the small region around them that is affected by planar buckling. The grain boundaries are a two dimensional interruption of the planar continuity that is extended over lengths that are order of magnitude larger that the nanorods interruption. This together with the evidence that one of the main effects of higher repetition rates is the reduction of the growth grains dimension (figure 5.4) suggest that the deficient pinning potential measured when the field is applied parallel to the *ab*-planar direction is caused by the interruption of the *ab* crystalline planes occurring at the grain boundaries.

It is worth remembering that the scenario presented for the Ba_2YNbO_6 doped $YBa_2Cu_3O_{7-\delta}$ deposited at laser pulses repetition rates of 5 and 10 Hz is common in pinning enhanced $YBa_2Cu_3O_{7-\delta}$ thin films in which the secondary phases forms heteroepitaxial nanorods [57, 65, 74, 118] while the presence of a strong *c*-axis pinning without a reduction of the *ab*-planes pinning was achieved only in carefully tuned $BaZrO_3$ doped $YBa_2Cu_3O_{7-\delta}$ [6, 134]. In general while it is common to increase the isotropic pinning without disrupting the *ab*-planar continuity, it is complex to introduce a strong anisotropic pinning along the *c*-axis direction without depressing the planar J_c.

The Ba_2YNbO_6 doped $YBa_2Cu_3O_{7-\delta}$ thin film deposited at a laser pulses repetition rate of 10 Hz shows a strong *c*-axis pinning potential revealing the presence of *c*-axis directional defects that were not clearly shown by the transmission electron microscopy. Furthermore the isotropic pinning introduced by the densely packed nanoparticles is not effective at low field ($B \leq 1$ T) and at these field values the connectivity issues and low energies flux jumps nullify the pinning effects. Similarly the pinning enhancement that should be provided by the simultaneous presence of nanorods and nanoparticles in the Ba_2YNbO_6

doped $YBa_2Cu_3O_{7-\delta}$ deposited at 5 Hz are also probably denied by the reduced connectivity.

5.1.5 Concluding remarks to the analysis of the effects of the deposition rate on the nanostructure and the superconducting properties

The analysis performed in this section demonstrated that the laser pulses repetition rate heavily influence the $YBa_2Cu_3O_{7-\delta}$ grains morphology and consequently the overall connectivity and continuity of the *ab* crystalline planes. Higher repetition rates generates smaller growth grains with reduced connectivity and planar continuity. Such reduced connectivity and continuity is found to generate a reduction of the critical current values J_c when the field is applied parallel to the $YBa_2Cu_3O_{7-\delta}$ *ab*-planes.

The laser pulses repetition rate influences also the nanostructure of the Ba_2YNbO_6. Long linear nanorods are obtained at low deposition rates (1 Hz), at 5 Hz are obtained shorter nanorods and simultaneously nanoparticles and at 10 Hz the nanoparticles are the dominant Ba_2YNbO_6 nanostructure. It would be possible to tune the Ba_2YNbO_6 nanorods-nanoparticles ratio to achieve an optimal pinning landscape by tuning the repetition rate as done with the $BaZrO_3$ [134] but the connectivity issues evidenced have a larger detrimental effect on the pinning properties than the enhancing effect expected from the sinergetic combination of 0D nanoparticles and 1D *c*-axis oriented nanorods.

The best results in mid-low field (0 T to 2 T) values where obtained by Ba_2YNbO_6 doped $YBa_2Cu_3O_{7-\delta}$ thin films deposited at 1 Hz. On the other hand the high density pinning landscape generated in the Ba_2YNbO_6 doped $YBa_2Cu_3O_{7-\delta}$ thin film deposited at 10 Hz provides enough pinning force to overcome the related connectivity issue when the field applied is above 2 T; a possible application niche for the 10 Hz thin films could then be found in specialized equipment for high magnetic field.

5.2 Ba_2YNbO_6 perovskite additions to $YBa_2Cu_3O_{7-\delta}$: deposition parameter optimization

There are several parameters that define the process in a pulsed laser deposition. The substrate - target distance, the laser fluence, the oxygen pressure, the substrate temperature and the laser pulse repetition rate all influence the quality of the deposited thin film. The substrate - target distance, the laser fluence and the oxygen pressure are related more to the target ablation and plume diffusion process than to the film growth, furthermore they have been optimized over the years. The last two are the parameters that directly influence the film growth process. A complete study on the effects of the laser puses repetition rate is discussed in the previous section, while in this brief final section of the chapter the study of the properties of the Ba_2YNbO_6 doped $YBa_2Cu_3O_{7-\delta}$ thin film is concluded with the optimisation of the substrate temperature in the pulsed laser deposition. This final section will not include an in depth study of the nanostructure similar to the one reported in the previous sections of the chapter but will focus on the grain connectivity and the superconducting properties of a large number of films.

5.2.1 Ba_2YNbO_6 doped $YBa_2Cu_3O_{7-\delta}$ pulsed laser deposition target preparation and thin films deposition

The target used in the pulsed laser deposition is the one that was ablated to deposit the thin films analysed in the previous section.

The substrate temperature was modified to study its effects on the growth and the superconducting properties of Ba_2YNbO_6 doped $YBa_2Cu_3O_{7-\delta}$ thin films deposited at different laser pulses repetition rate. It is difficult to predict the effects of the substrate temperatures on the film growth as it simultaneously affects multiple mechanism of the process. As an example an higher substrate temperature is certainly related to higher mobility of the ions moving on the growing film surface and at the same time high substrate temperatures in a low oxygen pressure environment may speed up an oxygen content reduction process. Thus in order to identify a processability window, if not the optimum, a set

of Ba_2YNbO_6 doped $YBa_2Cu_3O_{7-\delta}$ thin films deposited at different substrate temperatures and different laser pulse repetition rate were grown. In particular repetition rate of 1, 5 and 10 Hz and substrate temperatures of 740 and 760 °C were investigated and compared to the results obtained on thin films deposited at a substrate temperature of 780 °C. In the table 5.7 below are summarized the pulsed laser deposition parameters adopted for the deposition of the Ba_2YNbO_6 doped $YBa_2Cu_3O_{7-\delta}$ thin films analysed in this section.

Parameter	Value
Substrate Temperature	740,760,780 °C
Chamber Pressure	0.3 mbar flowing O_2
Laser Fluence	2 Jcm^{-2}
Repetition Rate	1, 5, 10 Hz
Number of Pulses	4500
Annealing Time	1 hr
Annealing Temperature	520 °C
Annealing Pressure	500 mbar O_2

Table 5.7: Pulsed laser deposition parameters

All the Ba_2YNbO_6 doped $YBa_2Cu_3O_{7-\delta}$ thin films deposited were measured to be of $\approx$ 0.4 μm thickness.

5.2.2 Surface Topology: Grain Connectivity

The analysis discussed in the previous section showed that the grain connectivity has a major influence on the superconducting properties, in particular when the magnetic field is applied parallel to the $YBa_2Cu_3O_{7-\delta}$ *ab*-planar direction the critical current values appear to be reduced in the Ba_2YNbO_6 doped $YBa_2Cu_3O_{7-\delta}$ thin films featuring small growth grains. For this reason a study of surface topography can not be neglected even in this brief analysis of the superconducting properties.

In order to provide clear visual impact the images of the surface topography were separated into three. In figure 5.10 are reported the surface topographies for all the thin films produced with a substrate temperature of 740 °C, in figure 5.11 those deposited at 760 °C and in figure 5.12 those at 780 °C. In all the figures from top to down the laser pulses rate varies from 1 Hz to 10 Hz.

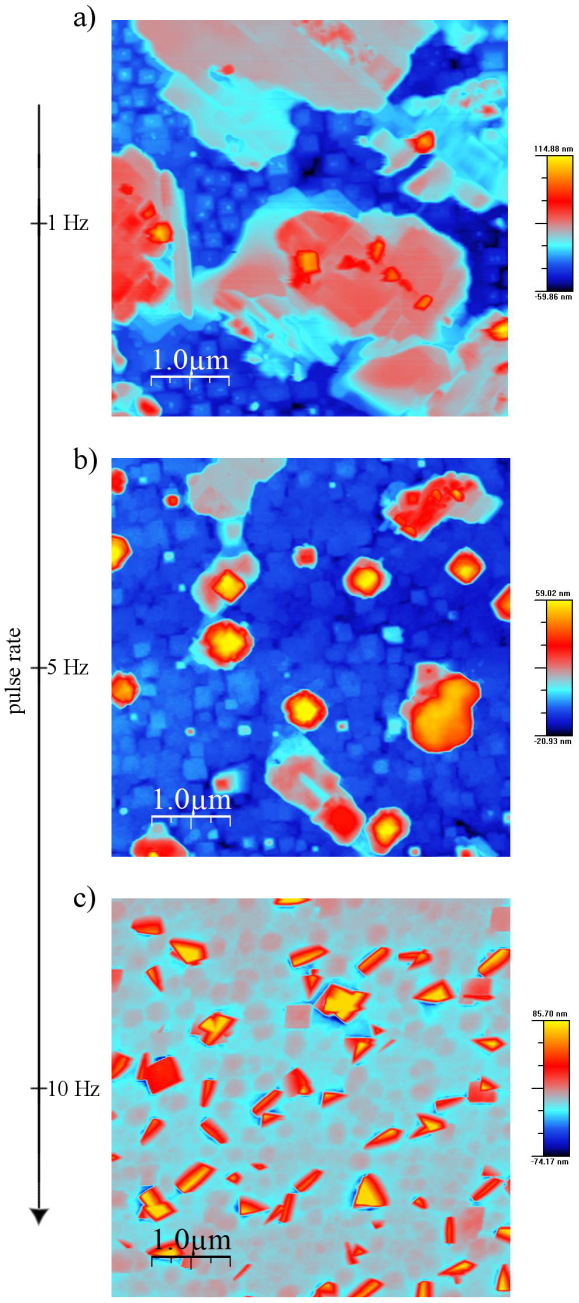

Figure 5.10: Atomic Force Microscopy surface image (5 μm $\times$ 5 μm) of 5%*mol* Ba_2YNbO_6 doped $YBa_2Cu_3O_{7-\delta}$ thin films deposited at a substrate temperature of 740 °C; a) repetition rate of 1 Hz; b) repetition rate of 5 Hz; c) repetition rate of 10 Hz;

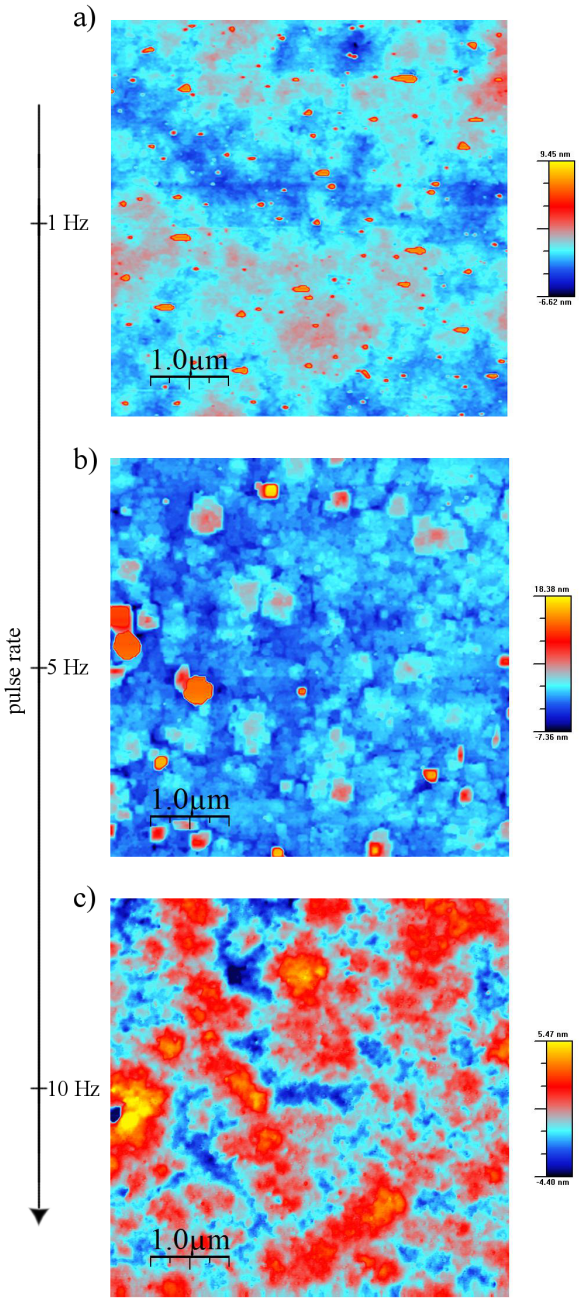

Figure 5.11: Atomic Force Microscopy surface image (5 μm $\times$ 5 μm) of 5%*mol* Ba_2YNbO_6 doped $YBa_2Cu_3O_{7-\delta}$ thin films deposited at a substrate temperature of 760 °C; a) repetition rate of 1 Hz; b) repetition rate of 5 Hz; c) repetition rate of 10 Hz;

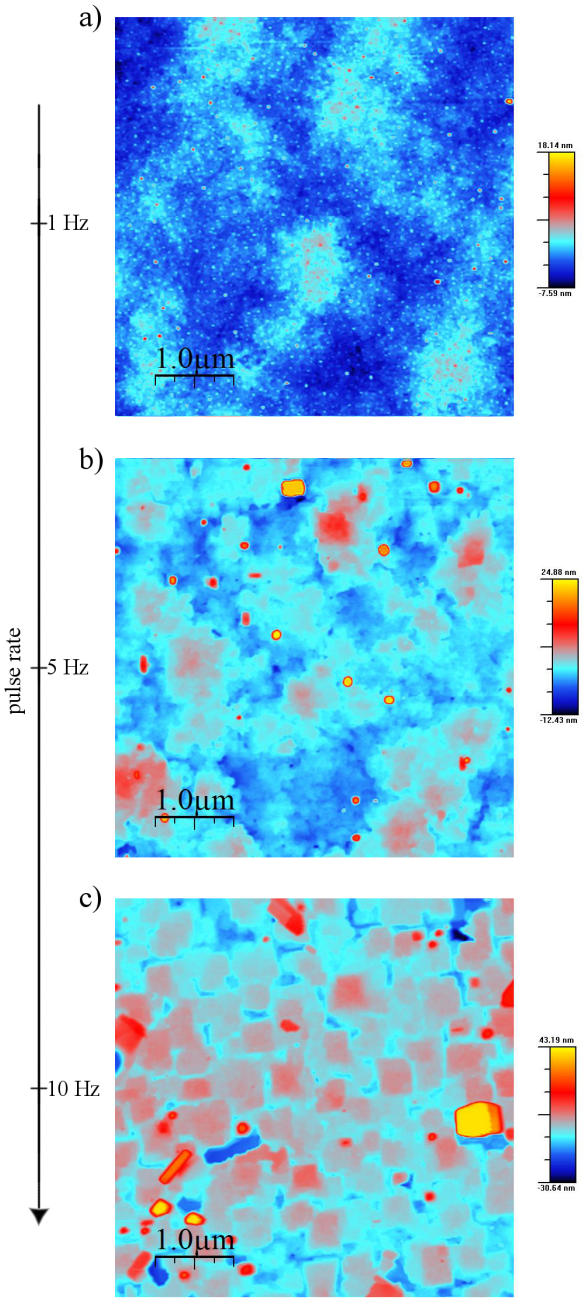

Figure 5.12: Atomic Force Microscopy surface image (5 μm $\times$ 5 μm) of 5%*mol* Ba_2YNbO_6 doped $YBa_2Cu_3O_{7-\delta}$ thin films deposited at a substrate temperature of 780 °C; a) repetition rate of 1 Hz; b) repetition rate of 5 Hz; c) repetition rate of 10 Hz;

The first clear feature evidenced by these atomic force microscopy study is the presence of outgrowths on the surfaces of the thin films deposited at a substrate temperature of 740 °C (figure 5.10). These outgrowths where recently reported in the case of pure $YBa_2Cu_3O_{7-\delta}$ on RABiTS for substrate temperatures from 740 °C and below [135]. Nevertheless several authors have investigated and characterized the outgrowths on the surface of pulsed laser ablated $YBa_2Cu_3O_{7-\delta}$ on different substrates [136, 137].

The outgrowths are reported to be *a*-axis $YBa_2Cu_3O_{7-\delta}$ grains, misaligned *c*-axis grains and non superconducting grains made by Y_2BaCuO_5, $CuYO_2$, CuO, $BaCuO_2$ and Ba_2CuO_3. It is possible to distinguish between the outgrowths formed by superconducting $YBa_2Cu_3O_{7-\delta}$ grains and those formed by non superconducting phases with the atomic force microscopy. The outgrowths formed by $YBa_2Cu_3O_{7-\delta}$ (*a*-axis $YBa_2Cu_3O_{7-\delta}$ and misaligned *c*-axis $YBa_2Cu_3O_{7-\delta}$) are reported as block-shaped while those formed by non superconducting phases are semi-spherical. From the images reported in figure 5.10 it is evident the outgrowths are block-shaped thus are $YBa_2Cu_3O_{7-\delta}$ grains. The superconducting outgrowths are described as predominantly *c*-axis $YBa_2Cu_3O_{7-\delta}$ grains parallel to the substrate surface that nucleate on the substrate at the same time of the desired *c*-axis $YBa_2Cu_3O_{7-\delta}$ perpendicular to the substrate surface when the substrate temperature is below a certain threshold.

In the present case this lower temperature limit is found to be 740 °C. Furthermore a significant increase in the size of the outgrowths is also reported to occurs during long deposition. This size increment is related to precipitates formation at the edge of the outgrowths as well as to the merging of neighboring *c*-axis parallel grains. A similar behaviour is found in figure 5.10 where the size of the outgrowths on the surface of the thin film deposited at a laser pulses repetition rate of 1 Hz is much larger than that observed for the thin films deposited at 5 and 10 Hz. Although the quality of these films is reduced by the presence of these outgrowths, it is significant to make a final comment on the dimension and shape of the *c*-axis perpendicular grains that are visible below the outgrowths. These grains are almost perfectly rectangular, their size is $\approx$ 300 nm and do not seem to change with the variation of laser pulses repetition rate. From the images in figure 5.11 and 5.12 it is evident that the outgrowths are absent.

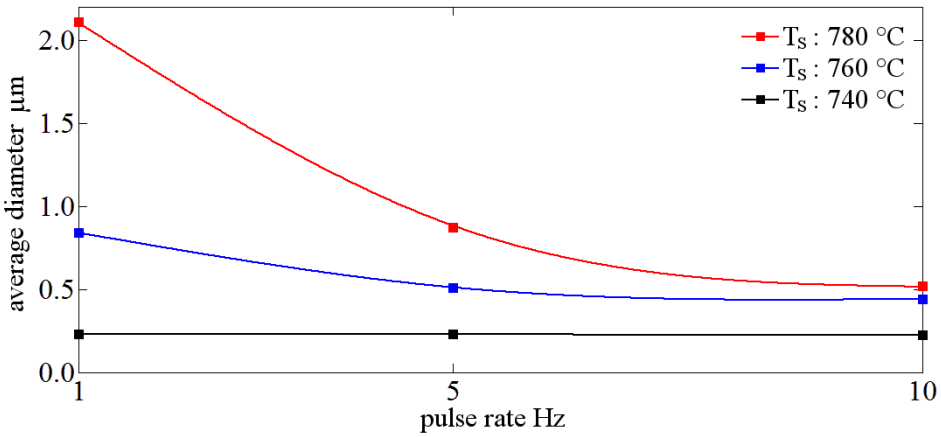

Figure 5.13: Average grain size measured from AFM analysis of 5%*mol* Ba_2YNbO_6 doped $YBa_2Cu_3O_{7-\delta}$ thin film deposited at a substrate temperature of 740, 760 and 780 °C as a function of laser pulse rate

Figure 5.13 compares the average grain size measured from the AFM in figure 5.10, 5.11 and 5.12, which shows a well defined trend. The size of the grains and thus the connectivity increases when the substrate temperature is increased and when the laser pulses repetition rate is decreased. It is important remembering that a reduction of the pulses laser repetition rate corresponds to an increase in the maximum time allowed to the ions migration on the surface. Referring to a standard model of nucleation and growth, the grain size analysis shows that an increase in ions mobility as well as the time allowed to their migration shifts the balance between nucleation and growth towards the latter. In the previous section it was shown that thin films composed of larger grains have better superconducting properties than films composed by smaller grains. Therefore, if this trend were to be confirmed, the films with the best superconducting properties should be those deposited with a substrate temperature of 780 °C.

A last consideration can be made comparing the surface topographies of the thin film deposited at 1 Hz and 760 °C (figure 5.11a) with the one deposited at 5 Hz and 780 °C (figure 5.12b). It is evident that the two images are similar thus indicating the possibility to achieve similar results with lower mobility (lower substrate temperature) and longer migration times (lower laser pulse repetition

rate) or higher mobility and smaller migration times.

5.2.3 The superconducting properties: T_c, $J_c(B)$ and $J_c(B,\theta)$

To conclude the last section of the chapter are shown the results obtained from the analysis of the superconducting properties. The variation of transition temperature T_c and critical current density as a function of the applied magnetic field intensity $J_c(B)$ and as a function of the applied magnetic field direction $J_c(B,\theta)$ are reported.

5.2.3.1 Transition temperature, T_c

In figure 5.14 is visualized the T_c variation with the substrate temperature. Each curve is referred to a laser pulse repetition rate. The T_c values are also summarized in tabular form in table 5.8.

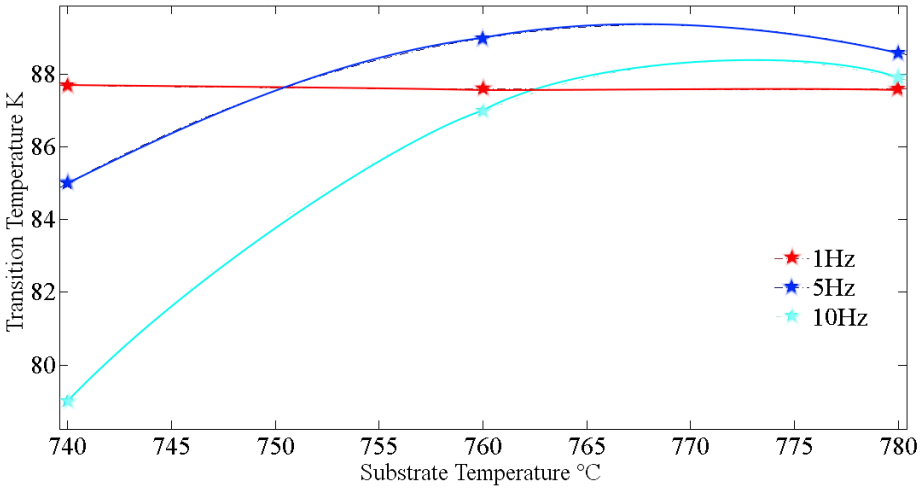

Figure 5.14: Visualisation of the transition temperature values measured for 5%*mol* Ba_2YNbO_6 doped $YBa_2Cu_3O_{7-\delta}$ thin films deposited at a substrate temperature of 740, 760 and 780 °C and laser pulses repetition rates of 1, 5 and 10 Hz

The transition temperature values measured for the thin films deposited at a

substrate temperature of 760 °C has the same behaviuor discussed in the previous section for the thin films deposited on the substrate kept at 780 °C. The T_c reduction is $\approx$ 3 K as $T_c \approx$ 88 K are measured for all the samples.

A different T_c trend is observed in thin films deposited on substrates kept at 740 °C. In these thin films the T_c values appears to be influenced by the laser pulses repetition rate and the T_c measured for the thin films deposited at 10 Hz shows a severe reduction down to $\approx$ 79 K. The main difference in these films is the presence of the outgrowths discussed earlier in the section. It is possible that the $YBa_2Cu_3O_{7-\delta}$ c-axis grains aligned parallel to the substrate surface introduce high levels of strain and distortion reducing the T_c. The fact that the size of these outgrowths changes with the variation of the laser pulses repetition rate could be the reason why only in when these outgrowth are present the T_c values also changes with the variation of the repetition rate.

A possible explanation to the T_c variation with the laser pulses repetition rate can be found considering that the strain and distortion are responsible for the reduced T_c values. These are generated at the interfaces between two phases (or c-axis parallel $YBa_2Cu_3O_{7-\delta}$ grains and c-axis perpendicular $YBa_2Cu_3O_{7-\delta}$ grains) thus larger interfaces induce larger T_c reduction. Taking into account that the an increase of the laser pulses repetition rate decrease the sizes of the outgrowths but at same time increase their density and thus increase the interfacial area (figure 5.10), the relation between T_c values and the laser pulses repetition rates is evident.

	1 Hz	5 Hz	10 Hz
740 °C	87.8 K	85K	79 K
760 °C	87.9 K	89 K	88.2 K
780 °C	87.8 K	88.8 K	88.8 K

Table 5.8: Transition temperature values for 5%*mol* Ba_2YNbO_6 doped $YBa_2Cu_3O_{7-\delta}$ thin films deposited at a substrate temperature of 740, 760 and 780 °C and laser pulses repetition rates of 1, 5 and 10 Hz.

5.2.3.2 The critical current density

The critical current values measured on thin films deposited on substrate kept at temperature values smaller then 780 °C are all reduced (figure 5.15). A reduction of the substrate temperatures appears to reduce the critical current values regardless of the repetition rate. As a matter of the fact that the detrimental effects generated by connectivity issues has been evidenced and discussed in the previous section and that the atomic force microscopy analysis revealed that larger grains (better connectivity) where generated at high substrate temperatures a similar behaviour of the critical current values was expected.

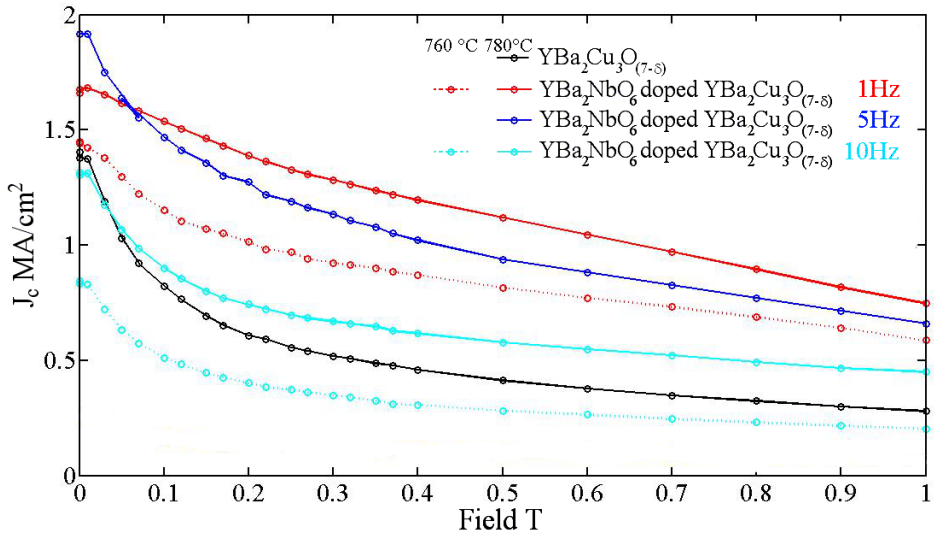

Figure 5.15: Critical current density variation with the applied magnetic field value measured on 5%*mol* Ba_2YNbO_6 doped $YBa_2Cu_3O_{7-\delta}$ thin films deposited at a substrate temperature of 760 and 780 °C and laser pulses repetition rates of 1, 5 and 10 Hz. The field is applied parallel to the *c*-axis of the $YBa_2Cu_3O_{7-\delta}$, T = 77 K.

A self explanatory summary plot is reported in figure 5.16, the critical current density values measured at 0.5 T and 1 T are plotted as a function of the pulse rate and for the samples deposited at a substrate temperature of 760 °C and 780 °C.

In figure 5.17 the critical current density variation with direction of the applied

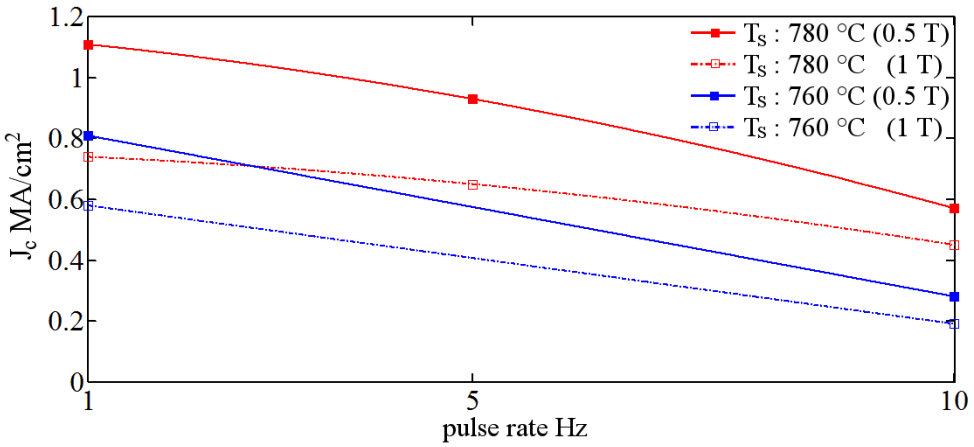

Figure 5.16: Critical current density measured at 0.5 T and 1 T on 5%*mol* Ba_2YNbO_6 doped $YBa_2Cu_3O_{7-\delta}$ thin films deposited at a substrate temperature of 760 and 780 °C as a function of laser pulse rate. The field is applied parallel to the *c*-axis of the $YBa_2Cu_3O_{7-\delta}$, T = 77 K.

magnetic field is reported. These data do not add new knowledge on the system analysed and the consideration done in the last section could be repeated. Once again the relevant results is that the best performances are obtained by the thin films deposited on substrate kept at 780 °C.

An interesting observation is obtained by the comparison of the $J_c(B)$ and the $J_c(B,\theta)$ of the thin film deposited at 760 °C and 1 Hz with those of the thin film deposited at 780 °C and 5 Hz. The J_c values obtained in these films are similar and also the topographies were similar. This is an important evidence that, as stated before, it is possible to reduce the deposition time (increase the laser pulses repetition rate) without affecting the superconducting properties increasing the ions mobility (increase the substrate temperature). Unfortunately, even if the above is true, the substrate temperature (mobility) has an upper limit. When temperatures above 780 °C are used new phenomena are introduced and the superconductive properties are worsened probably by reductions in oxygen content. In particular Ba_2YNbO_6 doped $YBa_2Cu_3O_{7-\delta}$ thin films deposited on substrate kept at temperatures of 800 and 820 °C shows T_c values below 80 K.

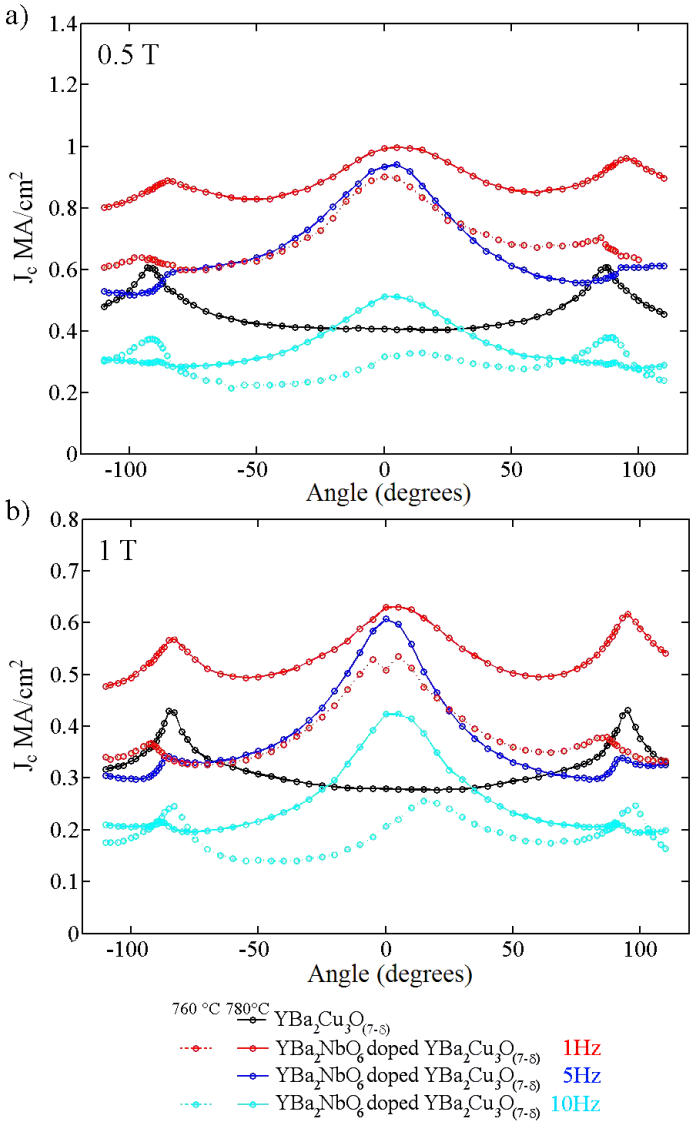

Figure 5.17: Critical current density variation with the direction of the applied magnetic field measured on 5%*mol* Ba_2YNbO_6 doped $YBa_2Cu_3O_{7-\delta}$ thin films deposited at a substrate temperature of 760 and 780 °C and laser pulses repetition rates of 1, 5 and 10 Hz. a) Applied magnetic flux density = 0.5 T, T = 77 K; b) Applied magnetic flux density = 1 T, T = 77 K.

5.2.4 Concluding remarks to the deposition parameters optimization

In this last section the relevance of grain size on the Ba_2YNbO_6 doped $YBa_2Cu_3O_{7-\delta}$ thin films is once again evidenced. The connection between the temperature at which the substrate is kept during the deposition with the films grains morphology is analysed.

Within the parameter range analysed the optimal superconducting properties for the Ba_2YNbO_6 doped $YBa_2Cu_3O_{7-\delta}$ system are found in the thin films that are deposited on substrates kept at 780 °C with a laser pulse repetition rate of 1 Hz.

A temperature of $\approx$ 780 °C seems to be an optimal value since further increments require additional processing to equilibrate the oxygen content. If post annealing processes are not considered a substrate temperature $\approx$ 780 °C is an upper limit on the processability parameter variation range. On the other hand, the laser pulses repetition rate of 1 Hz is the lowest rate analysed and the trend observed indicated that reducing the repetition rate would lead to larger growth grains and more ordered nanorods arrays. However, it is important to notice that even if there is not lower limit of processability for the laser pulse repetition rate, there is a lower efficacy limit. In other words adopting increasingly smaller repetition rate at a certain point will cease to be beneficial and from industry point of view will start to be disadvantageous. In fact, once the process ceases to be kinetically limited and reaches the thermodynamic equilibrium any further reductions in the repetition rate would have no influence.

Chapter 6

Ba_2YNbO_6 and Gd_3TaO_7 simultaneous doping of $YBa_2Cu_3O_{7-\delta}$

In the previous chapter an in-depth analysis of the effects of Nb addition to $YBa_2Cu_3O_{7-\delta}$ is presented. It is proved that niobium additions to $YBa_2Cu_3O_{7-\delta}$ produce Ba_2YNbO_6 nanorods and that in general additions to $REBa_2Cu_3O_{7-\delta}$ produce Ba_2RENbO_6 nanorods [5,118,138] which are similar to $BaZrO_3$ nanorods, $\approx$ 10 nm in diameter and $\approx$ 100 nm in length but with a larger splay than $BaZrO_3$ around the c-axis.

Another element, the tantallum, also showed similar properties to the niobium. Both niobium and tantallum are highly charged ions and do not substitute in the $YBa_2Cu_3O_{7-\delta}$ lattice but form non superconducting phases. One of the phases that has been reported to form in the $YBa_2Cu_3O_{7-\delta}$ doped with tantallum is the Ba_2YTaO_6 perovskite with a crystalline lattice that is identical to the Ba_2YNbO_6 [124]. Referring to the Ba_2YNbO_6 and Ba_2YTaO_6 perovskites the Nb and Ta are present as Nb^{+4} and Ta^{+4} coordinating 6 oxygen in an octahedral lattice site and the ionic radius of both the element is 0.082 nm. As a matter of the fact the Ba_2YNbO_6 and Ba_2YTaO_6 have identical crystalline lattices.

On the other hand Ba_2YTaO_6 is not the only phase reported to be generated by the tantallum addition, a defective pyrochlore RE_3TaO_7 has also been

reported [67]. Despite the different chemical composition and crystalline structure attributed to the nanorods formed by the addition of tantallum these have been described as very fine ($\approx$ 5 nm in diameter), continuous over the entire film thickness, highly linear and densely distributed thus different from the wider ($\approx$ 10 nm in diameter), shorter and less linear nanorods which are formed by the niobium addition.

Since the niobate and tantalate nanorods in $YBa_2Cu_3O_{7-\delta}$ are of rather different morphology the $YBa_2Cu_3O_{7-\delta}$ doped with niobium and the $YBa_2Cu_3O_{7-\delta}$ doped with tantallum have different superconducting properties. It is interesting to evaluate whether the addition of both niobium and tantallum of the same overall doping level results in an averaging effects or in an increased complexity of the system that could yield to an entirely different and new pinning landscape.

In this chapter is reported a study of simultaneous doping of $YBa_2Cu_3O_{7-\delta}$ with both Ba_2YNbO_6 and Gd_3TaO_7. The reason tantallum was added in the form of RE_3TaO_7 is that this was previously studied in our group as a pinning additive to $YBa_2Cu_3O_{7-\delta}$ thin films.

6.1 Ba_2YNbO_6 and Gd_3TaO_7 doped $YBa_2Cu_3O_{7-\delta}$ target preparation and thin films deposition

The Ba_2YNbO_6 and Gd_3TaO_7 doped $YBa_2Cu_3O_{7-\delta}$ target for the pulsed laser deposition was sintered adopting the process described in the previous chapter to produce densified target and minimize the particulate amount deposited on film surfaces (section 5.1.1). As anticipated in chapter 3, unlike the Ba_2YNbO_6 perovskite, the Gd_3TaO_7 powders were not prepared prior to the target sintering and the desired amount of 99.99% Gd_2O_3 and 99.99% Ta_2O_5 powders were directly added to a mixture of $YBa_2Cu_3O_{7-\delta}$ and Ba_2YNbO_6 powders. The final target stochiometry is 2.5%*mol* Ba_2YNbO_6 + 2.5%*mol* Gd_3TaO_7 doped $YBa_2Cu_3O_{7-\delta}$ doped $YBa_2Cu_3O_{7-\delta}$.

The pulsed laser deposition parameters chosen for the thin films analysed in this chapter are those that showed optimised growth for the 5%*mol* Ba_2YNbO_6 doped $YBa_2Cu_3O_{7-\delta}$. In particular, the substrate temperature was kept at 780

°C and the laser pulses repetition rate was set at 1 Hz. In table 6.1 is summarized the complete set of deposition parameters studied.

Parameter	Value
Substrate Temperature	780 °C
Chamber Pressure	0.3 mbar flowing O_2
Laser Fluence	2 Jcm^{-2}
Repetition Rate	1 Hz
Number of Pulses	4500
Annealing Time	1 hr
Annealing Temperature	520 °C
Annealing Pressure	500 mbar O_2

Table 6.1: Pulsed laser deposition parameters

The Ba_2YNbO_6 + Gd_3TaO_7 doped $YBa_2Cu_3O_{7-\delta}$ thin films deposited were measured to be of $\approx$ 0.35 μm thickness.

6.2 Crystalline structure analysis: x-ray diffraction data

Similarly to the crystalline structure characterisation performed on the first Ba_2YNbO_6 doped $YBa_2Cu_3O_{7-\delta}$ thin films produced the first results presented in this chapter are those obtained from the x-ray diffraction analysis. It is fundamental to investigate the crystalline structure and the orientation of the phases introduced in the thin films.

6.2.0.1 Crystalline phases identification

Figure 6.1 shows the x-ray diffraction pattern of a typical thin film.

The *(00l)* peaks of $YBa_2Cu_3O_{7-\delta}$ (or $(Y/Gd)Ba_2Cu_3O_{7-\delta}$) as well as the *(002), (004)* and *(008)* peaks of $Ba_2(Y/Gd)(Nb/Ta)O_6$ are labeled. A peak at $2\theta = 33.3°$ can be identified as the *(004)* diffraction peak of $(Y/Gd)_2O_3$. Furthermore traces of a copper rich cuprate are also present as indicated by the diffraction peaks *(008),(0010)* and *(0012)* at $2\theta = 25.9°$, $2\theta = 33.2°$ and $2\theta = 41.4°$ that can be associated to $(Y/Gd)Ba_2Cu_4O_8$.

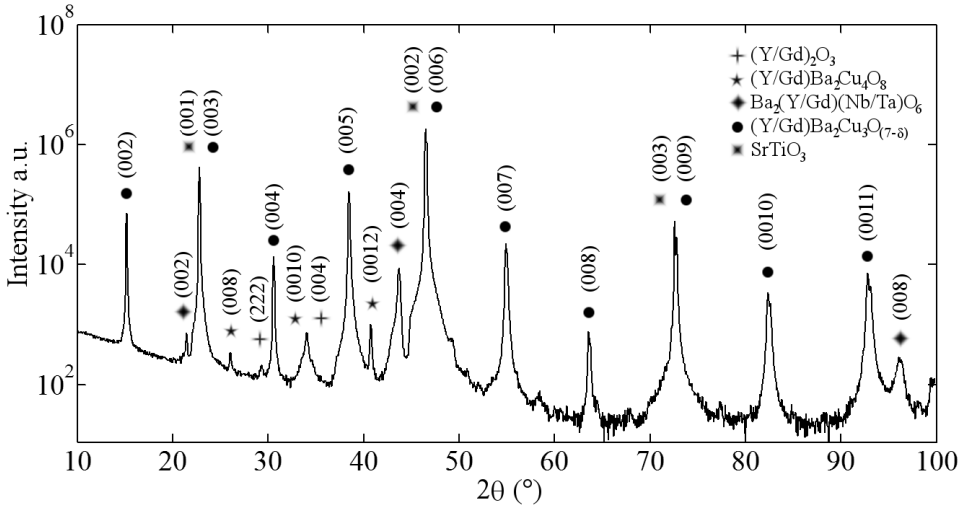

Figure 6.1: Bragg-Brentano scan of a $YBa_2Cu_3O_{7-\delta}$ + 2.5%*mol* Ba_2YNbO_6 + 2.5%*mol* Gd_3TaO_7 thin film deposited on $SrTiO_3$.

It is evident that Gd_3TaO_7 is absent and that a chemical reaction has generated new phases. It is possible to express a balanced chemical reaction that summarize the phases transformation and that is consistent with the phases observed by the x-ray diffraction reported in figure 6.1.

$$0.95\ YBa_2Cu_3O_{7-\delta} + 0.025\ Ba_2YNbO_6 + 0.025\ Gd_3TaO_7$$
$$\downarrow$$
$$0.85\ (Y/Gd)Ba_2Cu_3O_{7-\delta} + 0.05\ Ba_2(Y/Gd)(Nb/Ta)O_6 + 0.0375\ (Y/Gd)_2O_3 + 0.075\ (Y/Gd)Ba_2Cu_4O_8$$

Considering the nature of the ions present in the system is easy to understand the phases evolution observed. Gd can substitute onto the Y site since they have similar ionic radii. For the same reason Nb and Ta can cross-substitute. This allows Ta and Gd introduced as Gd_3TaO_7 together with the Ba_2YNbO_6 and Ba ions subtracted to the $YBa_2Cu_3O_{7-\delta}$ to form the complex perovskite $Ba_2(Y/Gd)(Nb/Ta)O_6$. Furthermore the $Gd_3TaO_7 \rightarrow Ba_2(Y/Gd)(Nb/Ta)O_6$ transformation generates a Gd excess and a Ba deficiency that together with the Gd $\leftrightarrow$ Y mutual substitution could be at the origin of the $(Y/Gd)_2O_3$ and

$(Y/Gd)Ba_2Cu_4O_8$ particles formation.

The previously reported [67] Gd_3TaO_7 phase does not form and the Ta participate to the formation of a perovskite structure similar to the reported Ba_2YTaO_6 [68, 109]. Ba_2YNbO_6 and Ba_2YTaO_6 have identical crystalline structure and the newly formed $Ba_2(Y/Gd)(Nb/Ta)O_6$ do not shows evident differences.

$(Y/Gd)Ba_2Cu_4O_8$ formation has been previously observed in coated $YBa_2Cu_3O_{7-\delta}$ superconductors affected by barium deficiency. In particular a barium depletion by reaction with a CeO_2 buffer layer has been reported to generate $(Y/Gd)Ba_2Cu_4O_8$ [139]. In the Ba_2YNbO_6 + Gd_3TaO_7 doped $YBa_2Cu_3O_{7-\delta}$ the $(Y/Gd)Ba_2Cu_4O_8$ formation can be related to the barium deficiency in the Gd_3TaO_7 reactant. $(Y/Gd)Ba_2Cu_4O_8$ has been reported also in films grown by metal-organic deposition, where it is described to be in the form of stacking fault defects [140].

Concluding the phase identification it is clear that the Ba_2YNbO_6 + Gd_3TaO_7 doped $YBa_2Cu_3O_{7-\delta}$ is a $Ba_2(Y/Gd)(Nb/Ta)O_6$ + $(Y/Gd)_2O_3$ doped $(Y/Gd)Ba_2Cu_3O_{7-\delta}$ thin film with additional traces of $(Y/Gd)Ba_2Cu_4O_8$.

6.2.1 Crystalline phases orientation

The phase orientation analysis is reported in figure 6.2. The $SrTiO_3$ curve is omitted since the $(Y/Gd)Ba_2Cu_3O_{7-\delta}$ can be taken as an orientation reference.

The *cube on cube* growth of the $Ba_2(Y/Gd)(Nb/Ta)O_6$ in the $(Y/Gd)Ba_2Cu_3O_{7-\delta}$ is evidenced by the x-ray ϕ scans: the *(202)* $Ba_2(Y/Gd)(Nb/Ta)O_6$ peak ($\chi = 45°$, $2\theta = 30.03°$) matches the *(102)* $(Y/Gd)Ba_2Cu_3O_{7-\delta}$ ($\chi = 57.06°$, $2\theta = 27.62°$) peaks. Furthermore considering the *out-of-plane* c-axis homogeneous orientation a full heteroepitaxy between the $(Y/Gd)Ba_2Cu_3O_{7-\delta}$, the $Ba_2(Y/Gd)(Nb/Ta)O_6$ and the $SrTiO_3$ substrate is estabilished.

The ϕ scan performed on the *(404)* peak ($\chi = 45°$, $2\theta = 48.518°$) is evidence that the $(Y/Gd)_2O_3$ is rotated 45° in-plane, as previously reported [141]. At a more accurate analysis a small fraction of the $(Y/Gd)_2O_3$ particles appears to be oriented with a minimum offset from the a and b crystalline directions of the $(Y/Gd)Ba_2Cu_3O_{7-\delta}$, a few degrees away from a *cube on cube* orientation. These broad $(Y/Gd)_2O_3$ ϕ peaks have been explained as a near coincidence site

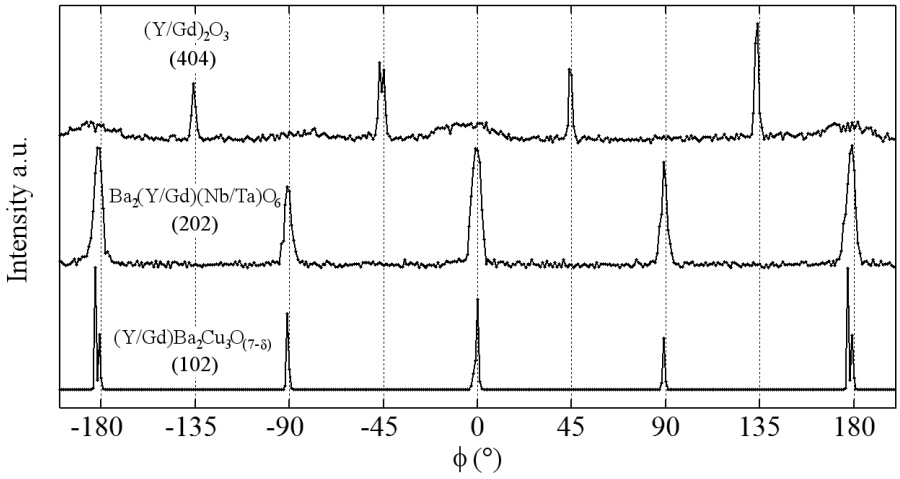

Figure 6.2: X-ray diffraction data from ϕ scans of *(102)* $YBa_2Cu_3O_{7-\delta}$, *(202)* Ba_2YNbO_6 and *(404)* $(Y/Gd)_2O_3$ from a 2.5%*mol* Ba_2YNbO_6 + 2.5%*mol* Gd_3TaO_7 doped $YBa_2Cu_3O_{7-\delta}$ thin film.

lattice matching that can possibly accommodate the large strain and structural differences between $(Y/Gd)_2O_3$ and $YBa_2Cu_3O_{7-\delta}$ [142]. However observing the intensity ratio between the peaks related to the $(Y/Gd)_2O_3$ rotated 45° and those related to the $(Y/Gd)_2O_3$ in a near coincidence matching it is evident that only traces of the latter can be found and that the $(Y/Gd)_2O_3$ can be considered as a rotated 45° in plane.

6.3 Cross-section transmission electron microscopy

Transmission electron microscopy cross-sectional images are reported in figure 6.3. At least two different nanostructural features can be clearly observed.

The first and more obvious feature is a set of fine segmented nanorods of ≈ 7 nm in diameter parallel to the $(Y/Gd)Ba_2Cu_3O_{7-\delta}$ *c*-axis. These nanorods are smaller than the Ba_2YNbO_6 nanorods which are ≈ 10 nm in diameter [5, 124], but larger than the nanorods of Gd_3TaO_7 [67] and Ba_2YTaO_6 [68] which are ≈ 5 nm in diameter. It is important to notice that while in the case of Gd_3TaO_7

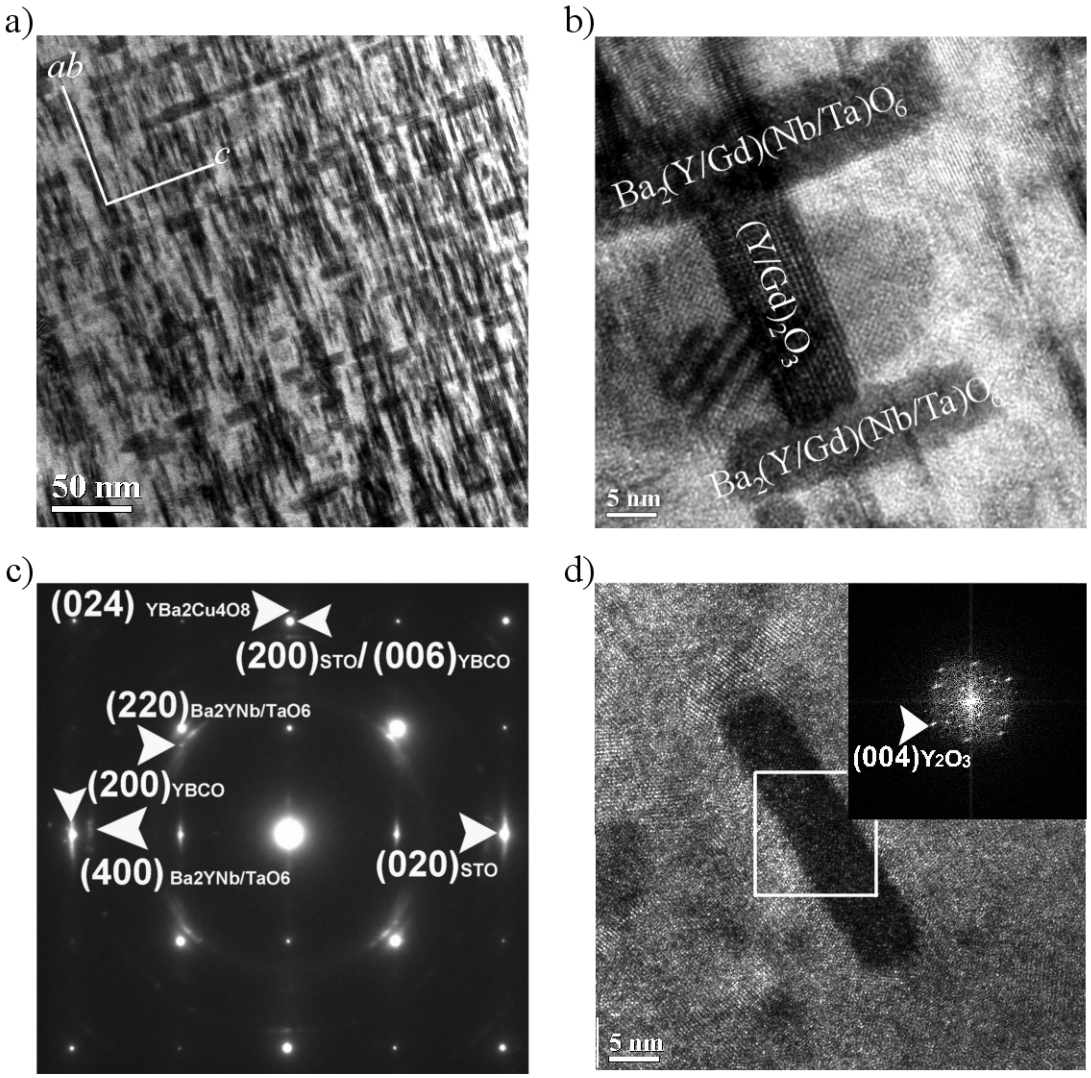

Figure 6.3: a) TEM image of a $YBa_2Cu_3O_{7-\delta}$ + 2.5%*mol* Ba_2YNbO_6 + 2.5%*mol* Gd_3TaO_7 thin film cross section; b) TEM image of plate-like nanoparticleof $(Y/Gd)_2O_3$ nucleated between two $Ba_2(Y/Gd)(Nb/Ta)O_6$ nanorods segments; c) Selected area electron diffraction pattern of the image in (a); d) TEM imafe of plate-like nanoparticle of $(Y/Gd)_2O_3$, inset (d) Fourier transform of the particle image. *(TEM images from Prof. H Wang research group at Texas A&M University).*

nanorods different nanostructural features could be related to different strains and lattice mismatch in the case of Ba_2YTaO_6 this is not possible because Ba_2YTaO_6 and Ba_2YNbO_6 have the identical crystalline lattice. However despite having the same crystalline lattice the Ba_2YNbO_6 forms nanorods larger in diameter than the Ba_2YTaO_6 hence this has to be related to different kinetics of the niobium and the tantallum. $Ba_2(Y/Gd)(Nb/Ta)O_6$ could be described as a mixture of Ba_2YNbO_6 and Ba_2YTaO_6 (with an additional Gd $\leftrightarrow$ Y substitution), hence an averaged growth kinetics of Ba_2YNbO_6 and Ba_2YTaO_6 is obtained , as might be expected. The average nanorod segment length is $\approx$ 30 nm, this is shorter than both the continuous Ba_2YTaO_6 that are long the entire film thickness and the short Ba_2YNbO_6 that are $\approx$ 80-100 nm. An average nanorods spacing of $\approx$ 28 nm nm can be calculated from image in figure 6.3a. Calculating the matching field for a triangular and a quadratic rods distribution (see section 4.2.3.2) the applied magnetic field value in which the pinning potential of the analysed thin films should be higher is between 2.64 T and 3 T, these values are larger than those reported for the Ba_2YNbO_6 inclusion with the same overall doping level.

A second nanostructural feature is clearly shown in figure 6.3b: a plate-like nanoparticle of RE_2O_3 (indicated as $(Y/Gd)_2O_3$) parallel to the $(Y/Gd)Ba_2Cu_3O_{7-\delta}$ *ab*-planes is connecting two adjoining $Ba_2(Y/Gd)(Nb/Ta)O_6$ nanorods segments. To confirm the crystalline nature of this plate-like nanoparticles as RE_2O_3 a Fourier transform confirming the structure of a $(Y/Gd)_2O_3$ particle is shown in figure 6.3d. These plate-like particles of $(Y/Gd)_2O_3$ are in the 25-30 nm width range and their extensions along the $(Y/Gd)Ba_2Cu_3O_{7-\delta}$ *c*-axis is $\approx$ 7 nm.

In order to confirm the phases identification obtained with the x-ray diffraction analysis in figure 6.3c is reported a selected area electron diffraction pattern of a large cross-sectional region. Diffraction spots that can related to $SrTiO_3$, $(Y/Gd)Ba_2Cu_3O_{7-\delta}$, $Ba_2(Y/Gd)(Nb/Ta)O_6$, $(Y/Gd)Ba_2Cu_4O_8$ are labeled and are consistent with the x-ray diffraction pattern reported in figure 6.1.

To conclude, the nanostructure investigation reported in this section is important to emphasize that the nanorods segmentation is a new structural feature, and that this is the first time it has been observed. The segmentation of the nanorods yields to an average segment length of $\approx$ 30 nm. An explanation of the phe-

nomenon may be in kinetic terms: the tantallum ion is heavier than the niobium thus it has a slower diffusion, this may generate a shortage in the tantallum supply as a reactant for the nanorods' growth thus preventing these from maintaining continuity as the film growth progresses. A new segment nucleates aligned along the (Y/Gd)$Ba_2Cu_3O_{7-\delta}$ c-axis with a preexisting segment thanks to the presence of a nucleation enhancing strain field generated within the (Y/Gd)$Ba_2Cu_3O_{7-\delta}$ by the nanoinclusion similarly to the $BaZrO_3$ and Ba_2YNbO_6 [133].

6.4 The superconducting properties: T_c, $J_c(B)$ and $J_c(B, \theta)$

The complex thin film crystalline structure composition made of three different nanoinclusion phases ($(Y/Gd)_2O_3$, $Ba_2(Y/Gd)(Nb/Ta)O_6$, (Y/Gd)$Ba_2Cu_4O_8$) and a possible RE (Gd $\leftrightarrow$ Y) variation do not influence the transition temperature. No suppression of the superconducting transition temperature was observed, the T_c values measured were $\approx$ 89 K.

Similarly to what observed in Ba_2YNbO_6 doped $YBa_2Cu_3O_{7-\delta}$ thin films a small reduction of the transition temperature values from the transition of the pure $YBa_2Cu_3O_{7-\delta}$ thin films is expected [5,57,68,118,119], when this is limited to a few Kelvin ($\approx$ 2 K), it is evident that the secondary non superconducting phases are stable and that the only source of T_c reduction are the induced $YBa_2Cu_3O_{7-\delta}$ lattice distortions.

6.4.1 The critical current density

In this section are compared the effects on the critical current density of Ba_2YNbO_6, $BaZrO_3$, and simultaneous Ba_2YNbO_6 - Gd_3TaO_7 doping. The critical current density reported are all measured on thin films of $\approx$ 300 nm thickness. The $BaZrO_3$ doped $YBa_2Cu_3O_{7-\delta}$ data are taken from one of the best performing films in literature deposited adopting a $YBa_2Cu_3O_{7-\delta}$ target covered by yttria-stabilized zirconia on 2% of the surface area [6] while a Ba_2YNbO_6 doped $YBa_2Cu_3O_{7-\delta}$ thin films of $\approx$ 350 nm thickness was specifically grown and measured for this comparison.

6.4.1.1 The critical current density: $J_c(B)$

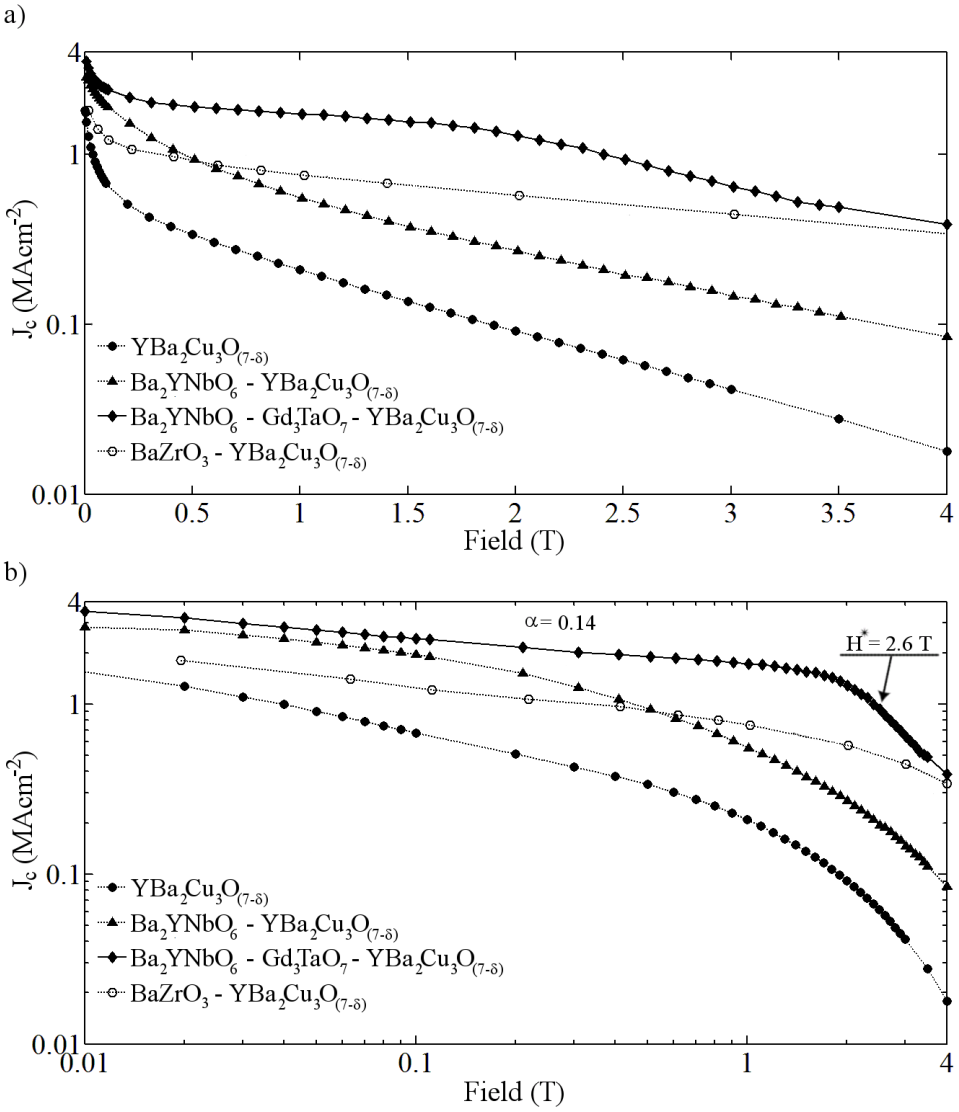

Figure 6.4: Critical current density variation with the applied magnetic field value measured on a pure $YBa_2Cu_3O_{7-\delta}$, a 5%*mol* Ba_2YNbO_6 doped $YBa_2Cu_3O_{7-\delta}$, a 2.5%*mol* Ba_2YNbO_6 - 2.5%*mol* Gd_3TaO_7 doped $YBa_2Cu_3O_{7-\delta}$ and a $BaZrO_3$ doped $YBa_2Cu_3O_{7-\delta}$ thin films [6]. The field is applied parallel to the *c*-axis of the $YBa_2Cu_3O_{7-\delta}$, T = 77 K. the data are on a log-linear plot (a) and a log-log plot (b).

In figure 6.4 is reported $J_c(B)$ measurements up to 4 T with the field applied parallel to the c-axis ($B \| c$) at 77 K for a pure $YBa_2Cu_3O_{7-\delta}$, a 5%*mol* Ba_2YNbO_6 doped $YBa_2Cu_3O_{7-\delta}$, a 2.5%*mol* Ba_2YNbO_6 - 2.5%*mol* Gd_3TaO_7 doped $YBa_2Cu_3O_{7-\delta}$ and a $BaZrO_3$ doped $YBa_2Cu_3O_{7-\delta}$ thin films. The thin films with the simultaneous doping of Ba_2YNbO_6 and Gd_3TaO_7 show the highest J_c of all the films studied in the entire field range analysed. An outstanding J_c value of 1.8 $MAcm^{-2}$ at 1 T and values above 1 $MAcm^{-2}$ up to 2.5 T are the best indications of the excellent potential of this new pinning landscape. Furthermore, from the data shown in figure 6.4b it is clear that the exponential J_c decay range (linear on double logaritmic axis) is extended to fields values above 2 T.

Another unusual feature related to this new pinning landscape is the net change in the slope of $J_c(B)$ that occurs as the field intensity approaches the value of matching fields ($\approx$ 2.6 T). This could be an indication of the effective defusing of the low energy depinning mechanisms and of a strong pinning capacity of the single nanorods. The J_c, in fact, start to decrease only when the fluxons are about to saturate the pinning sites.

The high pinning capacity of the Ba_2YNbO_6 + Gd_3TaO_7 doped $YBa_2Cu_3O_{7-\delta}$ thin films can also be deduced by the α values reported in table 6.2.

Dopant	α
$YBa_2Cu_3O_{7-\delta}$	0.47
Ba_2YNbO_6 doped $YBa_2Cu_3O_{7-\delta}$	0.35
$BaZrO_3$ doped $YBa_2Cu_3O_{7-\delta}$	0.25
Ba_2YNbO_6 + Gd_3TaO_7 doped $YBa_2Cu_3O_{7-\delta}$	0.14

Table 6.2: α values calculated from the $J_c(B)$ curves shown in figure 6.4.

The α value $\approx$ 0.14 calculated for the Ba_2YNbO_6 + Gd_3TaO_7 doped $YBa_2Cu_3O_{7-\delta}$ thin film is lower than the lowest previously reported value, an $\alpha \approx$ 0.19 reported in a specially grown $BaZrO_3$ doped $YBa_2Cu_3O_{7-\delta}$ where it was shown that an optimisation of the deposition process could produce a mixture of $BaZrO_3$ randomly distributed nanoparticles and splayed columnar defects that could synergetically reduce the depinning mechanism effectiveness [134]. In fact, the new pinning landscape produced by the Ba_2YNbO_6 + Gd_3TaO_7 simultaneous doping consists of segmented nanorods and plate-like nanoparticles that form a

synergetic pinning landscape similar to the one produce in the specially grown $BaZrO_3$ doped $YBa_2Cu_3O_{7-\delta}$. The two pinning landscapes show two key differences: the $Ba_2(Y/Gd)(Nb/Ta)O_6$ nanorods are smaller in diameter ($\approx$ 7 nm) than the $BaZrO_3$ nanorods ($\approx$ 10-15 nm); the $Ba_2(Y/Gd)(Nb/Ta)O_6$ nanorods are segmented while the $BaZrO_3$, similarly to the Ba_2YNbO_6, while not being continuous have an average length of $\approx$ 100 nm. The segmentation could be the key factor to explain the lower α, segmented rods could in fact gave rise to strongly pinned staircase vortices.

6.4.1.2 The critical current density angular dependence: $J_c(B, \theta)$

Investigating the angular dependence of J_c (figure 6.5) it is evident that the Ba_2YNbO_6 + Gd_3TaO_7 doped $YBa_2Cu_3O_{7-\delta}$ thin film shows superior pinning properties over a large angle ranges and not only when the field is applied parallel the $YBa_2Cu_3O_{7-\delta}$ c-axis.

The Ba_2YNbO_6 + Gd_3TaO_7 doped $YBa_2Cu_3O_{7-\delta}$ films show at low field values (figure 6.5a) a strong, narrow c-axis pinning peak and no variation of critical current respect the pure $YBa_2Cu_3O_{7-\delta}$ thin film is measured when the field is applied parallel to the $YBa_2Cu_3O_{7-\delta}$ ab-planes. The J_c values measured for this new pinning landscape with the field applied parallel to the $YBa_2Cu_3O_{7-\delta}$ c-axis of 1.8 $MAcm^{-2}$ is 3 times higher then the one measured for the Ba_2YNbO_6 doped $YBa_2Cu_3O_{7-\delta}$ and 6 times higher then the one measured for the undoped $YBa_2Cu_3O_{7-\delta}$.

The Ba_2YNbO_6 doped $YBa_2Cu_3O_{7-\delta}$ thin film shows results that are identical to those reported in the previous chapter: a noticeable J_c increase when the field is applied parallel to the $YBa_2Cu_3O_{7-\delta}$ c-axis together with a small J_c increase with fields applied parallel to the $YBa_2Cu_3O_{7-\delta}$ ab-planes.

Increasing the field intensity the strong, narrow c-axis pinning peaks of the Ba_2YNbO_6 + Gd_3TaO_7 doped $YBa_2Cu_3O_{7-\delta}$ films changes to a strong and broad peak. The segmented nanorods provide strong pinning to the vortices over a wide range of angular directions. The J_c values measured on the Ba_2YNbO_6 + Gd_3TaO_7 doped $YBa_2Cu_3O_{7-\delta}$ are higher then those measured on Ba_2YNbO_6 doped $YBa_2Cu_3O_{7-\delta}$ indicating that the pinning of the finer, segmented

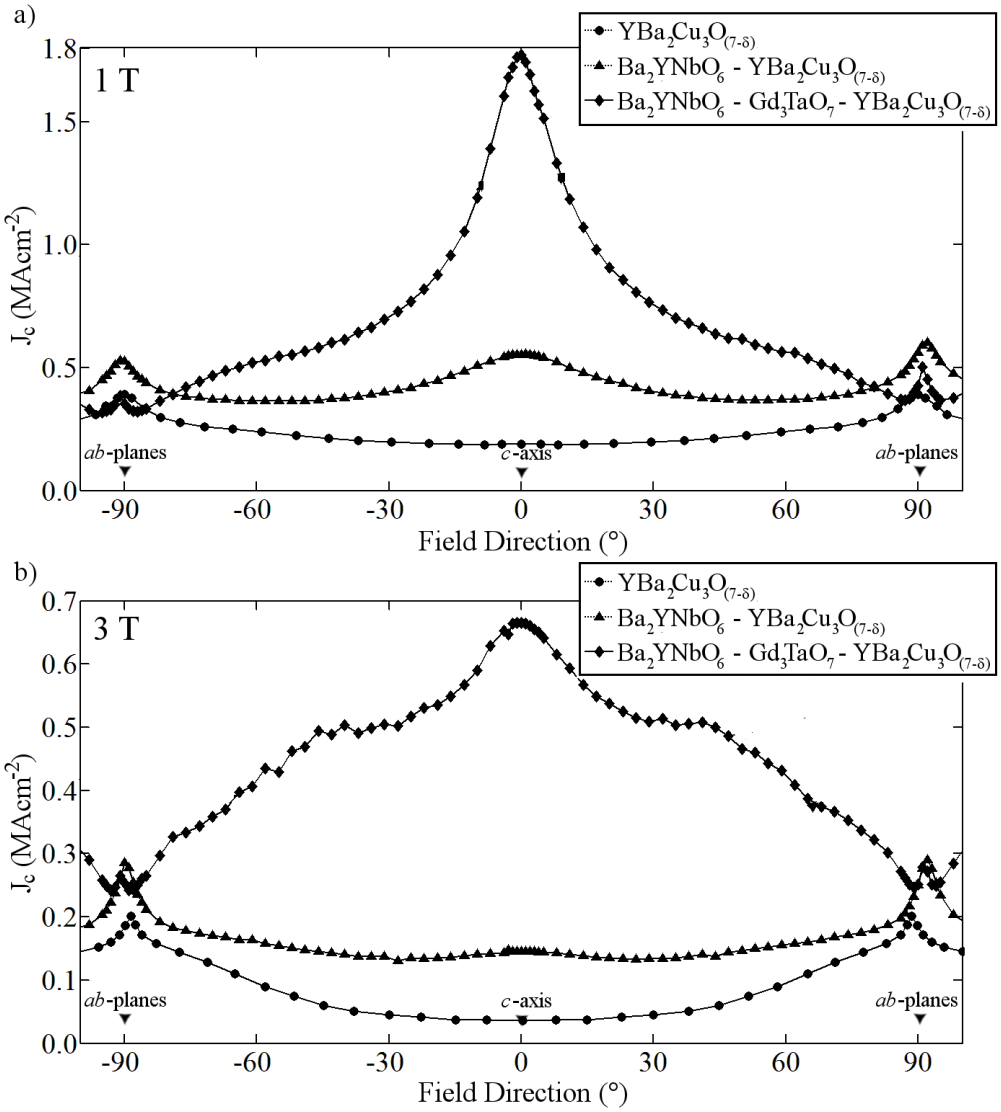

Figure 6.5: Critical current density variation with the direction of the applied magnetic field measured on a pure $YBa_2Cu_3O_{7-\delta}$, a 5%*mol* Ba_2YNbO_6 doped $YBa_2Cu_3O_{7-\delta}$, a 2.5%*mol* Ba_2YNbO_6 - 2.5%*mol* Gd_3TaO_7 doped $YBa_2Cu_3O_{7-\delta}$ and a $BaZrO_3$ doped $YBa_2Cu_3O_{7-\delta}$ thin films [6]. The field is applied parallel to the *c*-axis of the $YBa_2Cu_3O_{7-\delta}$. a) Applied magnetic flux density = 1 T, T = 77 K; b) Applied magnetic flux density = 3 T, T = 77 K.

$Ba_2(Y/Gd)(Nb/Ta)O_6$ nanorods together with $(Y/Gd)_2O_3$ plate-like nanoparticles is more effective compared to the coarser, non segmented Ba_2YNbO_6 rods.

6.4.1.3 A new pinning feature

A last interesting piece of information is the evolution of the angular J_c increasing the field (figure 6.6a). If a low field the most prominent feature is the strong *c*-axis pinning peak and substantially unmodified *ab*-planes peaks (figure 6.5a) increasing the field values a new feature start to become visible. This new pinning feature can be initially observed at 3 T and it appears as shoulders on the broad *c*-axis peak and increasing the field value these shoulders resolves into distinct peaks around $\pm$ 60°. The magnitude of this two peaks increases with increasing the field values and for field values of 5 T and above they become the dominant pinning peaks.

This additional pinning preferential direction is a new feature that is directly related to the new pinning landscape generated in the Ba_2YNbO_6 + Gd_3TaO_7 doped $YBa_2Cu_3O_{7-\delta}$ thin films. The existence of this additional preferential pinning direction can be explained using the vortex path model [143]. In this model the combination of *c*-axis pinning structures (segmented $Ba_2(Y/Gd)(Nb/Ta)O_6$ nanorods) and *ab*-planes structures (plate-like $(Y/Gd)_2O_3$ nanoparticles and $YBa_2Cu_3O_{7-\delta}$ *ab*-planes) results in staircase vortices that are pinned simultaneously by the different structures. These vortices are subjected to the strongest pinning at a characteristic angle determined by the distribution of defects and defects length (figure 6.6b). Since in this type of pinning are involved both the available species of additional pinning structure ($Ba_2(Y/Gd)(Nb/Ta)O_6$ nanorods and $(Y/Gd)_2O_3$ nanoparticles) the hypothetical matching field would have an higher value thus this pinning is more effective at high field values.

6.4.2 Concluding remarks to Ba_2YNbO_6 and Gd_3TaO_7 simultaneous doping of $YBa_2Cu_3O_{7-\delta}$

The study reported in this chapter is on the Ba_2YNbO_6 and Gd_3TaO_7 simultaneous doping of $YBa_2Cu_3O_{7-\delta}$. The expected mixture of Ba_2YNbO_6 coarse splayed nanorods and Gd_3TaO_7 fine dense linear nanorods was not generated.

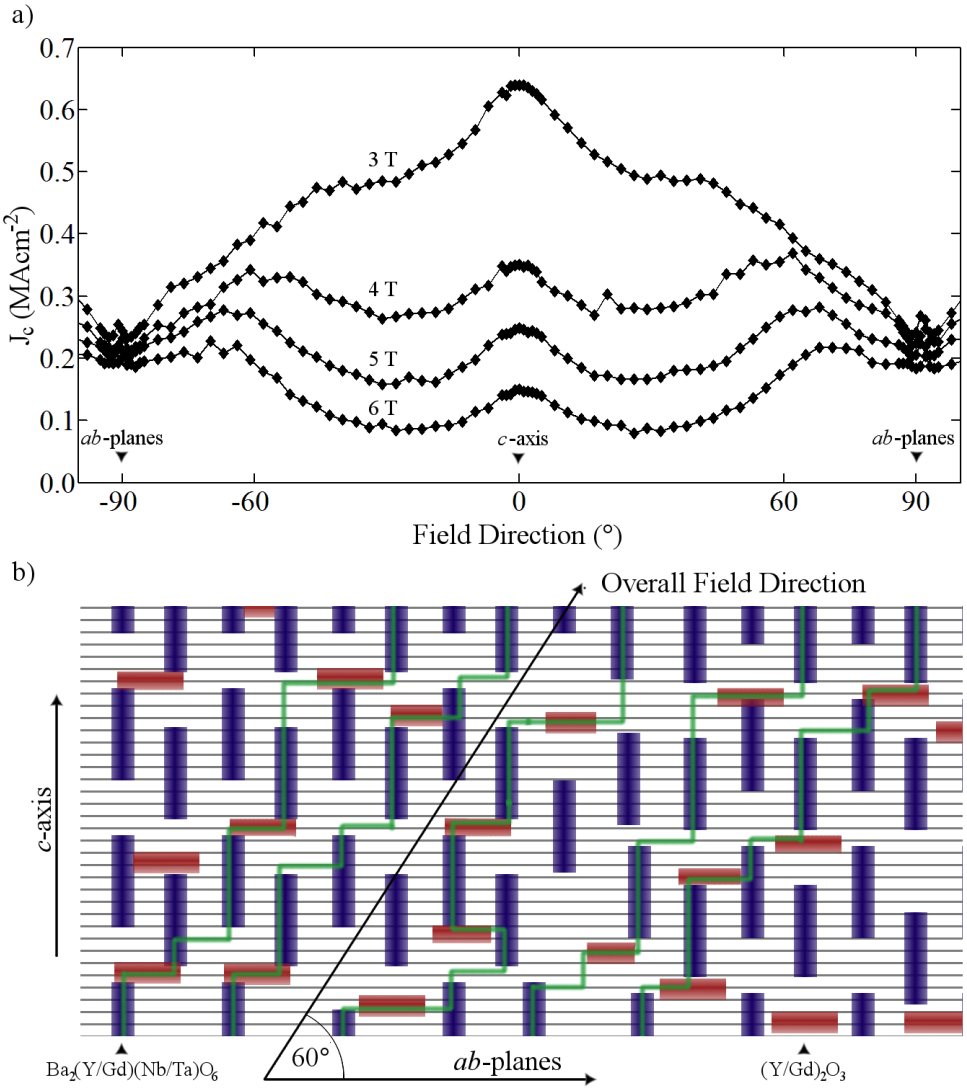

Figure 6.6: a) High field critical current density variation with the direction of the applied magnetic field measured on a 2.5%*mol* Ba_2YNbO_6 - 2.5%*mol* Gd_3TaO_7 doped $YBa_2Cu_3O_{7-\delta}$. Applied magnetic flux density = 3 T to 6 T, T = 77 K; b) sketch of vortices interacting simultaneously with nanorod segments along the *c*-axis and intrinsic and extrinsic defects along *ab*-planes.

Combining Ba_2YNbO_6 and Gd_3TaO_7, two well studied phases, a completely new self-assembled pinning landscape was generated instead. This pinning landscape is not a mere mixture of the landscape generated by Ba_2YNbO_6 and Gd_3TaO_7 but presents an optimal nanorods' architecture of fine, straight, segmented rods. Furthermore $(Y/Gd)_2O_3$ nanoparticles were fortuitously generated because the nanorods of $Ba_2(Y/Gd)(Nb/Ta)O_6$ formed were of different composition (poorer in rare earth, richer in barium) than the reactants Ba_2YNbO_6 and Gd_3TaO_7 that were added to the $YBa_2Cu_3O_{7-\delta}$ pulsed laser deposition target.

The critical current densities measured at 77 K are greatly enhanced compared to previously studied pinning additives. In particular J_c values above 1 $MAcm^{-2}$ for fields up to 2.5 T were achieved and this is a new benchmark in the $YBa_2Cu_3O_{7-\delta}$ thin films properties. Furthermore new pinning features around 60° were observed for the first time proving the possibility of tuning the pinning landscape in order to generate thin films with an arbitrary preferential pinning direction. Applications where the magnetic field is applied obliquely to the superconductor could greatly benefit from the use of this new pinning landascape.

Chapter 7

Conclusions and further work

The study presented in this thesis investigated the use of novel secondary non superconducting phases to generate nanostructured $YBa_2Cu_3O_{7-\delta}$ thin films produced by pulsed laser deposition from a single composite target with enhanced flux pinning and improved performance in applied magnetic fields.

First an intensive study on the addition of a niobium based non superconducting phase was completed. At the time the pinning additive known to be effective for the production of nanorods and the creation of a *c*-axis pinning peak were $BaZrO_3$ (a zirconium based perovskite) [57], RE_3TaO_7 (tantallum based pyrochore) [67] and $BaSnO_3$ (a tin based perovskite) [64]. With the exception of the RE_3TaO_7 all the other phases are barium based perovskites. These perovskites form a different pinning landscape thanks to different ions kinetics and different lattice mismatches. Thus the $YBa_2Cu_3O_{7-\delta}$ thin films doped with different perovskites have different properties.

It was known that in bulk samples adding niobium or tantallum to $YBa_2Cu_3O_{7-\delta}$ forms Ba_2YNbO_6 or Ba_2YTaO_6 [109] but at the time of that study RE_3TaO_7 was the only phases reported in pulsed laser deposited $YBa_2Cu_3O_{7-\delta}$ thin films doped with tantallum while an early study reported the successfull production of Ba_2NbErO_6 perovskite in $ErBa_2Cu_3O_{(7-\delta)}$ [118, 119].

The first step of the research work reported in this thesis is the demonstration of the possibility to introduce Ba_2YNbO_6 nanorods in $YBa_2Cu_3O_{7-\delta}$ together with providing the experimental evidence of the potential of broad *c*-axis pinning peaks. The broad *c*-axis pinning peak was related to the morphology of the novel

Ba_2YNbO_6 nanorods, that was found to be different from those reported before. The nanorods resulted to be shorter, wider and with a larger *c*-axis splay than the those generated by the other known pinning additives [5].

Once discovered, the potential of Ba_2YNbO_6 as pinning additive, a study of the effects of the deposition rate and substrate temperatures on Ba_2YNbO_6 doped $YBa_2Cu_3O_{7-\delta}$ thin films was performed. The study demonstrated that fast deposition rates induce smaller growth grains and the formation of Ba_2YNbO_6 nanoparticles togheter with the ordered Ba_2YNbO_6 nanorods. The thin films produced adopting high deposition rates while proved to be highly effective at high field values show a severe reduction of the intrinsic $YBa_2Cu_3O_{7-\delta}$ *ab*-planes pinning. This reduction is related to the large amount of discontinuity introduced to the $YBa_2Cu_3O_{7-\delta}$ crystall *ab*-planes. On the other hand Ba_2YNbO_6 doped $YBa_2Cu_3O_{7-\delta}$ thin films deposited at low deposition rate showed that it is possible to introduce Ba_2YNbO_6 and increase the pinning potential along the *c*-axis without reducing the connectivity or the $YBa_2Cu_3O_{7-\delta}$ crystall quality thus without reducing the *ab*-plane pinning potential. In conclusion Ba_2YNbO_6 doped $YBa_2Cu_3O_{7-\delta}$ thin films with enanched *c*-axis togheter with good *ab*-planes pinning potential were succesfully deposited. These Ba_2YNbO_6 doped $YBa_2Cu_3O_{7-\delta}$ thin films stand out because they show a low anisotropy of the angular dependence of the critical current greatly reducing the design difficulties encountered in many coated conductors applications.

The last part of the thesis is devoted at a new research that arises from the desire to investigate the effects on the pinning of a synergistic combination of morphologically different nanoinclusions. In particular the combination of the wide, short splayed Ba_2YNbO_6 nanorods and the fine, long, higly linear Gd_3TaO_7 nanorods was investigated. This work demonstrated that in a niobium and tantallum combined scenario the tantallum partecipate to the formation of a perovskyte and do not form Gd_3TaO_7. A tantallum based perovskite Ba_2YTaO_6 was also recently reported in tantallum doped $YBa_2Cu_3O_{7-\delta}$ [68], however also the Ba_2YTaO_6 perovskite is morphologically different from the Ba_2YNbO_6 being fine, long and highly linear like the previously reported Gd_3TaO_7 nanorods.

A completely new pinning landscape was produced by depositing thin films from a Ba_2YNbO_6 + Gd_3TaO_7 + $YBa_2Cu_3O_{7-\delta}$ PLD target. The structural

and morphological characterization of these films showed that the these films are mainly made of (Y/Gd)$Ba_2Cu_3O_{7-\delta}$ with fine, linear, segmented nanorods of Ba_2(Y/Gd)(Nb/Ta)O_6 and $(Y/Gd)_2O_3$ plate-like nanoparticles inclusions. This new defect landscape produced in the thin films is capable of generating state-of-the-art pinning properties. Astonishingly high critical currents are not the only effect: for the first time possibility to achieve self segmentation of nanorods was demostrated, and for the first time additional new pinning features around 60° were observed.

Owing to the very high critical currents obtained, exceeding the industry standard $BaZrO_3$, it is likely that the results obtained in this work will attract the interest of many research groups from different area of the field. Furthermore, modifying the ratio of niobium and tantallum and the ratio between Ba_2(Y/Gd)(Nb/Ta)O_6 and $(Y/Gd)_2O_3$ will almost certanly demonstrate the tunability of the pinning landscape, and a new era will begin in which it will be possible to produce superconductors specifically designed for pinning in a predetermined direction.

A direct continuation of this work should investigate the effects of the simultaneous niobium tantallum doping in a simplified system. At first $YBa_2Cu_3O_{7-\delta}$ films doped only with Ba_2YNbO_6 and Ba_2YTaO_6 produced with different of Nb:Ta ratios could be grown in order to investigate the tunability of the segmentation. In a second stage $(Y/Gd)_2O_3$ could be added to the Ba_2YNbO_6 and Ba_2YTaO_6 doping to evaluate the importance of the synergistic combination, and find the optimal balance between plate like nanoparticles and segmented nanorods. In a last stage Gd, as well as other rare earths, could be used to partially substitue the Y riproducing the otpimal pinning landscape obtained in this work but with an increased knoledge of the single constituent effects and increased freedom on the composition of the films.

In addition a study of the pinning properties at temperatures below 77 K of the system demonstrated in this dissertation could provide additional evidence of the effective possibility of tuning nanoengineered $YBa_2Cu_3O_{7-\delta}$ in order to achieve optimal pinning along arbitrary directions.

Appendix

Publications related to the research described in this dissertation are presented in this section. The publications order is the following:

- Ercolano G *et al.* "Enhanced flux pinning in $YBa_2Cu_3O_{7-\delta}$ thin films using Nb-based double perovskite additions". *Supercond. Sci. Technol.*, 23:022003, 2010.

- MacManus-Driscoll J L *et al.* "High current, low cost YBCO conductors-what's next?". *Supercond. Sci. Technol.*, 23:034009, 2010.

- Ercolano G *et al.* "State-of-the-art flux pinning in $YBa_2Cu_3O_{7-delta}$ by the creation of highly linear, segmented nanorods of $Ba_2(Y/Gd)(Nb/Ta)O_6$ together with nanoparticles of $(Y/Gd)_2O_3$ and $(Y/Gd)Ba_2Cu_4O_8$". Submitted to *Supercond. Sci. Technol.*

A general table of the crystallographic parameters of non-superconductive second phase materials used as pinning phases in $YBa_2Cu_3O_{7-\delta}$ films is also reported.

Supercond. Sci. Technol. **23** (2010) 022003 (6pp) doi:10.1088/0953-2048/23/2/022003

RAPID COMMUNICATION

Enhanced flux pinning in $YBa_2Cu_3O_{7-\delta}$ thin films using Nb-based double perovskite additions

G Ercolano[1], S A Harrington[1], H Wang[2], C F Tsai[2] and J L MacManus-Driscoll[1]

[1] Department of Materials Science and Metallurgy, University of Cambridge, Pembroke Street, Cambridge CB2 3QZ, UK
[2] Department of Electrical and Computer Engineering, Texas A&M University, College Station, TX 77843, USA

E-mail: ge228@cam.ac.uk

Received 31 August 2009, in final form 11 December 2009
Published 13 January 2010
Online at stacks.iop.org/SUST/23/022003

Abstract
The addition of a new niobate double perovskite pinning phase to $YBa_2Cu_3O_{7-\delta}$ thin films grown by pulsed laser deposition is reported. The YBa_2NbO_6 phase self-assembles into stacks of ~10 nm second phase particles, aligned with the *c*-axis of the $YBa_2Cu_3O_{7-\delta}$. The $YBa_2Cu_3O_{7-\delta}/YBa_2NbO_6$ composite thin films have enhanced critical current, by a factor of 2, at 1 T ($H \parallel c$) over the pure $YBa_2Cu_3O_{7-\delta}$, whilst maintaining a high transition temperature. Niobium does not substitute in the $YBa_2Cu_3O_{7-\delta}$ matrix. This, together with the high stability of the second phase formed, makes it an ideal pinning additive.

1. Introduction

Improved performance of high temperature superconductors (HTS) in magnetic fields is a highly sought after goal to make HTS conductors commercially viable. There are two routes to achieve higher current carrying performance, (a) controlled nano-engineering of superconducting materials to enhance flux pinning [1–8] and (b) growth of thicker highly epitaxial material in a simple and cost-effective manner through applying novel processing routes. With industrial applications in mind, the current focus should now be to produce efficient, reproducible and cost-effective nanopinning defect arrays. To achieve these end goals it is necessary to: (1) select an ion or phase addition which produces a secondary pinning phase which forms in a *wide* processing window, and (2) to understand and hence control the second phase assemblage. The group IV and group V ion additions, more specifically Zr^{4+}, Hf^{4}, Ta^{5+} and, as shown in this work, Nb^{5+}, appear to be the best to meet the first goal [9] and we are now at the stage of beginning to understanding the second one.

$YBa_2Cu_3O_{7-\delta}$ (YBCO) thin films containing such additions with improved J_c (up to a factor of 5) in magnetic field was first demonstrated by the introduction of $BaZrO_3$ (BZO) [10]. Through careful process optimization, the results with BZO have been further substantially improved over the last 5 years [11, 12]. More recently, with the aim of producing minimally chemically and structural perturbative effects, rare earth tantalates (RE_3TaO_7, RTO) have been studied. Compared to BZO, these have been found to yield greater tunability of particle assemblage, and no T_c reduction. In a short space of time, this has led to a J_c increase by up to a factor of 10 [13]. Further studies on the RTO addition effects and on the process optimization have been performed and will be published in the future.

It is important to note that for the PLD technique, when deciding on new pinning additions to YBCO the phase which forms is not necessarily the one which is added to the YBCO, but is the one which is the most thermodynamically and epitaxially stable. Hence, if Zr^{4+} is added to YBCO, $Ba(Zr, Y)O_3$ forms [10]. In this paper we present the results of addition of another large, highly charged ion, Nb^{5+}, (see table 1) which does not substitute for the Cu site in YBCO and hence which has great potential to form a benign second

Table 1. Ionic charge and radius of critical ion additions for second phase formation, and percentage lattice mismatch with respect to YBCO (along *ab* and *c*). Critical pinning ion addition indicates that the ion is not a component of the YBCO phase and that addition of the pure element to YBCO will, for reasons of thermodynamic stability and epitaxial stabilisation, lead to the pinning addition phase in column 1.

	Critical ion pinning addition/ionic radius (Å) for 6 fold co-ordination	% Misfit to YBCO *ab*	% Misfit to YBCO *c*
YBa_2NbO_6	Nb^{5+}/0.78	9.42	8.34
$BaZrO_3$	Zr^{4+}/0.86	8.11	7.03
$BaSnO_3$	Sn^{4+}/0.83	6.77	5.72
Sm_3TaO_7	Ta^{5+}/0.78	−2.33	−7.99
Yb_3TaO_7	Ta^{5+}/0.78	−4.74	−11.04

phase addition. The charge and size of the ion are important for minimizing the level of substitution in the YBCO lattice. Zr^{4+} and Sn^{4+} (table 1) can substitute for Y^{3+} (whose ion radius is 1.159 Å for 8 fold co-ordination), whereas Ta^{5+} and Nb^{5+} are less likely to substitute for Y^{3+} because of the more dissimilar ion sizes and ion valences.

We study the addition of a double perovskite Nb-based phase (YBa_2NbO_6) to YBCO. This phase is the most stable Nb-related compound when in equilibrium with YBCO, explaining why when we add Nb_2O_5 or $BaNbO_3$ to YBCO, the double perovskite YBa_2NbO_6 still forms [14–16]. We find that nanoparticles of the phase self-assemble in a manner similar to the tantalates [13] and BZO [17]. Addition of Nb_2O_5 to bulk YBCO has been shown to enhance J_c [18]. However this enhanced material was not well understood until later [14–16] when segregation into YBCO + YBa_2NbO_6 was observed. The stability and compatibility of the YBa_2NbO_6 compound with YBCO made it a candidate for novel substrates [19], as well as for new buffer layers for high quality HTS thin films and electronic devices [20, 21]. Double perovskites, of general formula $A_2BB'O_6$, have attracted much interest in other research fields because their high flexibility in lattice parameter and magnetic behaviour [22–25]. YBa_2NbO_6 has the advantage over many of the double perovskite phases, e.g. the well studied $FeSr_2MoO_6$ phase, in that there is less propensity for the cations to have a mixed valence [26], which would then cause unwanted local oxygen stoichiometry changes in the YBCO lattice.

The use of YBa_2NbO_6 as a secondary phase to improve pinning in YBCO epitaxial films on ZrO_2 single crystalline substrates has been reported with negative results [27]. The physical properties and chemical compatibility make YBa_2NbO_6 an ideal candidate as a pinning addition to YBCO. However, difficulty in obtaining adequate oxygenation of composite bulk material [28] resulted in depressed transport properties. This is not an obstacle to YBa_2NbO_6 doped thin film growth as high surface to volume ratio and small grain size allows full oxygenation in a rapid manner. Here we present success in producing pinning engineered $YBa_2Cu_3O_{7-\delta}/YBa_2NbO_6$ thin films with high critical currents grown by pulsed laser deposition.

2. Experimental methods

PLD targets were made by mixing and grinding pure YBCO powder (SCI Engineered Materials) (99.999%) with the desired amount of YBa_2NbO_6 powder in an agate mortar, the latter were produced as single phase by the solid state reaction method, namely mixing, grinding of 99.99% Y_2O_3, $Ba(NO_3)_2$, and Nb_2O_5 powders followed by reaction at 1450 °C for 24 h. The mixed powders were pressed in the form of a cylindrical target and sintered at 950 °C for 12 h in flowing O_2 in a dedicated tubular furnace. Films were grown by PLD on (001) $SrTiO_3$ (5 mm × 10 mm) single crystal substrate (Pi-Kem Ltd). Deposition were performed with a Lambda Physik KrF excimer laser ($\lambda = 248$ nm) in 30 Pa flowing O_2, and the substrate temperature was kept at 770 °C. A repetition rate of 5 Hz and 4500 pulses were used for all films, which were measured to be of 0.5 μm thickness.

The transport critical current density was measured using a conventional four-point probe method and a $\sim$1 μV cm^{-1} criterion on photolithographically patterned bridges of 250 μm width. The angular dependence of J_c at 77 K and 0.5 T was measured with the applied magnetic field rotated in a plane perpendicular to the current flow direction to an angle θ with the *c*-axis of the film.

The crystallographic structure and orientation of the films were studied using x-ray diffraction in Bragg–Brentano geometry. Lattice parameters were refined using *eva* software, using the positions of high angle peaks to minimize errors. Cross-sectional transmission electron microscopy (TEM) and selected area electron diffraction patterns (SADP) were also undertaken to determine the crystal structure and sizes of the nanoparticles formed within the YBCO matrix.

3. Results and discussion

Figure 1(a) displays the results of x-ray analysis of the YBa_2NbO_6 powder produced by solid state reaction. These results agree with the data recorded in the JCPDS or in more recent studies [29]. No impurities or secondary phases peaks are found. The lattice parameter calculated from the x-ray data is 0.844 nm ± 0.001 nm.

The x-ray diffraction data from the deposited films (figure 1(b)) shows peaks related to (00*l*) planes from the YBCO and the $SrTiO_3$ for both undoped and doped samples. This means that the films are *c*-axis oriented, which is the standard orientation for YBCO thin films on (001) $SrTiO_3$. Additionally, the data from the doped sample only shows the peaks related to the (00*l*) planes of YBa_2NbO_6, indicating that the additive phase is aligned out-of-plane with the YBCO. A small peak at 34°, possibly arising from the (111) planes of YBCO is present in both the undoped and doped sample data. No other secondary phases were present.

The (00*l*) orientations of both phases is expected from the crystallographic matching of these double and triple perovskite cells (shown schematically in figure 2(a)). Looking along the $[010]_{YBCO}$ direction, 3 unit cells of the cubic YBa_2NbO_6 match 2 unit cells of YBCO giving a lattice mismatch strain along the *c*-axis of YBCO, $((3a_{YBa_2NbO_6} - 2c_{YBCO})/2c_{YBCO})$, of +8.34%.

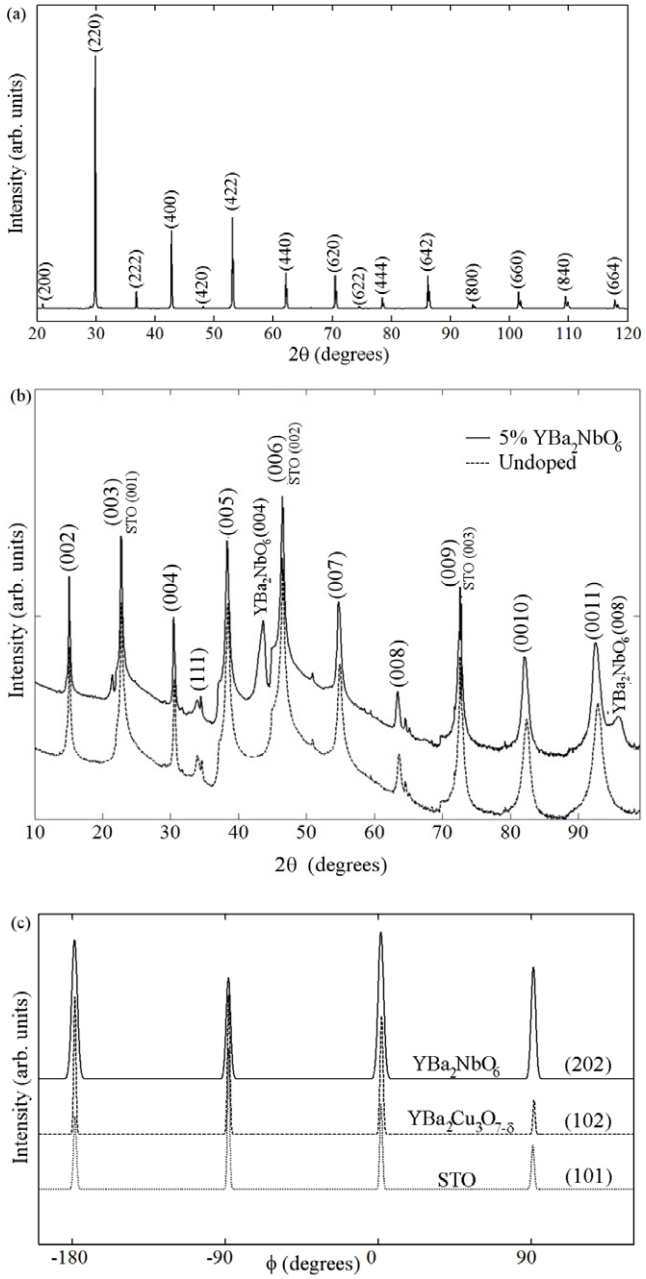

Figure 1. X-ray diffraction data for YBa_2NbO_6 in the form of pure precursor powder and when embedded within YBCO films. (a) X-ray diffraction spectrum of YBa_2NbO_6 powder reacted at 1450 °C. (b) X-ray diffraction data for undoped $YBa_2Cu_3O_{7-\delta}$ and a 5 mol% YBa_2NbO_6 doped film grown on $SrTiO_3$; (c) ϕ scan of (101) $SrTiO_3$, (102) YBCO, (202) YBa_2NbO_6 from a 5 mol% YBa_2NbO_6 doped film.

In the doped film all the (00*l*) peaks from the YBa_2NbO_6 are shifted to higher angles compared to the bulk values giving a lattice parameter of 0.830 nm ± 0.001 nm compared to the bulk value of 0.844 nm ± 0.001 nm. Hence, there is a compressive strain of 1.7% along the *c*-axis, much lower than the theoretical value of 8.34% assuming the YBCO lattice is not distorted (table 1). The YBCO (00*l*) peaks are shifted to in the opposite direction to the YBa_2NbO_6 peaks, i.e. to lower angles, and the '*c*'-axis is extended to a value of 11.73 Å giving

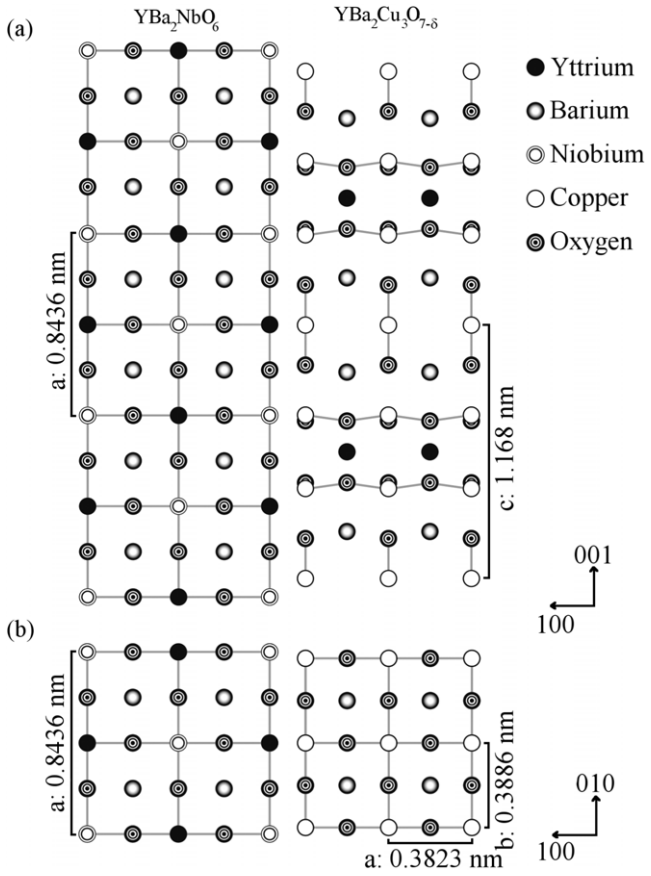

Figure 2. Crystallographic matching of YBCO with YBa_2NbO_6. (a) *b*-axis view and (b) *c*-axis view.

a tensile strain of 0.4%. The extended *c*-axis is not likely to arise from reduced oxygen content since the sample T_c is not reduced, as shown later. The *overall* strain is lower than the theoretical value and indicates partial strain relief by formation of misfit dislocations. Dislocation formation has previously been reported in BZO doped YBCO [17]. Nevertheless, the fact that the YBCO is locally partially strained in tension gives the possibility of additional pinning from strain fields in the vicinity of the YBCO/YBa_2NbO_6 interfacial regions.

To assess the *in-plane* texture, phi scans were recorded as shown in figure 1(c). The (202) YBa_2NbO_6 peaks reveal in-plane alignment and match both the (101) STO and (102) YBCO peaks, confirming that the perovskite particles have grown aligned 'cube on cube' with the YBCO. These results combined with the out-of-plane x-ray data suggest full heteroepitaxy between the YBCO, YBa_2NbO_6 and the substrate.

The cube-on-cube in-plane orientation determined from the phi scan is represented in the crystallographic model of figure 2(b). Looking down the $[001]_{YBCO}$ direction, 1 unit cell of YBa_2NbO_6 matches 2 unit cells of YBCO giving an in-plane lattice mismatch (*a* and *b* average) strain of +9.42%. The lattice mismatch of YBa_2NbO_6 with YBCO is larger than other widely studied pinning phases additions (table 1). This large mismatch should be beneficial for low field (<1 T, 77 K) pinning due the localized strain fields that will

arise [30] but likely produces shorter and wider self-assembled columnar array, contrasting with tantalate columns where the lattice mismatch is very small and long, narrow columns are produced [13]. They are more similar to $BaZrO_3$ nanorods which have similar lattice mismatch with YBCO [17, 31]. The next basic research challenges to be addressed for niobate pinning additions to YBCO are (a) determining the optimum level of niobate addition, (b) tuning the column sizes and distributions.

Cross-section transmission electron micrographs of a 5 mol% YBa_2NbO_6 doped sample (figures 3(a) and (b)) show nanorods aligned along the *c*-axis of the YBCO. The rods are 10–15 nm in diameter and their spacing is roughly 40 nm, giving a matching field of 1.3 T. Some random particles were also observed as indicated by the white arrows drawn along the *ab* planes. The inset to figure 3(a) shows a selected area diffraction pattern of a region around the nanoparticles. A set of streaky diffraction dots for (004) YBa_2NbO_6 is observed. Streaky dots rather than clearly distinguished spots has been reported in similar systems previously [33] and is an indication of a large YBCO *c*-plane distortion created by the YBa_2NbO_6 nanorod additions. $d(004)$ estimated from the diffraction pattern is ∼0.214 nm, indicating $a \sim 0.856$ nm, broadly consistent with the x-ray measurements.

Figure 3(b) shows a higher magnification image revealing fringes arising from the lattice mismatch between the YBa_2NbO_6 and YBCO lattices. Since a relatively slow growth rate, 5 Hz, was used, the appearance of both self-assembled columns and random particles are anticipated, similar to the case of $RETa_3O_7$ additions [32]. The rods are wider (up 15 nm as opposed to 5 nm) and shorter (∼100 nm as opposed to the whole film thickness) than tantalate rods, most likely because of the large mismatch strain which enhances the self-assembly kinetics [13].

At the interface between the film and substrate, a dark layer (about 10–20 nm thick) is observed which clearly shows different contrast than the rest of the film. This is in agreement with previous observations of asymmetric in-plane J_c seen in YBCO + $RETa_3O_7$ films arising from interface disorder [34]. It is not clear if the nanorods nucleated within this darker layer or on the substrate surface.

An atomic force micrograph of the film surface (figure 3(c)) shows superficial particles ∼15–20 nm in diameter uniformly distributed over the surface. These particles are consistent with the nanorods terminating at the sample surface. The size of the particles observed with the AFM is larger than the rods observed with the TEM. This could be due to the fact that we are observing the surface where there is higher mobility and possible agglomeration of surface particles immediately after the growth is terminated.

Despite the 5 mol% doping level and the large lattice mismatch between the phases, only a minimal reduction of the transition temperature is observed (figure 4(a)), with a transition temperature of 89 K. This value indicates that the Nb does not poison the YBCO, but remains 'locked' in the second phase. In addition, the 0.4% strain level measured in the YBCO does not lead to any significant T_c reduction. Similar T_c reductions were also observed in ∼5 mol% BZO doped

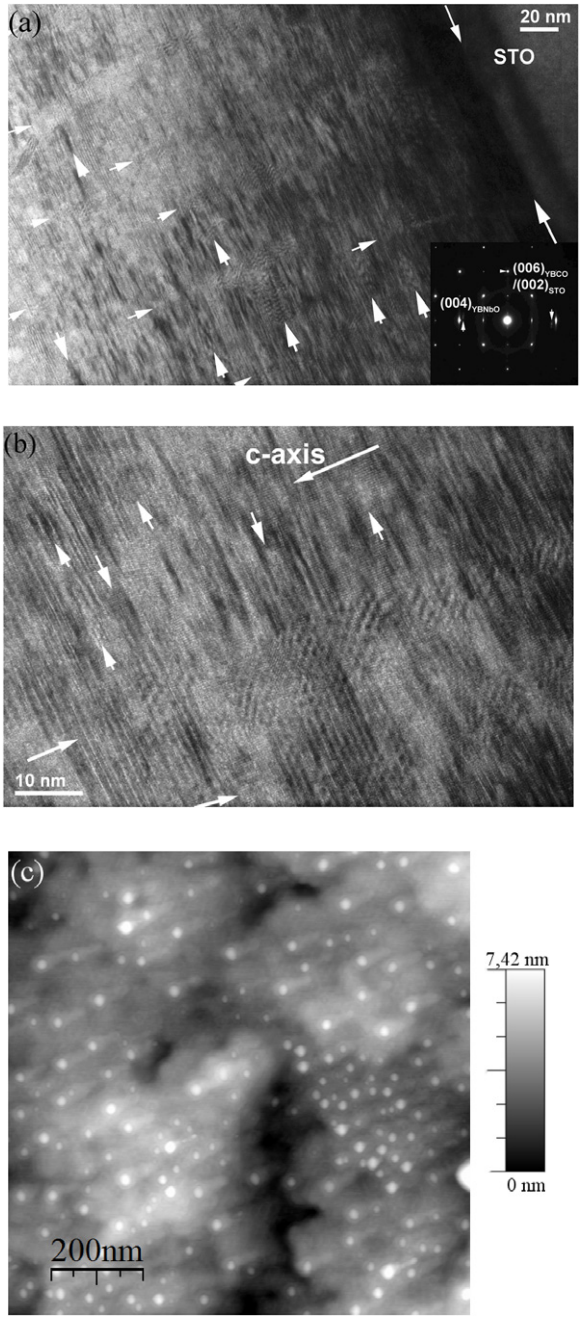

Figure 3. Microstructures of YBCO + 5 mol%YBa_2NbO_6 films. (a) and (b) TEM cross-sectional images (lower and higher magnifications, respectively). White arrows in the direction of the *c*-axis mark the positions of self-assembled nanorods along *c*. White arrows perpendicular to the *c*-axis indicate the positions of random nanoparticles as well as the interface between the substrate and the film. Inset to (a) shows selected area diffraction pattern of region in vicinity of nanoparticles. Moire fringes arising from lattice mismatch between YBa_2NbO_6 and YBCO are observed in (b); (c) AFM image showing nanoparticles at the surface.

systems [13]. However, in this case, since we are forming a double perovskite instead of a single perovskite as for BZO, the same mol% addition of double perovskite yields *twice* the volume of inclusions as the single perovskite. Hence, the small T_c reduction is, in fact, less than might be expected. J_c versus magnetic field measurements up to 1 T ($H \parallel c$) at

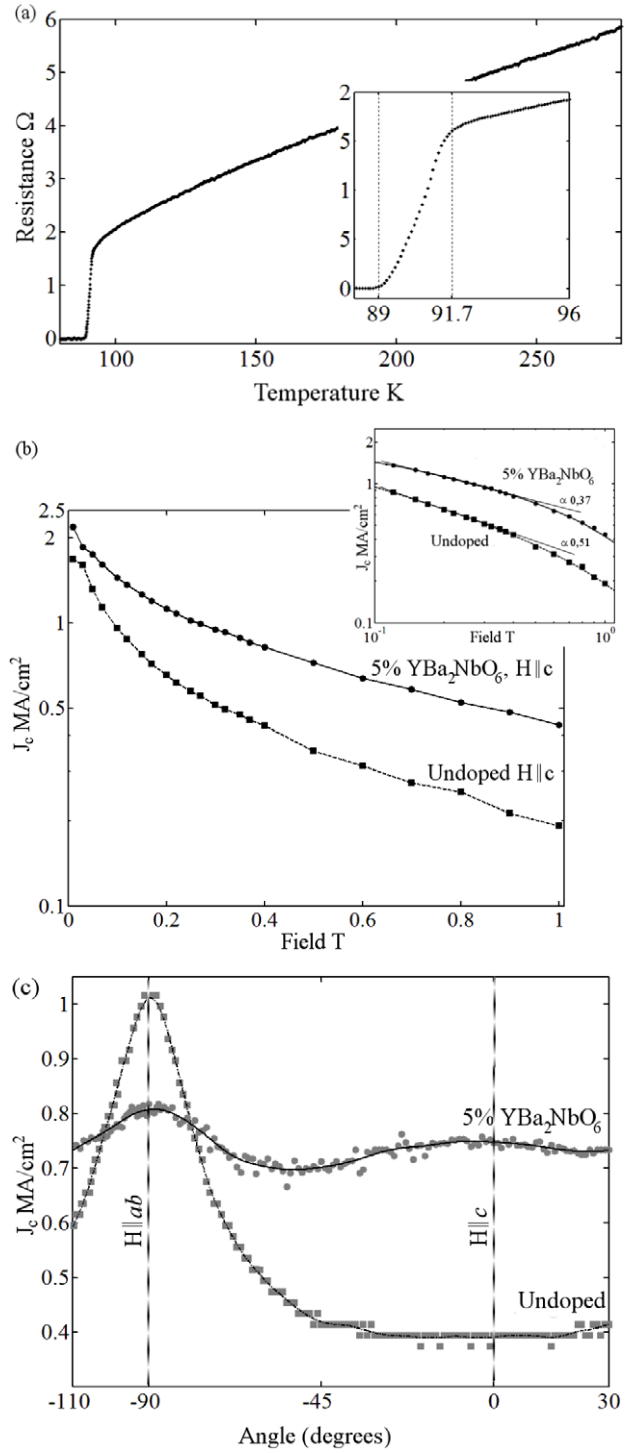

Figure 4. Transport properties of 0.5 μm micron thick YBCO + 5 mol%YBa_2NbO_6 films on STO. (a) Resistance versus temperature for a thin film doped with 5 mol% YBa_2NbO_6. Inset shows magnified region of the superconducting transition; (b) critical current density versus applied magnetic field at 77 K, $H \parallel c$. Inset shows data on log–log axis; (c) angular dependence of the critical current density at 77 K, 0.5 T.

77 K (figure 4(b), with log–log plot shown inset) indicates that the doped sample has better performance over the whole field regime analysed, with J_c of the doped sample being by a factor of ∼2 higher at 1 T.

The improved angular dependence of J_c in the YBa_2NbO_6 doped sample compared with pure YBCO, measured at 0.5 T and 77 K, is shown in figure 4(c). The doped sample shows a reduced anisotropy compared with the pure YBCO. This lower anisotropy results from the increased J_c when the field is aligned with the YBa_2NbO_6 nanorods. The *ab* peak is depressed somewhat presumably by the interruption of the intrinsic layer pinning by the highly continuous niobate nanorods. Compared with the typical shape of the angular dependence of pinning enhanced YBCO, for example in YBCO + BZO and YBCO + RTO, the YBa_2NbO_6 nanorods produce a very broad '*c*'-axis peak which make the particles effective over a relatively large angular range. The large breadth of the peak is possibly related to the large mismatch strain which produces relatively short and wide rods (figure 3). A significant fraction of random isotropic pinning which would improve J_c for all angles but have little effect on the shape of the angular dependence of J_c with magnetic field does not seem to be present as the *ab* peak is lower in the doped sample than in the pure YBCO.

In conclusion a new pinning additive, the double perovskite YBa_2NbO_6, was used to produce self-assembled non-superconducting nanorods within YBCO thin films. Additional flux pinning was observed not only when the magnetic field was aligned along the *c*-axis but also over a relatively large angular range. Improvements in J_c of a factor ∼2 at 1 T at 77 K were measured. The minimal poisoning and potential for high tunability of YBa_2NbO_6 puts it in a similar category to RE_3TaO_7 pinning additions (which has distinct advantages to BZO). The higher lattice mismatch of YBa_2NbO_6 with YBCO also gives potential to induce extra pinning from strain effects. Further optimization of growth conditions starting from our preliminary results will almost certainly lead to further enhancements of critical current density.

Acknowledgments

The work was supported by the European Commission as part of NESPA, Nano-Engineered Superconductors for Power Application, a framework of the Marie Curie Research Training Network, funded within the EU's 6th framework programme. JLM-D acknowledges support from the Marie Curie Excellence Grant 'NanoFen', (MEXT-CT-2004-014156), and HW acknowledge support from the US NSF (DMR-0709831).

References

[1] Civale L *et al* 1990 *Phys. Rev. Lett.* **65** 1164
[2] Civale L *et al* 1991 *Phys. Rev. Lett.* **67** 648
[3] Konczykowski M *et al* 1991 *Phys. Rev.* **44** 7167
[4] Kim D H *et al* 1997 *IEEE Trans. Appl. Supercond.* **7** 1997
[5] Puig T *et al* 2008 *Supercond. Sci. Technol.* **21** 034008
[6] Sparing M *et al* 2007 *Supercond. Sci. Technol.* **20** S239–46
[7] Maiorov B *et al* 2007 *Supercond. Sci. Technol.* **20** S223–9
[8] Kursumovic A *et al* 2009 *Supercond. Sci. Technol.* **22** 015009
[9] Driscoll J *et al* 2006 *US Patent Specification* 0025310
[10] MacManus-Driscoll J L *et al* 2004 *Nat. Mater.* **3** 439
[11] Mele P *et al* 2008 *Supercond. Sci. Technol.* **21** 015019

[12] Mairov B *et al* 2009 *Nat. Mater.* **8** 398
[13] Harrington S A *et al* 2009 *Supercond. Sci. Technol.* **22** 022001
[14] Strukova G K *et al* 1993 *Supercond. Sci. Technol.* **6** 589
[15] Strukova G K *et al* 1996 *Physica* C **267** 67
[16] Pillai C G S and George A M 1992 *J. Mater. Sci. Lett.* **11** 1639
[17] Goyal A *et al* 2005 *Supercond. Sci. Technol.* **18** 1533
[18] Kuwabara M and Kusaka N 1988 *Japan. J. Appl. Phys.* **27** L1504
[19] Paulose K V *et al* 1992 *Physica* C **193** 273
[20] Sathiraju S *et al* 2005 *IEEE Trans. Appl. Supercond.* **15** 3009
[21] Grekhov I *et al* 1997 *Physica* C **276** 18
[22] Brandle C D and Fratello V J 1990 *J. Mater. Res.* **5** 2160
[23] Koshy J *et al* 1999 *Bull. Mater. Sci.* **22** 243
[24] Aguiar J A *et al* 1998 *Physica* C **307** 189
[25] Aguiar J A *et al* 1997 *Phys. Rev.* **58** 2454
[26] Rager J *et al* 2004 *J. Am. Ceram. Soc.* **87** 1330
[27] Jia J-H *et al* 1995 *Mod. Phys. Lett.* **9** 439
[28] Vlakhov E *et al* 1997 *J. Mater. Sci. Lett.* **16** 763
[29] Barnes P W *et al* 2006 *Acta Crystallogr.* B **62** 384
[30] MacManus-Driscoll J L *et al* 2004 *Appl. Phys. Lett.* **84** 5329
[31] Li J *et al* 2006 *Microsc. Microanal.* **12** 566
[32] Harrington S *et al* 2010 *Nanotechnology* accepted
[33] Yamada K *et al* 2008 *Appl. Phys. Lett.* **92** 112503
[34] Harrington S *et al* 2009 *Appl. Phys. Lett.* **95** 022518

Supercond. Sci. Technol. **23** (2010) 034009 (5pp) doi:10.1088/0953-2048/23/3/034009

High current, low cost YBCO conductors—what's next?

J L MacManus-Driscoll[1], S A Harrington[1], J H Durrell[1], G Ercolano[1], H Wang[2], J H Lee[2], C F Tsai[2], B Maiorov[3], A Kursumovic[1] and S C Wimbush[1]

[1] Department of Materials Science and Metallurgy, University of Cambridge, Pembroke Street, Cambridge CB2 3QZ, UK
[2] Department of Electrical and Computer Engineering, Texas A&M University, College Station, TX 77843, USA
[3] MPA-STC, Los Alamos National Laboratory, Los Alamos, NM 87545, USA

E-mail: jld35@cam.ac.uk

Received 12 November 2009, in final form 1 December 2009
Published 22 February 2010
Online at stacks.iop.org/SUST/23/034009

Abstract
The Holy Grail for high temperature superconducting conductors is achieving high current material in a simple and cost-effective way. The current status is encouraging but even after more than twenty years of intense worldwide research, there are still many new avenues to be explored. Innovative functional oxide materials science is central to future progress. This paper discusses three key areas of our research focusing on new directions: highly tailored flux pinning using the new core pinning additives R_3TaO_7 and RBa_2NbO_6 for control of nanostructure formation; pinning using magnetic phase additives such as $RFeO_3$ with the potential for a magnetic contribution to the flux pinning; and the use of liquid assisted growth enabling very high growth rates leading to thick films with no critical current degradation.

1. Introduction

Over the last decade, progress in the manufacture of high quality, long length, high current coated conductors based on the second generation superconducting material $YBa_2Cu_3O_{7-\delta}$ (YBCO) for a variety of transport and magnetic applications has been impressive [1]. In particular, in just the past few years, great progress has been made with practical flux pinning approaches [2, 3]. There has also been some success in minimizing the complicated series of buffer and seed layers required between metal substrate and YBCO coating [4]. Less attention has been paid to exploring radical new routes to forming conductors by fast, more cost-effective routes. Of course, the weak link problem of YBCO grains [5] means that high angle grain boundaries need to be circumvented and this is no mean feat. The future for coated conductors will involve attaining the required performance at minimal cost. Approaches involving both optimization and further scaling up of the current processing routes as well as exploring new horizons for achieving higher performance by more scalable routes are required.

The areas which we believe represent new frontiers and could ultimately lead to a step-change include highly tailored core pinning, practical magnetic pinning, and the use of rapid liquid assisted growth [6].

2. Experimental details

Composite deposition targets were prepared in-house from commercial $YBa_2Cu_3O_x$ powder (SCI Engineered Materials, 99.99%) together with the appropriate additives of R_2O_3 and Ta_2O_5 (for R_3TaO_7 where R is a rare earth) or Y_2O_3, $BaCO_3$ and Nb_2O_5 (for YBa_2NbO_6) or Y_2O_3 and FeO (for $YFeO_3$). Targets of varying compositions from 0.5 to 10 mol% were prepared by mixing, pressing and sintering at 985 °C in flowing oxygen for 12–24 h. A pure YBCO target was also prepared under the same conditions for control purposes.

The substrates used were single crystal $SrTiO_3$(001) or buffered metallic tapes (~150 nm $La_2Zr_2O_7$ grown on RABiTS Ni–W by dip coating and *ex situ* processing [7]). Samples were grown in a deposition atmosphere of 30 Pa of flowing oxygen at either 760–795 °C by standard pulsed laser deposition (PLD) or at 815 °C by PLD incorporating hybrid liquid phase epitaxy (HLPE). In the HLPE process, a sub-micron thick BaO–CuO liquid layer is first deposited and

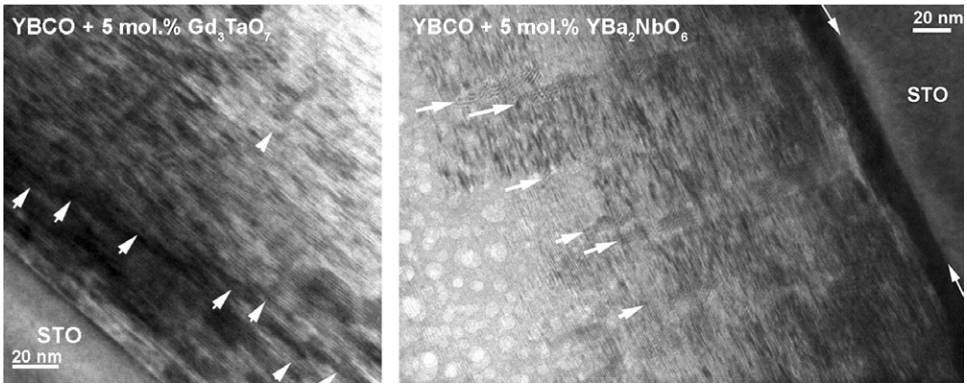

Figure 1. Cross-sectional TEM of films of YBCO + 5 mol% Gd_3TaO_7 and YBCO + 5 mol% YBa_2NbO_6 pinning additions grown under similar conditions, namely 770 °C and 790 °C respectively at 5 Hz on $SrTiO_3$. Self-assembled nanocolumns of the respective pinning addition are indicated with arrows.

growth of the YBCO occurs under this layer [8]. Subsequent to deposition, all samples were annealed *in situ* in a static oxygen pressure of 50 kPa to achieve optimum oxygenation. Film thicknesses were typically in the range 0.5–2.5 μm.

Films were structurally characterized by x-ray diffraction (XRD) and transmission electron microscopy (TEM). Magnetic properties were measured in a cryogenic vibrating sample magnetometer (VSM) equipped with a 1 T electromagnet. Electrical properties were measured by a standard four-probe technique in an 8 T superconducting magnet following photolithographic patterning and ion beam etching to form bridge structures of typically 50–125 μm width and 1 mm length. For angular measurements of the critical current density, J_c, the field was applied in the maximum Lorentz force configuration and rotated from normal to the film surface ($\theta = 0°$) to parallel to it ($\theta = 90°$).

3. Results

3.1. Core pinning

Several new approaches to the enhancement of core pinning in YBCO through the incorporation of novel nanostructural inclusions have been tested and developed. The most widely studied and successful method so far involves incorporation of $BaZrO_3$ nanoparticles but there are many other additions which are also effective [9]. The current research focus should now be on tailoring nanopinning additions to achieve desired and controlled arrays, the optimal array (whether it be random, correlated or a combination of both geometries) being dependent on the application field and temperature, and the growth method to be used. In order to nanoengineer the materials, the kinetics and thermodynamics of phase formation of the particular phase(s) formed when additions are made to YBCO films needs to be understood. The mechanism of formation of the nanostructured inclusions depends on the lattice mismatch with the YBCO and the kinetics of self-assembly (mobility of the constituent ions) which depend on the growth temperature relative to the melting point of the phase, but is also readily controllable by PLD by altering the growth rate.

Table 1. Pinning ion additions made to YBCO films, stable phases formed, and lattice misfits to YBCO.

Pinning ion addition	Stable phase in YBCO film	Misfit to YBCO *ab*	Misfit to YBCO *c*
Ta^{5+}	Yb_3TaO_7	−4.8%[a]	−10.9%
Ta^{5+}	Gd_3TaO_7	−2.4%[a]	−8.7%
Zr^{4+}	$BaZrO_3$	+8.4%[b]	+7.5%
Nb^{5+}	YBa_2NbO_6	+9.3%[b]	+8.5%

[a] Rotated 45° to cube-on-cube.
[b] Cube-on-cube.

With the knowledge that Group IV and Group V ions do not readily substitute into the YBCO lattice, but instead form stable heteroepitaxial second phases [10], we have investigated Ta^{5+} and Nb^{5+} additions to YBCO films [11–13] in the form of Yb_3TaO_7 ($a = 1.039$ nm), Gd_3TaO_7 ($a = 1.065$ nm) and YBa_2NbO_6 ($a = 0.8436$ nm), as alternatives to the common Zr^{4+} ion addition in the form of $BaZrO_3$ ($a = 0.4181$ nm). The lattice mismatches of each of these phases to YBCO ($a = 0.3828$ nm, $b = 0.3887$ nm, $c = 1.1665$ nm), calculated from the bulk lattice parameters, for the most promising core pinning additions we have developed are shown in table 1.

Figure 1 compares TEM images of nanocolumns of Gd_3TaO_7 and YBa_2NbO_6, showing Gd_3TaO_7 nanocolumns to be straighter and more continuous than YBa_2NbO_6 nanocolumns. If we also consider the known form of $BaZrO_3$ nanocolumns [14], we find that lattice misfit and nanocolumn size and perfection are interrelated, the finest and most continuous columns arising from lower in-plane lattice misfit to YBCO [11].

Angular critical current measurements of so far optimized R_3TaO_7-added samples show the superior flux pinning obtained with these additives compared to pure films. By growing under conditions which produce a composite random nanoparticle/correlated nanocolumn microstructure, J_c values of 1.1 MA cm^{-2} at 1 T (figure 2(a)) and 0.7 MA cm^{-2} at 3 T were obtained compared to 0.2 MA cm^{-2} and 0.04 MA cm^{-2} at the same fields for pure YBCO (all at 77 K, $H \parallel c$). The YBa_2NbO_6-added samples generally show broader *c*-axis peaks which are consistent with the more discontinuous columns obtained (figure 2(b)).

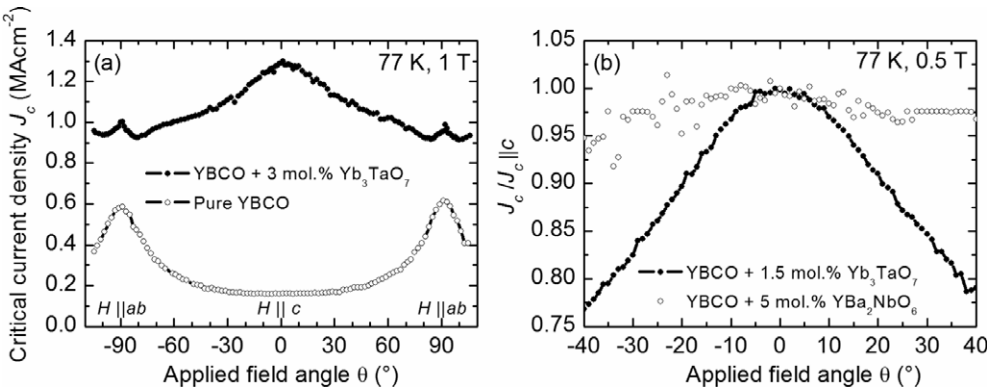

Figure 2. Angular J_c data at 77 K for 0.5 μm thick YBCO films with additions of Yb_3TaO_7 or YBa_2NbO_6. (a) Data at 1 T for 5 mol% Yb_3TaO_7 additions compared to pure YBCO showing a large enhancement in J_c, particularly for fields applied in the c direction. (b) Data at 0.5 T comparing 1.5 mol% Yb_3TaO_7 and 5 mol% YBa_2NbO_6 additions normalized to $J_c \parallel c$ in order to emphasize the broader c-axis peak obtained for YBa_2NbO_6.

3.2. Pinning by magnetic phase additions

In practical high temperature superconductors, even with the introduction of artificial pinning centres, the self-field J_c is still 5–10 times lower than the theoretical limit. The realizable advantages of magnetic pinning over 'standard' non-magnetic pinning originate from the additional magnetic interaction that this provides [15]. Whereas normal materials interact with the superconducting order parameter via the coherence length ξ (on the order of nanometres in the high-T_c materials), magnetic materials have a potential interaction over length scales of the penetration depth λ which is much larger (hundreds of nanometres). This larger interaction volume implies that a lower density of pinning centres will be required to achieve effective pinning and that consequently the disruption to the superconducting phase (and its resultant properties) will be minimized. Beyond the basic studies of magnetic pinning [16–18], the main hurdle to overcome is to introduce magnetic material in such a way as to avoid significant 'poisoning' of the superconducting phase. This requires forming very stable second phases that effectively 'lock away' the magnetic ion addition while remaining magnetic themselves. Our exploratory studies [19] have indicated $YFeO_3$ to be a suitable addition. $YFeO_3$ belongs to the family of rare earth orthoferrites, $RFeO_3$, which exhibit weak ferromagnetism as a result of a slight canting of their predominantly antiferromagnetically coupled Fe^{3+} moments [20]. Their structure is that of four distorted perovskite units assembled into an orthorhombic unit cell (a = 0.5282 nm, b = 0.5596 nm, c = 0.7605 nm) [21], thereby suggesting a high likelihood of structural compatibility with YBCO.

There is no measurable reduction in the superconducting critical temperature T_c for a 1 mol% $YFeO_3$ addition [22, 23], indicating an effective segregation of the magnetic species. Randomly dispersed magnetic nanoparticles of sub-5 nm size (upper right panel of figure 3) were observed leading to a 2–3 times increase in J_c at self-field and a 10 times increase at 6 T compared to pure YBCO. Increasing the dopant amount leads to a slight suppression of T_c and consequent reduction in the J_c enhancement. The particles have a good in-plane lattice parameter match to YBCO resulting in a strain of just 0.12% in-plane (for a 45° in-plane rotation of the $YFeO_3$ unit cell relative to the YBCO) and 2.4% out-of-plane. The coercivity $\mu_0 H_c$ is found to be rather small at around 6 mT (lower right panel of figure 3), due to the small particle size causing a superparamagnetic response at the temperatures of interest, and the measured saturation field is around 0.2 T. The random particle arrangement results in random pinning producing an upwards shift in J_c for all field angles (figure 3).

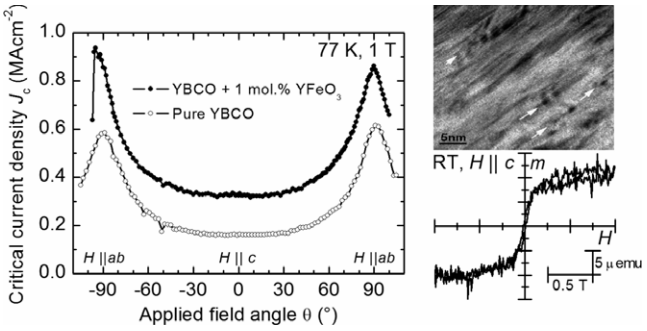

Figure 3. Angular J_c measurements at 77 K, 1 T of a 1 μm thick film of YBCO with 1 mol% $YFeO_3$ additions compared with a control sample of pure YBCO. Upper right panel shows a cross-sectional TEM image of a 1 mol% magnetically doped film, with arrows indicating the positions of several sub-5 nm dopant nanoparticles. Lower right panel is the room temperature (RT) magnetic hysteresis loop (magnetic moment m versus applied field H) of a sample with 5 mol% $YFeO_3$ additions.

3.3. Rapid, innovative growth of coated conductors

Rapid liquid assisted growth of YBCO + 5 mol% $BaZrO_3$ coated conductors was achieved on metallic substrates by HLPE. Samples of two different thicknesses were grown in 4 min (1 μm film) and 10 min (2.5 μm film). The XRD rocking curves of the (004) peak of the $La_2Zr_2O_7$ buffer gave a rolling direction FWHM of 5.4° and a perpendicular direction FWHM of 9.1°. The XRD rocking curves for the

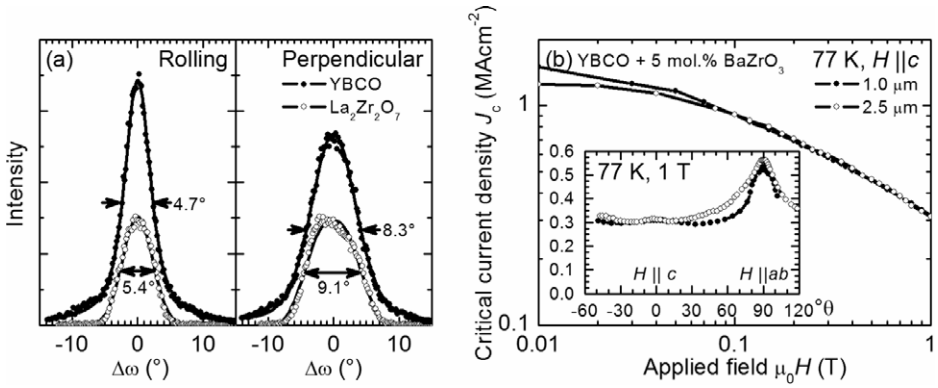

Figure 4. Characterization of coated conductors of YBCO + 5 mol% $BaZrO_3$ grown by HLPE on ∼100 nm dip-coated $La_2Zr_2O_7$-buffered RABiTS Ni-W. (a) X-ray rocking curves of YBCO layer and $La_2Zr_2O_7$ buffer layer, and (b) J_c as a function of field applied parallel to *c* and (inset) as a function of applied field angle θ at 1 T.

(005) peak of the YBCO layer grown on the buffer by HLPE are improved over the buffer by approximately 0.7° in each case, to 4.7° and 8.3°, respectively (figure 4(a)). Transport measurements (figure 4(b)) show that high J_c material can be achieved on a rapidly grown, dip-coated buffer and that there is no degradation in the J_c of the superconductor with thickness. Hence, it is relatively easy to grow 5 μm thick material *in situ* in under 20 min and still achieve self-field J_cs of around 1 MA cm^{-2}. The several advantages of the HLPE method can be summarized as follows: (a) the film texture is improved over the substrate and so the method allows for the use of much cheaper, rapidly grown substrate-buffer materials; (b) the growth rate is several times faster than standard methods; (c) there is no degradation in J_c with thickness. Finally, we note that for a given I_c, a potential advantage in being able to grow thick material having a moderate J_c over thinner material with higher J_c is that preliminary investigations indicate that flux creep rates are lower in thicker material [24].

4. Conclusions

There are several potential new avenues to be explored for achieving low cost, high performance superconducting conductors. Highly tailored core pinning, practical magnetic pinning, and rapid liquid assisted growth are key areas. Phases formed from Group IV and V ion additions are ideal for achieving strong, tunable core pinning. The strain between the particles and the YBCO matrix influences the form of their distribution which directly impacts on the field and temperature dependent pinning behaviour. The main challenge for practical magnetic pinning is to form stable, non-poisoning phases. $YFeO_3$ is one such phase and has been shown to enhance pinning at low (1 mol%) levels. Finally, rapid, easy growth of thick YBCO by HLPE on ∼100 nm dip-coated $La_2Zr_2O_7$-buffered RABiTS Ni–W gives conductors with $I_c > 250$ A grown in a matter of minutes.

Acknowledgments

This work has been supported by the European Commission (Marie Curie Excellence Grant 'NanoFen', MEXT-CT-2004-014156), the UK EPSRC ('Novel materials nanoengineering for enhanced performance of superconducting coated conductors and functional oxides'), and the EU RTN 'NESPA'. SAH is supported by the Mays Wild Research Fellowship of Downing College, Cambridge. SCW is supported by The Leverhulme Trust with supplementary funding from The Isaac Newton Trust.

References

[1] American Superconductor, Superpower, Southwire 2009 *USDOE High Temperature Superconductivity Program Peer Review (Alexandria, VA, Aug. 2009)* available at http://www.htspeerreview.com
[2] Yamada Y *et al* 2005 *Appl. Phys. Lett.* **87** 132502
[3] Kang S *et al* 2006 *Science* **311** 1911
[4] Stan L, Feldmann D M, Usov I O, Holesinger T G, Maiorov B, Civale L, DePaula R F, Dowden P C and Jia Q X 2009 *IEEE Trans. Appl. Supercond.* **19** 3459
[5] Dimos D, Chaudhari P and Mannhart J 1990 *Phys. Rev.* B **41** 4038
[6] Ohnishi T, Huh J-U, Hammond R H and Jo W 2004 *J. Mater. Res.* **19** 977
[7] University of Cambridge and Nexans SuperConductors GmbH, Chemiepark Knapsack, 50351 Hürth, Germany 2008 *European Patent Application* 201373
[8] Kursumovic A, Maiorov B, Durrell J H, Wang H, Zhou H, Stan L, Harrington S, Wimbush S, Holesinger T G and MacManus-Driscoll J L 2009 *Supercond. Sci. Technol.* **22** 015009
[9] Foltyn S R, Civale L, MacManus-Driscoll J L, Jia Q X, Maiorov B, Wang H and Maley M 2007 *Nat. Mater.* **6** 631
[10] Driscoll J L and Foltyn S R 2004 *US Patent Specifiation* 20060025310
[11] Harrington S A, Durrell J H, Maiorov B, Wang H, Wimbush S C, Kursumovic A, Lee J H and MacManus-Driscoll J L 2009 *Supercond. Sci. Technol.* **22** 022001
[12] Harrington S A, Durrell J H, Wang H, Wimbush S C, Tsai C F and MacManus-Driscoll J L 2009 *Nanotechnology* at press
[13] Ercolano G, Harrington S A, Wang H, Tsai C F and MacManus-Driscoll J L 2009 *Supercond. Sci. Technol.* at press
[14] Mele P, Matsumoto K, Horide T, Ichinose A, Mukaida M, Yoshida Y, Horii S and Kita R 2008 *Supercond. Sci. Technol.* **21** 032002
[15] Blamire M G, Dinner R B, Wimbush S C and MacManus-Driscoll J L 2009 *Supercond. Sci. Technol.* **22** 025017

[16] Jan D B, Coulter J Y, Hawley M E, Bulaevskii L N, Maley M P, Jia Q X, Maranville B B, Hellman F and Pan X Q 2003 *Appl. Phys. Lett.* **82** 778
[17] Lange M, Van Bael M J, Moshchalkov V V and Bruynseraede Y 2002 *Appl. Phys. Lett.* **81** 322
[18] Yang Z, Lange M, Volodin A, Szymczak R and Moshchalkov V V 2004 *Nat. Mater.* **3** 793
[19] Wimbush S C, Yu R, Bali R, Durrell J H and MacManus-Driscoll J L 2009 *Physica* C at press doi:10.1016/j.physc.2009.10.117
[20] Treves D 1962 *Phys. Rev.* **125** 1843
[21] Coppens P and Eibschütz M 1965 *Acta Crystallogr.* **19** 524 PDF 73-1345
[22] Wimbush S C, Durrell J H, Bali R, Yu R, Wang H, Harrington S A and MacManus-Driscoll J L 2009 *IEEE Trans. Appl. Supercond.* **19** 3148
[23] Wimbush S C, Durrell J H, Tsai C F, Wang H, Jia Q X, Blamire M G and MacManus-Driscoll J L 2009 *Supercond. Sci. Technol.* submitted
[24] Feldmann M, Holesinger T, Maiorov B and Civale L 2009 *Results presented at the USDOE High Temperature Superconductivity Program Peer Review (Alexandria, VA, Aug. 2009)* available at http://www.htspeerreview.com

State-of-the-art flux pinning in $YBa_2Cu_3O_{7-\delta}$ by the creation of highly linear, segmented nanorods of $Ba_2(Y/Gd)(Nb/Ta)O_6$ together with nanoparticles of $(Y/Gd)_2O_3$ and $(Y/Gd)Ba_2Cu_4O_8$

G. Ercolano[1], M. Bianchetti[1], S. C. Wimbush[1], S. A. Harrington[1], H. Wang[2], J. H. Lee[2] and J. L. MacManus-Driscoll[1]

[1]Department of Materials Science and Metallurgy, University of Cambridge, Pembroke Street, Cambridge CB2 3QZ, UK

[2]Department of Electrical and Computer Engineering, Texas A&M University, College Station, TX 77843, USA

E-mail: ge228@cam.ac.uk

Abstract. Self-assembled, segmented nanorods of *c*-axis aligned $Ba_2(Y/Gd)(Nb/Ta)O_6$ as well as randomly-distributed nanoparticles of $(Y/Gd)_2O_3$ and $(Y/Gd)Ba_2Cu_4O_8$ were grown into $YBa_2Cu_3O_{7-\delta}$ (YBCO) thin films by pulsed laser deposition. The complex pinning landscape proves to be extremely effective, particularly at higher fields where the segmented vortices yield a plateau in critical current density (J_c) with field angle around 60°. In 0.3 μm thick films, the J_c values are higher than 1 $MAcm^{-2}$ at 2.5 T ($H \| c$-axis). Owing to the combined interactions of the vortices with the different pinning centres, interesting new features are observed at high fields in the angle-dependence of J_c.

1. Introduction

Even though conductors based on $YBa_2Cu_3O_{7-\delta}$ (YBCO) have reached an extremely sophisticated stage of technological development with exemplary critical current performance arising from nanoengineering of pinning centres [1-8], since higher current conductors mean lower production costs, achieving even stronger flux pinning by simple means is still a highly sought-after goal.

Probably the most successful method for engineering flux pinning in YBCO is by the introduction of an epitaxial non-superconducting secondary phase, e.g. $BaZrO_3$ [9-11]. Ta and Nb additions to YBCO have more recently been studied based on the fact that they are highly charged (5+) ions that should perform in a similar way to Zr and not substitute into the YBCO lattice. Tantalate additions to YBCO produce excellent pinning performance via the formation of very fine, dense nanorods whose composition has been ascribed to either a defective pyrochlore, RE_3TaO_7 (RE = rare earth, Gd being the most widely studied) [12], or to the double perovskite, Ba_2YTaO_6 [13]. Niobate additions produce Ba_2RENbO_6 nanorods [14-17] which are similar to $BaZrO_3$ nanorods — wider, shorter and less linear than the tantalate rods [14] (diameter ~ 10–15 nm, splayed around the *c*-axis). The niobate rods remain highly effective pinning centres at low fields aligned along the *c*-axis, although considering the entire field range tantalate rods are superior overall.

Since the niobate and tantalate nanorods in YBCO are of rather different morphology and hence give different performance characteristics, it is interesting to consider whether addition of both of these second phases of the same overall level results in an averaging effect or whether further complexity is induced in the system, thereby yielding an entirely different pinning landscape. In fact, the situation is a mix of the former and the latter with the final result that the nanostructure created fortuitously yields an overall superior pinning performance, particularly at higher fields.

2. Experimental methods

Films were grown by pulsed laser ablation of a composite target of appropriate composition. Targets were prepared by mixing and grinding pure $YBa_2Cu_3O_{7-\delta}$ powder (SCI Engineered Materials 99.99%) with 2.5 mol% of Ba_2YNbO_6 powder and 2.5 mol% of Gd_3TaO_7. Ba_2YNbO_6 powder was produced by mixing and grinding stoichiometric quantities of 99.99% Y_2O_3, $Ba(NO_3)_2$ and Nb_2O_5 followed by solid state reaction at

1450°C for 24 h in flowing O_2. Gd_3TaO_7 was introduced in the target by adding the desired amount of 99.99% Gd_2O_3 and 99.99% Ta_2O_5 powders to the $YBa_2Cu_3O_{7-\delta}$ powder. The target mixture was pressed in a cylindrical die (diameter = 2 cm) and sintered at 950°C for 12 h in flowing O_2. Pulsed laser ablation was performed using a Lambda Physik KrF excimer laser (λ = 248 nm). The substrates were single crystal $SrTiO_3$ (100) held at 780°C, and the substrate temperature was monitored using a pyrometer. 4500 laser pulses at a 1 Hz repetition rate were used to produce 0.3 μm thick films. Films where post-annealed *in situ* at 520°C for 1 h in 500 mbar O_2 atmosphere.

Phase and orientation analysis were performed using x-ray diffraction. Cross sectional transmission electron microscopy (TEM) was used to determine the size, distribution and structure of the nanoparticles and nanorods. A conventional four-point electrical measurement on photolithographically patterned bridges of 50 μm width was used to determine the critical current density, J_c, using a 1 μVcm^{-1} criterion. The angular dependence of J_c was measured by rotating the applied magnetic field in a plane perpendicular to the current direction (maximum Lorentz force configuration).

3. Results and discussion

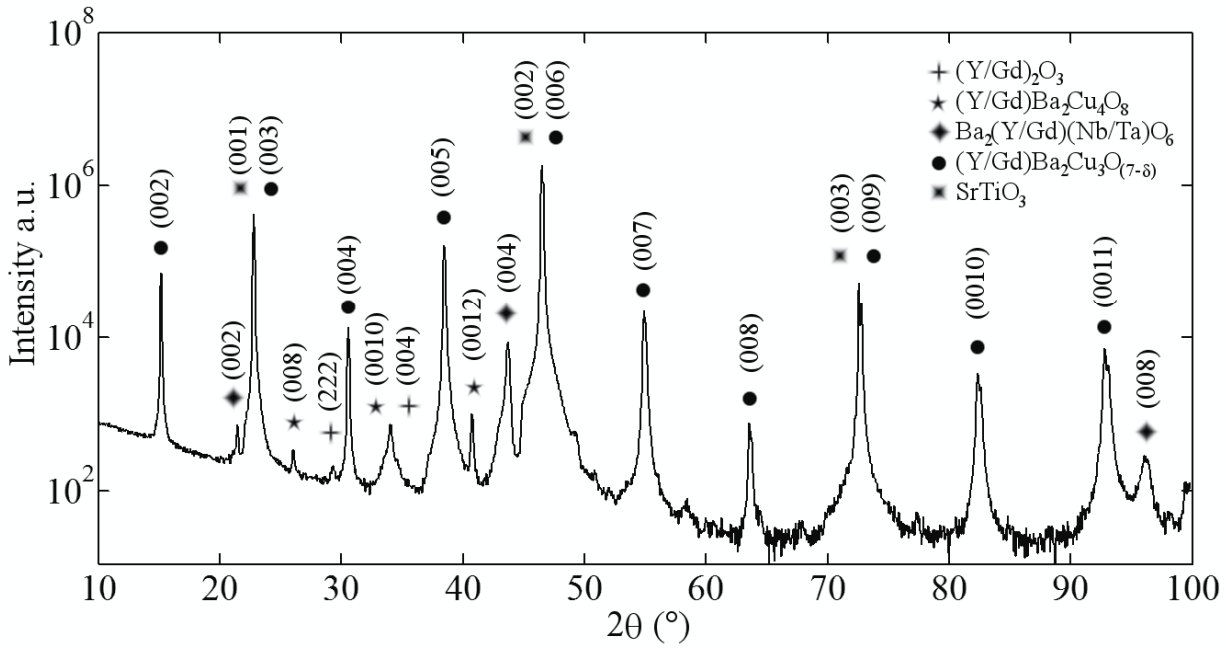

Figure 1. Bragg-Brentano scan of a $YBa_2Cu_3O_{7-\delta}$ + 2.5 mol% Gd_3TaO_7 + 2.5 mol% Ba_2YNbO_6 sample.

Figure 1 shows the x-ray diffraction pattern of a typical film. The (00*l*) peaks of YBCO as well as the (002) and (004) peaks of $Ba_2(Y/Gd)(Nb/Ta)O_6$ (2θ = 21.5°, 2θ = 43.2°) are labelled. A peak at 2θ = 33.3° is identified as the (004) peak of $(Y/Gd)_2O_3$. $(Y/Gd)Ba_2Cu_4O_8$ is also present as evidenced by the (008), (0010), and (0012) peaks (2θ = 25.9°, 2θ = 33.2°, 2θ = 41.4°).

A balanced chemical reaction consistent with the phases observed by XRD is shown below:

$$0.95\ YBa_2Cu_3O_{7-\delta} + 0.025\ Ba_2YNbO_6 + 0.025\ Gd_3TaO_7 \rightarrow 0.85\ (Y/Gd)Ba_2Cu_3O_{7-\delta} + 0.05\ Ba_2(Y/Gd)(Nb/Ta)O_6 + 0.0375\ (Y/Gd)_2O_3 + 0.075\ (Y/Gd)Ba_2Cu_4O_8$$

Gd and Y can easily cross-substitute for one another since they have similar ionic radii. For the same reason, Nb and Ta can also cross-substitute. This allows the double perovskite $Ba_2(Y/Gd)(Nb/Ta)O_6$ to grow within the $(Y/Gd)Ba_2Cu_3O_{7-\delta}$ lattice. Furthermore the excess Gd and the Ba deficiency produced by the $Gd_3TaO_7 \rightarrow Ba_2(Y/Gd)(Nb/Ta)O_6$ transformation together with the Gd ↔ Y cross-substitution is the origin of the $(Y/Gd)_2O_3$ and $(Y/Gd)Ba_2Cu_4O_8$ formation. The previously reported [12] Gd_3TaO_7 phase does not form here because in the presence of Nb the $Ba_2(Y/Gd)(Nb/Ta)O_6$ phase is more stable. $(Y/Gd)Ba_2Cu_4O_8$ forms

because of the barium deficiency in the Gd_3TaO_7 reactant. $YBa_2Cu_4O_8$ has previously been observed in coated conductors where there is barium deficiency owing to its depletion by reaction with CeO_2 [18]. Also $YBa_2Cu_4O_8$ has been reported in films grown by metal-organic deposition, where it is in the form of stacking fault defects [19].

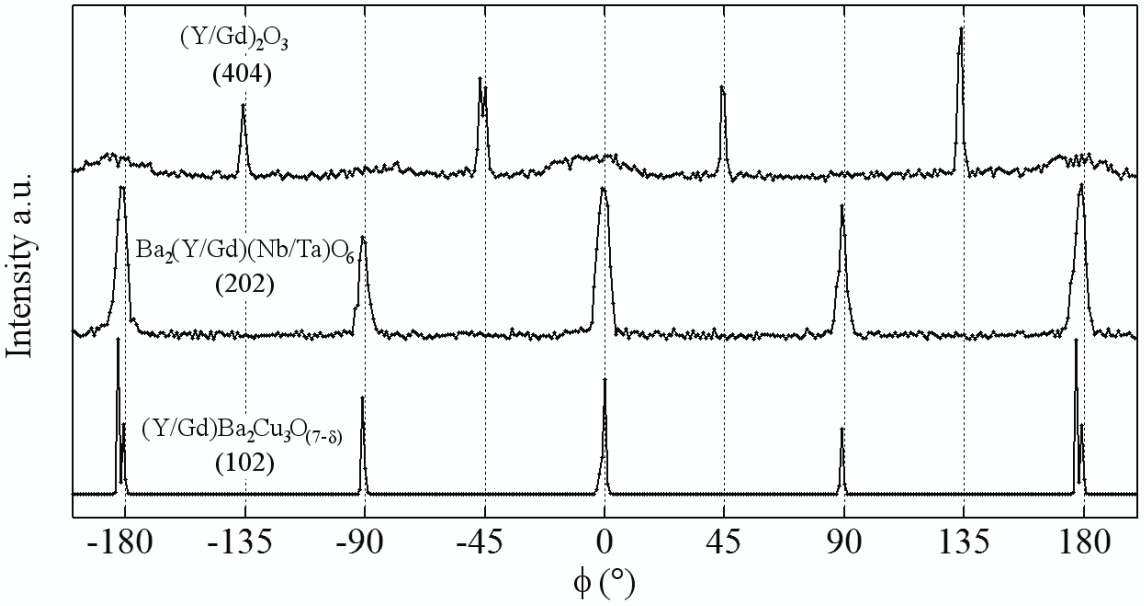

Figure 2. X-ray ϕ scans of the (202) $Ba_2(Y/Gd)(Nb/Ta)O_6$ and the (404) $(Y/Gd)_2O_3$ peaks from a $YBa_2Cu_3O_{7-\delta}$ + 2.5 mol% Gd_3TaO_7 + 2.5 mol% Ba_2YNbO_6 sample.

$Ba_2(Y/Gd)(Nb/Ta)O_6$ is aligned cube-on-cube with the $(Y/Gd)Ba_2Cu_3O_{(7-\delta)}$ as shown in the x-ray ϕ scans of figure 2. The $(Y/Gd)_2O_3$ is rotated both 45° in-plane, as previously reported [20] but also a few degrees away (with a broad range of angles) from the cube-on-cube orientation. These broader rotations are consistent with near coincidence site lattice matching to accommodate the very large strains and structural difference between $(Y/Gd)_2O_3$ and YBCO [21].

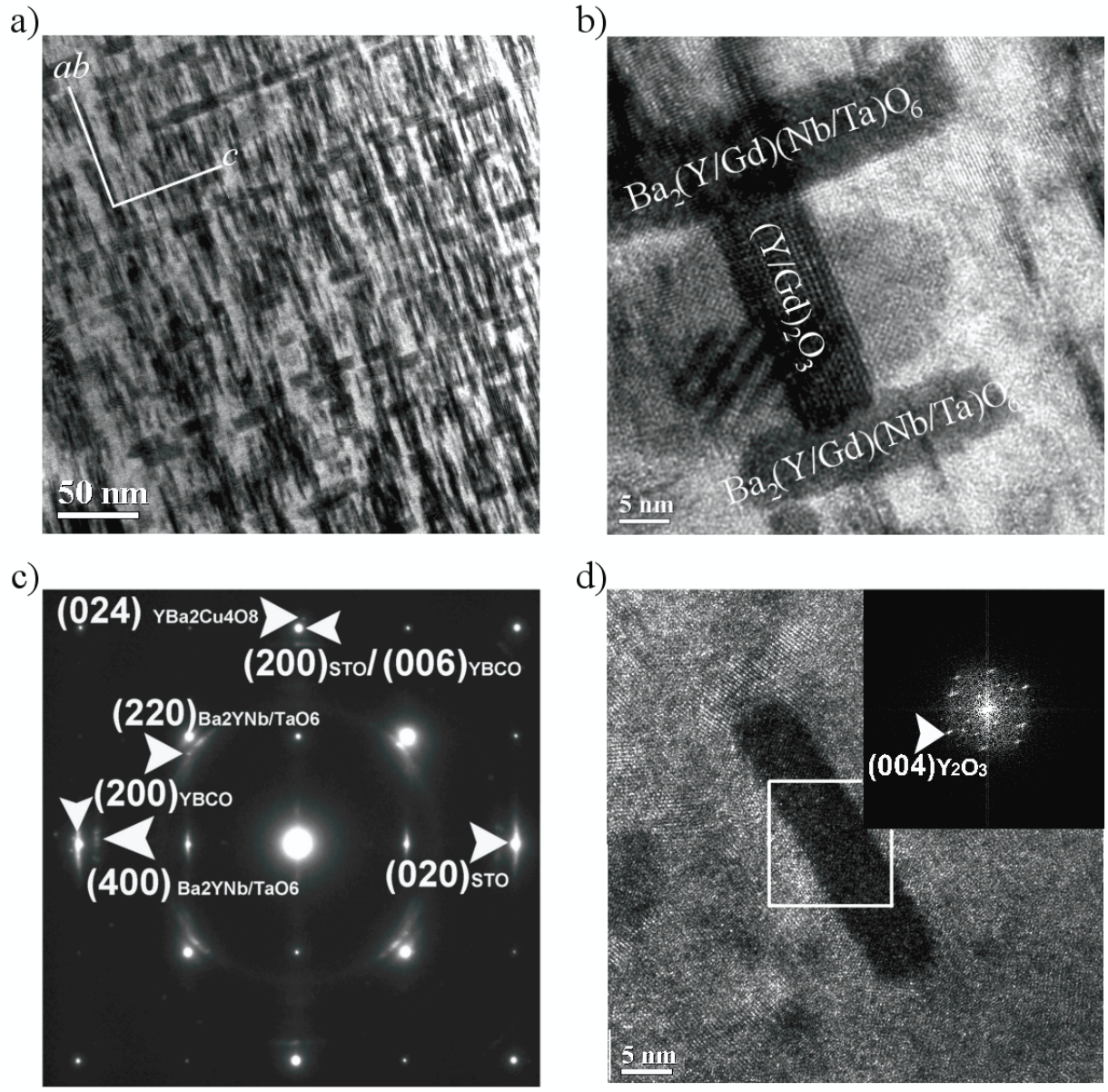

Figure 3. a) TEM image of the $YBa_2Cu_3O_{7-\delta}$ + 2.5 mol% Gd_3TaO_7 + 2.5 mol% Ba_2YNbO_6 sample cross section; b) TEM image of a plate-like nanoparticle nucleated between two rod segments; c) Selected area electron diffraction pattern of the image in (a); d) TEM image of a plate-like nanoparticles of $(Y/Gd)_2O_3$. Fourier transform of the image of particle.

TEM cross-sections show that there are at least two different nanoscale structural features present. Firstly, there is a set of *c*-axis aligned fine rods of ~7 nm in diameter, significantly smaller than the pure niobate rods of Ba_2YNbO_6 which are ~15 nm in diameter [14, 15], but larger than the pure tantalate rods of Gd_3TaO_7 which are ~5 nm in diameter [12]. Hence, the averaged growth kinetics of pure niobate and pure tantalate rods is obtained, as might be expected. Secondly, figure 3b shows a plate-like nanoparticle of RE_2O_3 nucleated along the *ab*-plane between two $Ba_2(Y/Gd)(Nb/Ta)O_6$ nanorods. Fig. 3c shows a selected area diffraction pattern of a region of the matrix and inclusions. $Ba_2(Y/Gd)(Nb/Ta)O_6$, $(Y/Gd)_2O_3$ and $YBa_2Cu_4O_8$ are present, consistent with the x-ray diffraction pattern of figure 1. A Fourier transform confirming the structure of a $(Y/Gd)_2O_3$ particle of 25 nm width is shown in figure 3d inset. Other particles of $(Y/Gd)_2O_3$ were observed to be in the 25 – 30 nm width range.

A fundamentally new structural feature, which has not been observed before, is the self-segmentation of the nanorods, yielding an average rod segment length of 30 nm. Kinetic effects of slower diffusion of the heavy Ta^{5+} ion compared to the Bb^{5+} ion may prevent rods from maintaining continuity as the film growth

progresses. Similar to $BaZrO_3$ and Ba_2YNbO_6 rods and because of the nucleation enhancing strain field generated within the YBCO, a new segment nucleates aligned along the *c*-axis with a segment below it [22]. The average rod length (30 nm) is shorter than both the continuous tantalate rod length (hundreds of nm) and the short niobate rods (~80-100 nm).

Despite the complexity of sample composition, the possibility of varying RE concentration across samples, as well as the three different nanoinclusion phases observed, no suppression of the superconducting transition temperature was observed. The T_c of ~ 89 K for all the samples indicates no substitution of Nb or Ta into the YBCO matrix, as might be expected for these higher valence ions.

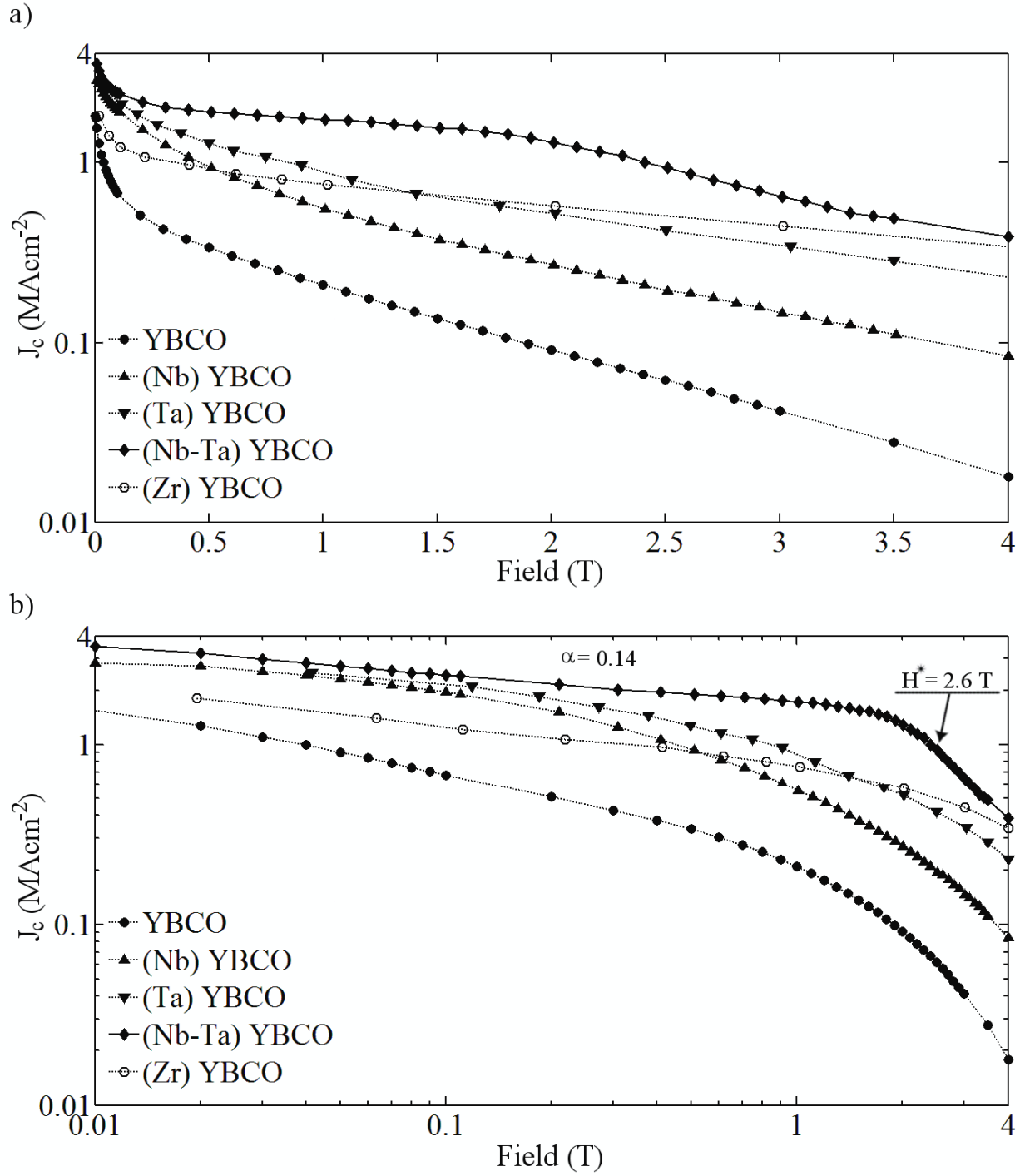

Figure 4. J_c versus applied magnetic field at 77 K, $H \parallel c$ for samples with Nb, Ta, Nb-Ta and Zr doping compared to a pure YBCO sample. Data on a log-linear plot (a) and a log-log plot (b). The (Zr) YBCO data is taken from [23].

$J_c(H)$ for fields applied parallel to the *c*-axis for the films of this study compared with the best reported films [23] of similar thickness (0.3μm) with other additions (Ta, Nb or Zr) is shown in figure 4. The sample with simultaneous addition of Nb and Ta has the highest J_c across the entire field range measured with a value of 1.8 $MAcm^{-2}$ at 1 T and values above 1 $MAcm^{-2}$ up to 2.5 T. Furthermore, as shown in figure 4b, the linear J_c decay range is increased from less than 1 T for pure YBCO, YBCO + 5 mol% Ba_2YNbO_6 ((Nb) YBCO) and YBCO + 5 mol% Gd_3TaO_7 ((Ta) YBCO) to ~2 T for combined Nb+Ta ((Nb-Ta) YBCO) samples, exceeding even that of YBCO + $BaZrO_3$ ((Zr) YBCO) (2% of the YBCO target surface area made of YSZ [23]). The matching field value calculated from the nanorod spacing of ~28 nm observed in the TEM image of figure 3a is ~2.6 T, consistent with the J_c plateau up to 2.5 T of figure 4. The α values calculated for the different additions are reported in table 1. The value of 0.14 for the (Nb-Ta) YBCO samples is lower than the best previously reported value which was 0.19 in a specially grown YBCO + $BaZrO_3$ sample where it was shown that optimisation of the pinning landscape could produce both randomly distributed nanoparticles and splayed columnar defects which together strongly reduce the depinning [24]. In fact, segmented rods were produced which gave rise to staircase vortices.

Table 1. Calculated α values for the different additions.

Sample	α
YBCO	0.47
(Nb) YBCO	0.35
(Ta) YBCO	0.26
(Nb-Ta) YBCO	0.14
(Zr) YBCO	0.25

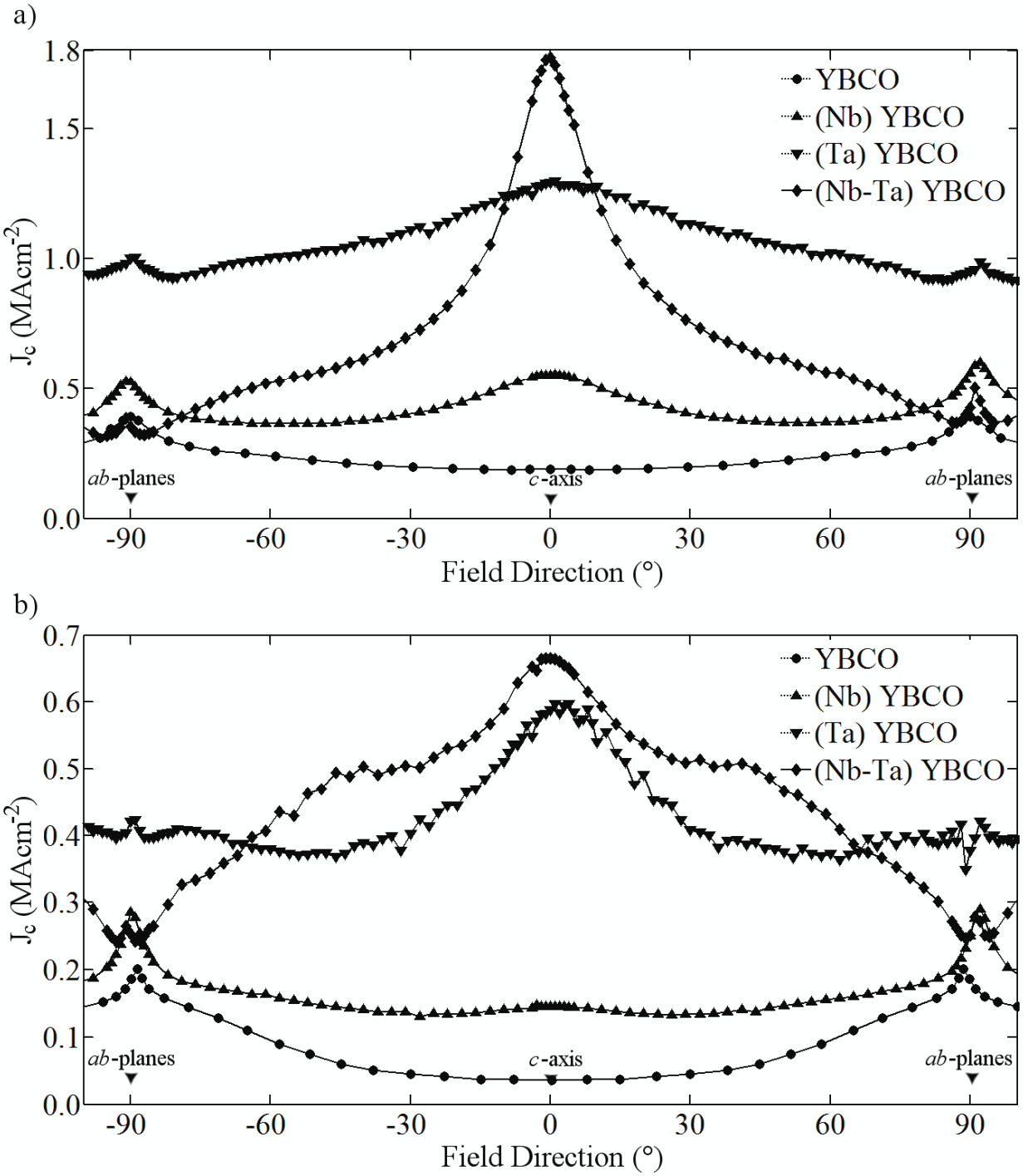

Figure 5. Angular dependence of J_c measured at 77 K for samples with Nb, Ta, and Nb-Ta doping compared to a pure YBCO sample at 1 T (a) and 3 T (b).

Superior properties were also found in the angular dependence of J_c of the (Nb-Ta) YBCO samples of this study. A strong, narrow *c*-axis pinning peak at low fields (1 T, figure 5a) changed to a strong, broad *c*-axis peak as the applied field increased (3 T, figure 5b). The broad peak is a feature already observed in (Nb) YBCO [14]. However the J_c values of the samples prepared in this work are higher than previously observed indicating more effective pinning by the finer, segmented rods compared to the coarser, shorter, non-segmented rods observed in the (Nb) YBCO samples.

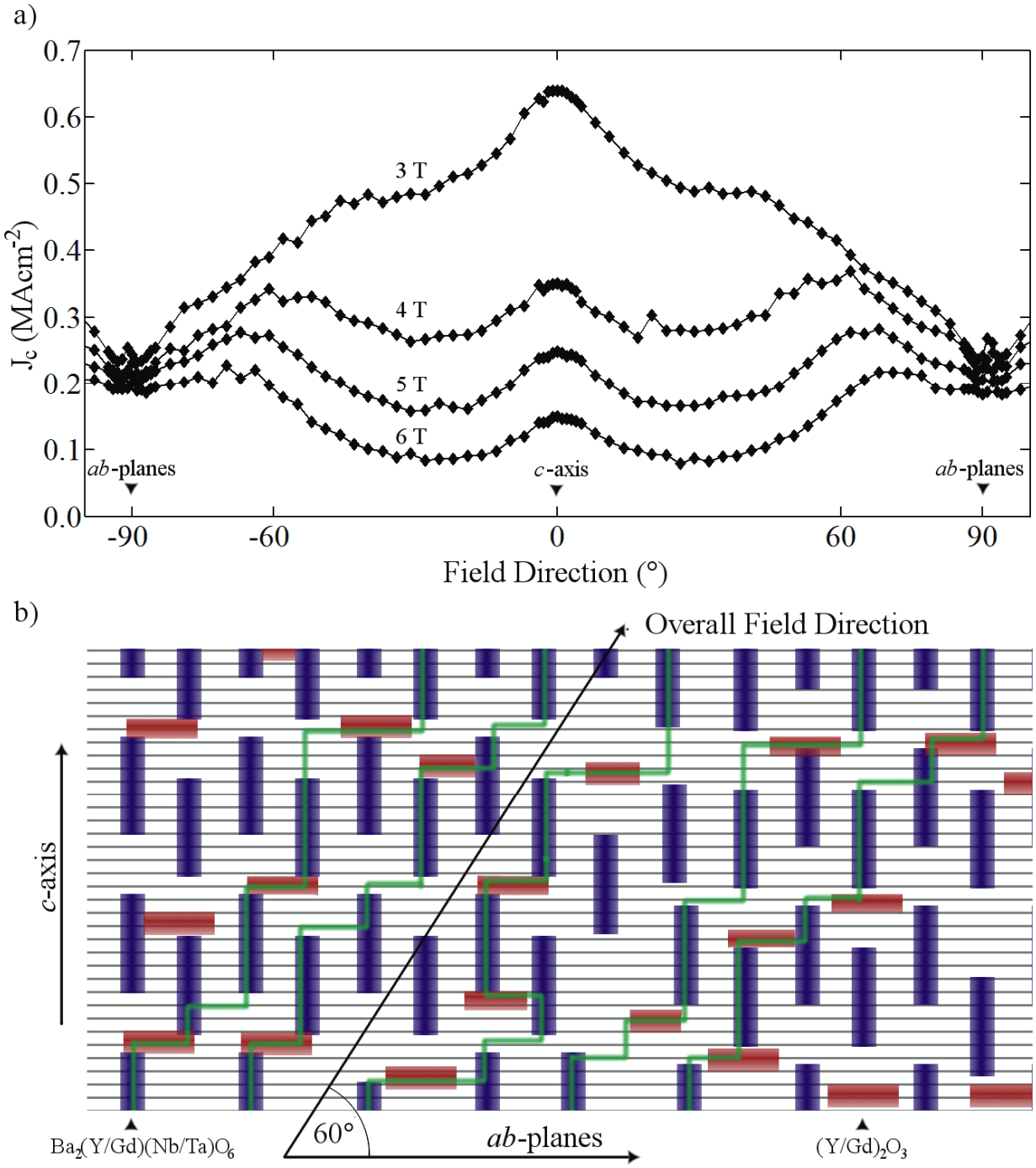

Figure 6. a) High field angular dependence of J_c measured at 77 K for a sample with (Nb-Ta) doping, applied fields ranging from 3 T to 6 T; b) A sketch of vortices interacting simultaneously with rod segments along the *c*-axis and intrinsic and extrinsic defects along the *ab*-planes.

Figure 6a shows the evolution of the angular J_c with increasing field. At low fields, the most prominent feature is the strong *c*-axis pinning peak contrasted with relatively weak *ab*-plane peaks (figure 5a). A shoulder initially observed on the c-axis peak resolves itself at fields beyond 3 T into distinct peaks at around +/- 60 degrees, that grow in magnitude with increasing field to dominate all other types of pinning at fields above 5 T. The existence of this additional preferential pinning direction is an interesting new feature arising from the novel pinning landscape that has been established in these samples. It can be explained in terms of a vortex path model [25] in which the combination of *c*-axis pinning structures (segmented $Ba_2(Y/Gd)(Nb/Ta)O_6$ nanorods) and ab-plane pinning structures (plate-like $(Y/Gd)_2O_3$ particles) results in staircase vortices that experience the strongest pinning at a characteristic angle determined by the particular distribution of defect lengths present (figure 6b). This type of pinning is most effective at high fields because

it utilises both available species of pinning structure and therefore has the capacity to strongly pin a greater overall vortex length.

4. Conclusion

A completely new self-assembled pinning landscape was produced in laser deposited YBCO films by combining the synergistic effects from both Ta and Nb additions which together yield an optimal nanorod architecture of fine, straight, segmented rods. $(Y/Gd)_2O_3$ nanoparticles were also generated in the matrix for reasons of cation compensation, namely because the rods of $Ba_2(Y/Gd)(Nb/Ta)O_6$ formed were of different average composition (poorer in rare earth, richer in barium) than the reactants of Ba_2YNbO_6 and Gd_3TaO_7 which were added to the YBCO PLD target. Greatly enhanced current densities were achieved at 77 K for applied fields higher than 2 T compared to previously studied pinning additives. A J_c of 1 $MAcm^{-2}$ was achieved at 2.5 T and 77 K in 0.3 μm thick films which is a new performance benchmark. In addition, new pinning features around 60° field angle were observed at > 3 T with the potential to extend the angular range of operation of YBCO-based coated conductors.

5. Acknowledgements

Work carried out at the University of Cambridge was performed under the auspices of NESPA, Nano-Engineered Superconductors for Power Application, a framework of the Marie Curie Research Training Network, funded within the EUs 6th framework program. The effort at Texas A&M University was supported by NSF-1007969. JLM-D acknowledges ERC Grant No. ERC-2009-adG 247276. SCW is funded by The Leverhulme Trust, with supplementary funding from The Isaac Newton Trust.

6. References

[1] Haugan T, Barnes P N, Wheeler R, Meisenkothen F, Sumption M. Addition of nanoparticle dispersions to enhance flux pinning of the $YBa_2Cu_3O_{7-x}$ superconductor. 2004, *Nature*, **430**, 867-870.

[2] Civale L, Marwick A D, Worthington T K, Kirk M A, Thompson J R, Krusinelbaum L, Sun Y, Clem J R, Holtzberg F. Vortex confinement by columnar defects in $YBa_2Cu_3O_7$ crystals: Enhanced pinning at high fields and temperatures. 1991, *Phys. Rev. Lett.*, **67**, 648-651.

[3] Gutierrez J, Llordes A, Gazquez J, Gibert M, Roma N, Ricart S, Pomar A, Sandiumenge F, Mestres N, Puig T, Obradors X. Strong isotropic flux pinning in solution-derived $YBa_2Cu_3O_{7-x}$ nanocomposites superconductor films. 2007, *Nature Materials*, **6**, 367-373.

[4] Puig T, Gutierrez J, Pomar A, Llordes A, Gazquez J, Ricart S, Sandiumenge F, Obradors X. Vortex pinning in chemical solution nanostructured YBCO films. 2008 *Supercond. Sci. Technol.*, **21**, 034008.

[5] Sparing M, Backen E, Freudenberg T, Huhne R, Rellinghaus B, Schultz L, Holzapfel B. Artificial pinning centres in YBCO thin films induced by substrate decoration with gas-phase-prepared Y_2O_3 nanoparticles. 2007, *Supercond. Sci. Technol.*, **20**, S239-S246.

[6] Mele P, Matsumoto K, Ichinose A, Mukaida M, Yoshida Y, Horii S, Kita R. Systematic study of the $BaSnO_3$ insertion effect on the properties of $YBa_2Cu_3O_{7-x}$ films prepared by pulsed laser ablation. 2008, *Supercond. Sci. Technol.*, **21**, 125017.

[7] Wimbush S C, Durrell J H, Bali R, Yu R, Wang H , Harrington S A, MacManus-Driscoll J L. Practical magnetic pinning in YBCO. 2009, *IEEE Trans. Appl. Supercond.*, **19**, 3148-3151.

[8] Reich E, Thersleff T, Huhne R, Iida K, Schultz L, Holzapfel B. Structural and pinning properties of $Y_2Ba_4CuMO_y$ (M = Nb, Zr)/ $YBa_2Cu_3O_{7-\delta}$ quasi-multilayers fabricated by off-axis pulsed laser deposition. 2009, *Supercond. Sci. Technol.*, **22**, 105004.

[9] Macmanus-Driscoll J L, Foltyn S R, Jia Q X, Wang H, Serquis A, Civale L, Maiorov B, Hawley M E, Maley M P, Peterson D E. Strongly enhanced current densities in superconducting coated conductors of $YBa_2Cu_3O_{7-x}$ + $BaZrO_3$. 2004, *Nature Materials*, **3**, 439-443.

[10] Mele P, Matsumoto K, Horide T, Ichinose A, Mukaida M, Yoshida Y, Horii S, Kita R. Incorporation of double artificial pinning centers in $YBa_2Cu_3O_{7-\delta}$ films. 2008, *Supercond. Sci. Technol.*, **21**, 015019.

[11] Mele P, Matsumoto K, Horide T, Ichinose A, Mukaida M, Yoshida Y, Horii S, Kita R. Ultra-high flux pinning properties of $BaMO_3$-doped $YBa_2Cu_3O_{7-x}$ thin films (M = Zr, Sn). 2008, *Supercond. Sci. Technol.*, **21**, 032002.

[12] Harrington S A, Durrell J H, Maiorov B, Wang H, Wimbush S C, Kursumovic A, Lee J H, MacManus-Driscoll J L. Self-assembled, rare earth tantalate pyrochlore nanoparticles for superior flux pinning in $YBa_2Cu_3O_{7-\delta}$ films. 2009, *Supercond. Sci. Technol.*, **22**, 022001.

[13] Wee S H, Goyal A, Specht E D, Cantoni C, Zuev Y L, Selvamanickam V, Cook S. Enhanced flux pinning and critical current density via incorporation of self-assembled rare-earth barium tantalate

nanocolumns within $YBa_2Cu_3O_{7-\delta}$ films. 2010, *Phys. Rev. B*, **81**, 14050.
[14] Ercolano G, Harrington S A, Wang H, Tsai C F, MacManus-Driscoll J L. Enhanced flux pinning in $YBa_2Cu_3O_{7-\delta}$ thin films using Nb-based double perovskite additions. 2010, *Supercond. Sci. Technol.*, **23**, 022003.
[15] Wee S H, Goyal A, Zuev Y L, Cantoni C, Selvamanickam V, Specht E D. Formation of Self-Assembled, Double-Perovskite, Ba_2YNbO_6 Nanocolumns and Their Contribution to Flux-Pinning and J_c in Nb-Doped $YBa_2Cu_3O_{7-\delta}$ Films. 2010, *Appl. Phys. Express*, **3**, 023101.
[16] Kai H, Horii S, Ichinose A, Kita R, Matsumoto K, Yoshida Y, Fujiyoshi T, Teranishi R, Mori N, Mukaida M. The effects of growth temperature on *c*-axis-correlated pinning centers in PLD $ErBa_2Cu_3O_{7-\delta}$ films with $Ba(Er_{0.5}Nb_{0.5})O_3$. 2010, *Supercond. Sci. Technol.*, **23**, 025017.
[17] Horii S, Yamada K, Kai H, Ichinose A, Mukaida M, Teranishi R, Kita R, Matsumoto K, Yoshida Y, Shimoyama J, Kishio K. Introduction of c-axis-correlated 1D pinning centers and vortex Bose glass in BaNbO doped $ErBa_2Cu_3O_y$ films. 2007, *Supercond. Sci. Technol.*, **20**, 1115-1119.
[18] Holesinger T G, Foltyn S R, Arendt P N, Kung H, Jia Q X, Dickerson R M, Dowden P C, DePaula R F, Groves J R, Coulter J Y. The microstructure of continuosly processed $YBa_2Cu_3O_y$ coated conductors with underlying CeO_2 and ion 'beam' assisted yttria stabilized zirconia buffer layers. 2000, *Jour. of Mat. Res.*, **15**, 1110-1119.
[19] Specht E D, Goyal A, Li J, Martin P M, Li X, Rupich M W. Stacking faults in $YBa_2Cu_3O_{7-x}$: Measurement using x-ray diffraction and effects on critical current. 2006, *Appl. Phys. Lett.*, **89**, 162510.
[20] Gapud A A, Kumar D, Viswanathan S K, Cantoni C, Varela M, Abiade J, Pennycook S J, Christen D K. Enhancement of flux pinning in $YBa_2Cu_3O_{7-\delta}$ thin films embedded with epitaxially grown Y_2O_3 nanostructures using a multi-layering process. 2005, *Supercond. Sci. Technol.*, **18**, 1502-1505.
[21] Garrison S M, Newman N, Cole B F, Char K, Barton R W. Observation of 2 in-plane epitaxial states in $YBa_2Cu_3O_{7-\delta}$ films on yttria-stabilized ZrO_2. 1991, *Appl. Phys. Lett.*, **58**, 2168-2170.
[22] Harrington S A, Durrell J H, Wang H, Wimbush S C, Tsai C F, MacManus-Driscoll J L. Understanding nanoparticle self-assembly for a strong improvement in functionality in thin film nanocomposites. 2010, *Nanotechnology*, **21**, 095604.
[23] Mele P, Matsumoto K, Horide T, Ichinose A, Mukaida M, Yoshida Y, Horii S. Enhanced high-field performance in PLD films fabricated by ablation of YSZ-added $YBa_2Cu_3O_{7-x}$ target. 2007, *Supercond. Sci. Technol.*, **20**, 244-250.
[24] Maiorov B, Baily S A, Zhou H, Ugurlu O, Kennison J A, Dowden P C, Holesinger T G, Foltyn S R, Civale L. Synergetic combination of different types of defect to optimize pinning landscape using $BaZrO_3$-doped $YBa_2Cu_3O_7$. 2009, *Nature Materials*, **8**, 398-404.
[25] Long N J. Model for the angular dependence of critical currents in technical superconductors. 2008, *Supercond. Sci. Technol.*, **21**, 025007.

Pinning ion addition	Stable Phase in $YBa_2Cu_3O_{7-\delta}$	Lattice Parameter [nm]	Lattice misfit to ab_{YBCO}	Lattice misfit to c_{YBCO}	Ref.
Nb^{+4}	Ba_2YNbO_6	0.422	+9.4%[a]	+8.4%	[5, 74] [123, 124]
Ta^{+4}	Ba_2YTaO_6	0.422	+9.4%[a]	+8.4%	[68]
Zr^{+4}	$BaZrO_3$	0.419	+8.8%[a]	+7.6%	[57–63]
Sn^{+4}	$BaSnO_3$	0.411	+6.8%[a]	+5.6%	[64–66]
Hf^{+4}	$BaHfO_3$	0.417	+8.3%[a]	+7.1%	[144]
Ir^{+4}	$BaIrO_3$	0.410	+6.5%[a]	+5.3%	[145]
Ti^{+4}	$BaTiO_3$	0.402	+4.4%[a]	+3.2%	[146, 147]
Y^{+3}	Y_2O_3	1.060	-2.8%[b]	-9.2%	[78, 142] [141, 148]
Ta^{+5}	Gd_3TaO_7	1.065	-2.4%[b]	-8.7%	[67]
Ta^{+5}	Yb_3TaO_7	1.039	-4.8%[b]	-10.9%	[67]

Table 1: Crystallographic parameters of non-superconductive second phase materials used as pinning phases in $YBa_2Cu_3O_{7-\delta}$ films ([a] cube-on-cube, [b] rotated 45° to cube-on-cube).

References

[1] Tinkham M. *Introduction to Superconductivity 2nd ed.* McGraw-Hill, New York, 1996. xi, 6

[2] Cava R J *et al.* Structural anomalies, oxygen ordering and superconductivity in oxygen deficient $Ba_2YCu_3O_x$. *Physica C*, 165:419–433, 1990. xi, 12, 13

[3] Singh R K *et al.* Pulsed laser deposition and charcterization on high-T_c $YBa_2Cu_3O_{7-x}$ superconducting thin films. *Mat. Sci. and Eng. RR*, 22:113–185, 1998. xi, 23, 25

[4] Paulose K V *et al.* Ba_2YNbO_6: synthesis, properties and compatibility with $YBa_2Cu_3O_{7-\delta}$. *Physica C*, 193:273–276, 1992. xii, 41, 42, 43, 44, 46

[5] Ercolano G *et al.* Enhanced flux pinning in $YBa_2Cu_3O_{7-\delta}$ thin films using Nb-based double perovskite additions. *Supercond. Sci. Technol.*, 23:022003, 2010. xii, 43, 44, 46, 48, 49, 104, 109, 112, 121, 145

[6] Mele P *et al.* Enhanced high-field performance in PLD films fabricated by ablation of YSZ-added $YBa_2Cu_3O_{7-x}$ target. *Supercond. Sci. Technol.*, 20, 2007. xvii, 89, 112, 113, 116

[7] Onnes H K. Investigation into the properties of sustances at low temperatures, which have led, amongst other things to the preparation of liquid helium. *Nobel lectures*, pages 306–336, 1913. 1

[8] Onnes H K. Liquid helium. *Comptes Rendus Hebdomadaires Des Seances de l'Academie Des Sciences*, 147:421–424, 1908. 1

[9] Onnes H K. Further experiments with liquid helium D - On the change of the electrical resistance of pure metals at very low temperatures, etc V The disappearance of the resistance of mercury. *Proceedings of the Koninklijke Akademie Van Wetenshappen te Amsterdam*, 14:113–115, 1911. 1

[10] Ochsenfeld R Meissner W. Ein neuer Effekt bei Eintritt der Supraleitfhigkeit. *Naturwissenschaften*, 21:787–788, 1933. 2

[11] London H London F. The electromagnetic equations of the supraconductor. *Proc. Roy. Soc.*, 149:71–88, 1935. 2

[12] Landau L D Ginzburg V L. To the Theory of Superconductivity. *Zh. Eksp. Teor. Fiz.*, 20:1064, 1950. 4

[13] Abrikosov A A. On the Magnetic Properties of Superconductors of the Second Group. *Soviet Phys. jetp-USSR*, 5:1174–1183, 1957. 5

[14] Abrikosov A A. Type II Superconductors and the vortex lattice. *Nobel Lecture*, 2003. 5

[15] Kleiner W H *et al.* Bulk solution of ginzburg-landau equations for type II superconductors: Upper critical field region. *Phys. Rev. A*, 133:1226, 1964. 5

[16] Kramer L. Thermodynamical behaviour of type-II superconductors with small k near the lower critical field. *Phys. Lett.*, 23:619, 1966. 5

[17] Schrieffer J R Bardeen J, Cooper L N. Theory of Superconductivity. *Physical Review*, 108:1175–1204, 1957. 7

[18] Cooper L N. Bound Electron Pairs in a Degenerate Fermi Gas. *Physical Review*, 104:1189–1190, 1956. 7

[19] M*ü*ller K A Bednorz J G. Possible highT_c superconductivity in the Ba-La-Cu-O system. *Zeitschrift fr Physik B Condensed Matter*, 64:189–193, 1986. 8

[20] Wu K M *et al.* Superconductivity at 93 K in a new mixed-phase Yb-Ba-Cu-O compound system at ambient pressure. *Phys. Rev. Lett.*, 58:908–910, 1987. 8

[21] Maeda H *et al.* A New High-T_c Oxide Superconductor without a Rare Earth Element. *Jpn. J. Appl. Phys*, 27:209–210, 1988. 8

[22] Hermann A M Sheng Z Z. Bulk Superconductivity at 120 K in the Tl-Ca/Ba-Cu-O system. *Nature*, 332:138–139, 1988. 8

[23] Nagamatsu J *et al.* Superconductivity at 39 K in magnesium diboride. *Nature*, 410:63–64, 2001. 8

[24] Larbalestier D C *et al.* Strongly linked current flow in polycrystalline forms of the superconductor MgB_2. *Nature*, 410:186–189, 2001. 8

[25] Buzea C and Yamashita T. Review of the superconducting properties of MgB_2. *Supercond. Sci. Technol.*, 14:R115–R146, 2001. 8

[26] Eom C B *et al.* High critical current density and enhanced irreversibility field in superconducting MgB_2 thin films. *Nature*, 411:558–560, 2001. 8

[27] Jin S *et al.* High critical currents in iron-clad superconducting MgB_2 wires. *Nature*, 411:553–565, 2001. 8

[28] Kamihara Y *et al.* Iron-Based Layered Superconductor: LaOFeP. *J. Am. Chem. Soc*, 128:10012–10013, 2006. 8

[29] Takahashi H *et al.* Superconductivity at 43 K in an iron-based layered compound $LaO_{1-x}F_xFeAs$. *Nature*, 453:376–378, 2008. 8

[30] Kamihara Y *et al.* Iron-based layered superconductor $La[O_{1-x}F_x]FeAs$ (x=0.05-0.12) with T_c=26 K. *J. Ame. Chem. Soc.*, 130:3296, 2008. 8

[31] Rotter M *et al.* Superconductivity at 38 K in the iron arsenide $(Ba_{(1-x)}K_{(x)})Fe_{(2)}As_{(2)}$. *Phys. Rev. Lett.*, 101:107006, 2008. 8

[32] Chen X H *et al.* Superconductivity at 43 K in $SmFeAsO_{1-x}F_x$. *Nature*, 453:761–762, 2008. 8

[33] Wu G *et al.* Superconductivity at 56 K in samarium-doped SrFeAsF. *J. of Phys:Cond. mat.*, 21, 2009. 8

[34] Dinger T R *et al.* Direct Observation of Electronic Anisotropy in Single-Crystal $YBa_2Cu_3O_{7-x}$. *Phys. Rev. Lett.*, 58:2687–2690, 1987. 10

[35] Chaudhari P *et al.* Critical Currents Measurements in Epitaxial Films of $YBa_2Cu_3O_{7-x}$ Compound. *Phys. Rev. Lett.*, 58:2684–2686, 1987. 10

[36] Larbalestier D C *et al.* Experiments concerning the connective nature of superconductivity in $YBa_2Cu_3O_7$. *J. Appl. Phys.*, 62:3308–3313, 1987. 10

[37] Dimos D *et al.* Orientation Dependence of Grain-Boundary Critical Currents in $YBa_2Cu_3O_{7-\delta}$ Bicrystals. *Phys. Rev. Lett.*, 61:219–222, 1988. 10

[38] Mayer B *et al.* Superconducting transport properties of $Bi_2Sr_2CaCu_2O_{8+x}$ bicrystal grain boundery junctions. *Appl. Phys. Lett.*, 63:996–998, 1993. 10

[39] Heine K *et al.* High-field critical current densities in $Bi_2Sr_2Ca_1Cu_2O_{8+x}/Ag$ wires. *Appl. Phys. Lett.*, 55:2441–2443, 1989. 10

[40] Yamada Y *et al.* Critical Current Density of Wire Type Y-Ba-Cu Oxide Superconductor. *Jpn. J. Appl. Phys.*, 26:865–866, 1987. 10

[41] Flükiger R *et al.* Metallurgy and critical current in $YBa_2Cu_3O_7$ wires. *Physica C*, 153:1574–1579, 1988. 10

[42] Wu X D *et al.* High-current $YBa_2Cu_3O_{7-\delta}$ thick films on flexible nickel substrates with textured buffer layers. *Appl. Phys. Lett.*, 65:1961–1963, 1994. 10

[43] Goyal A *et al.* Epitaxial superconductors on rolling-assisted biaxially-textured substrates (RABiTS): A route towards high critical current density wire. *Appl. Superconductivity*, 4:403–427, 1996. 10

[44] Larbalestier D *et al.* High-T_c superconducting materials for electric power applications. *Nature*, 414:368–377, 2001. 11

[45] Cava R J *et al.* Bulk Superconductivity at 91 K in Single-Phase Oxygen-Deficient Perovskite $Ba_2YCu_3O_{9-\delta}$. *Phys. Rev. Lett.*, 58:1676–1679, 1987. 12

[46] Beno M A *et al.* Structure of the single-phase high-temperature superconductor $YBa_2Cu_3O_{7-\delta}$. *Appl. Phys. Lett.*, 51:57–59, 1987. 12

[47] David W I F *et al.* Structure and crystal chemistry of the high-Tc superconductor $YBa_2Cu_3O_{7-x}$. *Nature*, 327:310–312, 1987. 12

[48] Tietz L A and Carter C B. Special grain boundaries in $YBa_2Cu_3O_{7-x}$ thin films. *Physica C Supercond.*, 182:241251, 1991. 12

[49] Linfeng Mei and Siu-Wai Chan. Enthalpy and entropy of twin boundaries in superconducting $YBa_2Cu_3O_{7-x}$. *J. Appl. Phys.*, 98:033908, 2005. 12

[50] Jorgenson J D *et al.* Structural and superconducting properties of orthorhombic and tetragonal $YBa_2Cu_3O_{7-x}$: The effect of oxygen stoichiometry and ordering on superconductivity. *Phys. Rev. B*, 36:5731–5734, 1987. 12

[51] Jorgenson J D *et al.* Oxygen ordering and the orthorhombic-to-tetragonal phase transition in $YBa_2Cu_3O_{7-x}$. *Phys. Rev. B*, 36:36083616, 1987. 12

[52] Blatter G *et al.* Vortices in high-temperature superconductors. *Rev. Mod. Phys.*, 66:1125–1338, 1994. 14

[53] Evetts J E. Flux Pinning by Phase Boundaries in Type-II Superconductors. *Phys. Rev. B*, 2:95–96, 1970. 16

[54] Coote R I *et al.* Flux Line Pinning by Large Normal Particles in Type-II Superconductors. *Can. J. Phys.*, 50:421–427, 1972. 16

[55] Campbell A M and Evetts J E. Flux vortices and transport currents in type II superconductors. *Adv. Phys.*, 21:199–428, 1972. 16

[56] Larkin A I and Ovchinnikov Y N. Pinning in type II superconductors. *J. Low Temp. Phys.*, 34:409–428, 1979. 16

[57] MacManus-Driscoll J L *et al.* Strongly enhanched current densities in superconducting coated conductors of $YBa_2Cu_3O_{7-x} + BaZrO_3$. *Nature Materials*, 3:439–443, 2004. 17, 39, 50, 59, 89, 112, 120, 145

[58] Foltyn S R *et al.* Materials science challenges for high-temperature superconducting wire. *Nature Materials*, 6:631, 2007. 18, 145

[59] Galluzzi V *et al.* $YBa_2Cu_3O_{7-\delta}$ films with $BaZrO_3$ inclusions for strong-pinning in superconducting films on single crystal substrate. *IEEE Trans. Appl. Supercond.*, 17:3628, 2007. 18, 145

[60] Peurla M *et al.* YBCO films prepared by PLD using nanocrystalline targets doped with $BaZrO_3$ or Y211. *IEEE Trans. Appl. Supercond.*, 15:3050–3053, 2005. 18, 145

[61] Ichinose A *et al.* Microstructures and critical current densities of YBCO films containing structure-controlled $BaZrO_3$ nanorods. *Supercond. Sci. Technol.*, 20:1144, 2007. 18, 145

[62] Ito M *et al.* Microstructure of $ErBa_2Cu_3O_{7-\delta}$ films with $BaZrO_3$ dispersion pinning centers for high J_c applications. *Physica C*, 426:1415, 2005. 18, 145

[63] Feldmann D M *et al.* 1000 Acm^{-1} in a 2 μm thick $YBa_2Cu_3O_{7-x}$ film with $BaZrO_3$ and Y_2O_3 additions. *Supercond. Sci. Technol.*, 23:115016, 2010. 18, 145

[64] Varanasi C V *et al.* Enhancement and angular dependence of transport critical current density in pulsed laser deposited $YBa_2Cu_3O_{7-x} + BaSnO_3$ films in applied magnetic fields. *Jour. of Appl. Phys.*, 102, 2007. 18, 39, 50, 120, 145

[65] Mele P *et al.* Systematic study of the $BaSnO_3$ insertion effect on the properties of $YBa_2Cu_3O_{7-x}$ films prepared by pulsed laser ablation. *Supercond. Sci. Technol.*, 21, 2008. 18, 39, 89, 145

[66] Mele P *et al.* Ultra-high flux pinning properties of $BaMO_3$-doped $YBa_2Cu_3O_{7-x}$ thin films (M = Zr, Sn). *Supercond. Sci. Technol.*, 21:032002, 2008. 18, 39, 145

[67] Harrington S A *et al.* Self-assembled, rare earth tantalate pyrochlore nanoparticles for superior flux pinning in $YBa_2Cu_3O_{7-\delta}$ films. *Supercond. Sci. Technol.*, 22, 2009. 18, 39, 59, 105, 108, 109, 120, 145

[68] Hun Wee S *et al.* Enhanced flux pinning and critical current density via incorporation of self-assembled rare-earth barium tantalate nanocolumns within $YBa_2Cu_3O_{7-\delta}$ films. *Phys. Rev. B*, 81, 2010. 18, 39, 59, 108, 109, 112, 121, 145

[69] Gutierrez J *et al.* Strong isotropic flux pinning in solution-derived $YBa_2Cu_3O_{7-x}$ nanocomposite superconductor films. *Nature Materials*, 6:367–373, 2007. 18, 63

[70] Hougan T *et al.* Addition of nanoparticle dispersions to enhance flux pinning of the $YBa_2Cu_3O_{7-x}$ superconductor. *Nature*, 430:367–373, 2004. 18

[71] Campbell T A *et al.* Flux pinnig effect of Y_2O_3 nanoparticulate dispersion in multilayered YBCO thin films. *Physica C: Supercond.*, 423:1–8, 2005. 18, 19

[72] Kang S *et al.* Strong enhancement of flux pinning in $YBa_2Cu_3O_{7-\delta}$ multilayers with columnar defects comprised of self-assembled $BaZrO_3$ nanodots. *Supercond. Sci. Technol.*, 20, 2007. 18

[73] Kang S *et al.* Flux pinning characteristic as a function of density of columnar defects comprised of self-assembled nanodots and nanorods in epitaxial $YBa_2Cu_3O_{7-\delta}$ films for coated conductor applications. *Physica C*, 457:41–46, 2007. 18

[74] Reich E *et al.* Structural and pinning properties of $Y_2Ba_4CuMO_y$ (M = Nb, Zr) / $YBa_2Cu_3O_{7-\delta}$ quasi-multilayers fabricated by off-axis pulsed laser deposition. *Supercond. Sci. Technol.*, 22, 2009. 19, 43, 89, 145

[75] Matsumoto K *et al.* Enhancement of critical current density of YBCO films by introduction of artificial pinning centers due to the distributed nanoscaled Y_2O_3 islands on substrates. *Physica C Supercond.*, 412:1267–1271, 2004. 19

[76] Matsumoto K *et al.* Effects of artificial pinning centers on vortex pinning in high-temperature superconducting films. *Physica C Supercond.*, 426-431:1091–1095, 2005. 19

[77] Mele P *et al.* Critical current enhancement in PLD $YBa_2Cu_3O_{7-x}$ films using artificial pinning centers. *Physica C Supercond.*, 445-448:648–651, 2006. 19

[78] Mele P *et al.* Tuning of the critical current in $YBa_2Cu_3O_{7-x}$ thin films by controlling the size and density of Y2O3 nanoislands on annealed $SrTiO_3$ substrates. *Supercond. Sci. Technol.*, 19:44, 2006. 19, 145

[79] Li A H *et al.* Effect of substrate surface modification using Ag nano-dots on the improvement of J_c and microstructures in $YBa_2Cu_3O_7$ thin films grown on $LaAlO_3$ (100) by pulsed laser deposition. *Journ. Electroceram.*, 16:605–609, 2006. 19

[80] Dang V S *et al.* Combination of Ag Substrate Decoration with Introduction of $BaZrO_3$ Nano-Inclusions for Enhancing Critical Current Density of $YBa_2Cu_3O_7$ Films. *Journ. Electroceram.*, 24:505–509, 2011. 19

[81] Aytug T *et al.* Enhancement of flux pinning and critical currents in $YBa_2Cu_3O_{7-\delta}$ films by nanoscale iridium pretreatment of substrate surfaces. *Jour. of Appl. Phys.*, 98, 2005. 19

[82] Aytug T *et al.* Analysis of flux pinning in $YBa_2Cu_3O_{7-\delta}$ films by nanoparticle-modified substrate surfaces. *Phys. Rev. B*, 74:184505, 2006. 19

[83] Aytug T *et al.* Substrate Surface Decoration With CeO_2 Nanoparticles: An Effective Method for Improving Flux Pinning in $YBa_2Cu_3O_{7-\delta}$ Films. *IEEE Trans. Appl. Supercond.*, 17:3720–3723, 2007. 19

[84] Crisan A *et al.* Sputtered nanodots: A costless method for inducing effective pinning centers in superconducting thin films. *Appl. Phys. Lett.*, 79:4547–4549, 2001. 19

[85] Sparing M *et al.* Artificial pinning centres in YBCO thin films induced by substrate decoration with gas-phase-prepared Y_2O_3 nanoparticles. *Supercond. Sci. Technol.*, 20:S239–S246, 2007. 19

[86] Cui X M *et al.* Enhancement of critical current density of $YBa_2Cu_3O_{7-\delta}$ thin films by nanoscale CeO_2 pretreatment of substrate surfaces. *Physica C Supercond.*, 466:1–4, 2007. 19

[87] MacManus-Driscoll J L *et al.* Guidelines for optimizing random and correlated pinning in rare-earth based superconducting films. *Supercond. Sci. Technol.*, 19:S55–S59, 2006. 19

[88] Civale L *et al.* Vortex confinement by columnar defects in $YBa_2Cu_3O_7$ crystals: Enhanced pinning at high fields and temperatures. *Phys. Rev. Lett.*, 67, 1991. 19

[89] Weber H W *et al.* Critical currents in neutron-irradiated YBCO and BISCCO single-crystals. *Supercond. Sci. Technol.*, 4:S103–S105, 1991. 19

[90] Jirong J *et al.* Irradiation effect of slow neutrons on melt-textured $YBa_2Cu_3O_{7-\delta}$. *Phys. Stat. Sol.*, 125:289–294, 1991. 19

[91] Wisniewski A *et al.* Comparison of neutron-irradiation effects in the 90-K and 60-K phases of YBCO ceramics. *Physica C*, 197:365–370, 1992. 19

[92] Kato T *et al.* Radiation effect of $YBa_2Cu_3O_{7-y}$ irradiated by γ-Rays and 14 MeV neutrons. *Jpn. J. Appl. Phys.*, 27:L2097–L2099, 1988. 19

[93] Vasek P *et al.* Gamma-irradiation of $YBa_2Cu_3O_{7-x}$ ceramics. *Solid State Com.*, 69:23–25, 1989. 19

[94] Kim D H *et al.* Effect of Heavy-Ion Irradiation on Transport Properties of $YBa_2Cu_3O_x$ Films. *Trans. on appl. Supercond.*, 7, 1997. 20

[95] Nakashima K *et al.* Effect of ion-irradiation and annealing on superconductive property of PLD prepared YBCO tapes. *Physica C Supercond.*, 463:665–668, 2007. 20

[96] Eisterer M *et al.* Neutron irradiation of coated conductors. *Supercond. Sci. Technol.*, 23:014009, 2010. 20

[97] Chudy M *et al.* Asymmetric angular dependence of J(c) in coated conductors prior to and after fast neutron irradiation. *Physica C Supercond.*, 470:1300–1303, 2010. 20

[98] Chudy M *et al.* Characterization of Commercial YBCO Coated Conductors After Neutron Irradiation. *IEEE Trans. Appl. Supercond.*, 21:3162–3165, 2011. 20

[99] Fuger R *et al.* Influence of neutron irradiation on high temperature superconducting coated conductors. *Physica C Supercond.*, 468:1647–1651, 2008. 20

[100] Yamada H *et al.* Flux pinning centres correlated along the c-axis in PLD-YBCO films. *Supercond. Sci. Technol.*, 17:58, 2004. 22

[101] Civale L *et al.* Influence of crystalline texture on vortex pinning near the ab-plane in $YBa_2Cu_3O_7$ thin films and coated conductors. *Physica C Supercond.*, 412:976–982, 2004. 22

[102] Takahashi K *et al.* Investigation of thick PLD-GdBCO and ZrO_2 doped GdBCO coated conductors with high critical current on PLD-CeO_2 capped IBAD-GZO substrate tapes. *Supercond. Sci. Technol.*, 19:924–929, 2006. 22

[103] Traito K *et al.* Magnetic field dependence of the critical current and the flux pinning mechanism in $YBa_2Cu_3O_{6+x}$ films doped with $BaZrO_3$. *Phys. Rev. B*, 73:224522, 2006. 22

[104] Horide T *et al.* Flux pinning properties of YBCO thin films deposited on $SrTiO_3$(100) and MgO(100) substrates. *Physica C Supercond.*, 412:1291–1295, 2004. 22

[105] Douglas B C and Graham K H. *Pulsed Laser Deposition of Thin Films.* Jhon Wiley & Sons, New York, 1994. 22, 51

[106] Kwok H S *et al.* Laser induced deposition of $YBa_2Cu_3O_{7-x}$ thin films. In *High-Temperature Superconductors*, pages 273–277, 1988. 22

[107] Horcas I *et al.* WSXM: A software for scanning probe microscopy and a tool for nanotechnology. *Rev. Sci. Instrum.*, 78:013705, 2007. 35

[108] Kuwabara M *et al.* Microstructure and Superconducting Properties in $YBa_2Cu_3O_{7-x}$ ceramics Doped with Nb_2O_5 and WO_3. *Jap. Jour. of Appl. Phys.*, 27:L1504–L1506, 1988. 40

[109] Greaves C and Slater PR. Nb and Ta Substitutions in $YBa_2Cu_3O_{7-x}$ and related phases − Structural Characterization of $La1.1Ba_{1.9}Cu_{2.1}M_{0.9}O_8$ (M=Nb, Ta). *Physica C*, 161:245–251, 1989. 40, 108, 120

[110] Strukova G K *et al.* Effect of Nb doping on properties of Y-Ba-Cu ceramics. *Supercond. Sci. Technol.*, 6:589–592, 1993. 40

[111] Strukova G K *et al.* A cubic phase in ceramic Y-Ba-Cu-O doped with Nb. *Physica C*, 267:67–73, 1996. 40

[112] Babu N H *et al.* New chemically stable, nano-size artificial flux pinning centres in (RE)-Ba-Cu-O superconductors. *Supercond. Sci. Technol.*, 16:L44–L45, 2003. 41

[113] Babu N H *et al.* Artificial flux pinning centers in large, single-grain (RE)-Ba-Cu-O superconductors. *Appl. Phys. Lett.*, 83:4806–4808, 2003. 41

[114] Yeoh W K *et al.* Improved Flux Pinning in Y-Ba-Cu-O Superconductors Containing Niobium Oxide. *IEEE Trans. Appl. Supercond.*, 19:2970–2973, 2009. 41

[115] Satiraju S *et al.* Studies on Ba_2YNbO_6 buffer layers for subsequent $YBa_2Cu_3O_{7-x}$ film growth. *IEEE Trans. Appl. Supercond.*, 15:3009–3012, 2005. 41

[116] Grekhov I *et al.* A new buffer layer for high-quality HTSC ultrathin film fabrication. *Physica C*, 276:18–24, 1997. 41

[117] Jia J H *et al.* Effect of the Second Phase on Critical Current Density in Nb-Added YBCO Films. *Mod. Phys. Lett.*, 9:439–443, 1995. 41

[118] Hori S *et al.* Introduction of c-axis-correlated 1D pinning centers and vortex Bose glass in BaNbO-doped $ErBa_2Cu_3O_y$ films. *Supercond. Sci. Technol.*, 20:1115–1119, 2007. 41, 59, 89, 104, 112, 120

[119] Kai H *et al.* Superconducting properties and microstructure of PLD-$ErBa_2Cu_3O_{7-\delta}$ film with $BaNb_2O_6$. *Physica C: Supercond.*, 463-465:895–899, 2007. 41, 59, 112, 120

[120] Kai H *et al.* Influence of Growth Temperature on Microstructure and Superconducting Properties of $ErB_2Cu_3O_{7-\delta}$ Films With $Ba(Er_0.5Nb_0.5)O_3$ Nanorods. *IEEE Trans. Appl. Supercond.*, 19:3435–3438, 2009. 41

[121] Kai H *et al.* The effects of growth temperature on c-axis-correlated pinning centers in PLD-$ErB_2Cu_3O_{7-\delta}$ films with $Ba(Er_0.5Nb_0.5)O_3$. *Supercond. Sci. Technol.*, 23:025017, 2010. 41

[122] Yamada K *et al.* Transmission electron microscopy characterization of nanorods in $BaNb_2O_6$-doped $ErB_2Cu_3O_{7-\delta}$ films. *Appl. Phys. Lett.*, 92:112503, 2008. 41

[123] Feldmann D M *et al.* Improved flux pinning in $YBa_2Cu_3O_7$ with nanorods of the double perovskite Ba_2YNbO_6. *Supercond. Sci. Technol.*, 23:095004, 2010. 43, 145

[124] Hun Wee S *et al.* Formation of Self-Assembled, Double-Perovskite, Ba_2YNbO_6 Nanocolumns and Their Contribution to Flux-Pinning and J_c in Nb-Doped $YBa_2Cu_3O_{7-\delta}$ Films. *Appl. Phys. Express*, 3:023101, 2010. 43, 104, 109, 145

[125] Barnes P W *et al.* Structure determination of $A_2M^{3+}TaO_6$ and $A_2M^{3+}NbO_6$ ordered perovskites: octahedral tilting and pseudosymmetry. *Acta Crystallogr.*, B62:384–396, 2006. 45

[126] Goyal A *et al.* Irradiation-free, columnar defects comprised of self-assembled nanodots and nanorods resulting in strongly enhanced flux-pinning in $YBa_2Cu_3O_{7-\delta}$ films. *Supercond. Sci. Technol.*, 18:1533–1538, 2005. 50

[127] MacManus-Driscoll *et al.* Systematic enhancement of in-field critical current density with rare-earth ion size variance in superconducting rare-earth barium cuprate films. *Appl. Phys. Lett.*, 84:5329–5331, 2004. 50

[128] Singh R K *et al.* Control of surface particle density in pulsed laser deposition of superconducting $YBa_2Cu_30_7$ and diamondlike carbon thin films. *Appl. Phys. Lett.*, 61:483–485, 1992. 51

[129] Wu W B *et al.* Particulate-free *a*-$YBa_2Cu_30_{7-x}$/$La_0.5Sr_0.5CoO_3$/*a*-$YBa_2Cu_30_{7-x}$ sandwiched thin film on (100)$SrTiO_3$ fabricated by pulsed laser deposition with a shadow mask. *Physica C*, 282:701–702, 1997. 51

[130] Boffa V *et al.* High-quality surface YBCO thin films prepared by off-axis pulsed laser deposition technique. *Physica C*, 276:218–224, 1997. 51

[131] Backen E *et al.* Improved pinning in YBCO based quasi-multilayers prepared by on- and off-axis pulsed laser deposition. *IEEE Trans. Appl. Supercond.*, 17:3733–3736, 2007. 51

[132] Cillessen J F M *et al.* Improved uniformity of multielement thin films prepared by off-axis pulsed laser deposition using a new heater design. *Rev. Sci. Instr.*, 67:3229–3237, 1996. 51

[133] Harrington S A *et al.* Understandig nanoparticle self-assembly for a strong impovement in functionality in thin film nanocomposites. *Nanotechnology*, 21, 2010. 56, 112

[134] Maiorov B *et al.* Synergetic combination of different types of defect to optimize pinning landscape using $BaZrO_3$-doped $YBa_2Cu_3O_{7-\delta}$. *Nature Materials*, 8, 2009. 56, 63, 89, 90, 114

[135] Liu L F *et al.* Effect of Deposition Temperature on the Epitaxial Growth of YBCO Thin Films on RABiTS Substrates by Pulsed Laser Deposition Method. *IEEE trans. on appl. supercond.*, 20:1553–1553, 2010. 96

[136] Norton M G *et al.* Surface outgrowths on laser-deposited $YBa_2Cu_3O_7$ thin films. *Physica C*, 233:321–326, 1994. 96

[137] Guo L P *et al.* Microstructure of outgrowths on the surface of laser-ablated $YBa_2Cu_3O_7$ thin films. *Physica C*, 241:30–36, 1995. 96

[138] Kai H *et al.* The effects of growth temperature on c-axis-correlated pinning centers in PLD-$ErBa_2Cu_3O_{7-\delta}$ films with $Ba(Er_0.5Nb_0.5)O_3$. *Supercond. Sci. Technol.*, 23, 2010. 104

[139] Holesinger T G *et al.* The microstructure of continuosly processed $YBa_2Cu_3O_y$ coated conductors with undelying CeO_2 and ion'beam'assisted yttria'stabilized zirconia buffer layers. *Jour. of Mat. Res.*, 15:1110–1119, 2000. 108

[140] Specht E D *et al.* Stacking faults in $YBa_2Cu_3O_{7-x}$: Measurement using x-ray diffraction and effects on critical current. *Appl. Phys. Lett.*, 89:162510, 2006. 108

[141] Gapud A A *et al.* Enhancement of flux pinning in $YBa_2Cu_3O_{7-\delta}$ thin films embedded with epitaxially grown Y_2O_3 nanostructures using a multi-layering process. *Supercond. Sci. Technol.*, 18:1502–1505, 2005. 108, 145

[142] Garrison S M *et al.* Observation of 2 in-plane epitaxial states in $YBa_2Cu_3O_{7-\delta}$ films on yttria-stabilized ZrO_2. *Appl. Phys. Lett.*, 58:2168–2170, 1991. 109, 145

[143] Long N J. Model for the angular dependence of critical currents in technical superconductors. *Supercond. Sci. Technol.*, 21, 2008. 117

[144] Zhang J L and Evetts J E. $BaZrO_3$ and $BaHfO_3$ - preparation, properties and compatibility with $YB_2Cu_3O_{7-x}$. *J. Mater. Sci.*, 29:778–781, 1994. 145

[145] Hanish J *et al.* Formation of $BaIrO_3$ precipitates and their contribution to flux pinning in Ir-doped $YB_2Cu_3O_{7-x}$ quasi-multilayers. *Appl. Phys. Lett.*, 86:122508, 2005. 145

[146] Alok K J and Khare N. Strongly enhanced pinning force density in YBCOBaTiO$_3$ nanocomposite superconductor. *Physica C Supercond.*, 469:810–813, 2009. 145

[147] Shingai Y *et al.* Improvement of superconducting properties by BaTiO$_3$ doping into ErB$_2$Cu$_3$O$_{7-\delta}$ films. *Physica C Supercond.*, 445-448:841–844, 2006. 145

[148] Mele P *et al.* Incorporation of double artificial pinning centers in YB$_2$Cu$_3$O$_{7-\delta}$ films. *Physica C Supercond.*, 468:1631–1634, 2008. 145